Roland Lachmayer · Behrend Bode · Stefan Kaierle *Editors*

Innovative Product Development by Additive Manufacturing 2021

Springer

Innovative Product Development by Additive Manufacturing 2021

Roland Lachmayer · Behrend Bode ·
Stefan Kaierle
Editors

Innovative Product Development by Additive Manufacturing 2021

Springer

Editors
Roland Lachmayer
Institut for Product Development
Leibniz University Hannover
Garbsen, Germany

Behrend Bode
Institut for Product Development
Leibniz University Hannover
Garbsen, Germany

Stefan Kaierle
Laser Zentrum Hannover e.V.
Hannover, Germany

ISBN 978-3-031-05917-9 ISBN 978-3-031-05918-6 (eBook)
https://doi.org/10.1007/978-3-031-05918-6

This Springer imprint is published by the registered company Springer Nature Switzerland AG
The registered company address is: Gewerbestrasse 11, 6330 Cham, Switzerland

Preamble—Innovative Product Development by Additive Manufacturing 2021

Additive manufacturing processes are already being used successfully in aviation, the automotive industry, mechanical engineering and toolmaking, medical technology and many other areas of our economy. The industry around additive manufacturing machines, materials, services and development tools already employs several hundred thousand people worldwide. Nevertheless, it can be said that additive manufacturing is still a relatively new discipline with high growth prospects and innovation potential that is far from being exhausted. Bionic shapes, graded materials and integrated high-efficiency effects are only at the beginning of their implementation in series products. The advantages of high flexibility, low material input and targeted individualization over conventional processes are far from exhausted.

Key competencies for product creation through additive manufacturing lie in design and development.

Building on the six conference volumes of previous years in German called "Konstruktion für die Additive Fertigung", the book "Innovative Product Development by Additive Manufacturing 2021" provides insights into the most current research and development topics on additive manufacturing.

The individual chapters are divided into the following focal points:

- Design and optimization
- Simulation, validation and quality assurance
- Specifications, potentials and solution finding

For the seventh time, the Institute for Product Development (IPeG) of the Leibniz University Hannover and the Laser Zentrum Hannover e.V. (LZH) held a workshop on the topic of additive manufacturing. This book contains the written elaboration of the papers presented during the workshop.

We would like to thank all participants and the scientific directorate for their contributions and reviews. We would also like to thank the State of Lower Saxony, Niedersachsen Additive and the Scientific Society for Product Development (WiGeP) for their support and provision of financial resources in the various research projects and for hosting the event.

Hannover, Germany
December 2021

Roland Lachmayer
Behrend Bode
Stefan Kaierle

Contents

About the Editors

Univ.-Prof. Dr.-Ing. Roland Lachmayer is founding director and head of the Institute for Product Development (IPeG) at the Leibniz University Hannover. He is a senator of the Leibniz University Hannover, spokesman of the graduate school ‘Tailored Light’, member of the scientific directorate of Laser Zentrum Hannover e.V., managing director of Scientific Society for Product Development (WiGeP) and since 2018 spokesman of the ERDF-funded research network GROTESK. Since 2019, Professor Lachmayer has headed the Additive Manufacturing task group of the PHOENIX-D cluster of excellence. His publications to date include work on development methodology as well as numerous publications on additive manufacturing.

Behrend Bode has been a research associate at the Institute for Product Development (IPeG) at the Leibniz University Hannover since 2019 and is working on the design of thermally and mechanically loaded components for additive manufacturing. Previously, he graduated from the Technical University of Braunschweig with a Master of Science degree in mechanical engineering with a focus on structural dynamics and worked in the field as a visiting researcher at the NASA Langley Research Center and in the automotive industry as a systems engineer.

Prof. Dr.-Ing. Stefan Kaierle is executive director at the Laser Zentrum Hannover e.V. and professor at the Leibniz University Hannover. He is a member of the Board of Stakeholders of the European Technology Platform Photonics21. Since 2011, he has also been working as Executive Editor-in-Chief of the Springer Nature Journal Light: Science & Applications.

Effect-Engineering by Additive Manufacturing

Tobias Ehlers, Ina Meyer, Marcus Oel, Behrend Bode, Paul Christoph Gembarski, and Roland Lachmayer

Abstract

With the help of effect-engineering, highly efficient additively manufactured products with a high-power density can be designed. The potential of product development lies in the conceptualization design and embodiment design phases, which have, however, only been methodically analyzed to a limited extent. Effect-engineering offers the possibility to resolve constructive contradictions and to influence disturbance variables. The research question answered in this article describes how a methodical procedure for effect-engineering must look to design highly efficient products for additive manufacturing. Simulation and multi-criteria optimization are particularly challenging in this context. For this purpose, a framework of effect engineering will be developed and the effects that offer significant added value for additive manufacturing will be shown. Furthermore, new system technologies in additive manufacturing are presented, which serve as enablers of the various effects. As a result of the contribution, the method of effect-engineering is successfully applied to two application examples.

Keywords

Effect-engineering • Design for additive manufacturing (DfAM) • Laser powder bed fusion (LPBF) • Particle damping • Multi-material components

T. Ehlers (✉) · I. Meyer · M. Oel · B. Bode · P. C. Gembarski · R. Lachmayer
Institute of Product Development , Leibniz University Hannover, An der Universität 1, 30823 Garbsen, Germany
e-mail: ehlers@ipeg.uni-hannover.de

R. Lachmayer et al. (eds.), *Innovative Product Development by Additive Manufacturing 2021*, https://doi.org/10.1007/978-3-031-05918-6_1

1 Introduction

The challenges facing our society are manifold and range from the generation of sustainable energy to nationwide mobility and healthcare. Examples include efficient power plants and energy storage systems as well as vehicle drive concepts, but also durable and affordable prostheses and implants. Limited resources are available to meet these challenges. This requires products that fulfill their function in an energy- and material-efficient manner throughout their entire life cycle [1, 2].

Engineers realize the functions of products at the component and system level with the help of effects based on natural laws [3]. The component shape is described by geometry and material. The technology of additive manufacturing enables freedom of design and material engineerings, such as internal structures and graded materials [4, 5]. This makes it possible to manufacture ultra-light components with high load-bearing capacity and functional integration in a resource-saving way.

Effects as working principles can be implemented in this way in a novel, improved, individual or combined way. However, only initial approaches are known for this, which only show the basic mode of operation and are mostly exploratory. For the next generation of product development of structural components, the technology of additive manufacturing, therefore, promises to open up great optimization potential [4].

There is now a whole range of scientific work on the design for additive manufacturing (DfAM), its potential, and the associated process [6–9]. Although the further development of manufacturing and process technology is being intensively accompanied scientifically, there is still a need for research about the interaction between the manufacturing process and the effects to be realized. The question of how to design for additive manufacturing processes has also received little attention so far in the DfAM research field [9, 10]. Only a few papers deal with the realization and optimization of effects through additive manufacturing [11–13] or the question of adapting the design process and suitable procedures, methods, and tools for the product development of additively manufactured components [9].

The decisive phases of conceptualization design and embodiment design have so far only been methodologically analyzed to a limited extent [9, 14, 15]. It is precisely in these phases that there is considerable potential for integrating and combining effects to increase the efficiency of the product and to be able to influence disturbance variables [3]. In particular, the core components of machines should be the focus here. Thus, effects such as damping and structural properties [16], heat and mass transport [17], as well as the guidance of electric or magnetic fields [18] can be combined. Occurring constructive contradictions of the effects can be significantly reduced using additive manufacturing [4, 6].

The aim should therefore be to realize effects through additive manufacturing in such a way that they guarantee optimum functionality with minimum use of resources. If several functions, for example, the conduction of magnetic flux, the reduction of eddy currents and heat transport, are to be realized simultaneously, the interactions are decisive and must be researched and implemented about multi-criteria optimization. To achieve these goals, theory-based concepts and models for the implementation of functions through “printed effects” must be developed, which exploit the material-technical and constructive design possibilities of additive manufacturing. This requires precise knowledge of the interactions between the material, manufacturing process and component design. To this end, this paper presents a framework for effect-engineering that will help to manufacture efficient products with a high degree of functional integration in the future. The potentials of effect-engineering are then demonstrated for two application areas. Finally, new manufacturing technologies in additive manufacturing are presented, which are essential for the implementation of effect-engineering.

2 Potentials of Effect-Engineering

Requirements are the basis of every product development. The requirements resulting from the higher-level objectives, such as a reduction in the use of resources, or an increase in efficiency or service life. The starting point for product development can also be social aspects such as the customer’s desire for increasingly individualized products [19] or the improvement of existing product properties [20], e.g. an increase in performance or improved biocompatibility of materials [21]. The derived requirements for the product are broken down into required product properties and functions [3]. Properties are measurable values that the component must fulfill, such as efficiency or maximum weight. Functions include the conversion of energy, signal or information. For this purpose, the function can be divided into sub-functions. To achieve the defined (sub) functions, suitable effects are combined and implemented in the design of a component. To implement novel design methodologies, it is necessary to extend the existing limits of manufacturing. The combination of different materials through multi-material manufacturing requires a comprehensive understanding of the material system thus created and thus a complete reconsideration of the manufacturing parameters. New concepts must also be developed for both manufacturing and recycling. Figure 1 shows the printed effects in the context of the development methodology to explain the relationship.

The design freedom of additive processes results in outstanding opportunities to mitigate conflicting goals that typically occur in the development process and thus to realize functions more efficiently in components. Up to now, components to be manufactured additively have already been designed about thermal and mechanical properties [22–24]. However, the constructive design is only based on experience. A holistic and systematic approach is missing [25].

Typically, to solve conflicting goals in development, contradictory “disturbing” effects are outsourced to sub-modules and each module is optimized separately. This means that potentials about the higher-level objectives of product development are not exploited.

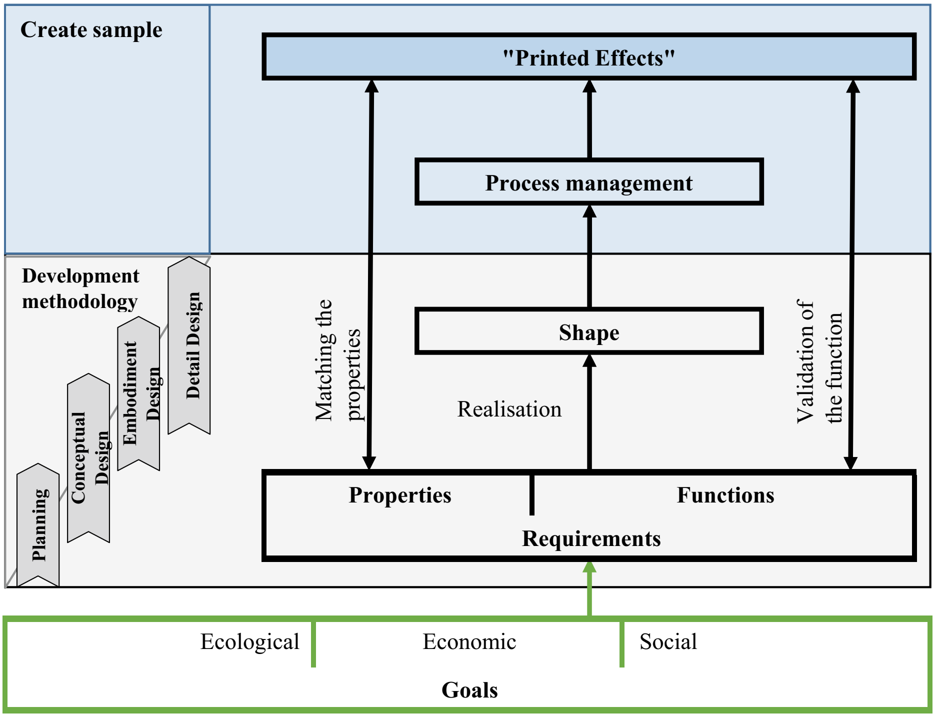

Fig. 1 Development methodology for integrated, highly efficient "printed effects"

However, the higher the realizable degree of effect integration, the better these superordinate objectives are implemented. Therefore, a new approach is needed in product development that takes a holistic view of the effects and attempts to optimize them not individually but in combination. Thus, there is an essential need for research to combine effects and to identify a compromise between contradictory effects, to methodically process them and to optimize the design on this basis.

A successful approach to resolving constructive contradictions is TRIZ or the further development TRIZ REVERSE [26–28]. TRIZ is a collection of methods for the systematic design of innovative products. A result is a methodical tool that can be used to specifically identify and solve contradictions in technical systems [27]. One of these methodological tools is the contradiction matrix in combination with the inventive principles [26, 27]. The inventive principles provide a solution approach for each contradiction, but not a complete solution [27]. The engineer's experiential knowledge is still required to formulate the solution approach.

TRIZ REVERSE is suitable for concretizing these solution approaches [27, 28]. Here, experts take a closer look at an effect and try to assign this effect to different inventive principles to provide solution proposals for different contradictions. In this way, expert knowledge is made generally accessible. TRIZ REVERSE is particularly relevant in the field of additive manufacturing to make new realizations of effects available to the general public.

In [27, 28], an optimization process for TRIZ REVERSE has already been developed, so that the first approaches to development environments have already been established, with the help of which constructive contradictions can be solved in a partially automated way. However, the multi-criteria interpretation of effects and their mappings in development environments remains challenging.

Furthermore, the interactions between the materials used, the manufacturing process and the effects must be systematically analyzed and the efficiency of the effects optimized based on this knowledge. Table 1 shows without claiming to be complete—a collection of effects that provide significant added value for additive manufacturing or could do so in the future.

In the following, the approach of effect-engineering will be exemplified. Effect-engineering is an approach to break down global requirements to local properties. Like in a topology optimization every element within the structure is evaluated and iteratively

Table 1 Effect collection

Nr	Effects	Application	Source
1	Biomedical effects	Drug delivery	[33]
		Tissue engineering	[33]
		Regenerative medicine	[33]
		Endovascular surgery	[34]
		Orthodontics	[34]
		Orthopedics	[34]
		Bioprinting	[35]
		Biomedical devices	[35]
2	Damping effects	Particle damping	
		● Blades and blisks	[36–38]
		● Brake discs	[16, 29]
		● Brake shoe holders	
		● Cutting tool holders	[30]
		● Gears	
		● Motorcycle triple clamps	[31]
		● Wheel carrier	[39]
		Internal structures	
		● Particle accelerators	[40, 41]

(continued)

Table 1 (continued)

Nr	Effects	Application	Source
		● Aerospace components	[42]
3	Electrical effects	Heating elements	[43]
		Electric motors	[44]
		Sensors	[45]
		Flexible circuits	[46]
		Resistive actuators	[47]
4	Magnetic effects	Electric motors	[6, 12, 18, 48]
		Optical lenses	[18, 49]
		Sensors	[50]
5	Shape memory effects	4D printing	[51]
		● Self-assembly	[52]
		● Multi-functionality or self-adaptability	[52–54]
		● Self-repair	[55]
		● Soft robotics	[56]
		Civil engineering	[57]
		High-load actuators	[58]
6	Thermal effects	Heat exchangers HX	[17, 59–62]
		Injection nozzle	[63]
		Injection molds	[64]
		Die casting	[65]
		Pistons	[66]
		Heat sink for Nd: YAG laser crystals	[67]
		Spark plug	[68]
		Gas turbine	[69, 70]
		Actuator	[47, 71]
		Sensors	[47]

decided which properties would benefit the component most. Additive manufacturing enables this approach by locally setting elements into structural materials, powder dampeners [29–31], heat conductors (by filling media into cooling channels, creating isolating air pockets or manufacturing multi-material parts) [32], void or others and therefore setting local properties [4]. To evaluate the efficiency the load on each element of a discretized model is analyzed. Figure 2 shows an example of this optimization process using a discretized beam on which a load spectrum of thermal (T) and mechanical (F, I) loads acts. In the initial situation, the multitude of elements is not loaded, or the material of the

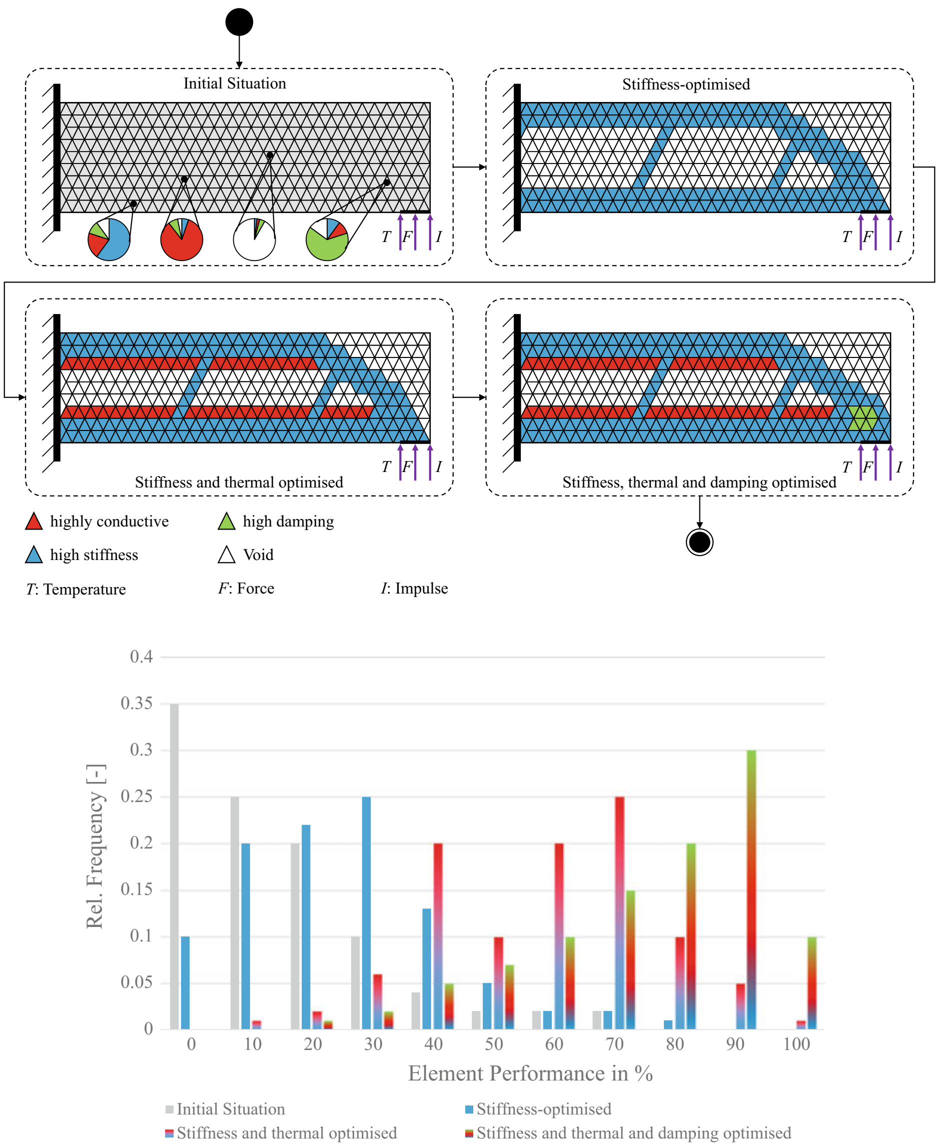

Fig. 2 Performance enhancement through effect-engineering

element is not suitable for the occurring load. To increase the performance, the component must be optimized. With optimization in terms of stiffness, the efficiency can be increased because the component mass can be saved. Nevertheless, with this design method, the component is still not optimally adapted to the further loads (thermal and impulse). To further improve additively manufactured components, more physical effects can be included.

For example, high heat dissipation can be achieved through multi-material production or the integration of cooling channels. To ultimately get the most out of the component, particle dampers should also be integrated into the component. It should be emphasized that the effect-engineering should be formulated as a single optimization problem to be able to calculate the best material distribution. The lower part of Fig. 2 shows an exemplary histogram for the element loading of the individual variants. The element performance is plotted on the abscissa. This describes the degree of stress on the element for the dominant stress type. With such an approach, the optimal material distribution can be realized with minimum weight and thus maximum efficiency, which also increases the power density.

Designing and evaluating these effects in a component is challenging because the internal effects have to be understood and characterized, and algorithms have to be adapted to decide where to put which property. To achieve effect-engineering, several challenges in product design must be mastered. Targeted multi-objective optimizers must be developed for the design, which determines the rough shape. In addition to the simulative design, development environments should be set up with which the process chain in mind [13].

Nevertheless, the methodical procedure for effect-engineering is highly application-specific and is to be shown exemplarily for the dynamic loadings and thermo-mechanical stresses.

The additional degree of freedom due to the combination of two materials allows the integration of a wide range of effects in the product development process. In particular, the use of copper with very high electrical and thermal conductivity in combination with a steel alloy as structural material offers a wide range of potential applications. Examples of utilizing thermal conductivity include the use of multi-material additive manufacturing in heat exchangers. Due to the high thermal conductivity of copper and a large surface area, the heat transfer between media is more efficient, so that the power density of the heat exchanger can be increased. At the same time, sufficient rigidity can be ensured at necessary points and on the housing through the use of steel.

Furthermore, other possible applications are conceivable. For example, tools, like dies in extrusion, can be cooled in a process-integrated manner by using copper in areas close to the surface. In combination with tool steel as secondary material, the necessary strengths for the forming process are nevertheless achieved. In contrast to cooling, induction heating can be used to achieve component heating in forming tools by utilizing the high electrical conductivity of copper. The required copper coil can be integrated directly into the tool using multi-material additive manufacturing.

Integrated coils can also be used to realize component-integrated sensors that detect effects based on electric or magnetic fields. For example, eddy-current testing can be performed by two coils to detect cracks or similar component failures that occur during the product life cycle. Another possible application is the integration of an electromagnetic flowmeter in areas that are located inside a component and therefore cannot be reached with conventional sensors.

To explain and concretize this, two application examples are presented and discussed below in which effect-engineering delivers significant added value. The examples illustrate that effect-engineering is an emerging field and that the potential of additive manufacturing is far from exhausted.

2.1 Application: Design of Particle-Damped Structural Components

Using the effect of particle damping, component vibrations can be reduced by up to a factor of 20 over a broadband [72, 73]. Here, the LPBF offers the possibility of integrating unmelted powder into cavities in a targeted manner [74]. Through particle interactions, the energy can be conducted out of the system and thus the high damping can be realized. A schematic representation of a particle damper can be seen in Fig. 3. In the figure, it can be seen that for a particle-damped beam the vibration amplitude decreases significantly compared to the fully-fused beam. Areas of application are, for example, cutting tool holders turbines/compressor blades or motorcycle triple clamps [31]. Thus, the conflict of objectives between these 3 variables can be resolved in terms of TRIZ REVERSE by the effect of particle damping. For example, the particle-filled cavity can be placed in the area of the neutral fiber so that the stiffness is hardly influenced. However, due to the high nonlinearity, modeling is challenging. For this reason, experimental parameter studies must be carried out to describe the effect so that mechanical substitute models can be derived on this basis. Subsequently, the aim is to build a multi-objective optimizer with which components can be optimized in terms of mass, stiffness and damping. It is particularly challenging to implement a substitute damping in the FDM model, which reproduces the force and frequency-dependent progression. Approaches to partially automated reconstruction must also be taken for the subsequent detailed design.

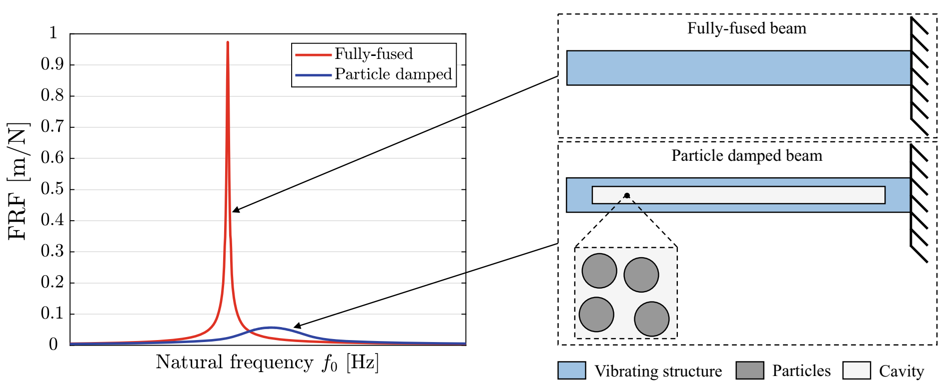

Fig. 3 Schematic representation of a particle damper

2.2 Application: Thermomechanical Systems

Thermal structures have to withstand several types of loading. Mechanical loads have to be transferred from the source (pressure, contact forces, …) to a sink (bearing, balanced against another pressure, …). The path that needs the least amount of material or mass can be found by topology optimization [75, 76]. Usually, the approach here is to remove material where stresses are low. Thermal stresses on the other hand arise from a heat flow through a part. This creates a temperature gradient from the source to the sink. Taking thermal expansion into account elements expand more than their lower temperature neighbors. The Youngs-modulus of the material renders these strains into very high stresses [77, 78]. The issue gets worse when considering that a full metal (or any other structural material) part usually works under high loads. Topology optimization just removes unnecessary mass. Due to the structure-borne loads like thermal stresses do not work out of the box because the right elements have to be removed to reduce stresses. This topic is not new and focuses on several optimization approaches [78–80]. Especially the design freedom created by additive manufacturing is pushing established algorithms to their limits. The presented approaches are all mostly a proof of concept for thermo-mechanical topology optimizations and only show 2D designs with filigree fractal structures similar to heat flow optimizations shown by Bendsøe and Sigmund [76].

Real-world components in high-temperature applications like pistons, exhaust washed structures, turbochargers or turbines experience several types of loads. Vibrations in combination with high demands on fatigue life prohibit fractal structures as described in [81, 82]. Additionally, the high temperatures weaken the material by increasing elastic and plastic deformation. Optimization for these applications must therefore include/derive thermal sinks like cooling channels, consider dynamic loads or at least favor coherent structures and consider mechanical loads.

The effect-engineering approach here is to discretize the structure and analyses each element for the cause of stress (Fig. 4). Then in iterative steps elements are converted to whatever distribute the loading in the structure. This can be, for example, a cooling channel, structural material, or simply void. In this way, not only mechanical loads but also thermal loads can be balanced. An example of an iterative process is presented below.

To ensure material integrity, mechanical and thermal loads must be distributed as evenly as possible across the structure. This is to avoid excessive stresses, damage, and failure in a component subjected to high temperatures and pressures.

2.3 Additive Manufacturing Technologies

The further development of additive manufacturing processes is crucial for the implementation of effect engineering. For example, commercial systems exist for the multi-material production of plastics as well as metals. Using fused layer modeling (FLM) printers, the

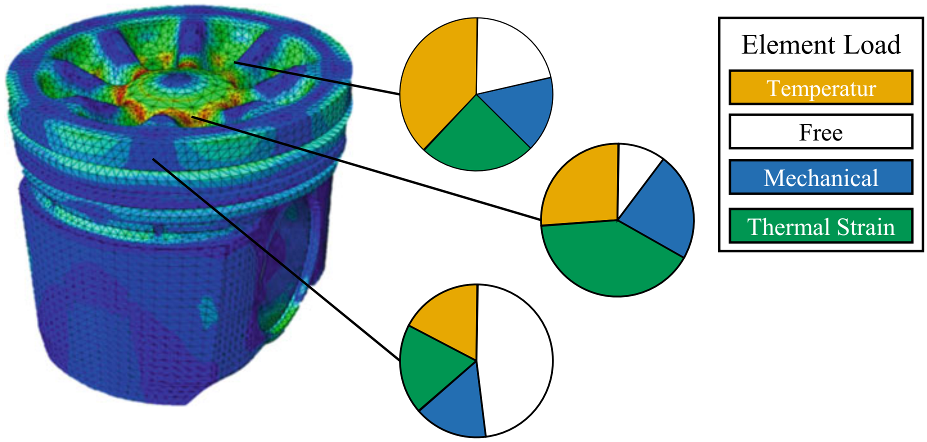

Fig. 4 Figure load distribution due to heat and pressure on a piston designed for additive manufacturing

material can already be varied locally through several nozzles or print heads and, for example, hard and ductile materials can be processed in one component. In addition, the system technology has already reached a stage where sensors can be integrated into components. Either by pausing the building process and inserting the electrical component or by integrating nanoparticles locally directly into the component. However, the latter process is still at the research level.

In the field of metallic multi-material production, systems for build-up welding already exist [83–85]. This makes it easy to produce multi-materials and graded materials. For example, copper cooling channels can be integrated into components or the component hardness can be graded.

In addition to build-up welding, there are also modified LPBF systems that can be used to produce multi-material components [86]. The multi-material design makes it possible to realize physically contradictory effects in one component. Using conventional manufacturing processes, these multi-material components, with arbitrarily complex geometries, can only be realized with intensive technical and economic effort [10].

Figure 5a shows an example of a system for additive manufacturing of multi-materials with the LPBF process that uses drums for the coating mechanism. The special feature is that the respective powder adheres to the surface of the drum by a vacuum and can be selectively detached within a build-up layer. As a result, complex 3D-multi-material components can be generated, which have an arbitrary material distribution in all three spatial directions (see Fig. 5b) Compared to buildup welding, the LPBF process is characterized by a higher precision of the process, which consequently leads to the high accuracy of the part geometry and better surface roughness [87]. Materials that are difficult to weld, such

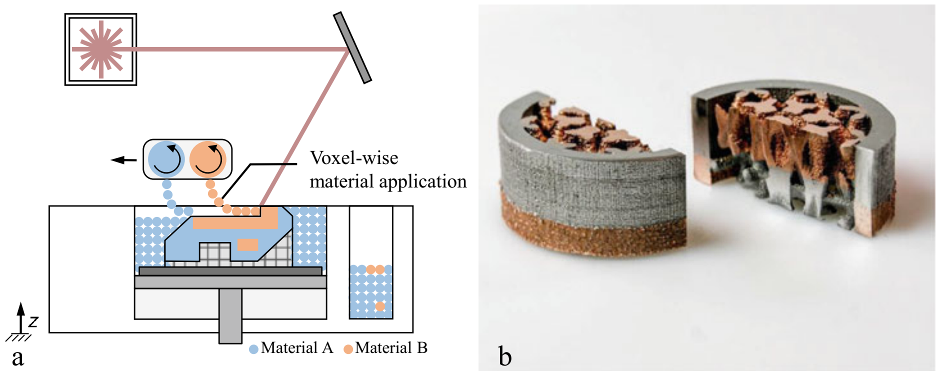

Fig. 5 Construction for the LPBF process with integration of a multi-material coater (**a**), exemplary example of a 3D multi-material component (**b**)

as titanium and aluminum, can be manufactured. However, the long production times and the small installation spaces are disadvantages

3 Conclusion

In this paper, a framework for effect engineering has been built. With the help of effect-engineering, highly efficient additively manufactured products with a high power density can be designed. It was shown that the potentials of product development lie in the phases of conceptualization design and embodiment design and that these have so far only been analyzed methodically to a limited extent. The method of effect-engineering provides the possibility to resolve constructive contradictions and to influence disturbance variables. The method is based on the TRIZ and TRIZ REVERSE approaches. It was discussed that with multi-physical loading, a multitude of effects must be integrated into a single component, such as heat transfer and dampening, to design efficient products. However, simulation and multi-criteria optimization remain challenging. As a result of the contribution, the method of effect engineering has been implemented in the process chain of additive manufacturing (Fig. 6). It can be seen that up to now especially the phases of planning, Pre- In- and Post-process have been methodically examined and now a methodical approach to the phases of conceptualization design and embodiment design has also been developed. As a result of the contribution, the method of effect engineering is successfully applied to two application examples.

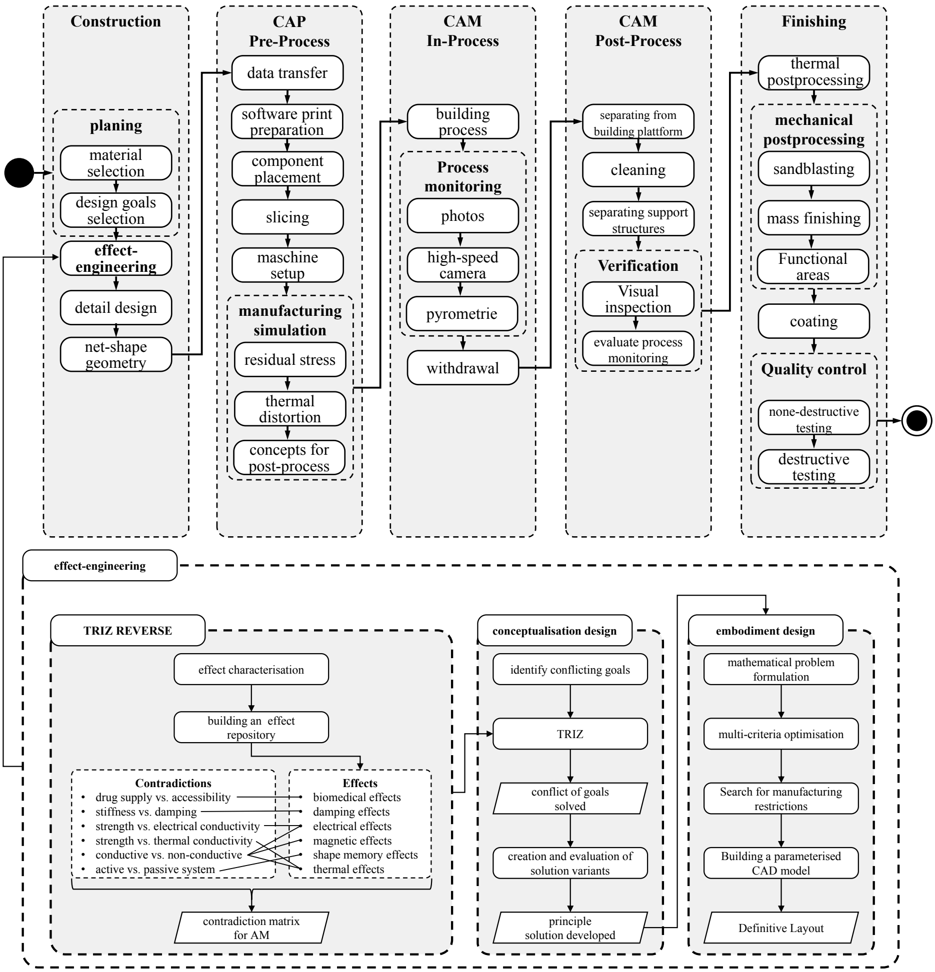

Fig. 6 Classification of effect engineering in the development process of additive manufacturing

References

1. Ehlers, T., Wurst, J., & Lachmayer, R. (2020). Bewertung der ökologischen und ökonomischen Nachhaltigkeit in der Additiven Fertigung. In R. Lachmayer, K. Rettschlag, & S. Kaierle (Eds.), *Konstruktion für die Additive Fertigung 2019* (pp. 177–199). Springer Berlin Heidelberg. https://doi.org/10.1007/978-3-662-61149-4_12
2. Wurst, J., Schneider, J. A., Ehlers, T., Mozgova, I., & Lachmayer, R. (2022). Corporate strategy based quantitative assessment of sustainability indicators at the example of a laser powder bed fusion process. In S. G. Scholz, R. J. Howlett, & R. Setchi (Eds.), *Sustainable design and*

manufacturing (pp. 34–44). Springer Singapore. https://doi.org/10.1007/978-981-16-6128-0_4
3. Roth, K. (2000). *Konstruieren mit Konstruktionskatalogen*, 3. Aufl., erw. und neu gestaltet. Springer. ISBN 9783540671428.
4. Lachmayer, R., Bode, B., Grabe, T., & Rettschlag, K. (2020). Integration spezifischer Effekte in Strukturbauteilen mittels additiver Fertigungsverfahren. In R. Lachmayer, K. Rettschlag, & S. Kaierle (Eds.), *Konstruktion für die Additive Fertigung 2019* (pp. 1–10). Springer Berlin Heidelberg. https://doi.org/10.1007/978-3-662-61149-4_1
5. Ehlers, T., Lippert, R. B., & Lachmayer, R. (2020). Bewertung von Strukturbauteilen aus gradierten Materialien für Selektives Laserstrahlschmelzen. In R. Lachmayer, R. B. Lippert, & S. Kaierle (Eds.), *Konstruktion für die Additive Fertigung 2018* (pp. 109–127). Springer Berlin Heidelberg. https://doi.org/10.1007/978-3-662-59058-4_7
6. Urbanek, S., Keuter, R., Peter, E., & Ponick, B. (2020). Effects of continuous rotor skewing in additively manufactured permanent magnet rotors. In *2020 International Symposium on Power Electronics, Electrical Drives, Automation and Motion (SPEEDAM)* (pp. 662–669). Sorrento, Italy, 24–26 June 2020. IEEE. https://doi.org/10.1109/SPEEDAM48782.2020.9161932
7. Adam, G. A., & Zimmer, D. (2014). Design for additive manufacturing—Element transitions and aggregated structures. *CIRP Journal of Manufacturing Science and Technology, 7*, 20–28. https://doi.org/10.1016/j.cirpj.2013.10.001
8. Hengsbach, F., Koppa, P., Holzweissig, M. J., Aydinöz, M. E., Taube, A., Hoyer, K.-P., Starykov, O., Tonn, B., Niendorf, T., Tröster, T., et al. (2018). Inline additively manufactured functionally graded multi-materials: Microstructural and mechanical characterization of 316L parts with H13 layers. *Progress in Additive Manufacturing, 3*, 221–231. https://doi.org/10.1007/s40964-018-0044-4
9. Kumke, M. (2018). *Methodisches Konstruieren von additiv gefertigten Bauteilen*. Springer Fachmedien Wiesbaden.
10. Lachmayer, R., & Lippert, R. B. (2020). *Entwicklungsmethodik für die Additive Fertigung*. Springer Berlin Heidelberg. ISBN 978-3-662-59788-0.
11. Rosa, F., Manzoni, S., & Casati, R. (2018). Damping behavior of 316L lattice structures produced by selective laser melting. *Materials & Design, 160*, 1010–1018. https://doi.org/10.1016/j.matdes.2018.10.035
12. Urbanek, S., & Ponick, B. (2018). Surface eddy current loss reduction in additively manufactured permanent magnet rotor active parts. In *2018 XIII International Conference on Electrical Machines (ICEM)* (pp. 1317–1322). Alexandroupoli, 03–06 Sept 2018. IEEE. https://doi.org/10.1109/ICELMACH.2018.8507151
13. Müller, P., Gembarski, P. C., & Lachmayer, R. (2021). Spezifikationen einer Entwicklungsumgebung zur Synthese einer patientenindividuellen Kurzschaftendoprothese der Hüfte. In H. Binz, B. Bertsche, D. Spath, & D. Roth (Eds.), *Stuttgarter Symposium für Produktentwicklung SSP 2021: Stuttgart, 20 Mai 2021, Wissenschaftliche Konferenz*. Fraunhofer-Institut für Arbeitswirtschaft und Organisation IAO. https://doi.org/10.18419/opus-11478
14. Yang, S., Tang, Y., & Zhao, Y. F. (2016). Assembly-level design for additive manufacturing: Issues and benchmark. In *Volume 2A: 42nd Design Automation Conference. ASME 2016 International Design Engineering Technical Conferences and Computers and Information in Engineering Conference*, Charlotte, North Carolina, USA, 21–24 Aug. 2016. American Society of Mechanical Engineers. https://doi.org/10.1115/DETC2016-59565
15. Tang, Y., Yang, S., & Zhao, Y. F. (2016). Sustainable design for additive manufacturing through functionality integration and part consolidation. In S. S. Muthu & M. M. Savalani (Eds.), *Handbook of sustainability in additive manufacturing* (pp. 101–144). Springer Singapore. https://doi.org/10.1007/978-981-10-0549-7_6

16. Künneke, T., & Zimmer, D. (2017). Funktionsintegration additiv gefertigter Dämpfungsstrukturen bei Biegeschwingungen. In H. A. Richard, B. Schramm, & T. Zipsner (Eds.), *Additive Fertigung von Bauteilen und Strukturen* (pp. 61–74). Springer Fachmedien Wiesbaden. https://doi.org/10.1007/978-3-658-17780-5_4
17. Zhang, C., Wang, S., Li, J., Zhu, Y., Peng, T., & Yang, H. (2020). Additive manufacturing of products with functional fluid channels: A review. *Additive Manufacturing, 36*, 101490. https://doi.org/10.1016/j.addma.2020.101490
18. Biermann, T., Ziebehl, A., Grabe, T., Röttger, J., Ley, P.-P., Wolf, A., & Lachmayer, R. (2021). Magnetically actuated solid body PDMS lens. In M. J. Digonnet & S. Jiang (Eds.), *Optical components and materials XVIII* (p. 30). Online Only, United States, 06–12 March 2021. SPIE. https://doi.org/10.1117/12.2578551
19. Lachmayer, R., Gembarski, P. C., Gottwald, P., & Lippert, R. B. (2017). The potential of product customization using technologies of additive manufacturing. In J. Bellemare, S. Carrier, K. Nielsen, & F. T. Piller (Eds.), *Managing complexity* (pp. 71–81). Springer International Publishing. https://doi.org/10.1007/978-3-319-29058-4_6
20. Ehlers, T., Lachmayer, R., Vajna, S., & Halle, T. (2020). Producibility. In S. Vajna (Ed.), *Integrated design engineering* (pp. 287–323). Springer International Publishing. https://doi.org/10.1007/978-3-030-19357-7_9
21. Harun, W., Kamariah, M., Muhamad, N., Ghani, S., Ahmad, F., & Mohamed, Z. (2018). A review of powder additive manufacturing processes for metallic biomaterials. *Powder Technology, 327*, 128–151. https://doi.org/10.1016/j.powtec.2017.12.058
22. Grabe, T., Lammers, M., Wang, S., Wang, X., Rettschlag, K., Sleiman, K., Barroi, A., Biermann, T., Ziebehl, A., Röttger, J., et al. (2021). Additive anufacturing of fused silica using coaxial laser glass deposition: Experiment, simulation and discussion. In H. Helvajian, B. Gu, & H. Chen (Eds.), *Laser 3D manufacturing VIII* (p. 32). Online Only, United States, 06–12 March 2021. SPIE. https://doi.org/10.1117/12.2577205
23. Reiher, T. (2018). *Intelligente Optimierung von Produktgeometrien für die additive Fertigung*. Dissertation, Shaker Verlag.
24. Wiberg, A., Persson, J., & Ölvander, J. (2019). Design for additive manufacturing – A review of available design methods and software. *RPJ, 25*, 1080–1094. https://doi.org/10.1108/RPJ-10-2018-0262
25. Emmelmann, C., Sander, P., Kranz, J., & Wycisk, E. (2011). Laser additive manufacturing and bionics: Redefining lightweight design. *Physics Procedia, 12*, 364–368. https://doi.org/10.1016/j.phpro.2011.03.046
26. Koltze, K., & Souchkov, V. (2010). *Systematische Innovation: TRIZ-Anwendung in der Produkt- und Prozessentwicklung* (1st ed.). Carl Hanser Fachbuchverlag.
27. Brockmöller, T., Mozgova, I., & Lachmayer, R. (2017). An approach to analyse the potential of tailored forming by TRIZ reverse. In *Proceedings of the 21st International Conference on Engineering Design (ICED 17)* (Vol. 4, pp. 445–452). Design Methods and Tools.
28. Kloock-Schreiber, D., Brockmöller, T., Schneider, J., Gembarski, P., Mozgova, I., & Lachmayer, R. (2020). TRIZ-reverse for PSS potential determination. Novi Sad, Serbia, sn
29. Künneke, T., & Zimmer, D. (2021). Konstruktionsregeln für additiv gefertigte Partikeldämpfer/design rules for additive manufactured particle dampers. *Konstruktion, 73*, 72–78. https://doi.org/10.37544/0720-5953-2021-11-12-72
30. Vogel, F. A., Berger, S., Özkaya, E., & Biermann, D. (2019). Vibration suppression in turning $TiAl_6V_4$ using additively manufactured tool holders with specially structured, particle filled hollow elements. *Procedia Manufacturing, 40*, 32–37. https://doi.org/10.1016/j.promfg.2020.02.007

31. Ehlers, T., & Lachmayer, R. (2021). Design of a motorcycle triple clamp optimised for stiffness and damping. In S. Pfingstl, A. Horoschenkoff, P. Höfer, & M. Zimmermann (Eds.), *Proceedings of the Munich Symposium on Lightweight Design 2020* (pp. 1–17). Springer Berlin Heidelberg. https://doi.org/10.1007/978-3-662-63143-0_1
32. Richard, H. A., Schramm, B., & Zipsner, T. (Eds.), *Additive Fertigung von Bauteilen und Strukturen*. Springer Fachmedien Wiesbaden. https://doi.org/10.1007/978-3-658-17780-5
33. Singh, S., & Ramakrishna, S. (2017). Biomedical applications of additive manufacturing: Present and future. *Current Opinion in Biomedical Engineering, 2*, 105–115. https://doi.org/10.1016/j.cobme.2017.05.006
34. Sabahi, N., Chen, W., Wang, C.-H., Kruzic, J. J., & Li, X. (2020). A review on additive manufacturing of shape-memory materials for biomedical applications. *JOM Journal of the Minerals Metals and Materials Society, 72*, 1229–1253. https://doi.org/10.1007/s11837-020-04013-x
35. Ahangar, P., Cooke, M. E., Weber, M. H., & Rosenzweig, D. H. (2019). Current biomedical applications of 3D printing and additive manufacturing. *Applied Sciences, 9*, 1713. https://doi.org/10.3390/app9081713
36. Scott-Emuakpor, O., George, T., Runyon, B., Holycross, C., Langley, B., Sheridan, L., O'Hara, R., Johnson, P., & Beck, J. (2018). Investigating damping performance of laser powder bed fused components with unique internal structures. In *Volume 7C: Structures and Dynamics. ASME Turbo Expo 2018: Turbomachinery Technical Conference and Exposition*, Oslo, Norway, 11–15 June 2018. American Society of Mechanical Engineers. https://doi.org/10.1115/GT2018-75977
37. Scott-Emuakpor, O., George, T., Runyon, B., Langley, B., Sheridan, L., Holycross, C., O'Hara, R., & Johnson, P. (2019). Forced-response verification of the inherent damping in additive manufactured specimens. In S. Kramer, J. L. Jordan, H. Jin, J. Carroll, & A. M. Beese (Eds.), *Mechanics of additive and advanced manufacturing* (Vol. 8, pp 81–86). Springer International Publishing. https://doi.org/10.1007/978-3-319-95083-9_15
38. Scott-Emuakpor, O., Beck, J., Runyon, B., & George, T. (2021). Determining unfused powder threshold for optimal inherent damping with additive manufacturing. *Additive Manufacturing, 38*, 101739. https://doi.org/10.1016/j.addma.2020.101739
39. Ganter, N. V., Ehlers, T., Gembarski, P. C., & Lachmayer, R. (2021). Additive refurbishment of a vibration-loaded structural component. *Proceedings of the Design Society, 1*, 345–354. https://doi.org/10.1017/pds.2021.35
40. Andresen, S. (2018). Untersuchung von Eigenschwingung und Leichtbaupotenzial unterschiedlicher Gitterstrukturen am Beispiel von Magnetuntergestellen von Teilchenbeschleunigern. In *NAFEMS DACH Regional Conference*.
41. Andresen, S., Bäger, A., & Hamm, C. (2020). Eigenfrequency maximisation by using irregular lattice structures. *Journal of Sound and Vibration, 465*, 115027. https://doi.org/10.1016/j.jsv.2019.115027
42. Cheng, L., Liang, X., Belski, E., Wang, X., Sietins, J. M., Ludwick, S., & To, A. (2018). Natural frequency optimization of variable-density additive manufactured lattice structure: Theory and experimental validation. *Journal of Manufacturing Science and Engineering, 140*. https://doi.org/10.1115/1.4040622
43. Koopmann, J. (2019). *Multimaterialdruck von integrierten elektrischen Strukturen mittels selektivem Laserschmelzen*. Dissertation, Kassel University Press GmbH.
44. Rudolph, J., Lorenz, F., & Werner, R. (2018). Herstellung elektrischer Motoren mittels 3D-Multimaterialdruck. *awIC, 3*. https://doi.org/10.14464/awic.v3i0.275
45. Binder, M., Anstaett, C., Reisch, R., Schlick, G., Seidel, C., & Reinhart, G. (2018). Automated manufacturing of mechatronic parts by laser-based powder bed fusion. *Procedia Manufacturing, 18*, 12–19. https://doi.org/10.1016/j.promfg.2018.11.002

46. Abt, M., Roch, A., Qayyum, J. A., Pestotnik, S., Stepien, L., Abu-Ageel, A., Wright, B., Ulusoy, A. C., Albrecht, J., Harle, L., et al. (2018). Aerosol-printed highly conductive Ag transmission lines for flexible electronic devices. *IEEE Transactions on Components, Packaging and Manufacturing Technology, 8*, 1838–1844. https://doi.org/10.1109/TCPMT.2018.2869977
47. Wang, G., Cheng, T., Do, Y., Yang, H., Tao, Y., Gu, J., An, B., & Yao, L. (2018). Printed paper actuator. In R. Mandryk, M. Hancock, M. Perry, & A. Cox (Eds.) *Proceedings of the 2018 CHI Conference on Human Factors in Computing Systems, CHI'18* (pp 1–12). Montreal QC Canada, 21–26 April 2018. ACM. https://doi.org/10.1145/3173574.3174143
48. Urbanek, S., Ponick, B., Taube, A., Hoyer, K.-P., Schaper, M., Lammers, S., Lieneke, T., & Zimmer, D. (2018). Additive manufacturing of a soft magnetic rotor active part and shaft for a permanent magnet synchronous machine. In *2018 IEEE Transportation Electrification Conference and Expo (ITEC)* (pp. 668–674). Long Beach, CA, USA, 13–15 June 2018. IEEE. https://doi.org/10.1109/ITEC.2018.8450250
49. Ziebehl, A., Biermann, T., Grabe, T., Röttger, J., Ley, P.-P., Wolf, A., & Lachmayer, R. (2021). *Potentials and challenges in additive manufacturing of nanoparticle-infused silicone optics.*
50. Wu, S.-Y., Yang, C., Hsu, W., & Lin, L. (2015). RF wireless lc tank sensors fabricated by 3D additive manufacturing. In *2015 Transducers—2015 18th International Conference on Solid-State Sensors, Actuators and Microsystems (TRANSDUCERS)* (pp. 2208–2211).
51. Momeni, F., Mehdi Hassani, N. S. M., Liu, X., & Ni, J. (2017). A review of 4D printing. *Materials & Design*, *122*, 42–79. https://doi.org/10.1016/j.matdes.2017.02.068
52. Tibbits, S. (2014). 4D printing: Multi-material shape change. *Archit Design, 84*, 116–121. https://doi.org/10.1002/ad.1710
53. Khademhosseini, A., & Langer, R. (2016). A decade of progress in tissue engineering. *Nature Protocols, 11*, 1775–1781. https://doi.org/10.1038/nprot.2016.123
54. Zarek, M., Mansour, N., Shapira, S., & Cohn, D. (2017). 4D printing of shape memory-based personalized endoluminal medical devices. *Macromolecular Rapid Communications, 38*. https://doi.org/10.1002/marc.201600628
55. Taylor, D. L., & Het Panhuis, M. (2016). Self-healing hydrogels. *Advanced Materials, 28*, 9060–9093. https://doi.org/10.1002/adma.201601613
56. Zolfagharian, A., Kaynak, A., & Kouzani, A. (2020). Closed-loop 4D-printed soft robots. *Materials & Design, 188*, 108411. https://doi.org/10.1016/j.matdes.2019.108411
57. Dolce, M., & Cardone, D. (2006). Theoretical and experimental studies for the application of shape memory alloys in civil engineering. *Journal of Engineering Materials and Technology, 128*, 302–311. https://doi.org/10.1115/1.2203106
58. Gustmann, T., Schwab, H., Kühn, U., & Pauly, S. (2018). Selective laser remelting of an additively manufactured Cu-Al-Ni-Mn shape-memory alloy. *Materials & Design, 153*, 129–138. https://doi.org/10.1016/j.matdes.2018.05.010
59. Kim, J., & Yoo, D.-J. (2020). 3D printed compact heat exchangers with mathematically defined core structures. *Journal of Computational Design and Engineering, 7*, 527–550. https://doi.org/10.1093/jcde/qwaa032
60. Niknam, S. A., Mortazavi, M., & Li, D. (2021). Additively manufactured heat exchangers: A review on opportunities and challenges. *International Journal of Advanced Manufacturing Technology, 112*, 601–618. https://doi.org/10.1007/s00170-020-06372-w
61. Scheithauer, U., Kordaß, R., Noack, K., Eichenauer, M. F., Hartmann, M., Abel, J., Ganzer, G., & Lordick, D. (2019). Potentials and challenges of additive manufacturing technologies for heat exchanger. In L. Castro Gómez & V. Manuel Velázquez Flores (Eds.), *Advances in heat exchangers*. IntechOpen. https://doi.org/10.5772/intechopen.80010

62. Wang, G., Gu, Y., Zhao, L., Xuan, J., Zeng, G., Tang, Z., & Sun, Y. (2019). Experimental and numerical investigation of fractal-tree-like heat exchanger manufactured by 3D printing. *Chemical Engineering Science, 195*, 250–261. https://doi.org/10.1016/j.ces.2018.07.021
63. Schneck, M., Horn, M., Schindler, M., & Seidel, C. (2022). Capability of multi-material laser-based powder bed fusion—Development and analysis of a prototype large bore engine component. *Metals, 12*, 44. https://doi.org/10.3390/met12010044
64. Shinde, M. S., & Ashtankar, K. M. (2017). Additive manufacturing–assisted conformal cooling channels in mold manufacturing processes. *Advances in Mechanical Engineering, 9*. https://doi.org/10.1177/1687814017699764
65. Armillotta, A., Baraggi, R., & Fasoli, S. (2014). SLM tooling for die casting with conformal cooling channels. *International Journal of Advanced Manufacturing Technology, 71*, 573–583. https://doi.org/10.1007/s00170-013-5523-7
66. Belgiorno, G., Boscolo, A., Dileo, G., Numidi, F., Pesce, F. C., Vassallo, A., Ianniello, R., Beatrice, C., & Di Blasio, G. (2021). Experimental study of additive-manufacturing-enabled innovative diesel combustion bowl features for achieving ultra-low emissions and high efficiency. *SAE International Journal of Advances and Current Practices in Mobility, 3*, 672–684. https://doi.org/10.4271/2020-37-0003
67. Grabe, T., Budde, J., Kranert, F., Wienke, A., Neumann, J., Kracht, D., & Lachmayer, R. (2020). Kühlkörper-Designansatz für einen in AlSi10Mg eingebetteten YAG-Laserkristall. In R. Lachmayer, K. Rettschlag, & S. Kaierle (Eds.), *Konstruktion für die Additive Fertigung 2019* (pp. 159–175). Springer Berlin Heidelberg. https://doi.org/10.1007/978-3-662-61149-4_11
68. Binder, M., Anstaett, C., Herzer, F., Horn, M., Schlick, G., Schilp, J., & Reinhart, G. (2018). Potentials and challenges of multi-material processing by laser-based powder bed fusion. In *Solid Freeform Fabrication 2018: Proceedings of the 29th Annual International Solid Freeform Fabrication Symposium – An Additive Manufacturing Conference,* Austin, Texas, USA, August 13–15, 2018.
69. Fu, W., Haberland, C., Klapdor, E. V., Rule, D., & Piegert, S. (2018). Streamlined frameworks for advancing metal based additive manufacturing technologies. *Journal of the Global Power and Propulsion Society, 2*, QJLS4L. https://doi.org/10.22261/JGPPS.QJLS4L
70. Walachowicz, F., Bernsdorf, I., Papenfuss, U., Zeller, C., Graichen, A., Navrotsky, V., Rajvanshi, N., & Kiener, C. (2017). Comparative energy, resource and recycling lifecycle analysis of the industrial repair process of gas turbine burners using conventional machining and additive manufacturing. *Journal of Industrial Ecology, 21*, S203–S215. https://doi.org/10.1111/jiec.12637
71. Zhang, Y.-F., Zhang, N., Hingorani, H., Ding, N., Wang, D., Yuan, C., Zhang, B., Gu, G., & Ge, Q. (2019). Fast-response, stiffness-tunable soft actuator by hybrid multimaterial 3D printing. *Advanced Functional Materials, 29*, 1806698. https://doi.org/10.1002/adfm.201806698
72. Ehlers, T., Tatzko, S., Wallaschek, J., & Lachmayer, R. (2021). Design of particle dampers for additive manufacturing. *Additive Manufacturing, 38*, 101752. https://doi.org/10.1016/j.addma.2020.101752
73. Ehlers, T., & Lachmayer, R. (2022). Design of particle dampers for laser powder bed fusion. *Applied Sciences, 12*, 2237. https://doi.org/10.3390/app12042237
74. Ehlers, T., & Lachmayer, R. (2020). Einsatz additiv gefertigter Partikeldämpfer – eine Übersicht. In R. Lachmayer, K. Rettschlag, & S. Kaierle (Eds.), *Konstruktion für die Additive Fertigung 2019* (pp. 123–142). Springer Berlin Heidelberg. https://doi.org/10.1007/978-3-662-61149-4_9
75. Da Silva de Siqueira, R., Mozgova, I., & Lachmayer, R. (2019). An interfacial zone evolutionary optimization method with manufacturing constraints for hybrid components. *Journal of Computational Design and Engineering, 6*, 387–397. https://doi.org/10.1016/j.jcde.2018.10.003

76. Bendsøe, M. P., & Sigmund, O. (2004). *Topology optimization: Theory, methods, and applications*. Springer Berlin Heidelberg. ISBN 978-3-642-07698-5.
77. Barron, R. F., & Barron, B. R. *Design for thermal stresses*. Wiley. ISBN 9780470627693.
78. Rodrigues, H., & Fernandes, P. (1995). A material based model for topology optimization of thermoelastic structures. *International Journal for Numerical Methods in Engineering, 38*, 1951–1965. https://doi.org/10.1002/nme.1620381202
79. Deaton, J. D., & Grandhi, R. V. (2013). Topology optimization of thermal structures with stress constraints. In *54th AIAA/ASME/ASCE/AHS/ASC Structures, Structural Dynamics, and Materials Conference*. Boston, Massachusetts; American Institute of Aeronautics and Astronautics. https://doi.org/10.2514/6.2013-1466
80. Haney, M. A. (2006). *Topology optimization of engine exhaust-washed structures*. Wright State University.
81. Caivano, R., Tridello, A., Codegone, M., & Chiandussi, G. (2021). A new methodology for thermostructural topology optimization: Analytical definition and validation. *Proceedings of the Institution of Mechanical Engineers, Part L: Journal of Materials: Design and Applications, 235*, 481–500. https://doi.org/10.1177/1464420720970246
82. Song, L., Gao, T., Tang, L., Du, X., Zhu, J., Lin, Y., Shi, G., Liu, H., Zhou, G., & Zhang, W. (2021). An all-movable rudder designed by thermo-elastic topology optimization and manufactured by additive manufacturing. *Computers & Structures, 243*, 106405. https://doi.org/10.1016/j.compstruc.2020.106405
83. Thivillon, L., Bertrand, P., Laget, B., & Smurov, I. (2009). Potential of direct metal deposition technology for manufacturing thick functionally graded coatings and parts for reactors components. *Journal of Nuclear Materials, 385*, 236–241. https://doi.org/10.1016/j.jnucmat.2008.11.023
84. Vaezi, M., Chianrabutra, S., Mellor, B., & Yang, S. (2013). Multiple material additive manufacturing – Part 1: A review. *Virtual and Physical Prototyping, 8*, 19–50. https://doi.org/10.1080/17452759.2013.778175
85. Bandyopadhyay, A., & Heer, B. (2018). Additive manufacturing of multi-material structures. *Materials Science and Engineering: R: Reports, 129*, 1–16. https://doi.org/10.1016/j.mser.2018.04.001
86. Anstaett, C., Seidel, C., & Reinhart, G. (2017). Fabrication of 3D-multi-material parts by laser beam based powder bed fusion. In *International Solid Freeform Fabrication Symposium* (pp. 1548–1556).
87. Wei, C., Zhang, Z., Cheng, D., Sun, Z., Zhu, M., & Li, L. (2021). An overview of laser-based multiple metallic material additive manufacturing: From macro- to micro-scales. *International Journal of Extreme Manufacturing, 3*, 12003. https://doi.org/10.1088/2631-7990/abce04

Design and Optimization

Wire-and-Arc-Additive-Manufacturing of a Component with a Pre-defined Hardness Profile

Lennart Hölscher, Torben Carstensen, and Thomas Hassel

Abstract

Wire-and-arc-additive-manufacturing (WAAM) can be employed with Gas-Metal-Arc-Welding, Gas-Tungsten-Arc-Welding or Plasma-Welding to manufacture steel parts with higher deposition rates than other additive manufacturing processes. WAAM can be used to produce graded components. A graded component can be described as a component with varying material properties, such as varying hardness. The work focuses on manufacturing a component out of G3Si1 with a pre-defined hardness profile. The targeted hardness profile was a constantly increasing hardness along the build direction. Since the hardness of steel is strongly dependent on the cooling rate, faster cooling rates in upper layers are desired. A calculation of the components thermal behavior was used to detect the necessary trends of the process parameters. Finally, a component with the planned process parameters was manufactured and the resulting hardness profile was evaluated.

Keywords

Wire-and-arc-additive-manufacturing • Graded component • Welding parameters

L. Hölscher (✉) · T. Carstensen · T. Hassel
Institut für Werkstoffkunde (Materials Science), Leibniz University Hannover, An der Universität 2, 30823 Garbsen, Germany
e-mail: hoelscher@iw.uni-hannover.de

R. Lachmayer et al. (eds.), *Innovative Product Development by Additive Manufacturing 2021*, https://doi.org/10.1007/978-3-031-05918-6_2

Nomenclature

Value	Unit	Description
b	m	Wall width
σ	$\frac{\mathrm{W}}{\mathrm{m}^2\mathrm{K}^4}$	Stefan-Boltzmann constant
c_{steel}	$\frac{\mathrm{kJ}}{\mathrm{kg\,K}}$	Specific heat capacity of G3Si
d_{wire}	m	Wire diameter
I	A	Current
m_{steel}	kg	Mass of one layer
q	J	Heat input
Q	kJ	Heat quantity
t	s	Duration
T_{steel}	K	Total temperature change
U	V	Voltage
v_{wire}	m/s	Wire feed speed
w	m	Weld bead width
x	m	Distance in build-up direction
α_{cond}	$\frac{\mathrm{W}}{\mathrm{m}^2\,\mathrm{K}}$	Conduction coefficient
α_{conv}	$\frac{\mathrm{W}}{\mathrm{m}^2\,\mathrm{K}}$	Convection coefficient
$\Delta T_{\mathrm{conduction}}$	K	Temperature change based on conduction
$\Delta T_{\mathrm{convection}}$	K	Temperature change based on convection
$\Delta T_{\mathrm{emission}}$	K	Temperature change based on emission
ε	1	Emission coefficient
η	1	Efficiency rate
λ	$\frac{\mathrm{W}}{\mathrm{m\,K}}$	Heat conductivity
ρ	$\frac{\mathrm{kg}}{\mathrm{m}^3}$	Density

1 Introduction

Additive manufacturing (AM) describes manufacturing processes, which allow the production of components by depositing material layer-wise on each other. AM offers the possibility to manufacture complex parts with low buy-to-fly ratios. The buy-to-fly ratio is the ratio of material input to output [1]. Different additive manufacturing processes for producing steel parts have been described in literature. These can be, amongst others subdivided into powder bed fusion (PBF) and direct energy deposition (DED) processes

[2, 3]. Examples for PBF processes are Selective-Laser-Melting (SLM) or Selective-Laser-Sintering (SLS) [4]. One way to differentiate DED processes is by the energy type. There are DED processes, which work with a laser like Laser-Metal-Deposition (LMD), with an electron beam (EBMD) or with an arc like the Wire-and-arc-additive-manufacturing (WAAM) process [3, 5]. WAAM can be done with different welding processes like Gas-Tungsten-Arc-Welding (GTAW), Gas-Metal-Arc-Welding (GMAW) or Plasma-Arc-Welding (PAW) [6].

Rodrigues et al. study the effect of different travel speeds on the hardness and microstructure. Therefore, two samples out of a low-carbon high-strength steel (AWS A5.28 ER110S-G) with different travel speeds are manufactured. It is shown, that the hardness decreases along the build direction. It is also shown, that with more heat input (=lower travel speed) the hardness shows a stronger decrease as with less heat input [7].

Marinelli et al. use GTAW to produce a component out of two different materials. Therefore, the authors build a component with two wires on top of a tantalum plate. They use one wire made from molybdenum and one tungsten wire. The first eight layers are produced with the molybdenum wire, while the ongoing six are manufactured with a tungsten wire. After the wire switch, a reduced wire feed speed is used to manufacture the first three layers. This leads to a non-uniform element composition within the work piece. The result is a component with a varying hardness through build-up direction [8].

To increase the build-up speed different cooling methods for WAAM have been studied. Reisgen et al. build-up work pieces out of G3Si1 to compare different cooling techniques. Water bath cooling, cooling with pressured air and aerosol cooling are compared with each other. For water bath cooling, the work piece is submerged, so that only the highest 10 mm are above the surface. Pressured air-cooling blows pressured air onto the work piece during idle times. Aerosol cooling works during the deposition process. Aerosol cooling blows a mixture of water and air, 500 mm behind the welding torch, onto the work piece. It is shown that water bath cooling has the highest cooling rates [9]. The cooling rate is an important factor for the work piece hardness. As faster, the cooling rate as harder the work piece.

Henckell et al. build a WAAM component out of low-alloyed steel (G4Si1/SG3) with two different contact-tip-working-distance (CTWD) in GMAW. Microhardness analysis show an increased hardness in the first layers, a constant hardness profile in the middle of the component and another hardness rise in the last few layers. The hardness profile is shown in Fig. 1. It was shown, that a higher CTWD led to shorter $t_{8/5}$-duration and thereby to a harder deposition. The $t_{8/5}$-duration describes the duration of a work piece to cool down from 800 to 500 °C. This is caused by the lower energy input per unit length due to the higher CTWD [10].

In this work, the process parameters are planned in a way so that the achieved hardness profile continuously increases through the build-up direction. The parameters to differ is the cooling duration between the layers, the travel speed and the wire feed speed. By evaluating the heat behavior of the work piece, process parameter trends, which lead to

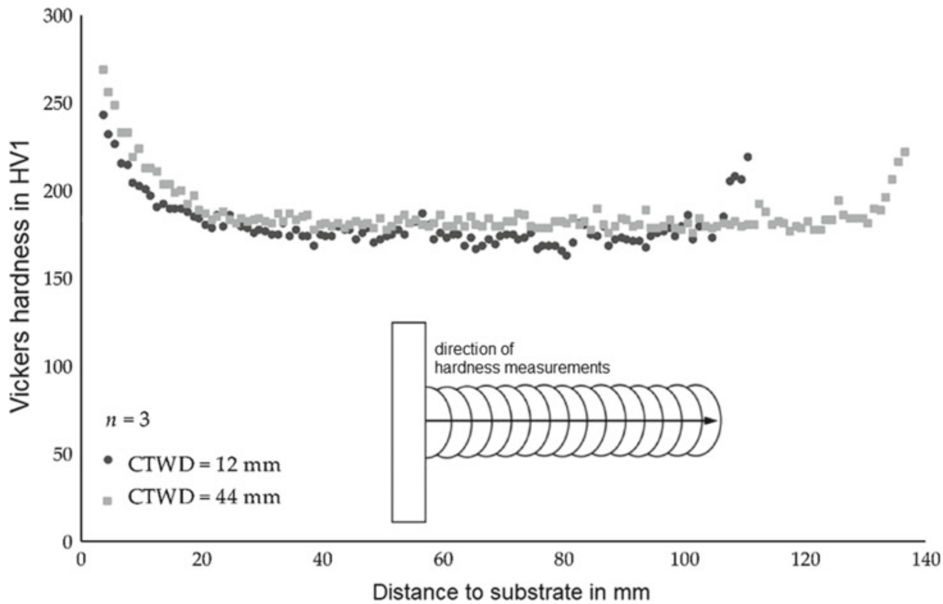

Fig. 1 Hardness profile along build-up direction, by [10] (licensed under creative-commons)

an increasing cooling rate are found. Higher cooling rates lead to a finer microstructure. Due to the Hall–Petch relationship, a finer microstructure results in a harder deposition [11].

The work piece hardness is an important factor for milling, since lower hardness leads to less tool wear and shorter milling times. WAAM parts often need to be removed from the substrate plate, with lower hardness in the lower layers, the used saw blades can last longer. WAAM can be used for building bridges, profiles, turbine blades and injection molding tools [12–14].

2 Materials and Methods

The specimen geometry can be descripted as a wall shaped component. It is manufactured by moving the torch along a distance of 40 mm for 30 stacked layers. It is deposited on a small substrate plate, which has the dimensions 12 × 7 × 70 mm. Since the small substrate plate cannot be properly connected to the welding power source. The plate is fixed on another substrate plate with two tack welds. To minimize heat conduction an air gap of 2 mm is left between the plates. The arc starting point is switched after each layer. The travel speed is set to 400 mm/min. The torch is kept at the same position 1 s after the arc start and 0.5 s before the arc stops. Before the pressured air cooling starts a waiting time of 1 s is held. The weld beads are deposited on a steel plate made out of S235J. The chosen welding process is Gas-Metal-Arc-Welding (GMAW). It is chosen, because it is widely applied in the industry and offers high build-up rates [15].

The manufacturing is done on a KUKA KR16 with an attached Abicor Binzel ROBO WH W 500 torch. The current is supplied by an EWM Titan XQ 400 puls inverter welding power source. Two work pieces are manufactured. One work piece is manufactured with constant parameters within the whole build-up process. A second work piece is manufactured with changing cooling durations, currents and travel speeds determined based on a calculation of the thermal development inside the component (see Sect. 3). The cooling is done after the deposition by blowing pressured air (5 bar) through a nozzle on the work piece. A welding wire specified as EN ISO 14341-A: G3 Si1-8 is chosen. It is chosen, because it is widely applied in the industry and shows a big hardness difference in TTT-diagram [16]. The chemical composition of the wire is shown in Table 1.

A mixture of Argon and CO_2 is used as process gas. The mixture is standardized in ISO 14175 as M21 with a composition of 82% Argon and 18% CO_2. The gas flow is set to 10 l/min. The CTWD is set to 12 mm. The torch is raised by 1.1 mm after each layer. All parameters are listed in Table 2.

Table 1 Chemical composition in weight percent (wt.%) according to EN ISO 14341-A [17]

C	Si	Mn	P	S	Ni	Cr	Mo	Cu	Fe
0.06–0.14	0.7–1	1.3–1.6	0.025	0.025	0.15	0.15	0.15	0.35	Balance

Table 2 Process parameters

	Reference work piece	Graded work piece
Travel speed	400 mm/min	Adapted based on Sect. 3
Interlayer cooling duration	5 s	Adapted based on Sect. 3
Cooling	Pressured air cooling at 145 l/min	Pressured air cooling at 145 l/min
Wire feed speed (v_{wire})	4 m/min	Adapted based on Sect. 3
Wire diameter (d_{wire})	1 mm	1 mm
Process gas	ISO 14175 M21	ISO 14175 M21
Gas flow	10 l/min	10 l/min
CTWD	12 mm	12 mm

The temperature of the work piece is monitored using FLIR A325 IR-camera. For calibration reasons a thermocouple of type N is placed inside a hole of the substrate plate.

After the deposition, the hardness is measured along the buildup direction using the micro hardness measuring method HV1 described in DIN EN ISO 6507. The distance between each hardness imprint is 0.34 mm. Measurements are conducted on a Micro-Vickers Hardness Testing Machine Qness Q10 A+.

3 Process Parameter Estimation

To estimate the process parameter trends to be used for producing the component with the constantly increasing hardness profile. A calculation of the thermal behavior is done. Therefore, the heat input amount is calculated with the current as I, the voltage as U and the travel duration as t as shown in Eq. 1:

$$q = \eta U I t \tag{1}$$

The η is used as efficiency factor; according to Haelsig et al. the efficiency factor for the here used short-circuit GMAW is $\eta = 0.85$ [18]. Based on the heat input the temperature increase can be calculated with Eq. 2.

$$Q = c_{\mathrm{steel}} * m_{\mathrm{steel}} * \Delta T_{\mathrm{steel}} \tag{2}$$

The equation describes c_{steel} as heat capacity of steel. c_{steel} is given by Spittel et al. for a temperature range between 100 and 1200 °C with an interval of 100 °C, in between linear interpolation is used to determine the right value. Above 1200 °C c_{steel} is set constant to 680 $\frac{\mathrm{kJ}}{\mathrm{kg\,K}}$ [19].

The mass of the newly deposited weld bead is calculated as $m_{\mathrm{steel}} = \frac{\pi}{4} * d_{\mathrm{wire}}^2 * v_{\mathrm{wire}} * t * \rho$ with v_{wire} as wire feed speed and d_{wire} as wire diameter. The factor t describes the elapsed time. The density (ρ) of steel with a carbon content of 0.06% is modeled according to Spittel et al. in the same manner as the heat capacity. Above 1200 °C ρ is set to 7400 $\frac{\mathrm{kg}}{\mathrm{m}^3}$.

The heat conduction calculation is based on Eq. 3, the conduction coefficient is calculated as $\alpha_{\mathrm{cond}} = \frac{\lambda}{c_{\mathrm{steel}} * \rho}$ [20]. λ is based on Spittel et al. and interpolated in the same manner as ρ and c_{steel} with $\lambda = 30\ \frac{\mathrm{W}}{\mathrm{m*k}}$ above 1200 °C [19].

$$\Delta T_{\mathrm{conduction}}(x, t) = \int \alpha_{\mathrm{cond}} * \frac{\partial^2 T}{\partial x^2} dt \tag{3}$$

The heat loss of the work piece takes place through two different mechanisms convection and emission, shown in Eqs. 4 and 5 [20].

$$\Delta T_{\text{convection}}(x,t) = \frac{\alpha_{\text{conv}} \int A * \Delta T\, dt}{m_{\text{steel}}\, c_{\text{steel}}} \tag{4}$$

$$\Delta T_{\text{emission}}(x,t) = \frac{\int \varepsilon * \sigma * A * T^4 dt}{m_{\text{steel}}\, c_{\text{steel}}} \tag{5}$$

σ is called Stefan-Boltzmann-constant and set to $\sigma = 5.67 * 10^{-8}\, \frac{\text{W}}{\text{m}^2\text{K}^4}$ [20]. The work piece surface is calculated as a half cylinder combined with a hemisphere with $A = \frac{\pi * b * (w-b)}{2} + 2\pi * \left(\frac{b^2}{4}\right)$ for the top surface and as cuboid with $A = 2 * w * h + 2 * b * h$ for each layer in between, with b as bead width and w as wall width. Based on previous experiments the wall grows by 1.1 mm every layer the width was set up to 50 mm and the wall thickness is set up to 6 mm.

After setting up the equations the coefficients α_{conv} and ε need to be estimated. Previous experiments were conducted by placing a thermocouple of type N inside the substrate plate, see Fig. 2. Together with the measured emission intensity of the infrared camera at the same position, an emission coefficient of $\varepsilon = 0.9$ can be calculated. The convection coefficient α_{conv} is calibrated by fitting the recorded thermal history of a previous experiment to the simulated thermal history. The best fitting is achieved using $\alpha_{\text{conv}} = 50\, \frac{\text{W}}{\text{m}^2\text{K}}$.

To achieve an increasing hardness higher cooling rates are desired. Higher cooling rates can be achieved through lower interlayer temperatures. The interlayer temperature is the temperature of the previously deposited layer shorty before depositing the next one.

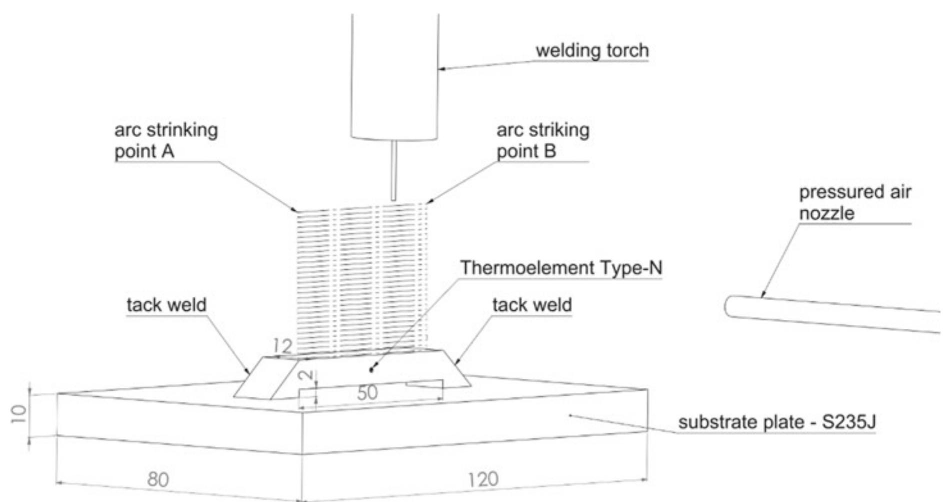

Fig. 2 Experimental set-up with substrate wall build-up strategy, cooling set-up and welding torch

To have especially low cooling rates in the beginning, the component is heated up to 250 °C.

Solving Eqs. 3–5, we observe an exponential cooling behavior. To get decreasing interlayer temperatures an exponential increase of interlayer cooling durations is advantageous. Since lower interlayer temperatures can be achieved faster, when less heat is put into the system, the current needs to decrease along the layers as well as the torch travel duration.

Based on the proposed model the following process parameter trends are planned:

- increasing the interlayer cooling duration exponential
- increasing the travel speed linear
- decreasing the current linear.

The interlayer cooling duration is planned so that the maximum interlayer cooling duration is below 3 min. Since an exponential behavior cannot be implemented into the robot control, a linear increase of the cooling duration is planned. This means that after each layer the cooling duration is extended by 5 s. The travel speed is varied within the limits of a stable process. The current cannot be controlled directly, but since current and wire feed are coupled dimensions, decreasing the wire feed will also decrease the current. Since a lower wire feed speed results in less material to be passed to the arc, the wall thickness decreases as well. The process parameters for each layer are shown in Table 3.

Using the shown equations and constants, the thermal history of the component is calculated. Since the equations only consider one dimensional heat transfer, it is assumed, that the temperature inside one layer is constant. In Fig. 3 the thermal history of the component is calculated. It can be observed, that the cooling rate is faster in the lower layers. However, since the layer temperature increases again with the heating up of the following layers the critical $t_{8/5}$-duration decreases with increasing layer number.

4 Results and Discussion

The reference work piece holds a height of only 22 mm, while the graded work piece holds a height of 32 mm. The deviation is caused by the process parameters. Especially the cooling duration affects the interlayer temperature and thereby the weld penetration, which then affects the layer height [21].

After the conduction of the experiments, the work pieces are cut in half and the micro hardness is captured. The resulting hardness profiles are shown in Fig. 4.

The hardness of the reference component (Fig. 4) shows a constant trend. Thermal imaging showed that the heat could not be conducted to the lower substrate plate. Thereby, the temperature of the component increased layer wise and the component cooled down as whole. No gradient is achieved. This is contrary to the behavior of the component in Fig. 1. This is because Henckell et al. deposited each layer after the previous layer

Table 3 Process parameters for work piece with hardness gradient

Layer no	Interlayer cooling duration (s)	Travel speed (mm/min)	Wire feed speed (m/min)
1	0	210	5.5
2	5	223	5.4
3	10	237	5.3
4	15	250	5.2
5	20	264	5.1
6	25	277	5.0
7	30	291	4.9
8	35	304	4.8
9	40	318	4.7
10	45	331	4.6
11	50	344	4.5
12	55	358	4.4
13	60	371	4.3
14	65	385	4.2
15	70	398	4.1
16	75	412	4.0
17	80	425	3.9
18	85	439	3.8
19	90	452	3.7
20	95	466	3.6
21	100	479	3.5
22	105	492	3.4
23	110	506	3.3
24	115	519	3.2
25	120	533	3.1
26	125	546	3.0
27	130	560	2.9
28	135	573	2.8
29	140	587	2.7
30	145	600	2.6

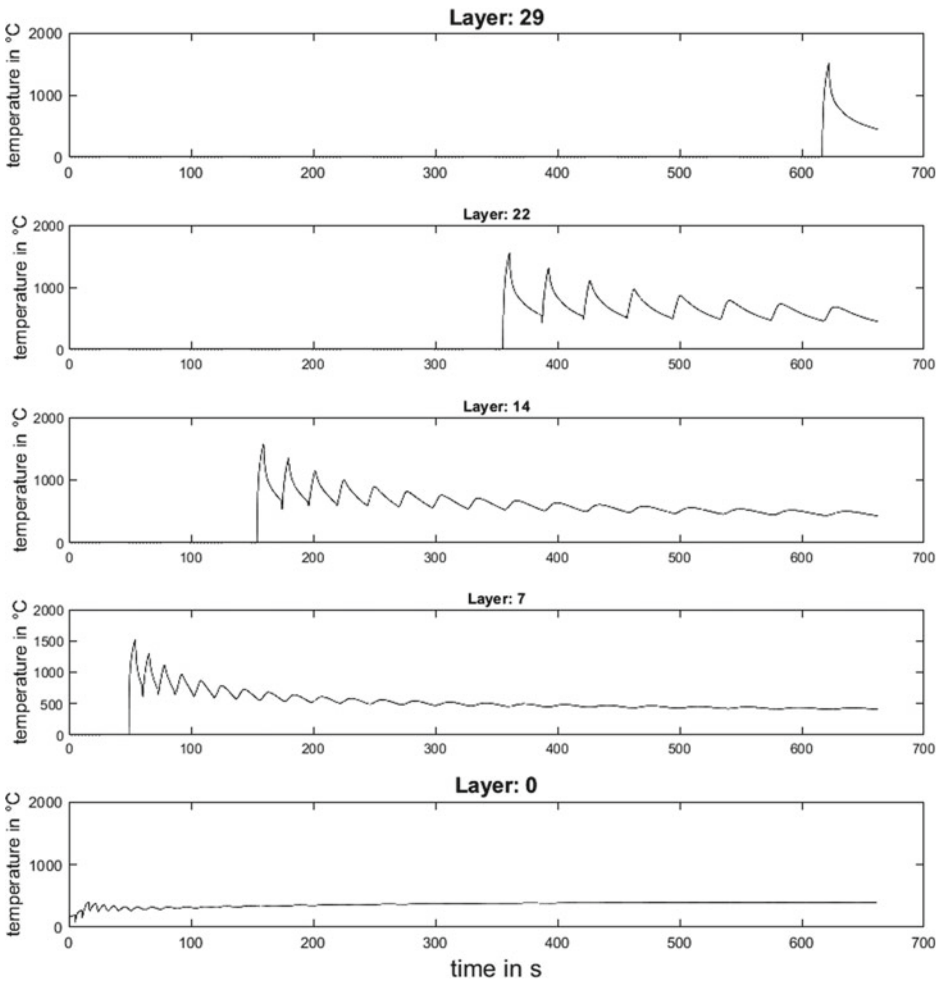

Fig. 3 Result of thermal calculation, across different layers

cooled down to a temperature of 100 °C [10]. Moreover, Henckell et al. did not use a heat isolating air gap under the substrate plate [10]. After depositing the last layer, the lower substrate plate had a temperature of 50 °C. Thereby, it can be said, that the tack welds together with a 2 mm air gap acted well as heat insulator. The mean value of the hardness over the component is 122 HV.

The hardness profile of the graded component (Fig. 4) shows a clear linear increase within the first layers. After 15 mm, the hardness only increases slightly. This is caused by too long cooling durations. The cooling duration let the work pieces cool down to room temperature and thereby to a constant interlayer temperature. This can be seen in

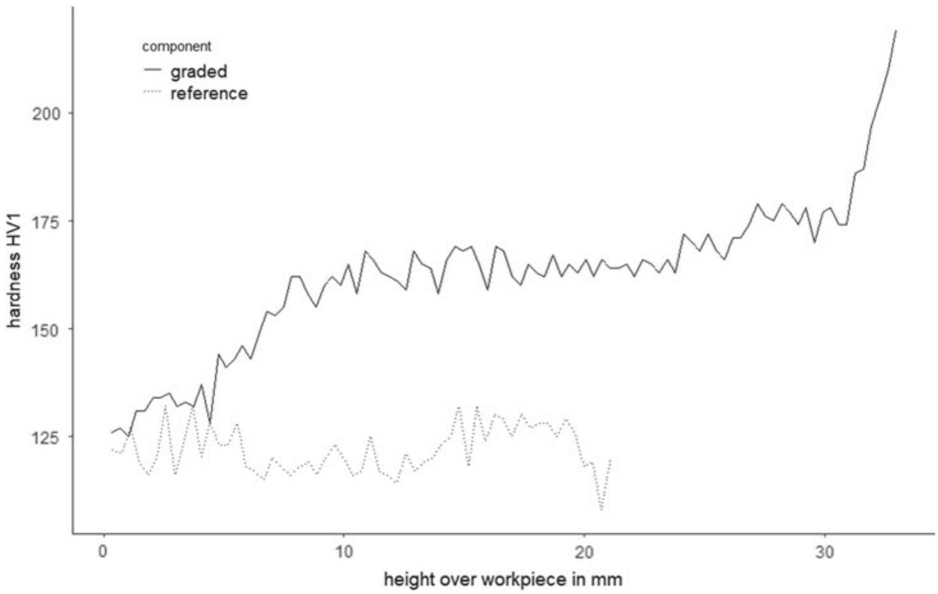

Fig. 4 Hardness profile of the manufactured components

Fig. 5 where a cutout of the layer temperature in the middle of the component is plotted. The interlayer temperature leaves the measurement range and consistently stays below

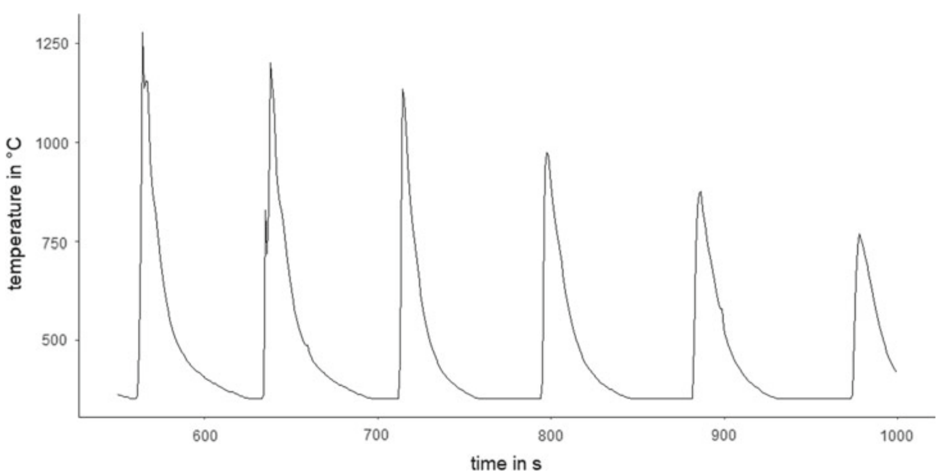

Fig. 5 Temperature in the 13th layer of the work piece during manufacturing of this and following layers

it. This could have been prevented with shorter cooling durations and a slower rise of cooling durations.

Faster cooling rates lead to a finer microstructure, which has a higher hardness than a coarse one. The cyclical reheating of deposited layers induced by the deposition of the following layers (see Fig. 5) produces tempering effects. Tempering is the reheating of already solidified material. Due to tempering effects, the grain grows to a coarse lamellar microstructure. Tempering also leads to increased grain sizes, which lowers the hardness [11].

The last layers of the work piece show an increased hardness. The main reason for the increased hardness in the last layers is the missing of tempering effects.

The work of Rodrigues et al. and Henckel et al. show a higher hardness especially in the first few layers. This is caused by faster cooling rates resulting out of lower interlayer temperature at the beginning. We were able to prevent this in our work through pre-heating and the planned process parameters. Even though the calculations were uncalibrated and just consider one dimensional heat transfer, we were still able to propose process parameter trends, which allow a hardness gradient in the work piece [7, 10].

A hardness cannot be foreseen in advance to the manufacturing process. This is caused by the tempering effects in the microstructure. A TTT-diagram only show the expected hardness based on one cooling cycle. In WAAM, the deposition runs through several heating and cooling cycles. This is why TTT-diagrams cannot be applied for expecting the deposition hardness in WAAM.

Since the thermal data, as plotted in Fig. 5, shows a cooling down to room temperature, shorter cooling durations would be possible. This could also be done by using a closed-loop cooling strategy, which uses the temperature of the last weld bead as input. Thereby, the building time could be reduced and bigger hardness gradients can be achieved.

An uncertainty of the experiment is the voltage and current setting. No matter the used power source, deviations in the voltage and current are inherent to the GMAW process. This influences the amount of heat input. Moreover, the difference of the heat input could be further increased by selecting an energy-reduced process (e.g. EWM coldArc) in the upper layers. A bigger difference between the energy input will also lead to a bigger difference within the $t85$-durations. Thereby, the amount of current per wire unit length can be reduced. Another way to further reduce the heat input into the upper layers is to lower the voltage [22].

A WAAM component with constant interlayer temperature would show a decreasing cooling rate along the build-up direction. This is caused by a rising heat capacity of the growing component.

Over the growth of the work pieces the mass of the work piece increases. Thereby, the thermal capacity of the component increases. This naturally leads to lower cooling rates. To have higher cooling rates even in upper layers changing the cooling process would be beneficial. Faster cooling rates could have been achieved through different cooling methods like aerosol spray or water bath cooling. This would also increase the hardness of the upper layers [9].

5 Summary and Outlook

The proposed process planning strategy allows the build-up of a component with a hardness gradient. The process planning strategy is based on decreasing the energy input per unit length, as well as increasing the cooling durations. The decrease of energy input per unit length could be boosted by also lowering the voltage as well as using energy-reduced processes in the top layers.

The hardness profile in the manufactured work piece is not strictly linear; this is caused by to long pauses between welding, which lead to a constant interlayer temperature. Shorter cooling durations could prevent this issue.

Future experiments can be conducted with a wire material holding a higher carbon equivalent value. This would lead to martensitic hardening. The reheating of the already deposited layers lead to a tempering effect. However, since the reheated microstructure is cooled down fast again and does not stay at a high temperature for a long duration, the tempering effect does not have a major impact on the martensitic microstructure.

Furthermore, a closed-loop cooling strategy, which controls the interlayer temperatures, can be tested. Another set of experiments could also include a change of the cooling processes during the build time.

Acknowledgements Funded by the Ministry for Science and Culture of Lower Saxony (MWK)—School for Additive Manufacturing SAM.

References

1. Joshi, S. C., & Sheikh, A. A. (2015). 3D printing in aerospace and its long-term sustainability. *Virtual and Physical Prototyping, 10*, 175–185. https://doi.org/10.1080/17452759.2015.1111519
2. Oliveira, J. P., Santos, T. G., & Miranda, R. M. (2020). Revisiting fundamental welding concepts to improve additive manufacturing: From theory to practice. *Progress in Materials Science, 107*, 100590. https://doi.org/10.1016/j.pmatsci.2019.100590
3. Venturini, G., Montevecchi, F., Scippa, A., & Campatelli, G. (2016). Optimization of WAAM deposition patterns for T-crossing features. *Procedia CIRP, 55*, 95–100. https://doi.org/10.1016/j.procir.2016.08.043
4. Hassel, T., & Carstensen, T. (2020). Properties and anisotropy behaviour of a nickel base alloy material produced by robot-based wire and arc additive manufacturing. *Weld World, 64*, 1921–1931. https://doi.org/10.1007/s40194-020-00971-7

5. Mukin, D., Valdaytseva, E., Hassel, T., Klimov, G., & Shalnova, S. (2020). Modelling of heat transfer process in non-vacuum electron beam additive manufacturing with $CuSi_3$ alloy wire. *Materials Today: Proceedings, 30*, 373–379. https://doi.org/10.1016/j.matpr.2019.12.380
6. Rodrigues, T. A., Duarte, V., Miranda, R. M., Santos, T. G., & Oliveira, J. P. (2019). Current status and perspectives on wire and arc additive manufacturing (WAAM). *Materials (Basel) 12*. https://doi.org/10.3390/ma12071121
7. Rodrigues, T. A., Duarte, V., Avila, J. A., Santos, T. G., Miranda, R. M., & Oliveira, J. P. (2019). Wire and arc additive manufacturing of HSLA steel: Effect of thermal cycles on microstructure and mechanical properties. *Additive Manufacturing, 27*, 440–450. https://doi.org/10.1016/j.addma.2019.03.029
8. Marinelli, G., Martina, F., Lewtas, H., Hancock, D., Ganguly, S., & Williams, S. (2019). Functionally graded structures of refractory metals by wire arc additive manufacturing. *Science and Technology of Welding and Joining, 24*, 495–503. https://doi.org/10.1080/13621718.2019.1586162
9. Reisgen, U., Sharma, R., Mann, S., & Oster, L. (2020). Increasing the manufacturing efficiency of WAAM by advanced cooling strategies. *Weld World, 64*, 1409–1416. https://doi.org/10.1007/s40194-020-00930-2
10. Henckell, P., Gierth, M., Ali, Y., Reimann, J., & Bergmann, J. P. (2020). Reduction of energy input in wire arc additive manufacturing (WAAM) with gas metal arc welding (GMAW). *Materials (Basel) 13*. https://doi.org/10.3390/ma13112491
11. Callister, W. D., & Rethwisch, D. G. (2015). *Materials science and engineering* (9th edn.). SI version. Wiley.
12. Kühne, R., Feldmann, M., Citarelli, S., Reisgen, U., Sharma, R., & Oster, L. (2019). 3D printing in steel construction with the automated wire arc additive manufacturing. *ce/papers, 3* , 577–583. https://doi.org/10.1002/cepa.1103
13. Karunakaran, K. P., Suryakumar, S., Pushpa, V., & Akula, S. (2010). Low cost integration of additive and subtractive processes for hybrid layered manufacturing. *Robotics and Computer-Integrated Manufacturing, 26*, 490–499. https://doi.org/10.1016/j.rcim.2010.03.008
14. Posch, G., Ferdinand, K., Hackl, H., & Chladil, H. (2014). Manufacturing of turbine blades by shape giving CMT-welding. In *Metal additive manufacturing conference*. Vienna, Austria.
15. Wang, L., Xue, J., & Wang, Q. (2019). Correlation between arc mode, microstructure, and mechanical properties during wire arc additive manufacturing of 316L stainless steel. *Materials Science and Engineering: A, 751*, 183–190. https://doi.org/10.1016/j.msea.2019.02.078
16. Seyffarth, P., Meyer, B., & Scharff, A. (2018). Großer Atlas Schweiß-ZTU-Schaubilder, second., aktualisierte und erweiterte Auflage, DVS Media GmbH.
17. DIN Deutsches Institut für Normung e. V. (2020). Welding consumables—Wire electrodes and weld deposits for gas shielded metal arc welding of non alloy and fine grain steels, 2020th ed., Beuth Verlag GmbH.
18. Haelsig, A., Kusch, M., & Mayer, P. (2012). New findings on the efficiency of gas shielded arc welding. *Weld World, 56*, 98–104. https://doi.org/10.1007/BF03321400
19. Spittel, M., & Spittel, T. (2009). Steel symbol/number: S275JRC/1.0128. In W. Martienssen & H. Warlimont (Eds.), *Metal forming data of ferrous alloys - deformation behaviour* (pp. 132–137). Springer.
20. Bejan, A. (1993). *Heat transfer*. Wiley.

21. Panda, B., Shankhwar, K., Garg, A., & Savalani, M. M. (2019). Evaluation of genetic programming-based models for simulating bead dimensions in wire and arc additive manufacturing. *Journal of Intelligent Manufacturing, 30*, 809–820. https://doi.org/10.1007/s10845-016-1282-2
22. Norrish, J., & Cuiuri, D. (2014). The controlled short circuit GMAW process: A tutorial. *Journal of Manufacturing Processes, 16*, 86–92. https://doi.org/10.1016/j.jmapro.2013.08.006

Toward a Design Compendium for Metal Binder Jetting

Heiko Blunk and Arthur Seibel

Abstract

In the field of metal additive manufacturing, the metal binder jetting process is mainly characterized by its cost advantage and a higher level of detail compared to the established laser powder bed fusion process. This allows the design freedom of additive manufacturing to be applied to an even wider range of industrial fields. However, to avoid costly iteration loops and to fully exploit the potential of metal binder jetting, design guidelines are needed that systematically identify the restrictions and possibilities of this process. Therefore, in this paper, a procedure for determining a comprehensive design compendium is presented.

Keywords

Additive manufacturing • Metal binder jetting • Design guidelines

1 Introduction

Additive manufacturing (AM) offers numerous advantages compared to conventional manufacturing processes. These include, among others, a high degree of geometric design

H. Blunk (✉) · A. Seibel
Fraunhofer Research Institution for Additive Manufacturing Technologies IAPT, 21029 Hamburg, Germany
e-mail: heiko.blunk@iapt.fraunhofer.de

A. Seibel
e-mail: arthur.seibel@iapt.fraunhofer.de

A. Seibel
Hamburg University of Technology TUHH, 21073 Hamburg, Germany

R. Lachmayer et al. (eds.), *Innovative Product Development by Additive Manufacturing 2021*, https://doi.org/10.1007/978-3-031-05918-6_3

freedom that enables highly complex components to be manufactured with minimal material input [1, 2]. However, widespread industrial applications are not yet given, as the low build rates of most AM technologies lead to high part costs [3]. Compared to laser powder bed fusion of metals (PBF-LB/M), which is currently the most commonly used 3D printing technology for metal parts, the metal binder jetting (MBJ) process has a higher build rate and resolution. In addition, MBJ allows the use of lower-cost metal powders, the elimination of support structures, and enables nesting of components, resulting in a greater utilization of the available build space, which results in significantly lower costs. Compared to the PBF-LB/M process, costs can be reduced by more than 60% [4]. Hence, the MBJ process is a promising alternative for the cost-effective production of metal components [5].

In contrast to the established metal injection molding (MIM) and powder injection molding (PIM) processes, the MBJ process is characterized by a higher design freedom and cost effectiveness at lower batch sizes. This is mainly due to the elimination of cost-intensive molds and dies. As a result, MBJ enables products to be launched more quickly without complex design adjustments. The achievable component properties and the application areas of the three processes are comparable [6].

However, most designers are accustomed to designing components for conventional manufacturing methods, such as milling and casting, and often have limited experience with designing products for additive manufacturing [7]. Costly and time-consuming iterative loops as well as an insufficient exploitation of the process possibilities are the outcome, which results in a significant influence of design guidelines on the acceptance of the corresponding AM technology. These enable the designer to identify not only the design limits, but also the possibilities that the technology offers [8]. Therefore, in order to exploit the potentials of MBJ and to enable a wide range of industrial applications, it is important to explore the design limitations of this new process and to translate the results into a comprehensive design compendium.

2 Metal Binder Jetting

The metal binder jetting process is based on developments at MIT and was marketed exclusively by ExOne until the first patents expired in 2010. Since then, several new companies have established themselves in this technology area. In this process, a liquid binder is applied to corresponding areas of a metal powder bed, then the powder bed is lowered, and a new layer of powder is applied. The component is thus built up layer by layer, as shown in Fig. 1. The layer thickness is typically approx. 42 µm, but can be increased to up to 200 µm depending on the system used. After the printing process, the components are cured in an oven. In this process step, the water content of the binder is outgassed and the parts solidify. The components are manually unpacked from the powder bed and loose powder is removed. These so-called green parts have a density of approx.

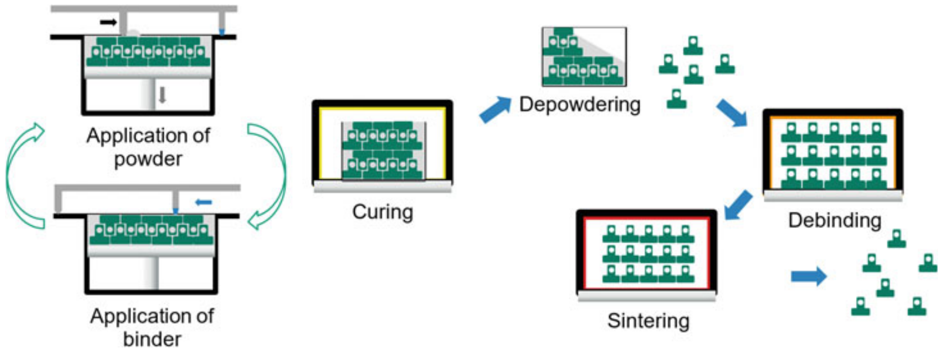

Fig. 1 Metal binder jetting process chain

60%. The green parts are brittle at this stage and can be destroyed by improper handling. The components are then placed on ceramic plates, also called setter plates, and are thermally debinded in another furnace at higher temperatures. After this process step, the components are very sensitive and may only be transported into the sintering furnace by means of the setter plates to prevent damage. During sintering, the components are very soft and may deform unintentionally due to shrinkage, friction between the components and the sintering base, as well as their own weight [9–12]. After sintering, the parts are solid and can be used or post treated if required. Instead of pure sintering, the parts can also be infiltrated with a material that has a lower melting point, such as bronze [13]. As this is a multi-material application, this variant is not considered in this paper.

3 Design Compendium

Based on previous experience with other additive manufacturing technologies, it has become evident that design guidelines are an essential contribution to the acceptance and implementation of an AM technology [14]. Despite existing guidelines, further in-depth research is required to identify all aspects and challenges of the MBJ process [8]. Previous guidelines are mainly limited to the established AM processes such as PBF-LB/M or fused deposition modeling [1, 15]. Other methods, for example, heuristic approaches, give a general overview of design possibilities of additive manufacturing processes, but cannot address the process and material specifics [16]. For metal binder jetting, only limited and far from all-encompassing guidelines are available so far; for example [9, 17].

3.1 Existing Design Guidelines

To evaluate the performance of additive manufacturing processes, benchmark parts have been developed in the past [18, 19]. These are a combination of geometric artefacts in various shapes to create one or more test specimens and can be classified as geometric, mechanical, and process benchmark parts [20, 21]. While the mechanical and process benchmark parts are used to determine mechanical characteristics as well as process-related parameters, geometrical benchmark parts are used to determine geometrical properties of components. However, in metal AM, these refer mainly to the PBF-LB/M process [1, 15]. By use of such geometries, several design guidelines have already been published for the production-oriented design of AM components. On the one hand, manufacturing service providers or machine manufacturers provide rough guidelines [9, 17, 22] that allow an initial assessment of the possibilities with the associated manufacturing system—but these do not show detailed process limits, see Table 1 as an example. On the other hand, more in-depth guidelines are available from publications of research results, which so far only deal with established metal AM processes [1, 23, 24].

The recommended guidelines given by the manufacturing services network 3D Hubs or the company Sculpteo are more conservative and small in scope, which means that a full utilization of the process options is not possible [25, 26]. Adam [15], on the other hand, has developed a guideline for the systematic development of design rules and applied it to the PBF-LB/M, selective laser sintering, and fused deposition modeling processes. However, due to the different process conditions and limitations, the resulting guidelines do not allow a full potential utilization of the respective manufacturing process, but rather provide a basis for further research. In addition, the ISO/ASTM 52910:2018 standard gives assistance for exploiting the possibilities of AM processes [27]. More details can be found in the ISO/ASTM 52902:2019 [28] standard that describes several test specimens that can be used to evaluate AM processes with regard to producible geometry elements. Such test specimens have also been used in research before [15]. Nevertheless, even these geometries do not allow a complete coverage of the interrelationships in the metal binder

Table 1 Basic recommendations for the MBJ process provided by Digital Metal [9]

Feature	Dimensioning
Minimum size	$1 \times 1 \times 3$ mm
Minimum radius	35 μm
Chamfers	35 μm step size in mounting direction
Resolution	35 μm
Wall thickness	≥300 μm down to 150 μm, depending on wall thickness and design
Bore holes	≥200 μm, depending on depth

jetting process chain, since, for example, the influences of the setter plate cannot be adequately taken into account.

Due to the comparable process steps of debinding and sintering in MIM and PIM, which are also required in MBJ, the findings can be well incorporated in MBJ-specific design guidelines. For example, basic rules for sintering-compatible design can be incorporated. Various publications and manuals already exist for this purpose, which show the possibilities and limitations of these processes [29–31]. However, in MBJ, the green parts have different properties compared to MIM and PIM green parts due to the difference in the manufacturing processes. Moreover, depending on the selected binder, solvent debinding can also be performed in the processes in addition to thermal debinding [32]. For this reason, a direct transfer of the design rules cannot be ensured and must first be verified within the scope of the investigations. Nevertheless, it is possible to build on general findings on sintering and shrinkage behavior as well as on minimizing warpage. These include, for example, the reduction of friction between the component and the setter plate or the avoidance of sudden changes in the cross-section of the component.

3.2 Approach to Compendium Development

Due to the differences in the manufacturing processes described above, a new approach is needed to account for process-related specifics and to identify process-related design guidelines. Therefore, it is essential to first identify the influences of the MBJ process on component design. In particular, the anisotropic and nonlinear behavior during the sintering process must be emphasized. In addition, the respective restrictions of the individual process steps (printing, debinding, and sintering) must be taken into account.

Figure 2 shows a first compilation of the influences of the individual process steps on

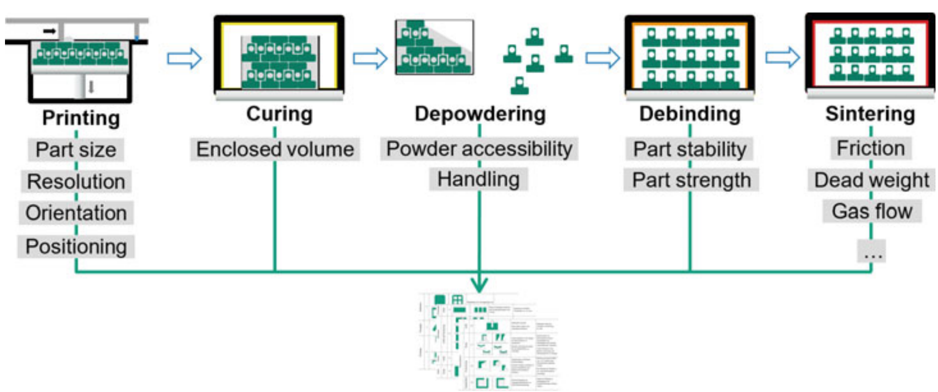

Fig. 2 Overview of influences on component design in the metal binder jetting process chain

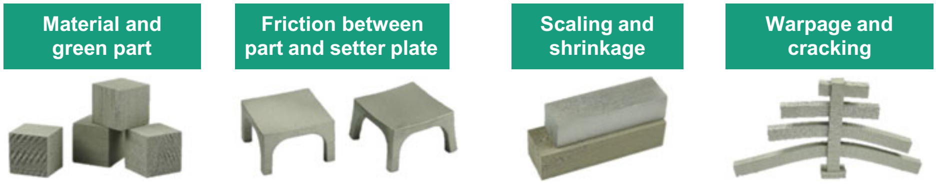

Fig. 3 Categorization of influences on component design in the metal binder jetting process chain

the dimensional accuracy of the manufactured components. For the sake of clarity, the influences are listed only once in each case, even if they occur in several process steps.

It can be observed that each process step adds further restrictions and conditions affecting component design—starting with the size of the component, the maximum of which is determined by the build space of the printer, through the accessibility of the powder for residue-free removal, to the dead weight of the components, which has a direct effect on the distortion in the sintering process. On closer examination, these influencing factors can be divided into the four groups shown in Fig. 3.

Based on all these boundary conditions, it is now possible to develop corresponding geometrical benchmark parts that take into account the physical effects of the individual process steps of MBJ and represent their influence in a measurable way. The categorization in groups makes it possible to examine the individual phenomena building on each other. Note that each of these groups has specific requirements for the design of the test specimens.

Influence of Material and Green Part Properties. Since the subsequent part properties are based on the condition of the material and the properties of the green parts, the material and green part characteristics are to be examined at the beginning of the investigations and then continuously monitored over a certain period of time. Since effects on the final part density (like the particle size distribution) are mostly known [33, 34], the intention is to monitor deviations in green part characteristics and determine their influence on the component properties. In addition to the particle size distribution of the material as well as its flowability, the dimensional accuracy of the green parts and their density will be of interest.

Influence of Friction between Part and Setter Plate. During the sintering process, shrinkage of the components takes place, which causes a relative movement between the component and the setter plate, which in turn is subject to frictional resistance. This has a direct effect on the dimensional accuracy of the sintered component. With larger friction, larger deformation is to be expected. Therefore, investigations are necessary to adequately determine the tribological influence of the setter plate on component deformation. Since setter plates can be used multiple times, it is recommended to account for aging phenomena by using differently designed and prepared plates.

Influence of Scaling and Shrinkage. Beyond material properties and friction, gravitation-induced shrinkage has a significant influence on the final part dimensions. It should be noted that shrinkage occurs unevenly in the three spatial directions and is greatest in the vertical direction. To determine the influences in a sufficient way, existing part artefacts need to be identified, abstracted, and transferred into test geometries. Subsequently, manufacturing needs to be carried out in different sizes, orientations, and combinations. Furthermore, to ensure reproducibility, the test geometries should be manufactured and examined several times over a certain period. This will also allow identification of deviations caused by changes in material and green part properties.

Influences of Warpage and Cracking. Furthermore, it is also necessary to investigate the distortion caused by gravity and to determine the influences on crack formation. The aim is to identify the largest possible overhangs at which the resulting bending moment is negligible and at what point ribs or sinter supports have to be used. In general, it should be noted that, as the overhang length increases, the bending moment increases and, accordingly, so does the deformation. As already known from the MIM process, sharp-edged cross-sectional changes favor the formation of cracks in the components [35]. To what extent and under what conditions such effects occur in the MBJ process remains to be investigated.

Derivation of a Design Compendium. Based on the knowledge gained until this point, a design compendium can be created. According to Mashes [24], the design compendium will include illustrative guidelines as well as design principles and design rules with explicit constraints to provide a comprehensive summary of the capabilities and limitations of the MBJ process in its entirety. In addition to the classical tabular structure, it is advisable to divide the guidelines into two categories, namely quantitative and qualitative. While qualitative guidelines contain basic recommendations for a design suitable for manufacturing, such as the use of radii or closed footprints, quantitative guidelines contain numerically detectable restrictions. These include, for example, feasible bore hole diameters or wall thicknesses.

4 Conclusion and Outlook

Additive manufacturing is still in a constant state of change, and new manufacturing processes and methods are being developed. One of these is the metal binder jetting process, which has the potential to significantly reduce the cost of producing additively manufactured components. To increase the industry acceptance of this relatively new technology, process-specific guidelines for the design of MBJ parts are needed.

In this paper, it was discussed that, despite the variety of design guidelines from other additive manufacturing processes, they cannot be directly transferred to the MBJ process. Among other things, this can be attributed to the different process steps and physical phenomena within the process chain. Here, only the MIM and PIM processes provide further assistance in identifying the design limits. Due to the related process steps, such as sintering, the rules for sinter-compatible design apply only in part to the MBJ process.

Furthermore, the boundary conditions and influencing variables of the MBJ process chain were identified and compiled. Based on these, a procedure was derived that makes it possible to determine limitations with regard to a manufacturable part design. By successively investigating the categories of the individual influencing variables "material and green part properties," "friction between part and setter plate," "scaling and shrinkage," as well as "warpage and cracking," it is possible to derive comprehensive guidelines for MBJ component design.

However, the identification of such design guidelines is only the first of several steps to enable the widespread industrial application of this AM technology. Following on from the creation of the design compendium, the aim has to be to make the process as simple and straightforward as possible to access. Consequently, in a next step, the developed design compendium can be implemented in CAD environments to further support the design process. This can be realized, for example, by a toolbox that checks existing components for violations of the design rules. Similarly, the rules can be integrated as constraints for a topology optimization to achieve a directly printable result [36]. However, these approaches assume that the designer is aware of the limitations and possibilities of the MBJ process.

References

1. Kranz, J. (2017). *Methodik und Richtlinien für die Konstruktion von laseradditiv gefertigten Leichtbaustrukturen.* Springer.
2. Femmer, T., Langefeld, B., Möhrle, M., Nauth, A., Schaukellis, M., & Schildbach, P. (2019). *Roland Berger: Additive Manufacturing – Taking Metal 3D Printing to the Next Level*.
3. Bundesministerium für Bildung und Forschung (BMBF). (2019). *Deutschland druckt dreidimensional. Additive Fertigung revolutioniert die Produktion.* Druck- und Verlagshaus Zarbock GmbH & Co. KG.
4. Digital Alloys. (2019). *Guide to metal additive manufacturing – Part 5 – Economics of metal additive manufacturing*.
5. Future Manufacturing. Magazin für intelligente Produktion. (2019). *Additive Fertigung/Augmented Reality*. VDMA-.
6. Digital Alloys. (2019). *Guide to metal additive manufacturing – Part 10 – Metal binder jetting.*
7. Emmelmann, C., Herzog, D., & Kranz, J. (2017). Design for laser additive manufacturing. In *Laser Additive Manufacturing* (pp. 259–279). Elsevier.
8. Seepersad, C. C., Allison, J., & Sharpe, C. (2017). The need for effective design guides in additive manufacturing. In *Proceedings of the 21st International Conference on Engineering Design (ICED 17)* (pp. 309–316).
9. Digital Metal. (2021). DM P2500-3D metal printing at its best. Retrieved June 17, 2021, from https://digitalmetal.tech/printer-line/design-and-function

10. Oh, J. W., Nahm, S., Kim, B., & Choi, H. (2019). Anisotropy in green body bending strength due to additive direction in the binder-jetting additive manufacturing process. *Korean Journal of Metals and Materials, 57*(4), 227–235.
11. Begum, N. N., Islam, M. K., Choudhury, I. A., & Mamat, A. B. (2017). Effect of injection parameters on green part mechanical properties for metal injection molding. *Optimization*, *9*(53.3), 150.
12. ExOne. (2021). Metal 3D Printers. Retrieved June, 17, 2021, from https://www.exone.com/en-US/3D-printing-systems/metal-3d-printers
13. Cordero, Z. C., Siddel, D. H., Peter, W. H., & Elliott, A. M. (2017). Strengthening of ferrous binder jet 3D printed components through bronze infiltration. *Additive Manufacturing, 15*, 87–92.
14. Kranz, J., Herzog, D., & Emmelmann, C. (2015). Design guidelines for laser additive manufacturing of lightweight structures in TiAl6V4. *Journal of Laser Applications, 27*(S1), S14001.
15. Adam, G. A. O. (2015). *Systematische Erarbeitung von Konstruktionsregeln für die additiven Fertigungsverfahren Lasersintern, Laserschmelzen und Fused Deposition Modeling*. Shaker.
16. Blösch Klein, A. (2020). *Design Heuristics for Additive Manufacturing*. Doctoral Dissertation, ETH Zurich.
17. ExOne. (2017). Manufacturing guidelines for ExOne metal sintered parts NH-PSC-GL-011.
18. Digital Metal. (2019). Additive manufacturing of small and complex metal parts. Höganäs AB, Höganäs.
19. Shah, P., Racasan, R., & Bills, P. (2016). Comparison of different additive manufacturing methods using computed tomography. *Case Studies in Nondestructive Testing and Evaluation, 6*, 69–78.
20. Rebaioli, L., & Fassi, I. (2017). A review on benchmark artifacts for evaluating the geometrical performance of additive manufacturing processes. *The International Journal of Advanced Manufacturing Technology, 93*(5), 2571–2598.
21. Mahesh, M. (2004). Rapid prototyping and manufacturing benchmarking.
22. Materialise. (2019). Konstruktionsrichtlinien – Aluminium – 3D-Metalldruck. Retrieved June 17, 2021, from https://www.materialise.com/de/academy-manufacturing/resources/konstruktionsrichtlinien
23. Wang, P., Song, J., Nai, M. L. S., & Wei, J. (2020). Experimental analysis of additively manufactured component and design guidelines for lightweight structures: A case study using electron beam melting. *Additive Manufacturing, 33*, 101088.
24. Mani, M., Witherell, P., & Jee, H. (2017). Design rules for additive manufacturing: A categorization. In *International Design Engineering Technical Conferences and Computers and Information in Engineering Conference* (Vol. 58110, p. V001T02A035). American Society of Mechanical Engineers.
25. Alkaios Bournias Varotsis. (2018). How to design parts for Binder Jetting 3D printing. Retrieved June 17, 2021, from https://www.3dhubs.com/knowledge-base/how-design-parts-binder-jetting-3d-printing/
26. Sculpteo. (2019). Edelstahl 316 Materialhandbuch. Retrieved June 17, 2021, from https://www.sculpteo.com/de/materialien/binder-jetting-materialien/metall-binder-jetting-edelstahl-316/
27. ISO/ASTM 52910:2018-07, Additive Fertigung – Konstruktion – Anforderungen, Richtlinien und Empfehlungen.
28. ISO/ASTM 52902:2019-07, Additive Fertigung – Testkörper – Allgemeine Leitlinie für die Bewertung der geometrischen Leistung additiver Fertigungssysteme (AM-Systeme).
29. German, R. M. (2008). Designing for metal injection moulding: A guide for designers and end-users.
30. Heaney, D. F. (Ed.). (2018). *Handbook of Metal Injection Molding*. Woodhead.

31. Smarslok, B., & German, R. M. (2005). Identification of design parameters in metal powder injection molding. *Journal of Advanced Materials, 37*(4), 3–11.
32. Burkhardt, C. (2013). *Metallpulverspritzguss: Fertigung komplexer Bauteile in höchster Präzision.* Verlag Moderne Industrie.
33. Bai, Y., Wagner, G., & Williams, C. B. (2017). Effect of particle size distribution on powder packing and sintering in binder jetting additive manufacturing of metals. *Journal of Manufacturing Science and Engineering*, *139*(8).
34. Mostafaei, A., De Vecchis, P. R., Nettleship, I., & Chmielus, M. (2019). Effect of powder size distribution on densification and microstructural evolution of binder-jet 3D-printed alloy 625. *Materials & Design, 162*, 375–383.
35. Heaney, D. F. (2019). Designing for metal injection molding (MIM). In *Handbook of Metal Injection Molding* (pp. 25−43). Woodhead.
36. Liu, J., Gaynor, A. T., Chen, S., Kang, Z., Suresh, K., Takezawa, A., To, A. C., et al. (2018). Current and future trends in topology optimization for additive manufacturing. *Structural and Multidisciplinary Optimization*, *57*(6), 2457–2483.

Development of a Coaxial Laser Wire System for the Additive Manufacturing of Functional Graded Materials using Direct Energy Deposition

Nick Schwarz, Alexander Barroi, Kai Biester, Laura Budde, Marius Lammers, Marijan Tegtmeier, Jörg Hermsdorf, Stefan Kaierle, and Henning Ahlers

Abstract

Laser wire Direct Energy Deposition (L-DED) is a manufacturing process capable of producing additively generated structures as well as repairing and coating of surfaces. The use of a coaxial system technology enables a direction-independent application of the weld deposit. For coaxial Laser Double-wire DED (LD-DED), a processing head with a centric wire feed for two wires has been developed. Using three single beams with a maximum output power of 220 W each and a wavelength of 970 nm, a combined focus point of 1.6 mm in diameter is realised. The single beams are guided using an optical fibre for each laser beam source. The advantages of the system are the small footprint, the individual control of the single laser beams and the ease of conversion to other applications. This paper describes the development of the coaxial laser-processing head for the Additive Manufacturing that is capable to produce functionally graded structures.

Keywords

Functional Graded Materials • Laser Double-wire Direct Energy Deposition • DiCoLas

N. Schwarz (✉) · A. Barroi · K. Biester · L. Budde · M. Lammers · M. Tegtmeier · J. Hermsdorf · S. Kaierle
Laser Zentrum Hannover e.V., Hollerithallee 8, 30419 Hanover, Germany
e-mail: n.schwarz@lzh.de

N. Schwarz · M. Lammers · H. Ahlers
Hochschule Hannover, Ricklinger Stadtweg 120, 30459 Hanover, Germany

R. Lachmayer et al. (eds.), *Innovative Product Development by Additive Manufacturing 2021*, https://doi.org/10.1007/978-3-031-05918-6_4

1 Introduction

Modern applications in engineering demand material properties that exceed the limitations of commonly used materials. These properties tend to be contradictory thus requiring the usage of at least two different materials in order to fulfill the requested behaviour. However, fusing two different materials with different properties concerning the mechanical and thermal behaviour are critical regarding thermal or mechanical stress in the fusion zone. Cracks occurring in the fusion zone limit the lifetime of built parts.

It is therefore desirable, to tailor the material properties according to the load conditions in the parts and create a smooth transition between the applied materials to avoid stress maxima. Functional Graded Materials (FGMs) are a promising approach to reduce the occurring stress, as they aim to control the composition across the part cross-section. Additive Manufacturing (AM) offers the possibility to adjust material properties in a volumetric and compositional manner. With its opportunity to build graded parts by applying layers of different material composition, the Laser Direct Energy Deposition (L-DED) is suitable to produce FGMs. This paper focuses on the development of system technology for the production of FGMs with a coaxial laser wire DED process.

2 State of the Art

2.1 Coaxial Laser Wire Direct Energy Deposition

Coaxial laser wire AM is characterized by a centric wire feed which enables direction-independent processing of various materials available in wire form. Multiple laser beams or one ring-shaped beam enveloping the wire usually induce the energy required to melt the wire and base material. While a ring-shaped beam is formed by a laser source and corresponding optics, two possible solutions exist for generating multiple beams. The first can be realized by a beam splitter which splits a focused beam into several individual beams that are directed into the process zone via deflective mirrors. Typically, diode lasers with wavelength ranges between 800 and 1100 nm and maximum laser output powers of up to 8 kW are used [1, 2]. The second method is characterized by the use of one laser source for each single beam. This condition implies that each single beam has to be collimated and focused with an own optical unit [3, 4] (cf. Fig. 1).

Depending on the system, the single beam is transmitted to the optics either directly from the laser diode or through an optical fibre that is connected to the optical unit by a fibre connector. Commonly used laser diode stacks reach a maximum output power of 220 W with a wavelength of 900–1,000 nm. A significant advantage of the multiple beam source technology is the possibility to individually control the laser power of each beam. This allows a more precise process control and introduces another tool for process design. Additionally, by using laser beam sources of different wavelengths, a further process

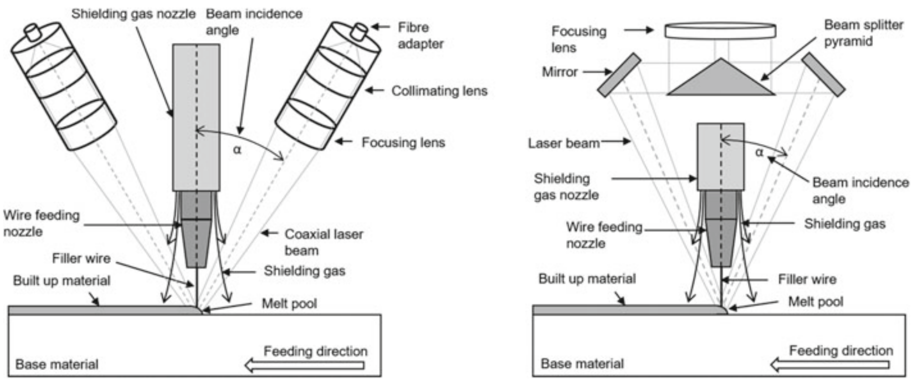

Fig. 1 Schematic comparison between the multiple diode principle (left) and the split beam principle (right)

parameter can be introduced thus aiming to improve the laser beam absorption of the processed material. The laser wire AM is a relatively clean process due to its high material utilization and the following absence of respirable particles. In comparison with other AM methods, the surface roughness is significantly lower [5]. A further advantage is the possibility of conductive or resistive preheating of the wire material which enables an increased deposition rate with a reduced necessary laser power. Wire based materials are cost efficient for AM but limited in the range of available materials.

Laser wire cladding is used for coating of surfaces, rapid repairing and in generative production of structures. The application of wear protection layers and the injection of alloying elements into surfaces are concrete applications. Furthermore, the process can be used to repair damaged components. Due to the high material utilization rate, the process is well suited for processing expensive materials [6].

2.2 Functional Graded Materials by Direct Energy Deposition

FGMs were first proposed in 1972 for the use in composite materials to mimic the structure and composition of natural materials such as bones or bamboo fibres [7]. Interest in FGMs raised, as they promise to improve mechanical, thermal and electrical properties that cannot be represented by conventional materials and joining compounds [8]. The interest in FGMs is increasing across the die casting industry [8], the aerospace industry [9], the nuclear power industry [10] as well as the biomedical industry [11] as just a few examples to be mentioned. The research in FGMs reflect the general interest in extending material properties by means of graded structures or transition zones. In general, functionally graded components can be divided into two categories [12, 13]. The first category includes materials that are created by a local change in the process parameters. Thus,

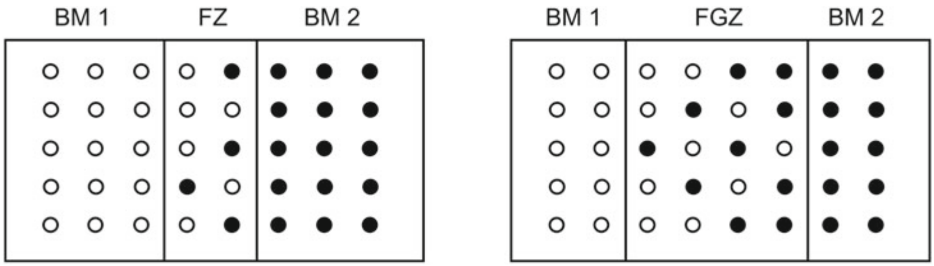

Fig. 2 Schematic drawing of a common multi material with a sharp Fusion Zone (FZ) between the Base Materials (BM) (left). Functional Graded Material with a defined Functionally Graded Zone (FGZ) (right)

differences in volume and density can be introduced in a targeted manner (cf. Fig. 2). Alternatively, a local change in the microstructure can be generated. The second category is characterized by a discrete or continuous transition of one material into a second material, also referred to as grading partners in the following [14, 15].

While Additive Manufacturing processes based on the Laser Powder Bed Fusion (LPBF) principle are particularly suitable for the volumetric adjustment of a component, various processes exist for the production of graded material transitions. These range from the production of thin layers by chemical vapor deposition [16] to the build-up of structures by double-wire electron beam build-up welding [17]. By simultaneously introducing two powder materials and changing the powder mixing ratio across the seam geometry, a graded transition from one grading partner to the other can be created using the DED method [8]. With a mixture of powder and wire feedstock, a graded transition is realized along a seam geometry or a components cross-section [18]. With a lateral L-DED double wire process, functionally graded parts were produced [19]. However, a coaxial double wire build up with two wire based materials is not realized yet.

2.3 Analysis of the Coaxial Processing Head LZH Coax-Head MKII

Representative for a coaxial laser wire processing head using the split beam principle, the LZH Coax-Head MKII from the Laser Zentrum Hannover e.V. is evaluated (cf. Fig. 3). The system uses a water-cooled, highly reflective pyramid to split a focused single beam into four single beams that are reflected by a mirror and guided into the processing zone under a beam incidence angle of approx. 14° to the middle axis. To prevent the mirrors and optical elements from damage by welding spatters, a crossjet is induced providing a pressurized air flow to protect the protective glass. Due to the beam splitter, the wire cannot be provided centrically in a straight manner but must be guided around the pyramid with bending radii of approx. 150 mm. While being suitable to change the wire without

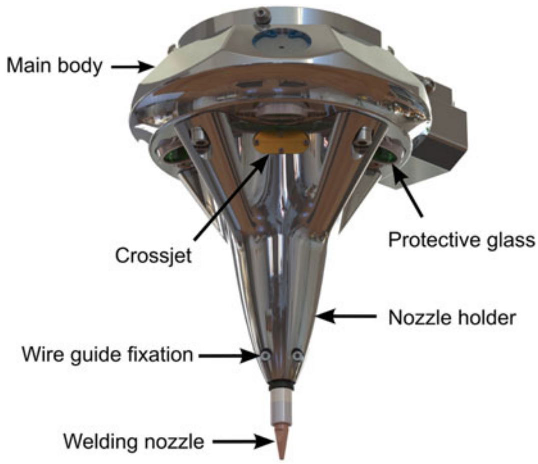

Fig. 3 Front view on the LZH Coax-Head MKII showing the main components of the processing head

detaching the entire feeding nozzle, the wrap around the beam splitter represents an extent of the free wire length between the wire feeding unit and the welding nozzle. Furthermore, it requires a cost-effective design to avoid an interference between the provided wire and the laser beams inside the processing head.

Process developments with the LZH Coax-Head MKII showed, that it can be beneficial to defocus the laser beam to a certain extent thus lowering the induced intensity while enlarging the laser spot diameter. However, a defocusing can only be achieved by moving the entire processing head in the vertical direction of the gantry. Following that, the stick-out of the laser wire decreases or increases depending on the adjustment in negative or positive vertical direction, making it a considerable factor in process development as the wire feeding behaviour changes with the stick-out length [20]. With a geometrical dimension of 210 mm in diameter and a height of approximately 235 mm, the accumulated mass of the LZH Coax-Head MKII is approx. 5 kg making it a relatively light-weight processing head on the market with a considerable small footprint. Due to its design, the LZH Coax-Head MKII is suitable to use a variety of laser beam sources [2].

2.4 Analysis of a Multiple Diode Processing Head Prototype

A prototype processing head (cf. Fig. 4) has been developed at the Laser Zentrum Hannover e.V. in order to investigate the system behaviour of a coaxial laser wire processing head that uses a single laser source for each laser beam. Optic tubes, as a simple yet promising and cost-efficient method to guide and shape the single beams, are used to focus the individual laser beams. The lenses are kept in place using retaining rings in a defined position. A SubMiniature version A (SMA) connector is used to provide a defined and precise coupling of the optical fibre with the optic tubes. The optical tubes are held

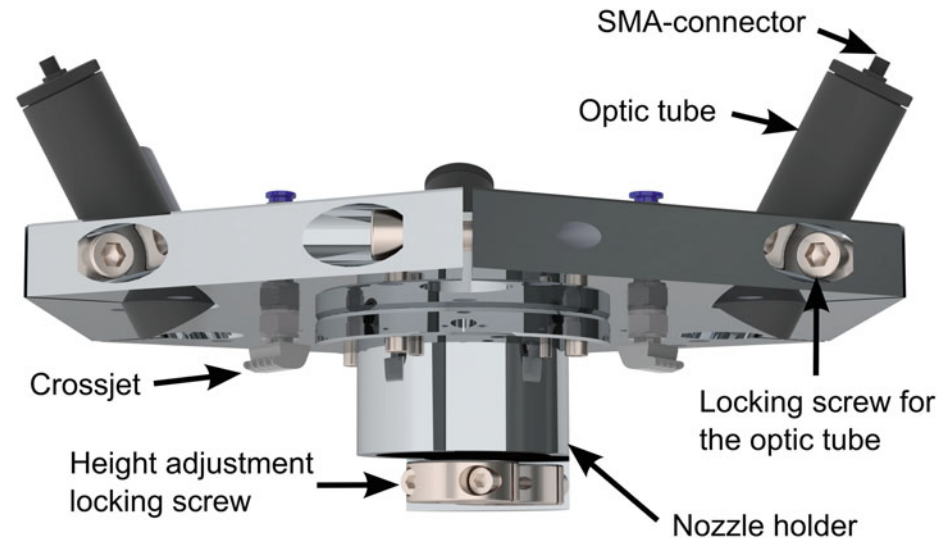

Fig. 4 Coaxial multi diode processing head prototype for a centric welding nozzle

in place by elastically deforming the base plate of the prototype processing head with a locking screw. The imposed radial load prevents the tubes from sliding out of their designated position. With a beam incidence angle of 30° combined with a focusing length of 250 mm, a common spot diameter of 2.3 mm is formed. To provide a proper wire guidance, a welding nozzle with a shielding gas connector is used that is clamped to the system by means of a radial load induced by a split ring. In preceding tests with the MK-II, laser output powers of 500 W were determined to be suitable to deposit 1.4718 stainless steel onto 1.0577 mild steel. Therefore, three laser diodes with a maximum single output power of 220 W were used to provide the necessary energy for processing the wire feedstock. Crossjets are provided to prevent damage to the focusing lens.

In order to assure that the system grants direction-independent weld deposition, circular welding seams of 1.4718 steel using a diameter of 0.8 mm were deposited on a base material of 1.0577 steel that revealed promising results in the macroscopic analysis (cf. Fig. 5). The microscopic analysis of straight single seams showed good results considering the dilution and interconnection of the welding seam to the substrate. The welding seams were found to be non-symmetric due to an off-axis placement of the wire mainly caused by the clamping mechanism of the welding nozzle holder.

Furthermore, the fixation mechanism of the optics turned out to cause a tilting of either the focusing or the collimating lens in case the applied load to keep the tubes in place was too high thus causing an elastic deformation of the tube. A tilted lens was found to cause a significant change in the process behaviour by displacing the single laser spot and reducing the supplied power to the melt pool. While welding with a wire diameter

Fig. 5 Circular single seam (left) and circular multi layer weld (right) of 1.4718 stainless steel deposited on 1.0577 steel

of 0.8 mm showed good results, trials with 0.6 mm and 1.0 mm wire diameter failed to generate reproducible results, failing in most cases due to either burn up of the wire or a lack of interconnection from the seam to the substrate.

Due to the burn up mainly occurring while using the 0.6 mm wire, the laser beam is expected to transfer too much heat into the welding wire before interacting with the substrate. The wire melts above its designated process zone and the molten material fails to connect with the substrate. In the case of the missing interconnection of the welding seam with the substrate while using the 1.0 mm wire, the relatively big spot diameter only grants a limited spot intensity thus being not sufficient to connect the molten wire material with the substrate.

In general, the precise alignment of the optical elements as well as the centric wire feeding nozzle can be determined to be key factors producing quality welding seams. The radial fixation of the optical unit was found to be problematic due to deformation behaviour followed by an implied load. Furthermore, using retaining rings for the positioning of the lenses is imprecise, as the position cannot be adjusted properly. Considering the burn up and the missing interconnection, a reduction of the laser beam diameter is preferable in order to reduce the energy that interferes with the wire above the designated welding zone and increases the intensity in the melt pool.

3 Development of a Coaxial Multiple Diode Double Wire Laser Processing Head

3.1 Derivation of Requirements

The analysis of common coaxial processing heads, mostly based on the split beam principle, has shown potential considering the wire feeding and guidance towards the processing zone as well as the geometrical dimensions of the processing head. The material supply towards the welding nozzle was determined as a key factor in laser wire AM. Small bending radii within the system that are mostly induced by the wire guidance around beam splitting elements represent a disruptive factor. In worst cases, the wire gets stuck causing a jam in the wire feeding section thus requiring maintenance of the processing head. Regarding the geometric dimensions of the processing head, small footprints are desired to reduce the applied mass to a gantry. Smaller footprints also allow the implementation in limited space. During trials it has been observed that defocusing the laser beam in order to increase the laser spot diameter can help to improve the process quality. With a fixed welding nozzle, defocusing of the laser beam is always accompanied by an adjustment of the stick-out between the work piece and the welding nozzle. The increase of the free wire length is limited and can lead to process interruptions if the maximum free wire length is exceeded and is therefore to be regarded as a critical influencing factor [20]. If the stick-out is reduced, a wire burn-up might potentially damage the welding nozzle and cause increased wear of the process technology.

Based on the points identified, a list of requirements that records the individual specifications was generated. Table 1 lists the main requirements of the system technology to be implemented. The most important elements are the avoidance of bending radii between the wire feeder and the welding nozzle as well as the possibility of defocusing the laser beam without changing the stick-out. Based on the principle, multiple diode laser wire AM is well suited for avoiding bending radii because the wire feeding unit can be placed exactly centrically above the welding nozzle. Although solutions with a centric wire feed using the split beam principle exist, these systems come up with a big footprint due to a high amount of beam shaping and guiding components necessary in order to guide the laser beam around the wire feedstock. The possibility of defocusing is to be made possible by means of an adjustment unit that allows the wire nozzle to be displaced by up to 5 mm. In order to avoid a burn up of the wire feedstock due to interaction between the laser beam and the wire above the designated process zone, a restriction to the height adjustment is necessary. The adjustment is only possible above the common laser focusing length. To ensure an easy connection of the laser fibre to the optics, a fibre SMA-connector shall be used.

Table 1 Extract from the specification list: changes are made based on the analysis of other coaxial processing heads

Requirements	Specification
Maximum laser output power	> 600 W
Avoiding bending radii	–
Passive cooling of the nozzle holder	–
Active cooling of the optics	–
Implementation of a crossjet	–
Free wire length	< 200 mm
Reduction of interfering geometry	< Ø 200 mm and ≤ 200 mm height
Reduction of the focusing length	< 200 mm
Reduction of the laser spot diameter	< 2 mm
Coupling from fibre to optics	SMA-connector
Quantity of laser beams	≥ 3
Reduction of processing head mass	≤ 5 kg
Beam incidence angle	≤ 30°
Nozzle height adjustment above laser focus	+5 mm

3.2 Prototypical Realisation of the Multiple Diode Coaxial Laser (DiCoLas) Processing Head

The multiple diode head can be divided into the two main assemblies “main body” and “nozzle holder” (cf. Fig. 6). The main body serves as a receptacle for the optical components and contains the cooling circuit of the processing head. In addition, the main body contains a central inlet for the wire guide enabling the wires to be fed directly into the double wire feeding nozzle. The nozzle holder contains the adjustment unit for changing the feeding nozzle position in relation to the focus point of the laser, the crossjets for the protection of the optics as well as the shielding gas supply towards the process zone. The main body is capable of adapting up to six laser beam sources via SMA-connectors and is designed to apply the same laser source used for the prototype processing head. Following that, fibre coupled laser diodes with a maximum output power of 220 W each and a wavelength of 970 nm are used.

To assure a high precision between the nozzle holder and the main body, close tolerances are necessary in order to guarantee a proper alignment of the nozzle middle axis and the common middle axis of the single laser beams. While the optical elements have a

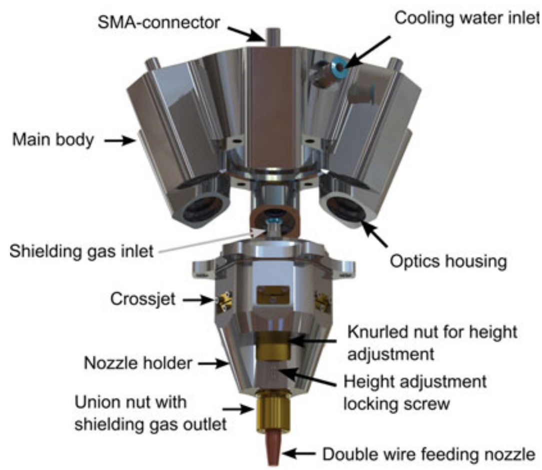

Fig. 6 View on the multiple diode processing head with the main body and the nozzle holder detached from another

high optical efficiency of above 99%, the nozzle itself is exposed to higher temperatures due to conducted heat from the welding material and reflected laser power. Therefore, a passive cooling is realized using the aluminium alloy EN AW6082 as the base material for each the main body and the nozzle holder in order to conduct heat from the nozzle towards the cooling circuit located in the main body. The material has a good thermal conductivity and an excellent machinability making it suitable to produce highly accurate fittings, especially to assure a proper alignment of the optical unit with the designated beam path of the system.

Figure 7 shows the exploded view of the optical unit that is split into two separate lens holders, one for the focusing lens and one for the adaption of the SMA connector with an integrated fitting for the collimating lens. The decoupling of the optical unit from the main body improves the possibility to maintain and clean the lenses and ensures a more

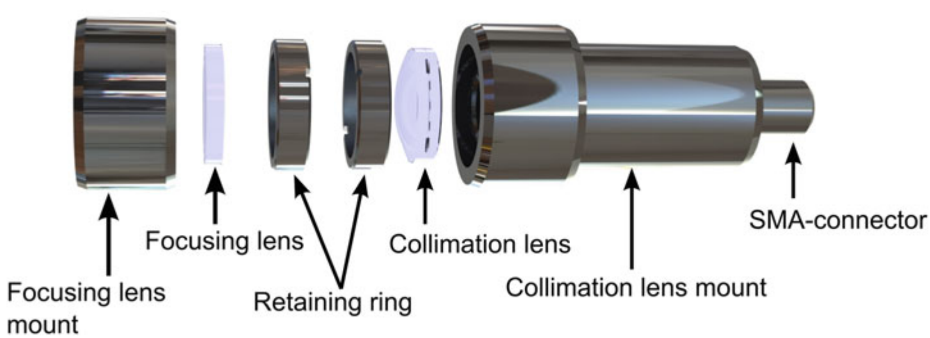

Fig. 7 Exploded view of the optic unit containing the focusing and collimating lens coupled with a SMA-connector

precise beam path by preventing a re-clamping of the main body during manufacturing. For the multiple diode processing head no shielding glasses are used. To maintain the correct position of the focusing and collimating lens, retaining rings are used to apply a static pressure in order to keep the lenses in place.

Figure 8 shows the cross-section of the height adjustment. A knurled nut (1) with an internal thread of low pitch ensures a precise adjustment of the wire guide. In order to maintain the set position, a radial load can be applied using two threaded pins (2), preventing the wire guide from shifting from its designated position. To ensure that the wire does not bend during feeding from the wire feeder to the double-wire nozzle, steel wire cores that are fixed in the wire guide by means of a threaded pin (3) are used. The pin prevents the wire core from being pushed out of its connector (4) in case a wire jam causes increased forces against the wire feeding direction. The entire wire guiding unit (5) can be replaced by another feeding solution, making the system suitable to adapt single wire feeding units or even powder feeding nozzles.

To prevent the wires from jamming inside the double wire nozzle (6), the nozzle holes have to be arranged exactly coaxially with the steel core connector. Since a screw connection cannot guarantee the alignment of the nozzle holes, a union nut (7) is used to apply an axial load to the wire guiding unit. A dowel pin (8) serves to position the double wire nozzle and prevents rotation during welding. In addition, the shielding gas is guided into the process zone through the union nut. The gas is first fed from the wire guide unit into the nut (9), where it is directed downwards through eight symmetrically distributed holes. Due to the double wire technology, the stick-out of the wires cannot be changed. It was set to 7 mm based on good cladding results with the coaxial processing head MKII. With

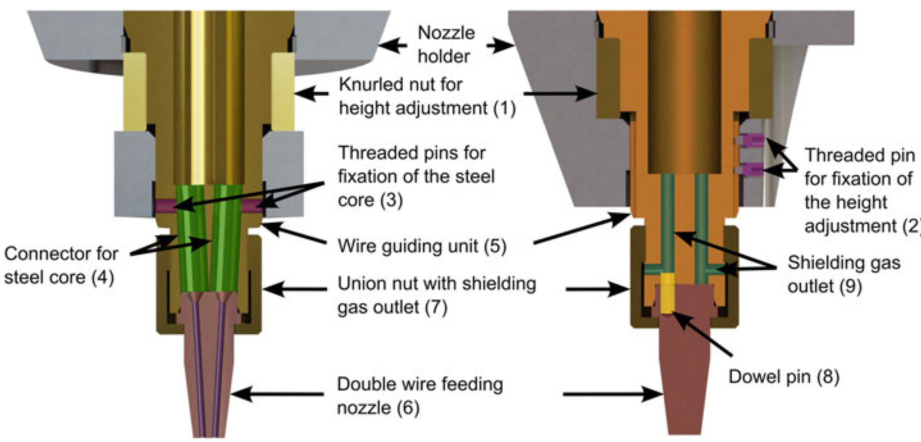

Fig. 8 Cross-section of the nozzle holder (left) showing the wire guiding towards the nozzle; Transverse section of the nozzle holder with regards to the fixation of the height adjustment and the shielding gas outlets (right)

a fibre core diameter of 400 µm, a collimating length of 25 mm and a focusing length of 100 mm, a spot diameter of approx. 1.6 mm is realized under a beam incidence angle of 25° to the processing heads' middle axis.

4 Conclusion

Based on the analysis of common coaxial laser systems and a single wire prototype for laser wire AM, a new processing head has been developed which is designated to process two wire based materials simultaneously with a coaxial welding nozzle in order to generate FGMs. The designed system is capable of processing wire feedstock with a diameter ranging from 0.6 to 0.8 mm. Preventing the optical elements from welding spatters as well as other particles was determined to be a major factor regarding a proper beam quality and expanding the lifetime of the optics. Therefore, a crossjet was implemented that induces a pressurized air stream of flat shape to blow welding spatters off the optical axis, preventing them from hitting the focusing lens. A first prototype system using optic tubes to fit the focusing and collimating lens showed good results in producing uniform circular welding seams. However, the radial clamping of the optic tubes could easily cause a tilting of either the focusing or collimating lens. Thus, an axial clamping of the lenses was preferred.

In direct comparison with the LZH Coax-Head MKII, a significant reduction of each weight and geometric dimensions can be achieved (cf. Fig. 9). Based on the different design approach using single beams emitted by individual laser diodes, a height reduction of 115 mm and a weight reduction of 3.5 kg from 5 to 1.5 kg can be achieved thus reducing the applied mass to a gantry system or a robotic arm significantly. Due to a centric bore, the wire does not need to be guided around a beam splitter and enables an easier and more fail resistant guidance to the double wire-feeding nozzle while maintaining a small footprint. The processing head was designed to apply up to six single diode stacks of

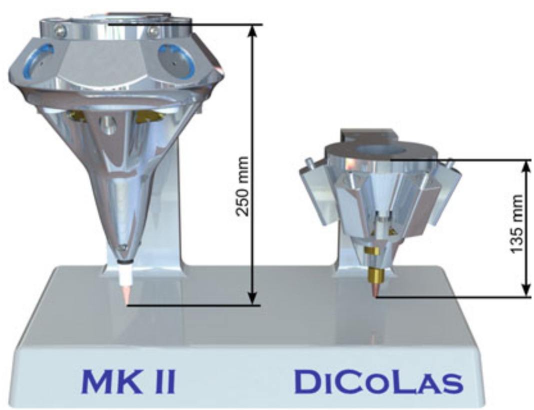

Fig. 9 Comparison of the geometrical dimension between the Coax-MKII (left) and the Multiple Diode Coaxial Laser (right)

220 W connected via fibres, enabling a maximum output power of approx. 1.3 kW which is significantly less than the maximum output power of the LZH Coax-Head MKII. This instance limits the applicable feeding velocity of the substrate and the wire, resulting in a lower build up ratio of the system.

The DiCoLas processing head will be tested after its production concerning its ability to produce FGMs from two different wire feedstock. The individual controllability of each single beam enables new strategies for process developments such as a rotating peak power between the single focus spots or an adaptive power input for each single beam based on thermal measurements. For future applications, the usage of laser diodes with different wavelengths in order to increase the material absorption ratio is a further factor worth to investigate. Furthermore, the usage of the processing head for single wire AM or the application with a powder nozzle is possible.

Acknowledgements Funded by the Ministry for Science and Culture of Lower Saxony (MWK) – School for Additive Manufacturing SAM.

References

1. Kelbassa, J., Gasser, A., Bremer, J., Pütsch, O., Poprawe, R., & Henrich Schleifenbaum, J. (2019). Equipment and process windows for laser metal deposition with coaxial wire feeding. *Journal of Laser Applications, 31*(2), 022320. https://doi.org/10.2351/1.5096112
2. Lammers, M., Hermsdorf, J., Kaierle, S., & Ahlers, H. (2020). Entwicklung von Laser-Systemkomponenten für das koaxiale Laser-Draht-Auftragschweißen von Metall- und Glaswerkstoffen. In *Konstruktion für die Additive Fertigung 2019* (pp. 245–260). Springer Berlin Heidelberg. https://doi.org/10.1007/978-3-662-61149-4_15
3. Matthews, B., & Hoppe, L. (2018). Smart additive manufacturing device. US 2018/03189292
4. Asano, K., Tsukamoto, M., Funada, Y., Sakon, Y., Abe, N., Sato, Y., Yoshida, M., et al. (2018). Copper film formation on metal surfaces with 100 W blue direct diode laser system. *Journal of Laser Applications, 30*(3), 032602. https://doi.org/10.2351/1.5040635
5. Shi, J., Zhu, P., Fu, G., & Shi, S. (2018). Geometry characteristics modeling and process optimization in coaxial laser inside wire cladding. *Optics & Laser Technology, 101*, 341–348. https://doi.org/10.1016/j.optlastec.2017.10.035
6. Chugreeva, A., Mildebrath, M., Diefenbach, J., Barroi, A., Lammers, M., Hermsdorf, J., Behrens, B.-A., et al. (2018). Manufacturing of high-performance Bi-metal bevel gears by combined deposition welding and forging. *Metals, 8*(11), 898. https://doi.org/10.3390/met8110898
7. El-Galy, I. M., Saleh, B. I., & Ahmed, M. H. (2019). Functionally graded materials classifications and development trends from industrial point of view. *SN Applied Sciences, 1*(11). https://doi.org/10.1007/s42452-019-1413-4
8. Ocylok, S., Weisheit, A., & Kelbassa, I. (2010). Functionally graded multi-layers by laser cladding for increased wear and corrosion protection. *Physics Procedia, 5*, 359–367. https://doi.org/10.1016/j.phpro.2010.08.157

9. Liu, Y., Liu, C., Liu, W., Ma, Y., Zhang, C., Cai, Q., & Liu, B. (2017). Microstructure and properties of Ti/Al lightweight graded material by direct laser deposition. *Materials Science and Technology, 34*(8), 945–951. https://doi.org/10.1080/02670836.2017.1412042
10. Shah, K., Haq, I. ul, Khan, A., Shah, S. A., Khan, M., & Pinkerton, A. J. (2014). Parametric study of development of Inconel-steel functionally graded materials by laser direct metal deposition. *Materials & Design (1980-2015), 54*, 531–538. https://doi.org/10.1016/j.matdes.2013.08.079
11. Bhavar, V., Kattire, P., Thakare, S., Patil, S., & Singh, R. (2017). A review on functionally gradient materials (FGMs) and their applications. *IOP Conference Series: Materials Science and Engineering, 229*, 012021. https://doi.org/10.1088/1757-899x/229/1/012021
12. Zhang, C., Chen, F., Huang, Z., Jia, M., Chen, G., Ye, Y., Lavernia, E. J., et al. (2019). Additive manufacturing of functionally graded materials: A review. *Materials Science and Engineering: A, 764*, 138209. https://doi.org/10.1016/j.msea.2019.138209
13. Lachmayer, R., Lippert, R. B., & Kaierle, S. (2020). Konstruktion für die Additive Fertigung 2018. *Springer, Berlin Heidelberg*. https://doi.org/10.1007/978-3-662-59058-4
14. Mahmoud, D., & Elbestawi, M. (2017). Lattice structures and functionally graded materials applications in additive manufacturing of orthopedic implants: A review. *Journal of Manufacturing and Materials Processing, 1*(2), 13. https://doi.org/10.3390/jmmp1020013
15. Zhang, N., Khan, T., Guo, H., Shi, S., Zhong, W., & Zhang, W. (2019). Functionally graded materials: An overview of stability, buckling, and free vibration analysis. *Advances in Materials Science and Engineering, 2019*, 1–18. https://doi.org/10.1155/2019/1354150
16. Kawase, M., Tago, T., Kurosawa, M., Utsumi, H., & Hashimoto, K. (1999). Chemical vapor infiltration and deposition to produce a silicon carbide–carbon functionally gradient material. *Chemical Engineering Science, 54*(15–16), 3327–3334. https://doi.org/10.1016/s0009-2509(98)00391-1
17. Osipovich, K. S., Astafurova, E. G., Chumaevskii, A. V., Kalashnikov, K. N., Astafurov, S. V., Maier, G. G., Kolubaev, E. A., et al. (2020). Gradient transition zone structure in "steel–copper" sample produced by double wire-feed electron beam additive manufacturing. *Journal of Materials Science, 55*(22), 9258–9272. https://doi.org/10.1007/s10853-020-04549-y
18. Li, L., Syed, W. U. H., & Pinkerton, A. J. (2006). Rapid additive manufacturing of functionally graded structures using simultaneous wire and powder laser deposition. *Virtual and Physical Prototyping, 1*(4), 217–225. https://doi.org/10.1080/17452750601141523
19. Weisheit, A., Fuchs, E., Bankowski, M., & Freyer, C. (2006). Multifunktionale Gradientenwerkstoffe für den Werkzeugbau. *Fraunhofer Institute for Laser Technology*: Aachen, Germany
20. Klingbeil, N. (2019). *Untersuchung des Drahtsystems zur Prozessstabilisierung für das drahtbasierte Laserauftragschweißen in der additiven Fertigung* (1st ed.). Apprimus Wissenschaftsverlag.

Joining Technology of Additively Manufactured Components: Design Measures for Optimizing the Strength of Adhesively Bonded Joints

Michael Ascher and Ralf Späth

Abstract

The size of components manufactured by laser powder bed fusion is limited by the available powder bed volume. To create larger structures, additively manufactured components can be combined with intermediate products to increase cost efficiency and amend the requirements. Joints of fiber-reinforced plastic profiles adhesively bonded with laser powder bed fusion manufactured aluminum couplers were investigated as examples. The geometric freedom of design in AM-processes enables optimization of the joint properties:

- Optimization of the adhesive application.
- Optimization of the adhesive distribution.
- Uniform stress distribution within the adhesive fill space.

To reveal the adhesive distribution during injection, tests with transparent acrylic models where carried out. The AM components' topology was optimized using finite element analysis to homogenize the stress distribution within the adhesive. The static strength and fatigue properties were validated experimentally. Results on adhesive distribution and fatigue behavior will be presented.

Keywords

Additive manufacturing • Adhesive bonding • Design measures

M. Ascher (✉) · R. Späth
Faculty of Mechanical Engineering, Institute for Construction and Production Technology, Professorship for Design and Lightweight Construction, Universität der Bundeswehr München, Werner-Heisenberg-Weg 39, 85577 Neubiberg, Germany
e-mail: michael.ascher@unibw.de

R. Lachmayer et al. (eds.), *Innovative Product Development by Additive Manufacturing 2021*, https://doi.org/10.1007/978-3-031-05918-6_5

1 Introduction

Additive manufacturing (AM) processes are limiting achievable component dimensions due to confined building spaces of the manufacturing machines. To create larger AM structures, the production facilities or even the underlying processes have to be adapted. Both measures lead to increased procurement or manufacturing costs. In many cases the benefits of AM processes are only needed at certain areas or non AM materials can contribute to the desired structures properties.

To ensure high fatigue strength and lightweight design, a comprehensive consideration of the resulting connection task is required. A joint is defined by the involved materials, the predominant physical effect that triggers the connection and the shape of its contact and auxiliary surfaces [1]. Those parameters can be optimized by taking advantage of the geometric freedom of design and the variety of materials that are underlying AM processes.

An application related example for highly demanded joints is the framework of the so-called “Hill Cruiser” (Fig. 1). The three-wheeled, drive-less, single-person vehicle was developed by the Professorship for Design and Lightweight Construction at Universität der Bundeswehr München.

The basic concept envisages a use in hiking sports. The dismountable vehicle can be carried during the ascent and enable the hiker to descend in an ergonomically advantageous way.

Primary design prerequisite is a minimum total mass. Therefore, the vehicle frame is made of carbon fiber- reinforced plastic (CFRP) and maximum functional integration is strived for. Instead of building the entire framework from CFRP, cost efficiency can be improved by connecting simple CFRP tubes with AM couplers to form a load-bearing hybrid framework. This enables functional integration in the AM couplers (e.g. disc brake

Fig. 1 Functional prototype of the Hill Cruiser

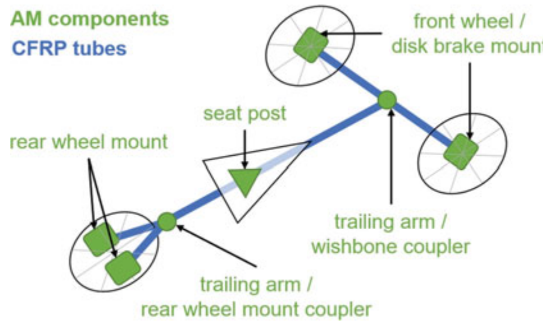

Fig. 2 Principal framework design and its resulting junctions

mount; wheel mount, seat post), as well as the individualization of the frame dimensions according to the anthropometric data of the customer (Fig. 2).

A large joint surface, a low notch effect and a comparatively high static and dynamic load capacity make adhesive bonding an optimal joining method for this application. In addition, it is conceivable that the AM couplers geometry can be adapted to the specific load case, and therefore be optimized to achieve a homogenous stress state in the adhesive.

The scientific issue addressed in this paper is the development of design solutions for a resilient and reproducible adhesive single lap joint (SLJ) between laser powder bed fusion (LPBF) manufactured couplers made of aluminum alloy AlSi10Mg and CFRP profiles, taking advantage of the design freedom that comes with the AM process. Tensile stress is considered as a basic load case. The adhesive used is a viscoplastic 2-component construction adhesive based on epoxy resin in which modified polyamine is used as a hardener [2]. After development of a method for optimal adhesive distribution by injection [3], the joint strength will be determined experimentally. The results are used to validate a finite element (FE) model, which is utilized for topology optimization of the AM component to minimize tensile stress in the adhesive.

2 State of the Art

2.1 Industrial Practice: Bonded Frame Structures

Bicycle frames are a typical application of bonded frame constructions. Fiber-reinforced plastic frames adhesively bonded using epoxy resin have been in use since the beginning of the 1980s. The connecting couplers were forged or die-cast from aluminum and the joining surfaces were conical, resulting in a very small adhesive gap [4]. Other variations include bonded steel joints with combined force fit, double lap shear joints or special press-fit sockets. [5]. Problems with the fatigue strength and high assembly effort prevented a wider acceptance on the market.

In 2015, the possibility of individual frame dimensions was tapped through AM processes [6]. Oval and round FRP profiles with different layer structures were joined using couplers based on titanium alloy. An adhesive was applied to the joining surfaces of the coupler before the joint components were connected. The frame tubes were aligned with a special assembly jig [7]. The couplers were manufactured by powder bed based melting [8] with the required thermal energy coming from a laser.

2.2 Structural Bonding of AM Components

For adhesive bonding of tubular cross-sections (circular joint geometries), overlapped bonding is preferable to butt bonding due to the choice of joint overlap, which enables optimal utilization of the adherends material strength. When the joint is subjected to shear or torsion, the adherend and adhesive layer deformation leads to an uneven stress distribution with pronounced stress peaks at the overlap ends. The distributions can be determined analytically (e.g. Frostig et al. [9]) or numerically using the boundary element code (BEASY) [10] (Fig. 3).

As a result, the bond strength depends on the deformation behavior of the joined parts and the adhesive layer, as well as the geometry of the bonding surface [11].

Regarding the use of AM processes to increase the strength of adhesive joints, the German Association for Welding and Allied Processes (Deutscher Verband für Schweißen und verwandte Verfahren e. V., DVS) recently published design recommendations for adhesive bonding of AM components, issuing design rules for components, joining zones, pre- and post-treatment measures, as well as the adhesive application [12]. Measures to reduce the stress peaks at the overlap ends include stiffening the joint components in the

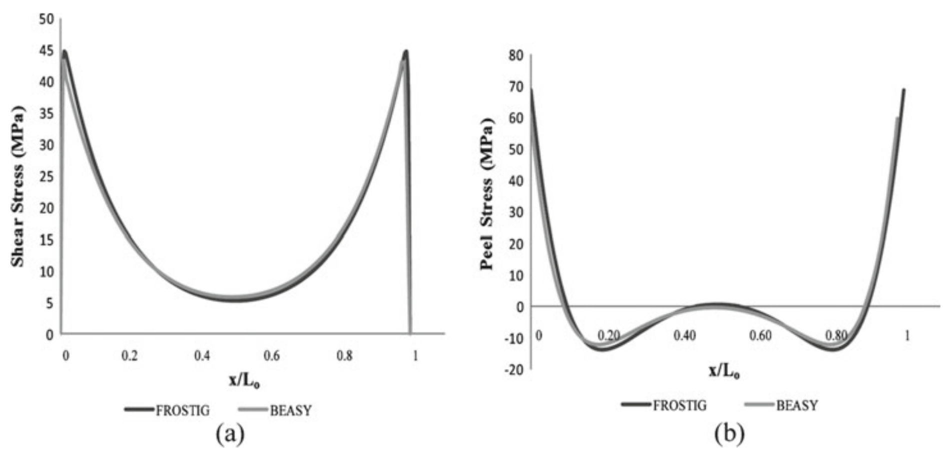

Fig. 3 Adhesive shear (**a**) and peel stress (**b**) distributions for the single lap joint [10]

area of the joining zone, lashing on one or both sides and enlarging the joining surface in combination with a mellow adhesive. The introduction of lattice structures in the bonding surfaces of SLJ's between polymers leads to anchoring points for the cured adhesive. By varying the cell geometry and wall thickness, the joint is adapted to the load type. For the adhesive application, reference is made to the use of internal channels, which help to completely fill the lattice structures with adhesive.

Studies on the effects of three-dimensional lattice structures and a variation of the filling degree on the tensile shear strength were carried out by Watschke [13]. Anchoring structures were printed into polypropylene test specimens and tensile shear tests were carried out in accordance with [14]. To prevent the typical bending up effect, the joint components were reinforced with aluminum sheets. A 2-component polyurethane adhesive was used. The tensile shear strengths determined for both measures were comparable to that of samples with a plasma pre-treated bonding surface [15].

The general bonding suitability of LPBF components made of AlSi10Mg using a single-component adhesive has already been demonstrated, with a bonding strength comparable to that of die-cast components, regardless of the bonding surfaces pre-treatment method [16].

3 Methodical Approach

To prevent defects in the adhesive layer that can be traced back to the way of application, parameters of the injection method must be considered. Explicitly, this means optical assessment of the adhesive distribution while varying the amount and position of injection bores as well as the inner channels geometry.

To determine joint strength and failure mode, static tensile and fatigue tests with joints made of the actual material pair (AlSi10Mg and CFRP) are to be executed. The results serve as confirmation of successful adhesive distribution (in case of non-adhesive failure) and simultaneously validate a FE model representing the structural- mechanical effects within the adhesive layer.

Based on this model, computer-aided topology optimization of the AM adherend is applied to minimize the first principle stress within the adhesive in order to increase the bonding strength [17].

4 Optimization of the Adhesive Application

4.1 Classification

Preliminary tests demonstrated that during conventional pre-application on the joint surfaces, the adhesive is partially pushed out during the unification of the joint components, which results in adhesive failure, and therefore, low bonding strength.

In the present investigations, the adhesive application was implemented by injection with a manually operated two-chamber cartridge squeezing device. The required quantity of the 2-component adhesive is dispensed in a pressure/time-controlled manner and mixed via a mixing nozzle. The joint components are placed in the desired position, separated by a fill gap, before the adhesive is injected sequentially into injection hole(s) within the AM component. The adhesive should completely fill the cavity between the adherends. According to the manufacturer's specifications [2] and in consistency with [11], the adhesive gap was set to 0.1 mm.

The aforementioned procedure can be applied to adhesive application from outside (external feed) as well as from inside (internal feed) (Fig. 4). An example of external feed is an AM coupler for the connection of several CFRP tubes. An example of internal feed are AM stiffening elements inside of CFRP tubes to increase the strength at bearing or load application points. As the basic mechanisms of internal and external feed correspond in terms of bonding strength and FE model characteristics, only external feed will be considered in the following.

The adherends were substituted with transparent acrylic components for visualization of the flow processes via videography while injecting. Compared to the typical, non-destructive and momentary testing methods of bonds such as active thermography [18], the use of laser shocks [19], ultrasonic based tests [20], shearography [21] or computer tomography [22] this approach enables the detection of defects and allows conclusions to be drawn about the injection process itself at little expense.

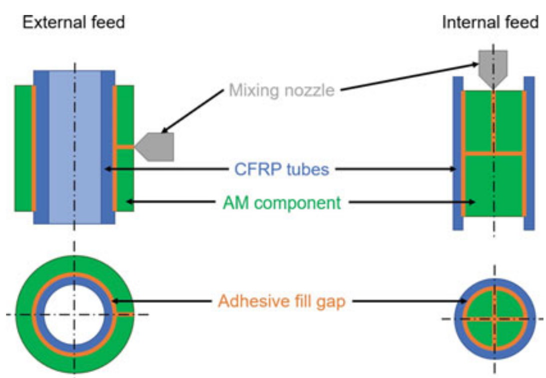

Fig. 4 Schematic adhesive injection with external feed (left) and internal feed (right)

4.2 External Feed

Reference joints without adhesive distribution geometries were used to define the optimization potential of the joint. In case of Sample #3 the adhesive was injected into one single injection bore until the adhesive leaked from the overlap end. In case of Sample #4 the adhesive was injected consecutively into two opposite injection holes in the same manner. Placing the samples in front of a 90°-angle-mirror allows the distribution pattern to be displayed over the circumference (Fig. 5).

Sample #3 shows that the adhesive cannot be fully distributed using a single injection bore without additional measures. Sample #4 suggests that this problem is partially caused by a displacement of the inner joint component during injection, which reduces the intended gap width on the opposite side. Since the volume flow rate of the effective annular gap flow is reduced by the gap space to the third power [23], the adhesive cannot be distributed evenly. Regardless of the misalignment, further conclusion can be drawn looking at the symmetry line of both specimens. Due to the requisite ratio of diameter to overlap length, it is not possible to feed half of the circumference using one injection bore along the overlap as the adhesive leakage occurs prior, indicating that centering measures are necessary to ensure an even adhesive gap, and that inner channels should be implemented to direct the adhesive along the circumference.

The adhesive gap is adjusted by centering surfaces that form an interference fit between the joint components. One solution for the adhesive distribution over the circumference is the implementation of a U-groove of 360° in a plane orthogonal to the longitudinal axis of the tube (Fig. 6).

By varying the parameters groove depth t, groove width b, and groove radius r, the full circumferential distribution was accomplished using two injection holes for overlap lengths ≤15 mm.

For longitudinal distribution with larger overlap lengths, various strategies proved to be effective (Fig. 7).

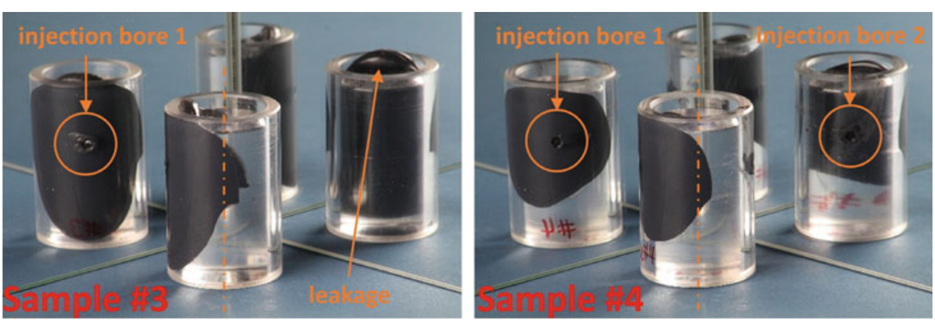

Fig. 5 Reference joints placed in front of a 90°-angle-mirror using one (#3, left) and two (#4, right) injection holes

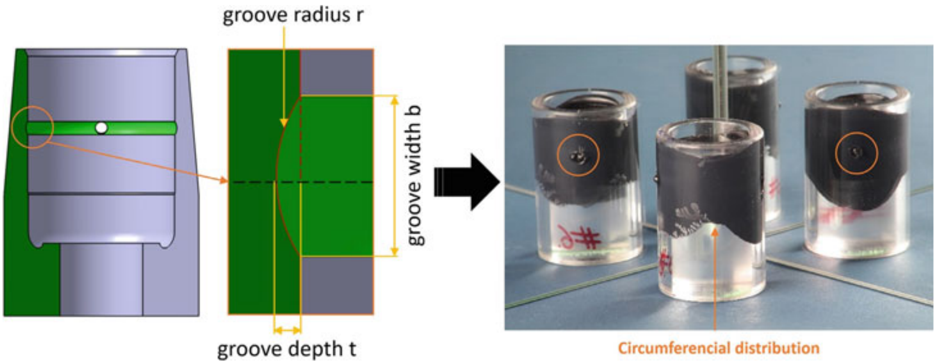

Fig. 6 Adhesive distribution over the circumference using a 360° U-groove

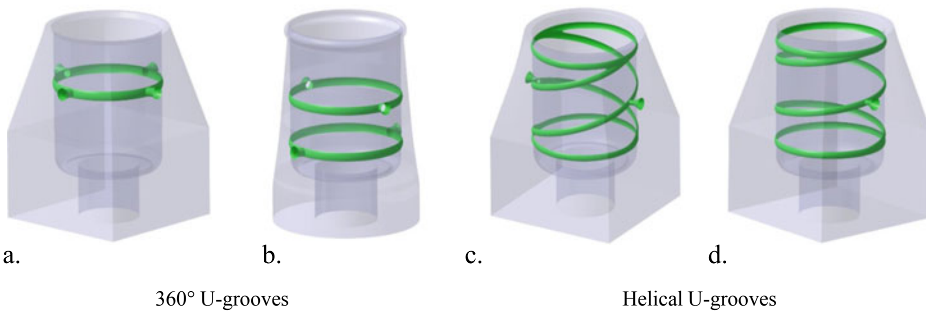

Fig. 7 Assortment of adhesive distribution geometries assessed in this work

For 15 mm < overlap length ≤30 mm, two additional injection holes can be put into the existing 360° groove (Fig. 7a). Furthermore, it is feasible to duplicate the aforementioned U-grooves of 360° over multiple planes along the longitudinal axis, each with two injection holes (Fig. 7b.). To avoid leakage of the adhesive from injection holes of adjacent planes, it is recommended to offset the two injection holes by 90° with respect to the neighboring planes. A realization of the longitudinal distribution by helical recesses is also possible (Figs. 7c/d and 8). The number of parallel helical grooves and the number of turns are useful variation parameters. Helical recesses are most suited if there are restrictions regarding the positioning of the injection bores along the overlap. However, they have a disadvantage of reducing the load bearing adhesive area more than circumferential recesses, and therefore, locally weaken the bond.

The centering measures and inner channels lead to an even and complete distribution of the adhesive. To prevent defects like air inclusions, the respective injection order from bottom to top (vertically) and clock- or counterclockwise (horizontally) must be met. If

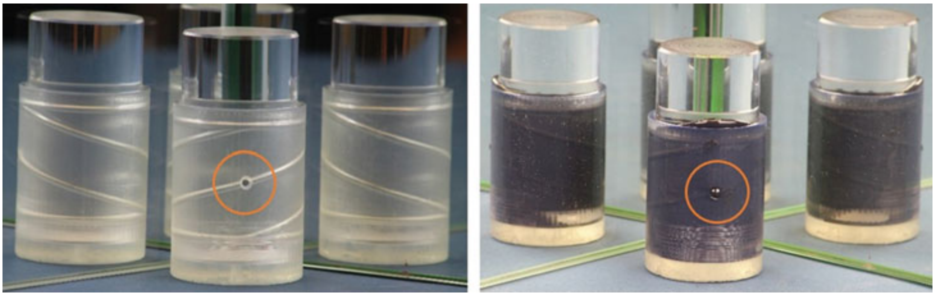

Fig. 8 Adhesive distribution along the overlap using helical U-grooves

there are no restrictions on positioning of the injection bores, the U-grooves of 360° are preferred.

5 Tests: Static Strength and Fatigue Behavior

5.1 Material Properties

Manufacturing Equipment. The AM joint components were produced in-house by the Professorship of Production Technology using an "SLM 125" from the manufacturer SLM Solutions Group AG (Lübeck). To suppress upskin and downskin effects, the test samples were printed vertically [16]. The manufacturing parameters for structural components correspond to a compromise between high strength, surface quality and dimensional accuracy, and thus reflect industrial practice.

Selected Materials. Due to the already confirmed bonding [16] and lightweight-construction [24] suitability, aluminum alloy AlSi10Mg was chosen for the LPBF components [25]. A fiber volume ratio of 55% and unidirectional fiber orientation characterize the CFRP tubes wound from resin impregnated layers. For high dimensional accuracy and constant surface properties, the outer surface of the tube is ground by the manufacturer CG TEC Carbon und Glasfasertechnik GmbH (Spalt) [26]. The 2-component adhesive "DP490" from the manufacturer 3 M Deutschland GmbH (Neuss) is a viscoplastic construction adhesive based on epoxy resin (Table 1).

Test specimens. The 9 test components consisted of a CFRP tube (D = 30 mm; t = 2 mm) which is connected at both ends to AM couplers by single lapped bonds with a 30 mm overlap length resulting in a 2827.43 mm^2 adhesive area. To obtain the intended adhesive gap of 0.1 mm across the largest possible area, for adhesive application, 4 injection holes and a single pitch circular groove (Fig. 7a) were printed into the AM aluminum couplers, as well as the interference fit (no machining on this surface). The clamping elements for connection to the test machine are bolted to the AM components (Fig. 9).

Table 1 Physical properties and strength characteristics of the adhesive "DP490" [2]

	Matrix	Hardener
Foundation	mod. epoxy resin	mod. polyamin
Viscosity (mPa s)	520,000	100,000
Density (23 °C) (g/cm^3)	1.0	1.0
Mixing ratio	2	1
Hardening (anaerob)	7d at 23 °C / 1d at 23 °C +1 h at 80 °C/ 2 h at 65 °C	
Operating temperature (°C)	−55… +120	
Lap shear strength (Mpa) [14]	26	

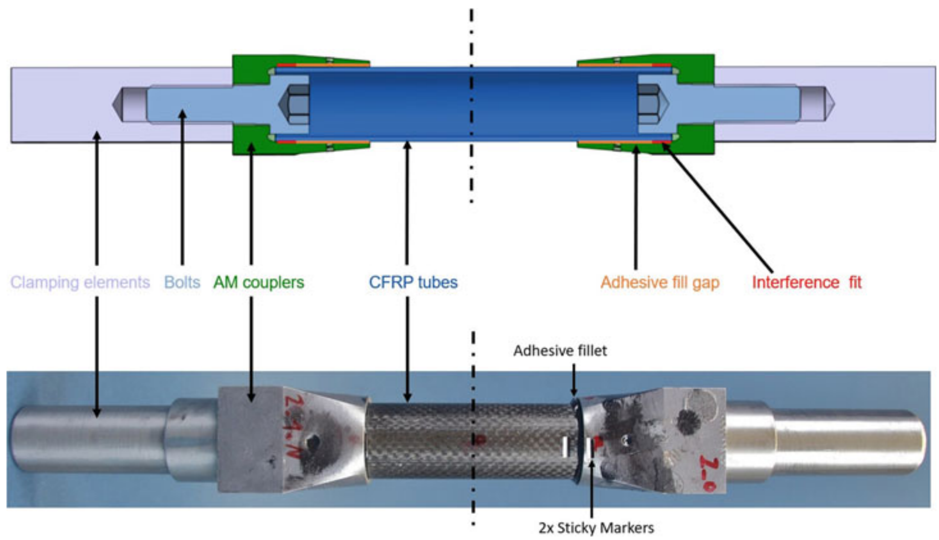

Fig. 9 Schematic representation and implementation of the test specimen

The manufacturing process was as follows:

- Pre-treatment of the joint components in consideration of [27]
  – Rinse with isopropanol
  – Mechanical pre-treatment with 3D sanding fleece
  – Cleaning in an ultrasonic bath with distilled water
  – Drying
  – Fastening the AM components with clamping elements using bolts.
- Bonding process
  – Connecting and alignment of the joint components with an interference fit

  - Injection the adhesive into the injection holes provided (note the respective order) until a uniform adhesive fillet is formed on the upper side.
- Hardening
  - 24 h at 23 °C, stored vertically
  - then 2 h at 60 °C, stored lying down (post-cross-linking).

Testing machines. Static tensile tests were carried out on a servo-hydraulic testing machine (Type: Trebel, Carl Schenck AG, Darmstadt). Wedge grips fix the specimens over a clamping length of 90 mm. An external video extensometer (LIMESS Messtechnik & Software GmbH, Krefeld) is used to measure the strain through the change in length between two special markers, applied at a distance of $L_0 = 8.0$ mm (Fig. 9).

To determine the fatigue strength, oscillation tests were carried out with a high-frequency pulsator (Type: Amsler 550 HFP, Zwick Roell AG, Ulm).

5.2 Tensile Test

The testing machine was operated such that the force on the joint steadily increases. This requirement was met with a constant test speed of 1.5 mm/min and the specimens were destroyed within a time of (65 ± 20) s.

Test results are documented in form of a stress–strain diagram (Fig. 10), from which the maximum measured stress (fracture stress) $\sigma_{B,1} = 26.61$ MPa is obtained. The measured strains are used to validate the FE model.

The fracture pattern (Fig. 11) shows that the joint failure is not a case of cohesive failure within the adhesive, but of adherend failure (delamination) in the CFRP tube.

Two tensile tests were carried out, resulting in identical fracture patterns and similar fracture strengths ($\sigma_{B,2} = 29.03$ MPa). Compared to the results of the preliminary tests

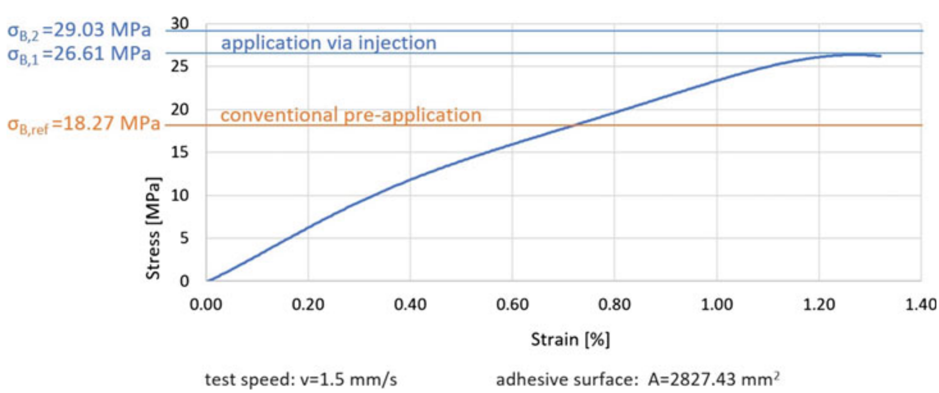

Fig. 10 Stress–strain diagram of an exemplary specimen

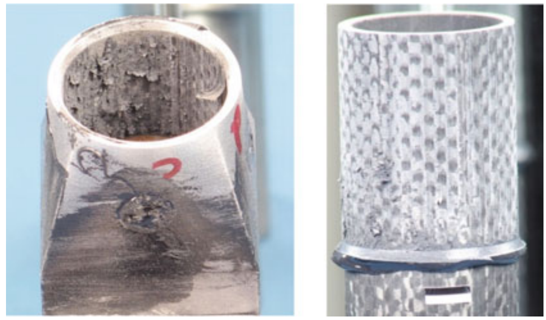

Fig. 11 Resulting fracture pattern of the static tensile test

($\sigma_{B,ref} = 18.27$ MPa, conventional pre-application of the adhesive on the joint surfaces) the fracture stress was increased by approximately 50%.

5.3 Fatigue Test

The fatigue strength of the joint was determined with oscillation tests. Seven test specimens were subjected to a cyclic load with sinusoidal progression at two different load levels with constant amplitude. To evaluate the mid- and long-term strength properties, the service life of the components must be in the range of 10^4–10^7 cycles. The stress amplitudes were determined to be $\sigma_{A1} = 7.5$ MPa and $\sigma_{A2} = 5$ MPa. A pulsating ($R = 0$) tensile load in the longitudinal direction of the tube was applied at a test frequency of 54 Hz. The durability of four tested specimens at the first load level and three tested specimens at the second load level are shown in Fig. 12.

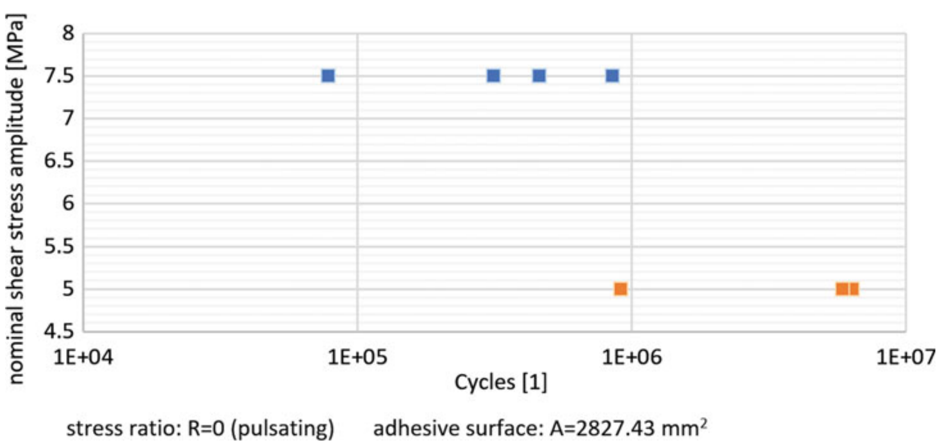

Fig. 12 Fatigue strength properties of 7 tested specimens

The evaluation of the test results according to a logarithmic normal distribution (failure probability of 50%) leads to a Wöhler (S–N) curve slope exponent of $k_{50\%} = 5.77$, as well as a service life of $N_{1,50\%} = 312{,}497$ and $N_{2,50\%} = 3{,}238{,}897$.

The fracture patterns show no differences compared to those of the static tensile test. Both the failure location (CFRP tube) and the failure mechanism (delamination) are the same.

To improve the strength potential of the joint, the interlaminar stresses between the unidirectional laminate layers of the CRFP tube must be reduced. It is expected that topology optimization to reduce the first principal stress within the adhesive layer will also affect the stress state of the laminate. Lower stresses imply a more uniform loading of the adhesive along the overlap length, which also implies lower local stress peaks in the adjacent laminate.

6 FEA-Based Strength Optimization of the Joint

6.1 Model Parameters

The software Hyperworks 2021 from Altair Engineering (Troy, Michigan) was used to carry out the linear-static strength analyses. Because of the small adhesive thickness (0.1 mm), a fine mesh density (min. edge length 0.02 mm) is required to resolve the underlying stress state. Due to the associated computational effort, the modelling of the described test structure is simplified by exploiting symmetries. The 3D model reflects a single bond of the test body as a quarter of the entire model.

The load is defined along the symmetry axis of the CFRP tube. The constraints are modeled in the area of the stress cone, where the bolts attach the coupler to the clamping elements (Fig. 9).

Due to the numerous iteration loops during the topology optimization, the computational effort was further lowered with the 3D quarter model assumed to be rotationally symmetric. This reduced the simulation to two dimensions enabling the use of shell elements with special boundary conditions. The appropriateness of this simplification is confirmed by a comparison of the nodal displacements as well as the course of the equivalent von Mises stress in the 2D and 3D model results (Fig. 13).

The material data used in the model was taken from literature (bulk data). For a more precise representation, the adhesive properties should take scale effects into account and should therefore be determined experimentally [28].

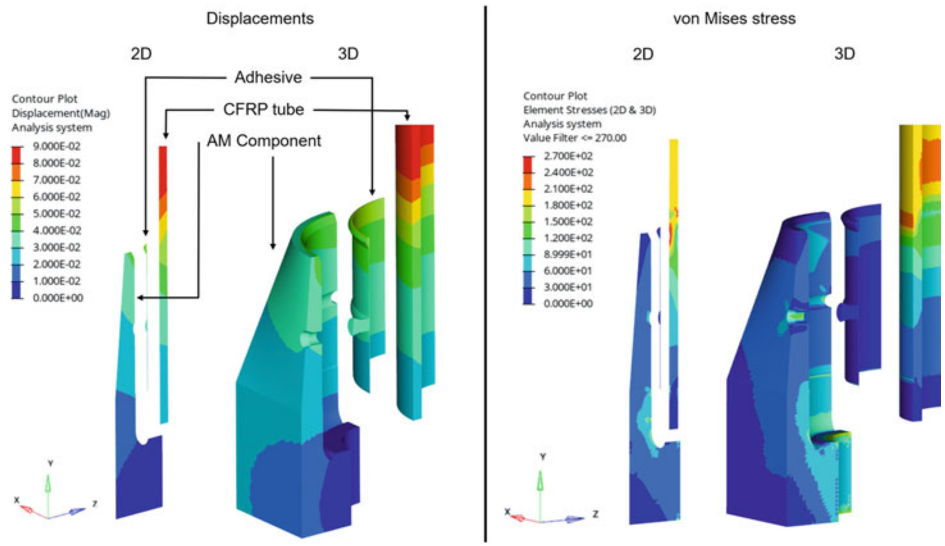

Fig. 13 Contour plot of nodal displacements in mm (left) and von Mises stress in MPa (right) in 2D and 3D model

6.2 Optimization Results

The objective of the topology optimization was to minimize the first principal stress within the adhesive layer. The optimization variable is the element density (ED) of the AM component, which is computed directly in Hyperworks and describes the presence of material at each location by a single value which varies between 1 (present) and 0 (absent). Since the circular outer contour of the CFRP tube is prescribed, the inner surface of the AM part was fixed to ED = 1. Figure 14 shows the result of the topology optimization after 52 iteration loops. For the geometric implementation, areas with low element density were either thined ($0.4 < \mathrm{ED} \leq 1$) or removed ($\mathrm{ED} \leq 0.4$).

The reanalysis of the new design leads to changes in the deformation behavior. The measures taken reduce the typical bending-up effect at the start of the overlap (Fig. 15).

Figure 16 shows the stress state for each design. The optimized design leads to a reduction of the maximum first principal stress within the adhesive layer by 36%. In the non-optimized version, high tensile stresses occur at the beginning of the overlap, while the end of the overlap is hardly involved in the force transmission. The optimized design distributes the transmitted force evenly along the overlap length which leads to a higher shear component (reduced peel stress), especially at the beginning of the overlap. Both designs show that the distribution geometries are hardly involved in the force transmission, and thus reduce the usable bonding surface.

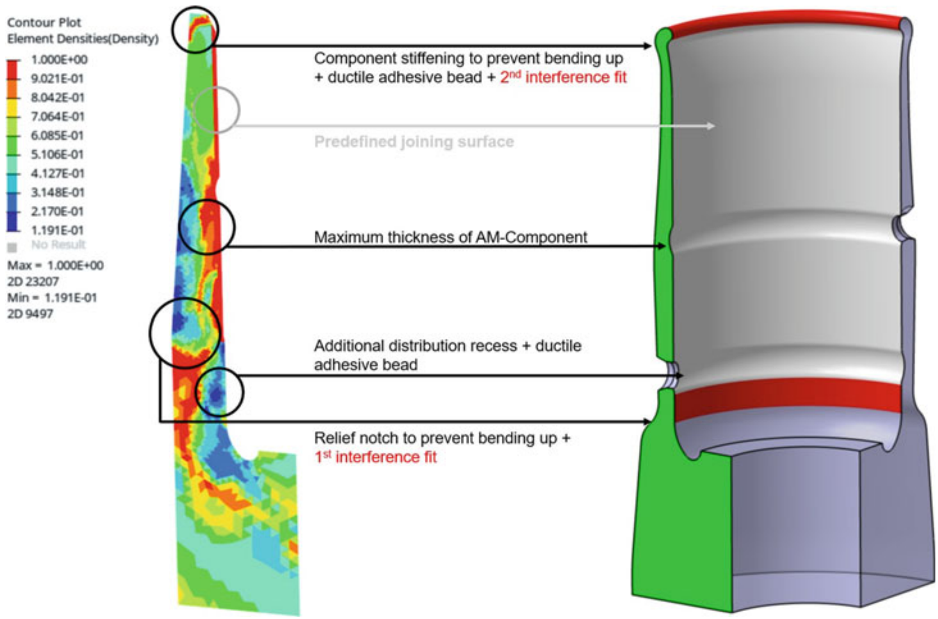

Fig. 14 Result of the topology optimization (ED contour) and design consequences to be derived from it

The results illustrate the potential to reduce the exposure of the adhesive layer through reduction of tensile stresses at the beginning of the overlap with a uniform utilization of the adhesive layer and a shift of the stress state towards shear to reduce peel stresses. This new geometry will be tested in the near future.

7 Conclusion

The overall objective of this paper was to maximize the strength of adhesively bonded joints between AM couplers made of AlSi10Mg and CFRP profiles exploiting the design freedom that is underlying AM processes.

The adhesive application was assessed first. Suitable geometries were developed to inject the adhesive into the AM adherend and distribute it within the adhesive gap. The effectiveness was qualitatively confirmed using visualization models. The resulting joint strength was quantified experimentally by static tensile and fatigue tests. Compared to preliminary tests, the failure location was shifted from the adhesive (adhesion failure) to the tube laminate (delamination), indicating that adhesive application by injection and distribution via inner channels is an improvement.

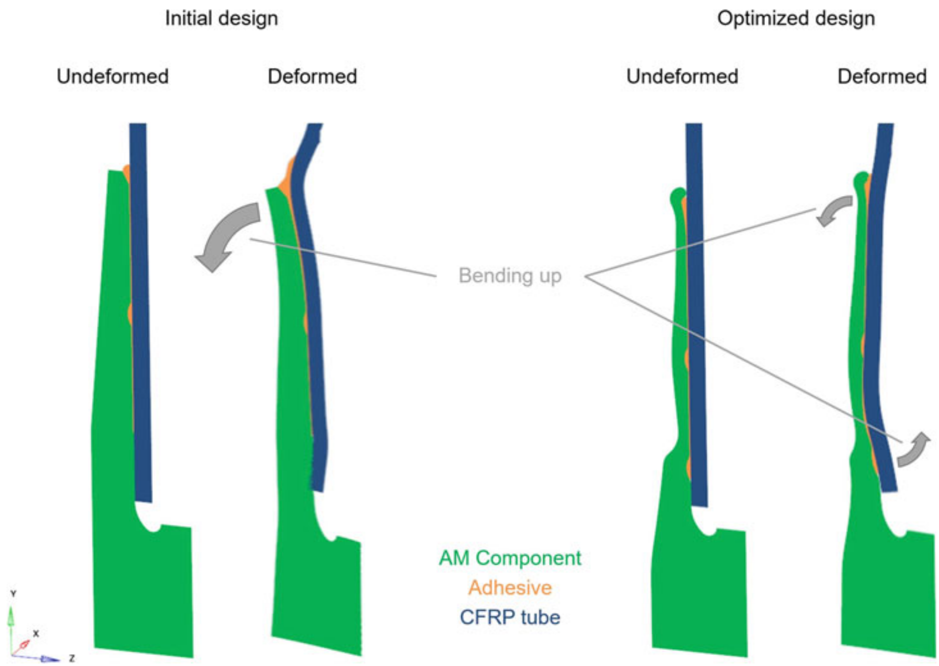

Fig. 15 Deformation behavior (scale exaggerated) before (left) and after (right) introducing the optimization measures

To homogenize the stress state within the adhesive layer and further increase the bonding strength, FE-based topology optimization of the AM adherend was performed to reduce the maximum first principal stress within the adhesive and even out the stress distribution along the overlap length. The numerical results show a reduction of 36% with the improved design and a shift of the stress state towards shear while reducing peel stresses.

8 Outlook

For a more accurate representation of the mechanical behavior of the adhesive within the FE model, the adhesive properties must be determined experimentally. The Young's modulus can be evaluated through tensile tests with a cast and punched substrate specimen [29]. The shear modulus can be measured by a thick adherends shear test [30]. From those two parameters the Poisson's ratio can be calculated.

After implementation of measured material parameters in the FE models, the 2D optimization cycle can be repeated with a corresponding 3D model used for numerical verification of the optimization measures. The 3D model can then be validated through

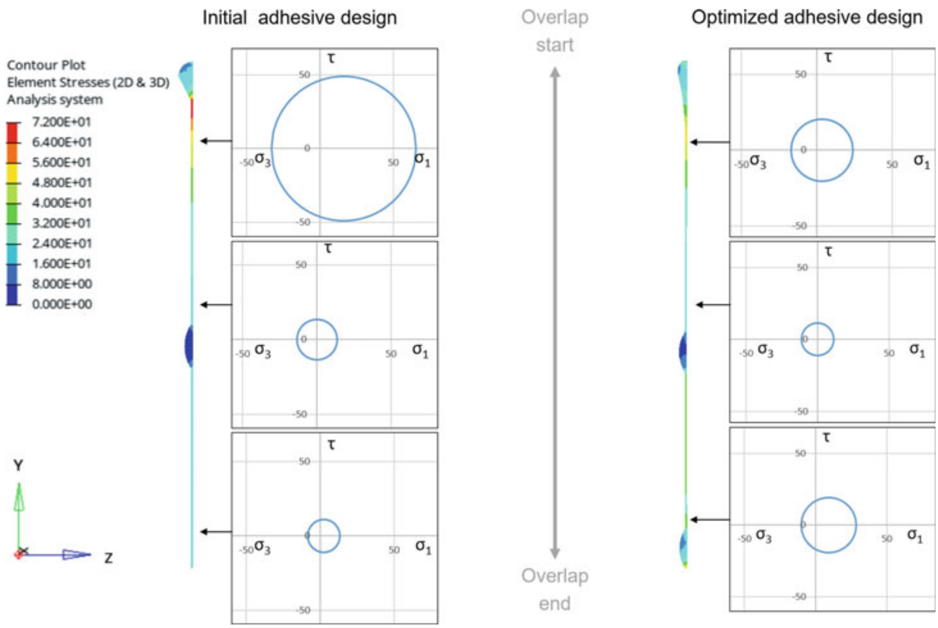

Fig. 16 Contour plot of von Mises stress and Mohr's circles along the overlap length

tensile tests with topology-optimized joints. In addition to the strains, the fracture strength of the joint (assuming cohesive fracture within the adhesive layer) should be compared with the calculation results. A strain energy based failure criteria can address the problem of stress singularities in the FE method [31]. This makes it possible to develop a FE model with any adhesive surface geometries (e.g. double lap shear joint), to apply complex load cases to it, and to make realistic service life predictions while reducing test effort.

References

1. Bauer, C.-O. (1991). *Handbuch der Verbindungstechnik*. Hanser.
2. 3M Deutschland GmbH. (2003). Material Data Sheet: Scotch-Weld DP 490.
3. Conermann, G. (2020). *Forschungsberichte des Instituts für Füge- und Schweißtechnik (No. 57): Injektionskleben von Strukturbauteilen mit hochreaktiven 2K-PUR-Systemen*. Shaker Verlag, Düren.
4. Green, J. M. (2001). *Bicycle accident reconstruction for the forensic engineer*. Trafford, Victoria, B.C.
5. Smolik, H.-C. (2010). Klebetechniken: Das Online-Glossar - www.smolik-velotech.de - Fahrradtechnik. Accessed: 03 June 2021. Retrieved from http://www.smolik-velotech.de/glossar/k_KLEBETECHNIKEN.htm

6. Vesenbeckh, F. (2016). Briten bringen maßgeschneiderte Rahmen mit 3D-Druck. Accessed: 03 June 2021. Retrieved from https://www.bike-magazin.de/mtb_news/mtb_neuheiten/neuheiten-robot-bike-r160
7. Atherton Bikes. (2019). Technology: How we build your bike. Accessed: 03 June 2021. Retrieved from https://www.athertonbikes.com/technology
8. International Organization for Standardization. (06/2018). *Additive manufacturing - General principles - Terminology*. (ISO/ASTM DIS 52900:2018-06).
9. Frostig, Y., Thomsen, O. T., & Mortensen, F. (1999). Analysis of Adhesive-bonded joints, square-end, and Spew-Fillet—High-order theory approach. *Journal of Engineering Mechanics, 125*(11), 1298–1307. American Society of Civil Engineers (ASCE). https://doi.org/10.1061/(ASCE)0733-9399(1999)125:11(1298)
10. Gonçalves, D. J. S., Campilho, R. D. S. G., Da Silva, L. F. M., & Fernandes, J. L. M. (2014). The use of the boundary element method in the analysis of single lap joints. *The Journal of Adhesion, 90*(1), 50–64. https://doi.org/10.1080/00218464.2013.763725
11. Habenicht, G. (2002). *Kleben: Grundlagen, Technologien, Anwendung (VDI-Buch)*. Springer.
12. DVS e.V. (04/2021). Gestaltungsempfehlungen zum Kleben additiv gefertigter Bauteile: Merkblatt DVS 1401.
13. Watschke, H., Türck, E., Vietor, T., Fischer, V., Stammen, E., & Dilger, K. (2020). Additiv gefertigte Bauteile erfolgreich kleben: Teil 2 - Konstruktive Maßnahmen zur Steigerung der Klebfestigkeit. *Schweissen & Schneiden, 72*(1–2), 30–35.
14. German Institute for Standardisation. (06/2006). *Adhesives - Determination of tensile lap-shear strength of bonded assemblies*. (EN 1465:2009-06).
15. Frascio, M., Mandolfino, C., Moroni, F., Jilich, M., Lagazzo, A., Pizzorni, M., Avalle, M., et al. (2021). Appraisal of surface preparation in adhesive bonding of additive manufactured substrates. *International Journal of Adhesion and Adhesives, 106*, 102802. https://doi.org/10.1016/j.ijadhadh.2020.102802
16. Fischer, V., Stammen, E., Dilger, K., Watschke, H., Türck, E., & Vietor, T. (2019). Additiv gefertigte Bauteile erfolgreich kleben: Teil 1 - Verfahrensbedingte Einflüsse auf die Klebbarkeit. *Schweissen & Schneiden, 71*(12), 814–820.
17. Hahn, O., & Wender, B. (1984). *Beanspruchungsanalyse von geometrisch und werkstoffmechanisch „unsymmetrischen" Metallklebverbindungen mit der Finite-Element-Methode*. VS Verlag für Sozialwissenschaften.
18. Šrajbr, C. (2014). *Forschungsberichte des Instituts für Füge- und Schweißtechnik (No. 34): Zerstörungsfreie Prüfung von Fügeverbindungen mit Induktions-Puls-Phasen-Thermografie*. Shaker Verlag.
19. Ehrhart, B., Ecault, R., Touchard, F., Boustie, M., Berthe, L., Bockenheimer, C., & Valeske, B. (2014). Development of a laser shock adhesion test for the assessment of weak adhesive bonded CFRP structures. *International Journal of Adhesion and Adhesives, 52*(6), 57–65. Elsevier BV. https://doi.org/10.1016/j.ijadhadh.2014.04.002
20. Flügge, W., Glück, N., Fröck, L., & Wald, C. Inspektionsmethoden für die wiederkehrende Prüfung hochelastischer Dickschicht- und Strukturklebungen in Schiffbauanwendungen. In: *FSM-Bericht 02/2021*.
21. Kryukov, I., Kahlmeyer, M., & Böhm, S. (2018). Gegenüberstellung der induktiv angeregten Shearografie und Thermographie als zerstörungsfreie Prüfverfahren zur Detektion klebrelevanter Fehler an hochfesten Strukturklebungen und elastischen Dickschichtklebungen. *Materials Testing, 60*(5), 526–532. https://doi.org/10.3139/120.111171
22. Aßmuth, V., Teutenberg, D., Meschut, G., Philipp, J., Stammen, E., & Dilger, K. (2020). Lokales Konzept zur Auslegung von elastischen Klebverbindungen (LoKAl). In: *DECHEMA*

Gesellschaft Für Chemische Technik Und Biotechnologie E.V. (Ed.), 20. Kolloquium Gemeinsame Forschung in Der Klebtechnik (pp. 85–87). Würzburg.

23. Tropea, C., Yarin, A. L., & Foss, J. F. (2007). *Handbook of experimental fluid mechanics*. Springer.
24. Großmann, A., & Mittelstedt, C. (2018). Lightweight construction with two-dimensional cellular solids in additive manufacturing. *PAMM, 18*(1). https://doi.org/10.1002/pamm.201800007
25. German Institute for Standardisation. (06/2020). *Aluminium and aluminium alloys - Castings - Chemical composition and mechanical properties*. (EN 1706:2020–06).
26. CG TEC Carbon und Glasfasertechnik GmbH. (2021). Technisches Datenblatt: CFK-Rohr Prepreg.
27. German Institute for Standardisation. (11/2003). *Structural Adhesives - Guidelines for surface preparation of metals and plastics prior to adhesive bonding*. (EN 13887:2003–11).
28. Johlitz, M. G. (2008). *Experimentelle Untersuchung und Modellierung von Maßstabseffekten in Klebungen*. Dissertation. Universität Des Saarlandes. https://doi.org/10.22028/D291-22500
29. International Organization for Standardization. (02/2012). *Plastics - Determination of tensile properties - Part 2: Test conditions for moulding and extrusion plastics*. (ISO 527-2:2012-02).
30. German Institute for Standardisation. (07/2011). *Structural adhesives - Determination of shear behaviour of structural bonds - Part 2: Thick adherends shear test*. (EN 14869-2:2011-07).
31. Shokrieh, M., Lessard, L., & Golubovic, A. (2007). Adhesively bonded carbon/titanium joints under in-plane and bending loads. *Iranian Polymer Journal (English Edition), 16*.

Restructuring of Product Architecture Towards Additive Manufacturing Through Functional Analysis for High Temperature Applications

Sebastian Werner, Veronica R. Molina, and Dietmar Göhlich

Abstract

Evaluation tables, which are often used for identification of potentially profitable additively manufactured (AM) parts, are widely based on AM-expert knowledge. In many applications these approaches suffer from deficient data quality in ERP and PLM systems. Furthermore, they exploit potential AM benefits such as function integration and resource efficiency through part consolidation only to a small extent. This paper proposes the use of product architecture (PA) as a baseline for functionality analysis in products. The introduced scenario based method uses a heuristic approach to restructure the conventional manufacturing-PA towards an AM-supporting PA by analysing the functional structure of the product. The current approach aims to prompt the integration of AM in product development by both expert and non-expert users. The feasibility of the proposed transformation methodology is demonstrated on a complex part assembly for high temperature applications.

Keywords

Product architecture for AM • Functional integration • High temperature applications • LPBF

S. Werner (✉) · V. R. Molina · D. Göhlich
Technische Universität Berlin, Straße des 17. Juni 135, 10623 Berlin, Germany
e-mail: sekretariat@mpm.tu-berlin.de

R. Lachmayer et al. (eds.), *Innovative Product Development by Additive Manufacturing 2021*, https://doi.org/10.1007/978-3-031-05918-6_6

1 Introduction

Laser beam powder bed fusion (LPBF) has been established as the leading AM technology for metal applications [2]. Technology developments and multi-laser systems have significantly increased part quality, machine reliability and process repeatability for LPBF processes. Improving production speed and reliability makes the integration of LPBF into industrial production lines feasible [32]. Thus, further efforts currently investigate the development and implementation of methods for the identification of AM-suitable part candidates in product portfolios [4, 7]. The main focus has been on the identification of part characteristics or indicators for added value through AM [16–18]. Such methods generally rely mostly on AM-expert knowledge and empiric decision making through iterative processes [11, 15]. Methods based on product architectures aim to address established AM-value adding indicators away from pure AM suitability and thus be applicable for non-experts. Rather than focusing solely on physical component characteristics, they also incorporate functional properties of the product and thus aims to further standardize identification methods for AM parts. In this paper, we propose a scenario based method to restructure PA for AM by analysing the functional structure to realise AM benefits like functional integration and part consolidation.

The benefits of LPBF offer significant potential for performance improvement in cooling and aerodynamic functions in high-temperature applications (HTA) products. In terms of functional requirements, due to demanding performance requirements for functional components and materials, HTA are one of the most economically relevant industrial applications for metal LPBF [20]. Thus, a selected assembly from a high-temperature application will be presented in this paper in its original product architecture (PA). Applying the proposed method, the PA is converted into an AM-supporting product architecture and thereby emphasizing the AM benefit of function integration.

The industrial applicability of LPBF has been proven throughout the metal industry, especially for turbomachinery and inherently, high-temperature applications. Additively manufactured gas turbine blades have passed full-load engine tests with improved internal cooling geometry, proving the advantageous potential of AM towards HTA performance [31]. Besides the potential of AM towards performance enhancement through novel design, functional improvement and functional integration have been proven in industrial applications. Euro-K GmbH produces multi-fuel burners for micro-gas turbines, which are able to simultaneously use gaseous and liquid fuels equally effectively [8]. General Electric's (GE) LEAP jet engine carries a novel fuel nozzle designed for AM, in which a twenty-component assembly was merged into a single one [34]. GE Additive forecasts that legacy parts produced using additive manufacturing can reduce the cost of production by 35% when replacing cast CoCr bleed air parts on a GE land/sea turbine. They showed that the process from identification to prototype required only ten months, a significant reduction in lead time compared to average 12–18 months lead time for an identical cast part [10].

Thus, although the industrial suitability of LPBF has been proven even for demanding fields such as HTA, well thought-out identification strategies are necessary for a widespread implementation of AM in industrial metal production.

2 State of the Art

2.1 Technical Assessment and AM Value-Added

The two aspects of part identification for LPBF-suitable parts emphasize either the potential for applications or the restrictions of the process. These are defined as opportunistic and restrictive criteria respectively, and range from material availability and original part complexity to end-of-life product benefits [1, 4, 16, 24].

Opportunistic part identification approaches essentially rely on AM value-added considerations of the user. As stated by industrial examples, for an AM-including product to be economically viable, the often higher costs of the AM process must be counterbalanced by added value over the product life cycle and shall be considered [14, 15]. The base of AM-potentials from an opportunistic perspective are *part complexity, level of customization* and *production volume* [5]. A higher detail level can be reached by scanning for AM candidates by *integrated design, individualization, lightweight design* and *efficiency*. Therefore, applying each of the mentioned criterion on all possible components and/or products should yield the AM candidates out of a given product portfolio [16].

The suitability of a component or product for AM is not fully depicted through opportunistic criteria, since (AM) manufacturability is not addressed, thus creating the need for restrictive criteria. The two fundamental restrictive criteria for additively manufacturable parts are *dimensions* not larger than build chamber volume and *powder material availability* [25]. A part filtering method uses known Design for Additive Manufacturing (DfAM) guidelines as excluding criteria to classify parts into non-AM-manufacturable, manufacturable with minor redesign, and as-is manufacturable. The filter method uses high-, medium and low impact criteria. Some examples are *hardware, material, load environment and cost* (high impact), *complexity, lead time and post processing* (medium impact), and *fatigue, surface finish, weight savings and customization potential* (low impact) [30]. Ongoing research is addressing part separation to fit components into build chamber [6, 12, 23].

Technical assessment approaches include questionnaire-based evaluation of single components [19, 21] and a two-step automated process through modularization of component groups [36]. The Trade-Off Matrix (TOM) follows the same questionnaire-based technical assessment method preceded by a K.O. criteria screening in order to rule out generally non-manufacturable parts (eg. part dimensions and material availability). Subsequently, an extensive series of questions to prove AM feasibility follows, subdivided into four categories: *change of manufacturing technology* (redesign potential for

AM-suitability), *lightweight potential* (redesign potential for weight reduction), *functional integration* (redesign potential for functionality improvement), *overall product optimization for additive manufacturing* (extensive redesign for AM) [18].

In addition to ongoing research, commercial solutions for part identification have already been introduced to the market in recent years. 3YourMind GmbH together with EOS GmbH released the Inventory Analysis software solution, based on pre-set and customisable evaluation criteria for an inventory scan and identification algorithm for printable parts. Additive Innovation GmbH advertises a software solution with user-definable test profiles for 3D-model database search towards identification of printable parts and data conversion for AM. Castor Technologies Ltd. offers the suggestion of part consolidation from assemblies based on material matching, joint types, and gap tolerances.

Current research and commercial software illustrate that, at the current state of the art, AM suitability screening of product portfolios is driven by physical or economic properties of the components in a product, and functional enhancement is applied to individual parts if applicable. The current paper aims toward function-driven, automatable identification methods, which have the potential to exploit the opportunities of product (redevelopment).

2.2 Product Architecture and Functional Integration

Thumm and Göhlich demonstrated the applicability and advantages of product architectures for the industrial product development context [33]. Current part identification methods as described in Sect. 2.1 evaluate products, or better yet, PA for AM at component level. Exemplary, Nie et al. propose a part consolidation based on a so-called Connectivity Matrix to reduce the number of interfaces in assemblies and thus reaching part consolidation [22]. The method introduced by Kim et al. focuses on eliminating joining operating which are difficult to disassemble at end of life. Their aim is to improve serviceability and maintenance using AM [13]. Furthermore, linking components and their connection types in an extended product architecture, based in conventionally fabricated products, can explore the potential of part consolidation for AM as proposed by Reichwein et al. Taken to a further step, volume manufacturability limits and guideline restrictions shall be accounted for. The use of Design Pattern Matrix (DPM) enables the creation of advantageous AM-based product design solutions [26, 27]. An opposite approach postulated by Ziebart considers a fully integrated machine and proposed to split it step by step considering functional requirements, serviceability, material selection, among other criteria [37].

Consideration of functional interdependencies in part consolidation enables integral design and thus, exploitation of the benefits of AM. Richter et al. describe the development of product architectures by analysing function principles and carriers to integrate functionality into parts [29]. Wagner extended this approach using the Design Pattern

Matrix (DPM). The DPM aims to associate design elements driven by manufacturing processes, such as AM in this case, with function carriers [35]. A holistic approach and framework to develop new product architectures considering development scenarios and manufacturing processes was presented by Richter [28]. Fröhlich et al. developed "function in a box" approach for multifunctional separation and embedding of and thus creation of product architectures [9].

Research addressing the design of product architectures for additive manufacturing are not AM specific [35], lack a generalised, reproduceable approach [29] or focus the conceptualisation rather than redesign of product architectures [28]. Reichwein et al. introduce an additional model to transform the product architecture towards AM and analysis focus on connections between parts emphasizing separation rather than functional integration [27].

3 PA-Assisted Method

The part identification methods as in Sect. 2.1 require product and AM expert input to outline product characteristics and set them into the evaluation framework. The use of employee workshops, fillable questionnaires, matrixes or other manually editable tools are widespread solutions. Commercial solutions are currently restricted to physical part characteristics as well. This results in the identification process shown in left side of Fig. 1. First, considering widespread AM-drivers and specific company strategy, the com-

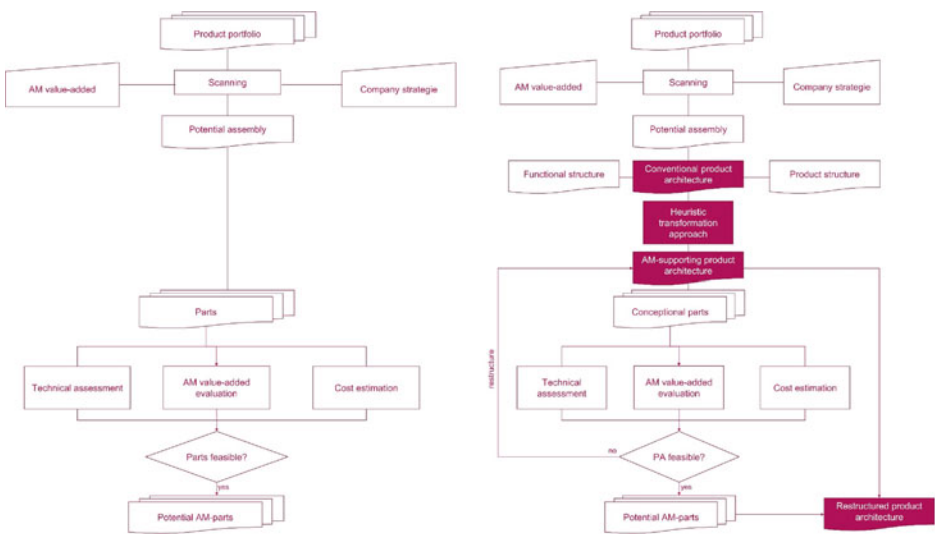

Fig. 1 Conventional (left) and PA-assisted (right) process for incorporating AM into a product

pany's product portfolio is scanned to identify potential assemblies. Possible filter metrics can include both opportunistic and restrictive criteria such as lead time, cost per weight, component build volume or component complexity. This step yields a set of potential assemblies to be analysed. The respective parts are evaluated by technical assessment, AM value-added and cost, resulting in a set of potential parts for AM.

Figure 1 (right) highlights the extension of the current part identification process and indicates the scope of the current paper. After identification of assemblies of interest, the respective PA for each assembly is generated based on information from PLM and ERP systems. This paper introduces a transformation method from conventional PA to AM-supporting PA. This AM-PA comprises conceptual parts which are evaluated for manufacturability and/or cost–benefit using DfAM Methods [3, 4] yielding the feasibility of the new PA. Eventually, the indicated restructuring loop and overall part identification process results in a restructured PA emphasizing integral design to incorporate the benefits of additive manufacturing, while assuring manufacturability. Finally, potential AM-parts are identified. Assembly compatibility is addressed by the designer on a qualitative level and has to be ensured quantitatively during embodiment design checking functional requirements and interfaces.

3.1 Heuristic Transformation Approach

We propose a three-stage transformation method which comprises scenario definition, transformation indication and evaluation. The transformation methods begins by defining the scenario, such as product re-development, service part scenario or, say, legacy part replacement. The definition of a specific scenario determines the prioritization of the criteria for eg. component exclusion or function fulfilment verification. In service scenarios, for example, interfaces to associated modules are fix and interchangeability and serviceability is prioritized. Therefore, the exchangeability of wear components has to be ensured.

The product architecture depends on the chosen AM-process significantly and the realisation of AM-value propositions depends on development aims and strategy. Therefore, definition of considered materials and manufacturing processes is essential in the scenario stage.

The product architecture shall be analysed at the lowest function/component interface level. The current method assumes a subfunction-component direct link in the CPA. In distinction to Reichwein et al. [27] the method proposes component selection as AM candidates by analysing product part functions instead of an across the board component consolidation and separation based on physical properties of components. After defining the identification scenario, the following iterative scheme is proposed to indicate transformation potential for CPA to AMPA in terms of functional integration and part consolidation:

1. *Which function is addressed by multiple parts?*
   For each part:
   if part adresses only this function: part consolidation else:
   1.1 *Check if Additional functions would be obsolete through part consolidation.*
   1.2 *Check if Additional functions could be integrated.*
   1.3 *Check if parts could be split.*
2. *Check if parts representing inner structure could get integrated in outer part with AM.*
3. *Check if design of parts in module is driven by conventional design -> consolidation.*
4. *Go back to Step 1 if necessary.*

   Note: In each step check if parts and/or functions within a module or at module interfaces are obsolete due to part consolidation and update PA accordingly.

As part of the downstream technical assessment, the following questions are proposed in order to underline manufacturability, profitability and assembly compatibility. This nonordered questionnaire can be expanded and detailed according to the specific scenario, machine characteristics and material requirements.

Evaluation questions:

- *Are any of the chosen parts standard parts or components with a semi-finished product characteristic, such as formed metal sheets,* etc.*?*
- *Check resulting conceptual component dimensions for printable volume*
- *Are all respective components for consolidation connected? (use of DSM or CAD-Model)*
- Is the service/module/etc. strategy being respected?

After Evaluation of the transformation indications, the AM-PA is derived from conventional PA. Subsequently, parts shall undergo a manufacturing process specific technical assessment, evaluation of realisation of AM-added value and cost estimation (see Sect. 2.1). As a result, restructuring and separating components using methods described in Sect. 2.2 could improve manufacturability with AM and reduce cost.

4 Application and Results

4.1 Conventional Product Architecture—2-Stage Main Nozzle

The method is applied to a fuel supply assembly for a 2-Stage turbo-annular combustion chamber used in gas turbines as shown in [4]. The conventional manufacturing driven product architecture comprises 25 different components divided into 5 Modules, whereas the “Distribution” module is found in the assembly 8 times distributed radially to the assembly’s middle axis. The overall assembly function is to mix fuels A and B with air from the compressor and transport the air–fuel mix to the combustion chamber. Module “Supply A” connects fuel A supply with “Manifold C”. “Manifold A” and “Manifold B” supply fuel B to “Manifold C” as well. Inside the module “Manifold C”, fuels A and B are homogeneously distributed to 8 different outlet positions directed to the “Distribution” modules. The fuel–air mixing functionality is carried out by the “Distribution” module. At the lowest functional level, specific functions such as thermal protection, mechanical sealing, fixation and positioning, liquid fuel atomization are listed in the conventional PA in Fig. 2. The presented product architecture is formulated in a non-proprietary language for the product. This level of abstraction supports the application of the transformation approach from Sect. 3 by reducing implications and assumptions induced by designer specific naming conventions. Functionalities and components at the lowest PA level—subfunction versus component—are linked and used as the base of analysis for the proposed method.

4.2 Heuristic Transformation Approach and AM-Supporting Product Architecture

The proposed method described in Sect. 3.1 is now applied to the conventional product architecture. For the first step in the transformation method, scope and scenario are defined. The scope of this study comprises restructuring of product architecture for small series production supporting product modification for rapid manufacturing with LPBF. In [6] Diegel et al. distinct three different approaches for redesigning AM-part: direct part replacement, adapt for AM and design for AM. the focus of this study is adaption for AM. Due to the legacy status of the assembly, serviceability and therefore exchangeability and interoperability are prioritized. Furthermore, modularity can only be changed inside defined service strategies and wear parts like filters should be exchangeable. Second is the aim of functional integration and part consolidation.

Figure 3 shows the results of the application of the transformation indication scheme on the conventional PA through colour and line-schemes. Both at subfunction and component level, resulting indicators/candidates for part consolidation (question 1 in method) are highlighted in solid coloured blocks. Given successful part consolidation, possibly obsolete functions and parts are indicated by a solid coloured line with a white background (question 1.1. in method). Functions which could be integrated into other components and component candidates for part separation are outlined with a discontinuous (questions 1.2 and 1.3 in Sect. 3).

The application of the transformation indication scheme through indicator tracing is summarized in the following list:

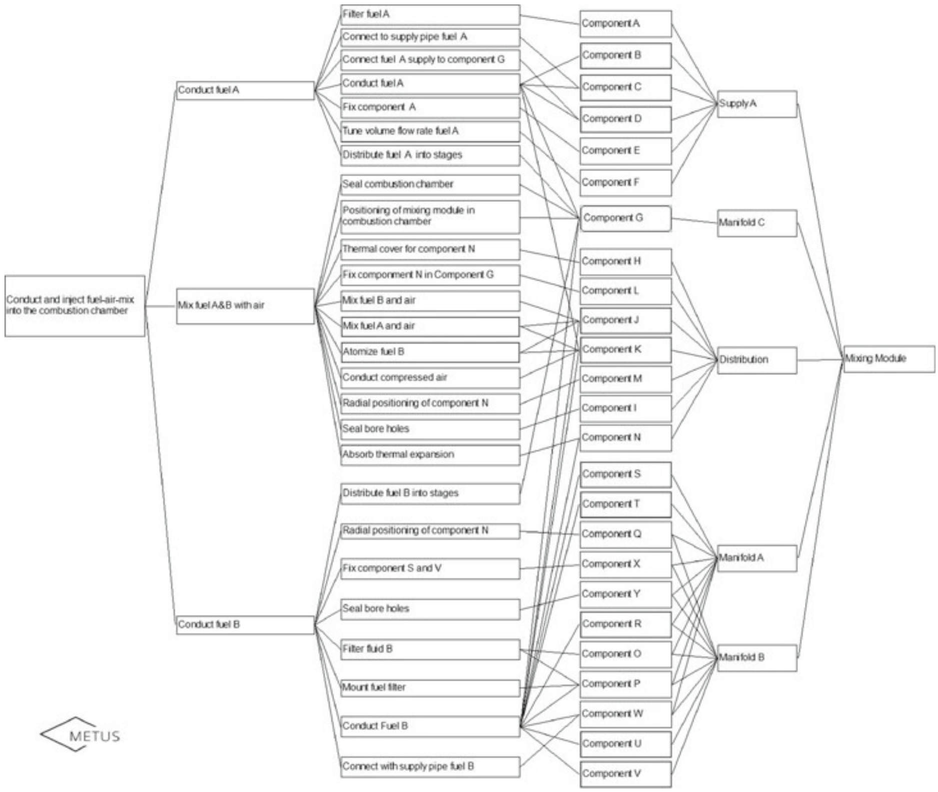

Fig. 2 Conventional product architecture[1]

- Function "Conduct Fuel B" is addressed by multiple parts.
  - Therefore, Components N, S, R, U and V are marked for consolidation into G
  - G could be split in a mechanical and a fluid functions related part.
  - Consequently, Components L, M, Q, X, Y, O, P and W are potentially obsolete as their function are unnecessary or could get integrated using AM.
  - Component I could be obsolete due to additive manufacturing of component G.
- Components J and K address same functions in the "Distribution" module and could be consolidated.
- Components B, C and D mainly address "Conduct fuel A" and are candidates for consolidation.
  - Components A, E and F are potentially obviate due to functional integration.

After indication of AM-Potential, evaluation based on the scenario described in 3.1 is performed. The result of the filtering process is shown in Fig. 4. Due to the priority of

[1] METUS Software by ID-Consult was used to define the product architectures.

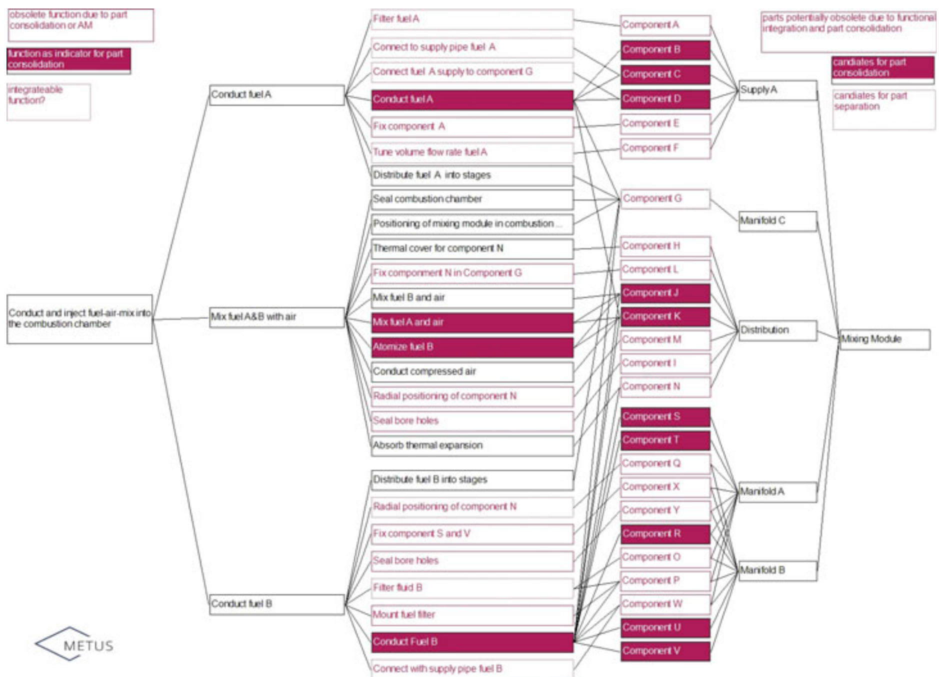

Fig. 3 Conventional product architecture with AM-transformation indication

serviceability, filtering and tuning subfunctions are not integrated, which has an effect on transformability of components A, E, F, O, P, W. Moreover, component B presents a semi-finished product characteristic and a modularization strategy is in place for “Supply A”, which rules out their integration into component G. The technical assessment excludes the consolidation of components J, K and I due to manufacturing restrictions of LPBF.

These considerations result in the AM-Supporting PA shown in Fig. 5. The AM-supporting PA can be used as baseline for conceptual design of the components and technical assessment, evaluation of AM-value propositions as well as cost estimation. Figure 6 shows a draft of the assembly derived from the conventional embodiment design and AM-supporting PA. Component G is split into two functional parts: a mechanical (G-AMI) and a fluid-related component (G-AMII) to achieve a “design to cost” approach. Former functionality of Manifolds A and B was integrated into G-AMII, with exception of those functions related to fuel filtering and connecting to supply pipe to comply with the service strategy. Component N is divided into an integrable section with functionality integrated into G-AMII and a stand-alone N-AM section.

The recommended AM-supporting PA comprises 15 different components compared to 25 in the conventional PA and 3 submodules compared to 5, respectively. Under consideration of assembly costs, the effect of the transformation appears to be even more

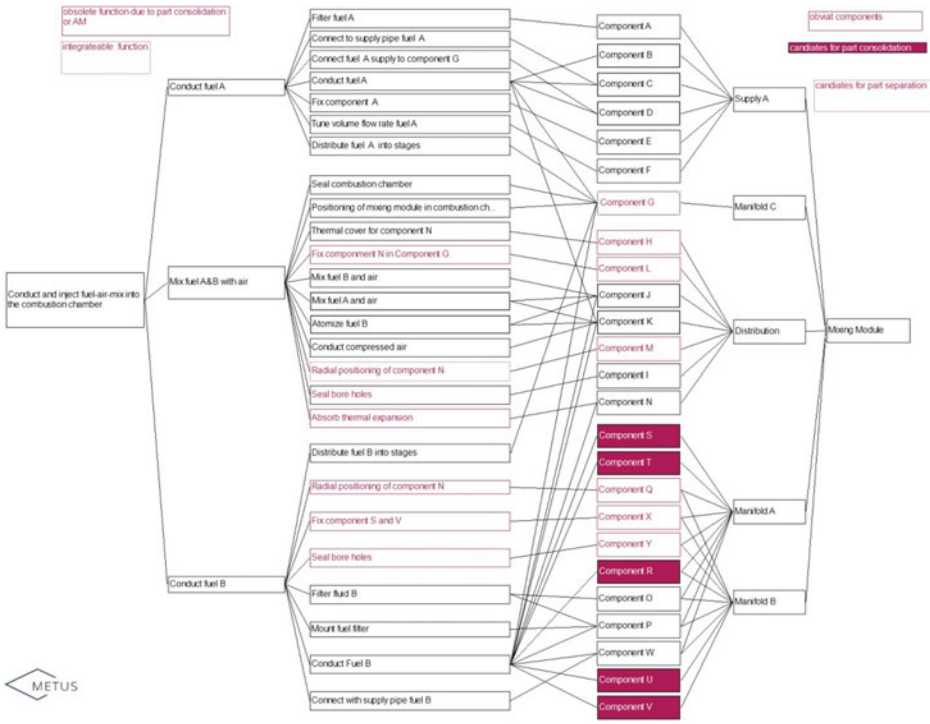

Fig. 4 Conventional PA after evaluation and filtering

beneficial by part consolidation in the "distribution" module due to the potential saving of previously 12 soldering connections as well as clamping operations necessary in a conventional PA.

In a last step, the components' physical correlations are analysed by means of DSM. Figure 7 compares the DSM for conventional and AM-supporting PA. The effect of part consolidation and therefore reduction of part interactions is clearly evident. Three main components (B, G-AMII and K) can be identified and interactions between to modules are reduced to three.

Following steps would require the conceptional design of component G-AMII for functional and manufacturing assessment as well as cost estimation as described in Sect. 3. The realisation of AM-value propositions in accordance with the strategic aims demands the evaluation of postprocessing and joining efforts to compare the AM with the conventional design as well.

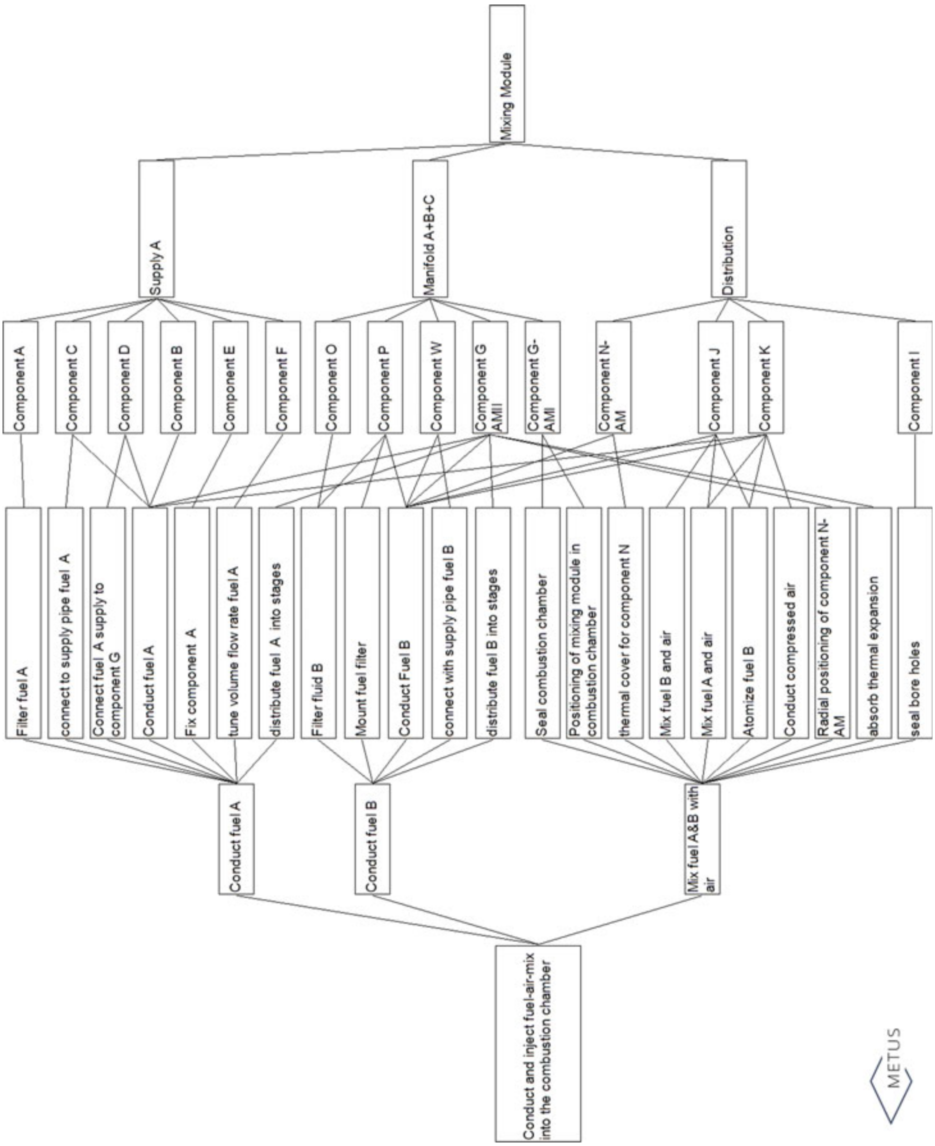

Fig. 5 AM-supporting PA after transformation from conventional PA

5 Conclusion and Outlook

Widely used methods for identifying potentially profitable additive manufactured parts, such as valuation tables suffer from poor data quality in ERP and PLM systems. Hence,

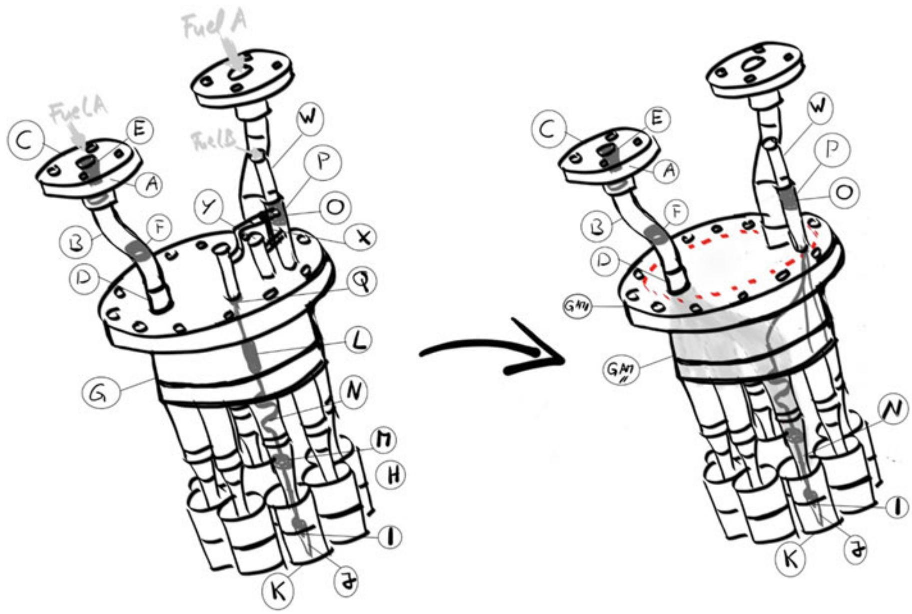

Fig. 6 Conceptual design of the AM-supporting PA

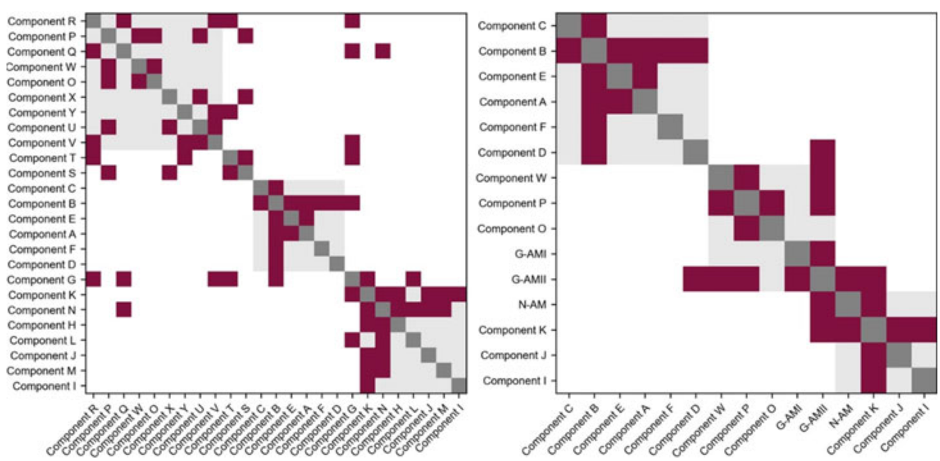

Fig. 7 DSM for conventional PA (left) and for AM-supporting PA (right)

they are largely based on AM expert and product expert knowledge. Utilizing product architectures as a tool in the identification process opens the door for a function-based AM potential identification approach in product portfolios and thus applicable by non-experts.

Additionally, potential AM benefits such as functional integration and resource efficiency through part consolidation are currently exploited on only a marginal scale. In this study, a method was developed to transform a product architecture based on conventionally manufacturing processes into an AM-supporting product architecture. To this end, a three-step iterative method was proposed. The heuristic transformation process in turn entails firstly the determination of a scenario and boundary conditions. Subsequently, a checklist is applied to the conventional PA for AM-indicator analysis, while making use of AM-potentials such as functional design concepts. Finally, the resulting candidates from indicator analysis are evaluated for applicability according to the scenario and boundary conditions. The entire process is aimed at generating redesigned components with significant functional integration to utilize the potential offered by AM.

The application of the method is demonstrated for a 2-Stage Main Nozzle used in gas turbines in an "adapt for AM" scenario. The complexity of the assembly is significantly reduced from five submodules to three and from25 different components to 15 respectively.

Future work will comprise technical assessment, cost estimation, design and manufacturing of the components to verify the effectiveness of the method regarding part identification for AM. Additionally, a formalized process to ensure manufacturability and assembly compatibility must be incorporated into the method. Furthermore, we will investigate the application of the transformation approach on product architectures from different fields to improve generalisation of the method. In our study we considered a service scenario with adaption for AM. Therefore, interactions with associated modules were fixed and not scope of the study. The presented method addresses manufacturing with LPBF. Consequently, investigations on how the chosen additive manufacturing method and scenario influence the restructuring of the product assembly will be conducted.

An additional field of research is the applicability of the developed methods in integrated and automated software solutions, especially focusing on standardized functional descriptions. The automation of the transformation process as well as the incorporation of further conventional and additive manufacturing processes is also in the research outlook. The aim is to integrate the method in existing part identification methods to enable a holistic scanning and design to cost approach on product portfolios.

Acknowledgements Our project "WvSC – HTA 2.0: HochTemperaturAnwendungen 2.0" is funded by the European Regional Development Fund. This work was carried out within the framework of the Werner-von- Siemens Centre for Industry and Science (https://wvsc.berlin/). We thank ID-Consult GmbH for providing us with the METUS software, which was a key software tool for our research. Simon Purschke and Johannes Albert (Siemens Energy AG) provided valuable feedback on the method and application.

Authors Contribution VM and SW developed the methodology, defined the product architectures, wrote the initial draft and finalised the script, DG supervised the research, commented and revised the script. All authors have read and agreed to the published version of the manuscript.

Conflicts of Interest The authors declare no conflict of interest.

References

1. Ahtiluoto, M., Ellman, A. U., & Coatanea, E. (2019). Model for evaluating additive manufacturing feasibility in end-use production. *Proceedings of the Design Society: International Conference on Engineering Design, 1*(1), 799–808.
2. AM Power. (2020). *AM Report 2020*. additive-manufacturing-report.com.
3. Bracken, J., Pomorski, T., Armstrong, C., Prabhu, R., Simpson, T. W., Jablokow, K., Cleary, W., & Meisel, N. A. (2020). Design for metal powder bed fusion: The geometry for additive part selection (GAPS) worksheet. *Additive Manufacturing, 35*.
4. Bracken, J. E., McComb, C., Simpson, T. W., & Jablokow, K. W. (2020). A review of part filtering methods for additive manufacturing. In *Volume 11A: 46th Design Automation Conference (DAC)*. American Society of Mechanical Engineers. https://doi.org/10.1115/DETC2020-22448
5. Conner, B. P., Manogharan, G. P., Martof, A. N., Rodomsky, L. M., Rodomsky, C. M., Jordan, D. C., & Limperos, J. W. (2014). Making sense of 3-D printing: Creating a map of additive manufacturing products and services. *Additive Manufacturing, 1–4*, 64–76.
6. Deka, A., & Behdad, S. (2019). Part separation technique for assembly-based design in additive manufacturing using genetic algorithm. *Procedia Manufacturing, 34*, 764–771.
7. Eddy, D. C., Krishnamurty, S., Grosse, I. R., & Steudel, M. (2020). Early design stage selection of best manufacturing process. *Journal of Engineering Design, 31*(1), 1–36.
8. EOS GmbH Electro Optical Systems. *Small burners, big variety. Success story industry*. https://www.eos.info/01_parts-and-applications/case_studies_applications_parts/_case_studies_pdf/en_cases/cs_m_industry_eurok_en.pdf.
9. Fröhlich, T., Klaiber, D., Türck, E., & Vietor, T. (2019). Function in a box: An approach for multi-functional design by function integration and separation. *Procedia CIRP, 84*, 611–617.
10. GE Additive. (2021). *GE Aviation and GE Additive engineers have switched four existing parts from castings to metal 3D printing—and see potential for hundreds more*. https://www.ge.com/additive/blog/ge-aviation-and-ge-additive-engineers-have-switched-four-existing-parts-castings-metal-3d
11. Ghiasian, S. E., Jaiswal, P., Rai, R., & Lewis, K. (2018). From conventional to additive manufacturing: determining component fabrication feasibility. In *Volume 2A: 44th Design Automation Conference*. American Society of Mechanical Engineers. https://doi.org/10.1115/DETC2018-86238
12. Keshari, A., Simeone, A., & Tiwari, M. K. (2021). Assembly design of additive manufacturing products: A computational framework for part separation. *Procedia CIRP, 96*, 121–126.

13. Kim, S., & Moon, S. K. (2020). A part consolidation design method for additive manufacturing based on product disassembly complexity. *Applied Sciences, 10*(3), 1100.
14. Klahn, C., & Fontana, F. (2017). Reminiscent of Marcel Duchamp in design reuse. In F. M. Da Silva, H. Bártolo, P. Bártolo, R. Almendra, F. Roseta, H. A. Almeida, & A. C. Lemos (Eds.), *Challenges for Technology Innovation: An Agenda for the Future* (pp. 277–280). CRC Press. https://doi.org/10.1201/9781315198101-48
15. Klahn, C., Fontana, F., Leutenecker-Twelsiek, B., & Meboldt, M. (2020). Mapping value clusters of additive manufacturing on design strategies to support part identification and selection. *RPJ* ahead-of- print, ahead-of-print, 100902.
16. Klahn, C., Leutenecker, B., & Meboldt, M. (2014). Design for additive manufacturing – supporting the substitution of components in series products. *Procedia CIRP, 21*, 138–143.
17. Knofius, N., van der Heijden, M. C., & Zijm, W. (2016). Selecting parts for additive manufacturing in service logistics. *Journal of Manufacturing Technology Management, 27*(7), 915–931.
18. Kruse, A., Reiher, T., & Koch, R. (2017). Integrating AM into existing companies - selection of existing parts for increase of acceptance.
19. Lachmayer, R., & Lippert, R. B. (2020). *Entwicklungsmethodik für die additive Fertigung*. Springer.
20. Lechner, C., & Seume, J. (Eds.). (2019). *Stationäre Gasturbinen*. VDI-Buch. Springer Vieweg.
21. Leutenecker, B., Klahn, C., & Meboldt, M. (2015). Indicators and design strategies for direct part production by additive manufacturing. *Conference proceedings International Conference on Engineering Design, 2015*, 1–10.
22. Nie, Z., Jung, S., Kara, L. B., & Whitefoot, K. S. (2020). Optimization of part consolidation for minimum production costs and time using additive manufacturing. *Journal of Mechanical Design, 142*(7), 831.
23. Oh, Y., Zhou, C., & Behdad, S. (2018). Part decomposition and 2D batch placement in single-machine additive manufacturing systems. *Journal of Manufacturing Systems, 48*, 131–139.
24. Page, T. D., Yang, S., & Zhao, Y. F. (2019). Automated candidate detection for additive manufacturing: A framework proposal. *Proceedings of the Design Society: International Conference on Engineering Design, 1*(1), 679–688.
25. Parks, T., Kaplan, B., Pokorny, L. R., & Williams, C. (2016). *Additive manufacturing: Which DLA- managed legacy parts are potential AM candidates? REPORT DL501T1* DL501T1. LMI.
26. Reichwein, J., Kaspar, J., Vielhaber, M., & Kirchner, E. (2019). Exploitation of AM-potentials by linking manufacturing processes to function-driven product design. *Proceedings of the Design Society: International Conference on Engineering Design, 1*(1), 739–748.
27. Reichwein, J., Rudolph, K., Geis, J., & Kirchner, E. (2021). Adapting product architecture to additive manufacturing through consolidation and separation. *Procedia CIRP, 100*, 79–84.
28. Richter, T. (2020). *A methodical framework supporting product architecture design in conceptualization*. Dr. Hut.
29. Richter, T., Watschke, H., Inkermann, D., & Vietor, T. (2016). *Produktarchitekturgestaltung unter Berücksichtigung additiver Fertigungsverfahren*. Saechsische Landesbibliothek- Staats- und Universitaetsbibliothek Dresden; Technische Universität Dresden.
30. Shepherd, J. J., & Meisel, N. A. (2019). Large-scale identification of parts suitable for additive manufacturing: An industry perspective. *Conference proceedings Solid Freeform Fabrication Symposium, 2019*, 33–44.
31. Siemens AG. (2017). *First 3D-printed gas turbine blades: Siemens awarded by American Society of mechanical engineers. Joint Press Release by Siemens and ASME.*

32. Stittgen, T., & Schleifenbaum, J. H. (2020). Towards operating curves of additive manufacturing equipment: Production logistics and its contribution to increased productivity and reduced throughput time. *Procedia CIRP, 93*, 14–19.
33. Thumm, B. R., & Göhlich, D. (2015). Product architecture design methodology for developing standardized modules. In: *International Conference on Engineering Design ICED15*.
34. Tomas Kellner. (2018). *The devil is in the details: How GE found a way to bring 3D printing to mass production.* https://www.ge.com/news/reports/devil-details-3d-printed-part-jet-engine-part-now
35. Wagner, C. (2018). *Funktionsintegration im Rahmen einer fertigungsgetriebenen Produktentwicklung*. Dissertation, Technische Universität Darmstadt.
36. Yang, S., Page, T., Zhang, Y., & Zhao, Y. F. (2020). Towards an automated decision support system for the identification of additive manufacturing part candidates. *Journal of Intelligent Manufacturing, 31*(8), 1917–1933.
37. Ziebart, J. R. (2012). *Ein konstruktionsmethodischer Ansatz zur Funktionsintegration.* Zugl.: Technische Universität Braunschweig, Diss., 2012, Verlag Dr. Hut.

Additive Manufacturing of Soft Robots

Felix Weigand and Arthur Seibel

Abstract

Soft robotics is an emerging field in science and technology that extends the area of classical robotics to new types of applications. Soft robots uniformly conform to their objects in contact without damaging them, but also without being damaged themselves by these objects. In the field of pneumatic soft robots, the classical production method is silicone injection molding. This method, however, is only economical for relatively large batch sizes. In this context, additive manufacturing (and especially silicone 3D printing) offers a promising alternative for small and medium batch sizes. In this paper, we describe the technology of silicone 3D printing, discuss the way to develop a comprehensive design compendium, and present the application of first design guidelines using an illustrative example.

Keywords

Soft robotics • Additive manufacturing • Silicone 3D printing • Design guidelines

F. Weigand (✉) · A. Seibel
Fraunhofer Research Institution for Additive Manufacturing Technologies IAPT, 21029 Hamburg, Germany
e-mail: felix.weigand@iapt.fraunhofer.de

A. Seibel
e-mail: arthur.seibel@iapt.fraunhofer.de

A. Seibel
Hamburg University of Technology TUHH, 21073 Hamburg, Germany

R. Lachmayer et al. (eds.), *Innovative Product Development by Additive Manufacturing 2021*, https://doi.org/10.1007/978-3-031-05918-6_7

1 Introduction

Soft robotics is a relatively young emerging field in robotics that deals with the design, fabrication, and control of soft structures [1–3]. Often inspired by skeletonless biological archetypes [4], soft robots have the ability of not damaging their environment [5], but also not being damaged by the environment themselves [6].

The application areas of soft robots typically involve interaction with a soft (living or nonliving) structure. Soft grippers, for example, can be used to grasp unknown or fragile objects [7]. And soft exosystems, for example, can be used to help rehabilitate humans [8]. Other application areas include soft surgical instruments [9], locomotion systems for unknown and unstructured environments [10, 11], and human–machine interfaces [12].

Pneumatically driven soft robots are usually manufactured using silicone injection molding [13]. However, this process requires investments in tooling and fixture construction, which are only profitable for medium and high batch sizes. However, if small quantities, individualized products, or prototypes are required, it is desirable for the soft robotic structure to be manufactured by additive manufacturing (also known as 3D printing) [14–16]. While other additive manufacturing technologies for silicones may become available in the future, extrusion technologies can currently be considered to be the forerunner. For this reason, we focus exclusively on extrusion-based silicone 3D printing in this paper.

The paper is organized as follows. After a brief introduction to (extrusion-based) silicone 3D printing in Sect. 2, a strategy for the development of design guidelines is presented in Sect. 3 in order to strengthen the acceptance of this technology in the industry. A case study in Sect. 4 demonstrates the application of first already developed guidelines and shows the potential of silicone 3D printing in soft robotics. Section 5 concludes this work and gives recommendations for future research.

2 Silicone 3D Printing

Several methods for additive manufacturing of soft robots have been reported in the literature so far, such as fused deposition modeling [17], selective laser sintering [18], stereolithography [19], as well as polyjet technology [20]. However, these methods use materials that do not have the desired elasticity and Shore hardness. For this reason, the authors suggest using (extrusion-based) silicone 3D printing for the production of the pneumatic structure of a soft robot, as it can process real silicones with low Shore hardnesses and high elongations at break.

2.1 Technology Description

Material extrusion processes utilize an extruder assembly and a nozzle to extrude a continuous strand of material onto a build platform. Although the silicone 3D printing process shares many similarities with the popular fused filament fabrication (FFF) process, the feedstock is not a filament but a liquid, which has a much higher viscosity when it is deposited compared to polymers that are typically used in FFF. This has significant implications for the process characteristics as well as the available freedom of design. Therefore, silicone 3D printing has to be viewed separately from the FFF process.

The number of available silicone 3D printing systems is still limited. So far, only three manufacturers offer systems that can be considered as ready for first industrial applications:

- LiQ320 3D printer (InnovatiQ, Germany) [21],
- S600D 3D printer (Lynxter, France) [22],
- Delta Tower Fluid (Deltatower, Switzerland) [23].

While all three systems use the same extruder system from ViscoTech (Germany) [24], the individual processes as well as the offered materials are slightly different. Attached to the extruder is a disposable static mixer (e.g., from Vieweg GmbH, Germany [25]) and a nozzle to deposit the material strand with the desired diameter. Both items are relatively low-cost and have to be regularly replaced. Nozzles are available with diameters ranging from 0.06 to 2 mm.

Like most other additive manufacturing processes, silicone 3D printing is a layer-based process where the same basic steps are repeated for each layer. The process consists of two main steps and some additional pre- and post- processing steps, which may vary between the three systems. Figure 1 illustrates the individual process steps using the LiQ320 system as an example. This system is used to develop the first design guidelines and the case study presented in this paper.

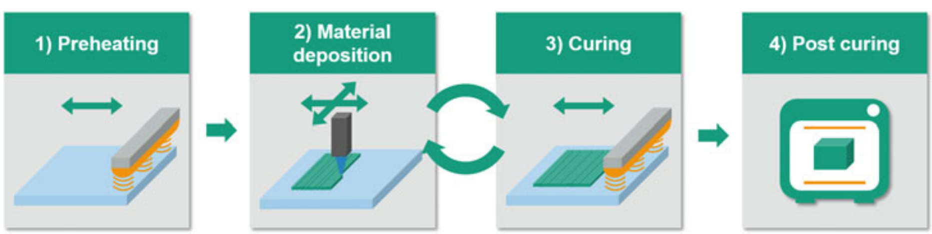

Fig. 1 Process steps of (extrusion-based) silicone 3D printing

(1) **Preheating**: At the beginning of the process, the ceramic build plate of the printer is preheated. This is done with a curing lamp, which can reach temperatures of up to 2000 °C. The lamp is directly attached to the extruder kinematics. The speed and travel distance of the lamp are usually defined by the settings for Step 3 and can thus be seen as a preliminary curing cycle. Since only InnovatiQ uses a heating lamp to accelerate the curing process, this step is not required for the other two systems.
(2) **Material deposition**: The kinematics of the printer are used to move the extruder along a predefined path. Along this path, a strand of material is extruded. The first layer is deposited directly onto the build platform, while each following layer is then deposited onto the previous one.
(3) **Curing**: After placing of each layer, the heating lamp moves across the build platform. The high temperature of the lamp accelerates the curing process of the silicone to a point where it hardens almost instantly.
(4) **Post curing**: To obtain the best component properties and ensure the silicone to be fully cured, it is advisable to include a final curing step inside an annealing oven as a final process step.

2.2 Processible Materials

In theory, it is possible to process any fluid or paste with extrusion-based 3D printing systems. There are, however, two limiting factors to be considered. The first one is the viscosity of the material after it is deposited onto the build platform, and the second one is the curing speed of the material. A material is only suitable for an extrusion- based 3D printing process if it is liquid enough to be pressed through the nozzle and at the same time solid enough not to lose its shape immediately after it is deposited. In addition, the material must be able to cure immediately so that the individual layers can be quickly placed on top of each other, without flattening due to their own weight.

Regarding silicones, it is possible to process one- or two-component silicones. Both exhibit a hyperelastic and viscoelastic behavior. Here, 'hyperelastic' means that the material is nonlinear and can experience high strains and 'viscoelastic' means that it exhibits a combination of elastic and viscous properties.

Figure 2a shows the stress-strain diagram of a typical silicone material. We can see the typical S shape, which is why it is not possible to assign a unique Young's modulus to such a material. Usually, the Young's modulus is given for a certain strain (such as E_{50} for 50% or E_{200} for 200% strain).

Silicone materials also experience the so-called Mullins effect [26]. During the first loading cycles, polymer chains brake at the micro level, which leads to a permanent change in the elastomeric network [27]. Figure 2b shows the loading–unloading behavior of a typical silicone material illustrating this phenomenon. We can observe that, during

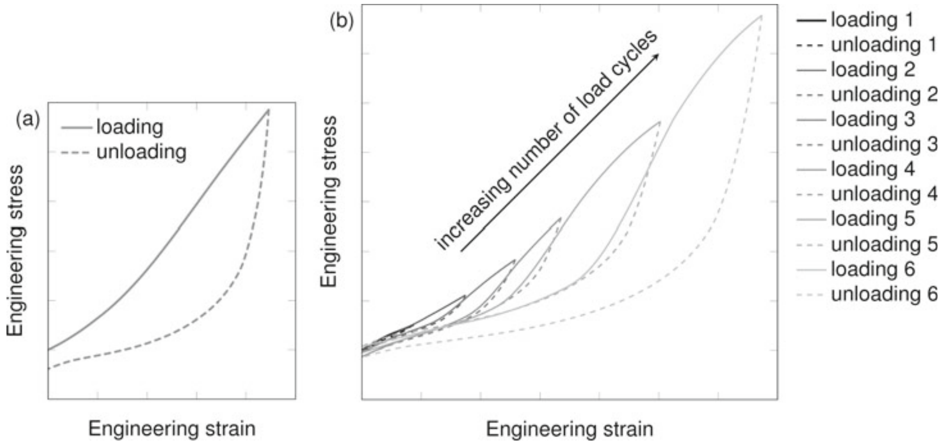

Fig. 2 Characteristic stress–strain behavior of silicone; **a** single deformation, **b** cyclic stepwise-increasing deformation

the first deformation cycles, the stiffness gradually decreases and the material response becomes more and more repeatable.

A major disadvantage of silicone materials, however, is their tendency to age, which leads to an increase in stiffness and thus embrittlement of the material. Environmental influences, such as temperature or various chemicals, can also accelerate aging [28].

3 Development of Design Guidelines

One of the most important arguments for using additive manufacturing (AM) is the great design freedom it has to offer. At the same time, this freedom is also the main reason why industrial applications have been rare so far. Just like any other manufacturing technology, AM technologies possess process-related restrictions that must be taken into account when designing a part. Considering these restrictions poses a particular challenge. Some design limits are common to all technologies, but others are unique for each single one.

To develop a comprehensive design compendium, there are many different design guidelines to be considered. To structure the development of design guidelines, they will be divided into two categories and two subcategories. The first category is *general design guidelines* that are relevant specifically for material extrusion technologies. They are independent from the manufacturing system or the material used. The second category is *specific design guidelines* that encompass all guidelines specifically relevant to the silicone 3D printing process.

Each category has the same two subcategories. The first one is *design for manufacturing*, which contains all guidelines describing the limitations of the manufacturing process.

In the case of general design guidelines, this subcategory describes rules regarding the staircase effect or the extrusion width, for example. In the case of specific design guidelines, it describes the characteristic values for process-related questions like "What is the minimum wall thickness?" and others. The second subcategory is *design for function*. Within this subcategory, coming from the intended application, design recommendations are given for realizing a specific function.

4 Case Study

The silicone gripper considered in this case study is a pneumatically actuated gripper with three fingers, as shown in Fig. 3 (see Fig. 7 for the actuated gripper). Each finger is approx. 50 mm long and consists of several air-filled chambers. Each chamber is 15 mm high, 15 mm wide, 5.2 mm deep, and has a wall thickness of 1 mm. The fingers are used simultaneously for gripping and can only be actuated together. They are arranged at 120° angles to each other and run together in a central connection, which can be directly plugged into a pressure source. Upon actuation, the air is distributed equally between all fingers. The gripper was originally designed for a multi-stage casting process [13] and is now to be redesigned in terms of silicone 3D printing. Since the functionality of the original component is already given, only design for manufacturing guidelines are relevant for the redesign.

4.1 Selection of Design Guidelines

The limitations of the casting process differ significantly from those of silicone 3D printing. Undercuts and cavities in particular are special challenges in the casting process. However, they are a basic requirement for producing a functional pneumatic actuator. The main challenges of pneumatic components suited for the silicone 3D printing process are the two following questions:

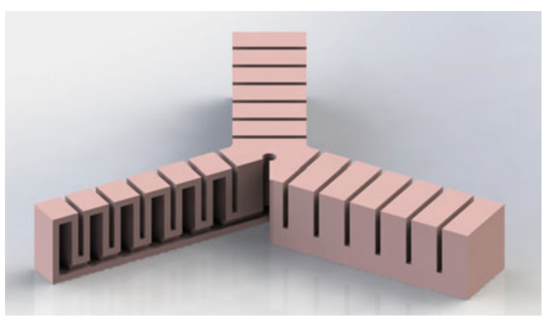

Fig. 3 Pneumatically actuated universal soft gripper

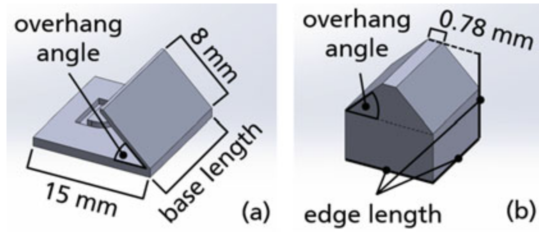

Fig. 4 Benchmark components for **a** identifying the minimum overhang angle and **b** determining the best configuration for a hermetically sealed cavity [29]

1. What is the minimum overhang angle for inclined surfaces?
2. Which wall thickness should be chosen to create airtight cavities?

In an experimental study conducted by the authors, two benchmark parts were developed and manufactured to determine the answers to these questions [29]. The first benchmark part is a solid base with an inclined wall, see Fig. 4a. This part is used to identify the minimum overhang angle and is thus printed in different configurations. The parameters varied are the overhang angle and the length of the wall. The second benchmark part consists of a cuboid with a prism on top that resulted in a test geometry of a house-like shape, see Fig. 4b. The geometry is hollow and is used to determine the best configuration for a hermetically sealed cavity. The wall thickness, the edge length of the cuboid, and the overhang angle are the relevant parameters that were varied for each of the printed benchmark parts.

The two developed design guidelines state [29]:

1. *Minimum overhang angle*: In general, overhang angles should be at least 50°. For continuous extrusion paths longer than 15 mm, angles between 40° and 50° are also feasible.
2. *Minimum wall thickness for hermetically sealed cavities*: For a 0.4 mm nozzle, the wall thickness should be at least 1.17 mm. This corresponds to at least three shells for an extrusion width of 0.39 mm (at an overhang angle of 45°).

Note that these two guidelines are only valid for InnovatiQ's LiQ320 3D printing system and Silastic 3D 3335 liquid silicone rubber from Dow Chemical (USA) and the minimum wall thickness for hermetically sealed cavities is angle-dependent (not analyzed here).

In addition to the specific design guidelines stated above, two general guidelines were also considered for the redesign of the gripper. The first guideline states that the wall thickness of thin walls should always be a multiple of the extrusion width. This avoids hollow areas (when the shells from the outside and the inside of the chamber wall are creating a gap that is too small for additional material) or material accumulation (when the shells from the outside and the inside of the chamber wall are overlapping) inside the chamber walls of the gripper.

The second general guideline states that very short extrusion paths should be avoided. This guideline is another design for manufacturing guideline to be considered for all material extrusion processes. Each time the print head stops to extrude material and moves to a new location, material has to be retracted inside the extruder to prevent excess material to leave the nozzle. This creates large pressure changes inside the extruder. Restarting the extrusion process creates a short time period where material is extruded unevenly. This can be minimized but is hard or even impossible to avoid completely. Therefore, the number of pressure changes should be kept minimal. Considering that, shells (also called perimeters) and infill structures should ideally consist of a single continuous path. This can be achieved by choosing a design with a consistent wall thickness and certain infill structures.

4.2 Application of Design Guidelines

To adapt the gripper to the requirements of silicone 3D printing, the critical areas of the original design have to be identified. For this purpose, the design features of a single actuator are analyzed. It consists of multiple hollow chambers connected to each other at their base. An air duct runs along the base, which guides the compressed air from the central connection into the individual chambers. The areas of the design to be adjusted are the horizontal overhangs and the wall thickness of the chambers (cf. Fig. 3).

In a first design iteration, the chambers were chamfered at the top to avoid horizontal overhangs. From the first specific design guideline described above, it is known that it is possible to manufacture an overhang angle of 45° successfully for continuous extrusion paths longer than 15 mm. All inclined surfaces of the gripper thus have an overhang angle of at least 45°, see Fig. 5 (blue). The second specific guideline states that at least three shells are required to create an airtight wall around the chamber. For the used extrusion width of 0.39 mm, this results in a wall thickness of 1.17 mm, which was used for the first iteration of the redesign, see Fig. 5 (red).

The first redesign was printed and tested. While the gripper was manufactured successfully and came out of the printer without any visible defects, the tests showed that the actuators were not completely sealed. Submerging the gripper in water while pressurizing it revealed that the air was escaping at the top of the chambers and from the duct. The reason for this is most likely the problem discussed in the second general design guideline (avoidance of very short extrusion paths) discussed above. The first redesign (Fig. 5, top) created a very small cross sectional area at the top of the chambers, which leads to many short extrusion paths (Fig. 5, bottom; red dotted line). To avoid this problem, for the second iteration of the redesign (Fig. 6, top), the inclined surfaces were rotated by 90° to create a surface with longer extrusion paths (Fig. 6, bottom; red dotted line). The minimum overhang angle was also increased from 45° to 50° (Fig. 6, top; blue), and an

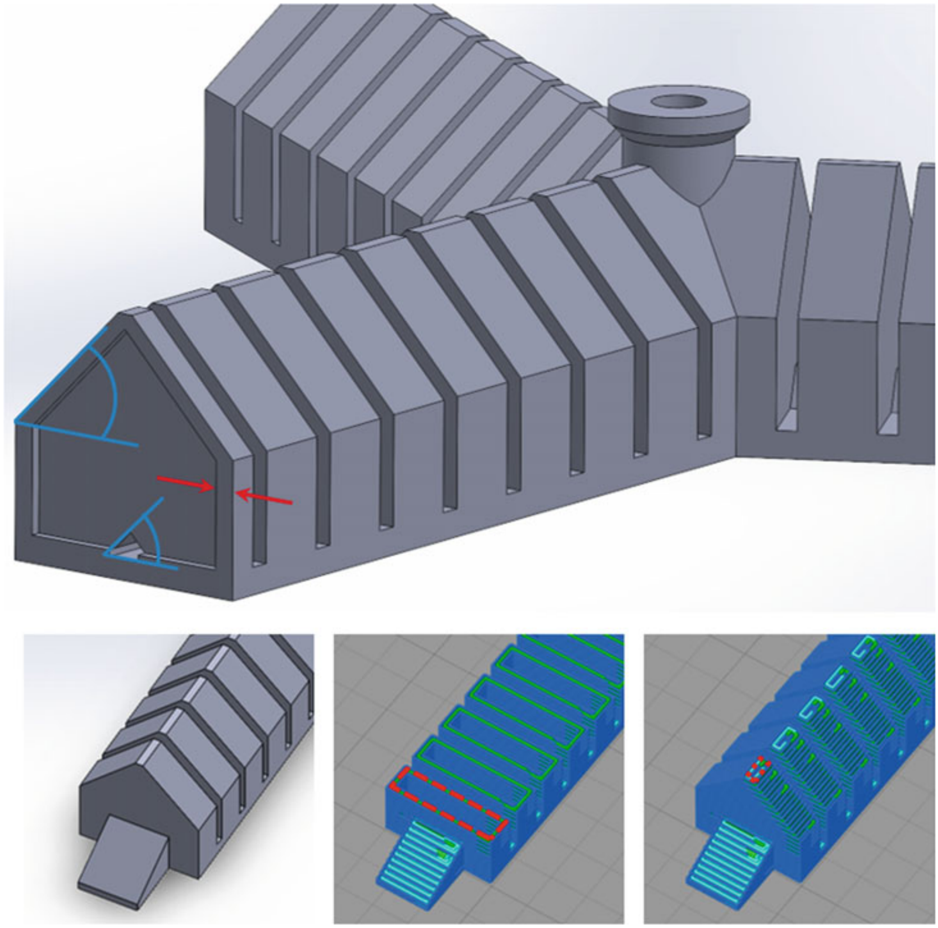

Fig. 5 First redesign iteration of the universal gripper with many short extrusion paths

additional shell was added (resulting in a wall thickness of 1.56 mm) to make sure that the air chambers and the duct are fully sealed (Fig. 6, top; red).

The second version of the gripper was successfully printed and tested in a water bath just like the first version. No rising air bubbles could be observed. The gripper was then mounted on a robot arm (DOBOT Magician from Variobotic GmbH, Germany) and activated using an electric pump. It was reliably used to handle fruits and vegetables, see Fig. 7. The desired motion of the fingers could be achieved and is comparable to the motion of the casted version of the gripper.

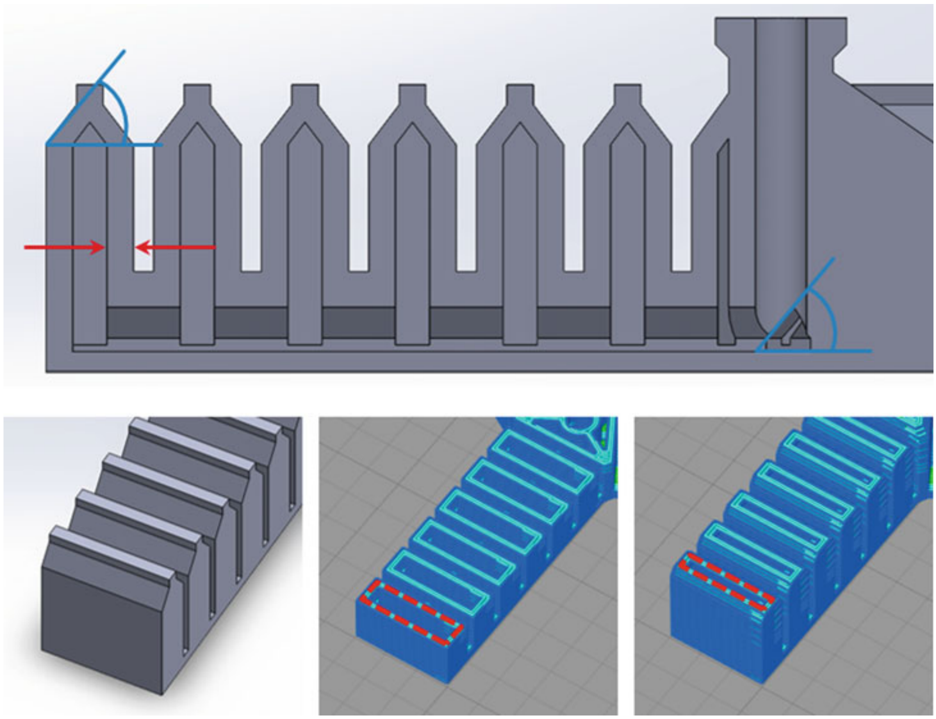

Fig. 6 Second redesign iteration of the universal gripper with longer extrusion paths

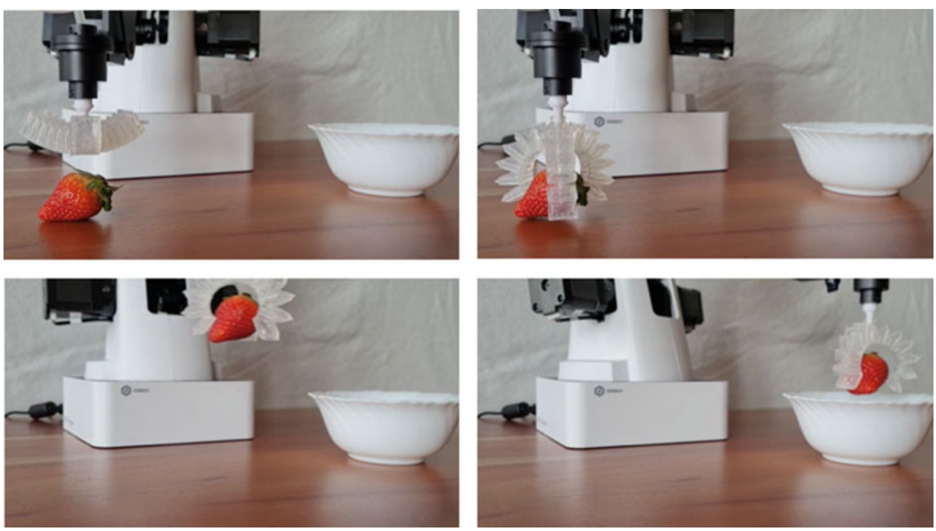

Fig. 7 3D printed universal gripper mounted on a robot arm when grasping a strawberry

5 Conclusions and Outlook

Soft robots can interact safely with humans as well as their environment, adapt well to differently shaped objects, and they are also inexpensive. Silicone 3D printing makes it possible to produce pneumatically driven soft robots with the desired properties in individualized form from a single piece. The presented case study shows that a deeper understanding of the capabilities and limitations of the process is necessary to redesign an existing part or to design a new one. Design guidelines can be an important tool to assist in the design process. The first guidelines developed by the authors and presented in this paper were successfully applied to redesign an existing universal gripper that was previously created for casting. The design guidelines also facilitated troubleshooting following the testing of the first design iteration. Since the minimum overhang angle and the minimum wall thickness for airtight cavities are scientifically validated values, other factors such as the length of the extrusion paths could quickly be identified as the main cause for leakage.

Silicone 3D printing is a relatively new technology, nearing its introduction to industrial usage. Therefore, the authors intend to further develop the presented guidelines and investigate additional ones. An additional topic to be considered in future research will be the durability of printed silicone parts as well as the aging of the material. Both should be investigated to ensure a successful introduction into industrial applications.

References

1. Rus, D., & Tolley, M. T. (2015). Design, fabrication and control of soft robots. *Nature, 521*(7553), 467–475.
2. Laschi, C., Mazzolai, B., & Cianchetti, M. (2016). Soft robotics: Technologies and systems pushing the boundaries of robot abilities. *Science Robotics*, *1*(1).
3. Polygerinos, P., Correll, N., Morin, S. A., Mosadegh, B., Onal, C. D., Petersen, K., Cianchetti, M., Tolley, M. T., & Shepherd, R. F. (2017). Soft robotics: Review of fluid-driven intrinsically soft devices; manufacturing, sensing, control, and applications in human-robot interaction. *Advanced Engineering Materials, 19*(12), 1700016.
4. Whitesides, G. M. (2015). Bioinspiration: Something for everyone. *Interface Focus, 5*(4), 20150031.
5. Ilievski, F., Mazzeo, A. D., Shepherd, R. F., Chen, X., & Whitesides, G. M. (2011). Soft robotics for chemists. *Angewandte Chemie, 123*(8), 1930–1935.
6. Martinez, R. V., Glavan, A. C., Keplinger, C., Oyetibo, A. I., & Whitesides, G. M. (2014). Soft actuators and robots that are resistant to mechanical damage. *Advanced Functional Materials, 24*(20), 3003–3010.
7. Shintake, J., Cacucciolo, V., Floreano, D., & Shea, H. (2018). Soft robotic grippers. *Advanced Materials, 30*(29), 1707035.
8. Chu, C. Y., & Patterson, R. M. (2018). Soft robotic devices for hand rehabilitation and assistance: A narrative review. *Journal of Neuroengineering and Rehabilitation, 15*(1), 1–14.

9. Runciman, M., Darzi, A., & Mylonas, G. P. (2019). Soft robotics in minimally invasive surgery. *Soft Robotics, 6*(4), 423–443.
10. Tolley, M. T., Shepherd, R. F., Mosadegh, B., Galloway, K. C., Wehner, M., Karpelson, M., Wood, R. J., & Whitesides, G. M. (2014). A resilient, untethered soft robot. *Soft Robotics, 1*(3), 213–223.
11. Katzschmann, R. K., DelPreto, J., MacCurdy, R., & Rus, D. (2018). Exploration of underwater life with an acoustically controlled soft robotic fish. *Science Robotics*, *3*(16).
12. Li, S., Peele, B. N., Larson, C. M., Zhao, H., & Shepherd, R. F. (2016). A stretchable multicolor display and touch interface using photopatterning and transfer printing. *Advanced Materials, 28*(44), 9770–9775.
13. The Soft Robotics Toolkit. Retrieved June 30, 2021, from https://softroboticstoolkit.com/book/pneunets-fabrication.
14. Truby, R. L., & Lewis, J. A. (2016). Printing soft matter in three dimensions. *Nature, 540*(7633), 371–378.
15. Wallin, T. J., Pikul, J., & Shepherd, R. F. (2018). 3D printing of soft robotic systems. *Nature Reviews Materials, 3*(6), 84–100.
16. Zhou, L. Y., Fu, J., & He, Y. (2020). A review of 3D printing technologies for soft polymer materials. *Advanced Functional Materials, 30*(28), 2000187.
17. Yap, H. K., Ng, H. Y., & Yeow, C. H. (2016). High-force soft printable pneumatics for soft robotic applications. *Soft Robotics, 3*(3), 144–158.
18. Scharff, R. B., Doubrovski, E. L., Poelman, W. A., Jonker, P. P., Wang, C. C., & Geraedts, J. M. (2017). Towards behavior design of a 3D-printed soft robotic hand. In *Soft robotics: Trends, applications and challenges* (pp. 23–29). Springer.
19. Peele, B. N., Wallin, T. J., Zhao, H., & Shepherd, R. F. (2015). 3D printing antagonistic systems of artificial muscle using projection stereolithography. *Bioinspiration & Biomimetics, 10*(5), 055003.
20. Bartlett, N. W., Tolley, M. T., Overvelde, J. T., Weaver, J. C., Mosadegh, B., Bertoldi, K., Whitesides, G. M., & Wood, R. J. (2015). A 3D-printed, functionally graded soft robot powered by combustion. *Science, 349*(6244), 161–165.
21. LiQ320 3D Printer. Retrieved June 30, 2021, from https://www.germanreprap.com/printer/LiQ320.aspx.
22. S600D 3D Printer. Retrieved June 30, 2021, from https://lynxter.fr/en/produit/machine.
23. Delta Tower Fluid 3D Printer. Retrieved June 30, 2021, from https://deltatower.ch/en/fluid-2.
24. 3D Printing. Retrieved June 30, 2021, from https://www.viscotec.de/en/industry-applications/3d-printing.
25. Dispensing Tips. Retrieved June 30, 2021, from https://www.dosieren.de/en/products/dispensing-tips.
26. Mullins, L. (1948). Effect of stretching on the properties of rubber. *Rubber Chemistry and Technology, 21*(2), 281–300.
27. Abidi, H., & Cianchetti, M. (2017). On intrinsic safety of soft robots. *Frontiers in Robotics and AI, 4*, 5.
28. Leslie, L. J., Jenkins, M. J., Shepherd, D. E. T., & Kukureka, S. N. (2008). The effect of the environment on the mechanical properties of medical grade silicones. *Journal of Biomedical Materials Research Part B: Applied Biomaterials, 86*(2), 460–465.
29. Weigand, F., Nguyen, A. M., Wolff, J., & Seibel, A. (2021). Toward industrial silicone 3D printing of soft robots. In *2021 IEEE International Conference on Soft Robotics (RoboSoft)* (pp. 523−526). IEEE.

Design Automation of a Patient-Specific Endoprosthesis with Multi- Objective Optimized Lattice Structures

Patrik Müller, Paul Christoph Gembarski, and Roland Lachmayer

Abstract

Additive manufacturing is a strong enabler for the individualization trend in product development and is also increasingly finding its way into medical technology. This is made possible by the immense design freedom as well as new modeling methods, which can transform the design phase in product development. This paper presents a process chain for automating the design synthesis of a parameterized hip endoprosthesis based on patient-specific computed tomographic image data. Expert systems are used to simplify and automate critical design steps of the endoprosthesis, which are specified at a high level of abstraction by the user's input of design goals. This process chain, in contrast to the conventional design synthesis, can also be extended with multi- objective optimization strategies, like a maximize bone-ingrowth through a surface layer with lattice structures, so that the efficiency of the automated design synthesis of the short stem endoprosthesis can be maximized.

Keywords

Patient-specific arthroplasty • Effect-engineering • Computational design synthesis • Parametric modelling • Customized short shaft endoprosthesis • Additive manufacturing

P. Müller (✉) · P. C. Gembarski · R. Lachmayer
Institute of Product Development, Leibniz University of Hannover, Garbsen, Germany
e-mail: mueller@ipeg.uni-hannover.de

P. C. Gembarski
e-mail: gembarski@ipeg.uni-hannover.de

R. Lachmayer
e-mail: lachmayer@ipeg.uni-hannover.de

R. Lachmayer et al. (eds.), *Innovative Product Development by Additive Manufacturing 2021*, https://doi.org/10.1007/978-3-031-05918-6_8

1 Introduction

Endoprosthesis are implants that partially or completely replace damaged body parts such as worn joints or defective bone material and remain permanently in the human body. With endoprosthesis in confectioned size systems, the requirements of anchoring implants can only be inadequately solved, since the bone has to be adapted to the endoprosthesis and healthy bone must also be removed [1]. Normally, they are manufactured by machining or casting. However, their geometric shape is limited due to accessibility for tools or demouldability. With the increasing demands on arthroplasty and the increased demand for surgical techniques that are gentle on the soft tissue and save bone, the importance of patient-specific solutions is also growing [2].

Additive manufacturing empowers these developments in the field of medical technology. This trend is based on the certainty that the patient's characteristics, as well as the influences of the individual lifestyle and the environment, have a significant influence on the respective disease and its therapy [3, 4]. With the possibilities of additive manufacturing, the conception and design of new structures are no longer limited to conventional manufacturing restrictions [5]. Thus, in addition to free shaping, complex lattice structures can be realized, which can produce various effects, such as maximum bone ingrowth while it functions as a scaffold [6]. The lattice structure exhibits better mechanical performances of the bone-anchored endoprosthesis which is determined by its porosity and relative density [7, 8].

With the help of Computational Design Synthesis (CDS), a model is presented that automates the synthesis of an individual short-shaft hip endoprosthesis for additive manufacturing. The automated design synthesis of the stem geometry is followed by effect-engineering in a highly integrative Computer-Aided Engineering Environment (CAEE). In effect-engineering, various physical effects, such as maximum bone ingrowth or adjustment of the Young's modulus between bone and implant, are implemented in the model to increase the efficiency of the short-shaft endoprosthesis. For this purpose, the process chain is extended by the optimization goal of maximum bone ingrowth through a surface layer with lattice structures.

2 Related Work

Technological advances in additive manufacturing are the basis for patient-specific design synthesis of (medical) products. The methods of CDS, which are described in Sect. 2.1, support the cost efficiency of the process. The subsequent effect-engineering with the multi-objective optimization approach, as described in Sect. 2.2, can maximize the requirements of the medical devices in terms of service life, functionality, and freedom from complications.

2.1 Computational Design Syntheses of Individualized Products

The development of products is an iterative and creative process in which decisions are made to create a product that meets the wishes and needs of the customer. Based on the wishes and needs of the customers, a problem is formulated, which is then transferred into a design by the developer through the search for a solution concept [9, 10]. The efficiency of the product depends significantly on the quality of the requirements description and the respective requirements implementation in the product [11]. This concept phase is particularly critical, because here the influence on costs is at a maximum and decisions in this phase have an impact on all later ones [12]. The growing demand for product differentiation leads to a high external product variety in this phase. However, this external product diversity carries the risk of internally induced variance and process complexity [13].

CDS is a research area based on the approach that various time-consuming and routine design tasks performed by an engineer in the context of product development can be (semi-)automated by computer-aided systems [14]. CDS-based tools automate the design synthesis through algorithmic procedures and have the ability to evaluate this model and provide feedback. Accordingly, the design models represent the flow-specific formulation of the respective design problem and describe not only the structure and the respective components, but also the parameters and their relationships to each other [15]. Thus, the CDS can also start early in the conception phase and supports the creative process of conceptualizing products. According to Chakrabarti et al., CDS is important mainly for two aspects. Often, the development of a new solution is complicated due to the limitation of knowledge or the consistency of requirements. Furthermore, the mental effort of the developer during the design process plays a major role, which can lead to errors [12]. The method aims to map numerous design variants based on various requirements as well as restrictions with the help of decision support systems and then to find an optimal geometry and topology for a component or assembly [16, 17]. Through this procedure, a defined external product variety can be offered and at the same time the internal component and process variety can be reduced.

A typical CDS framework for computer-aided solution of engineering design tasks is shown in Fig. 1.

The core of the framework consists of a loop through the phases generate, evaluate and guide, which are based on the representation. These three phases, which define the search process for a design solution based on the formulation of the design task, can be understood by humans and computer-aided systems alike. A human developer interprets the final design and can make adjustments to the formulation of the design task, if necessary, to improve the results of the next iteration.

In the representation phase of a schematic design solution, the level of detail and focus of the CDS is defined. For this, the class of the design problem has to be investigated, for example by identifying previous solutions or known methods to map the representation

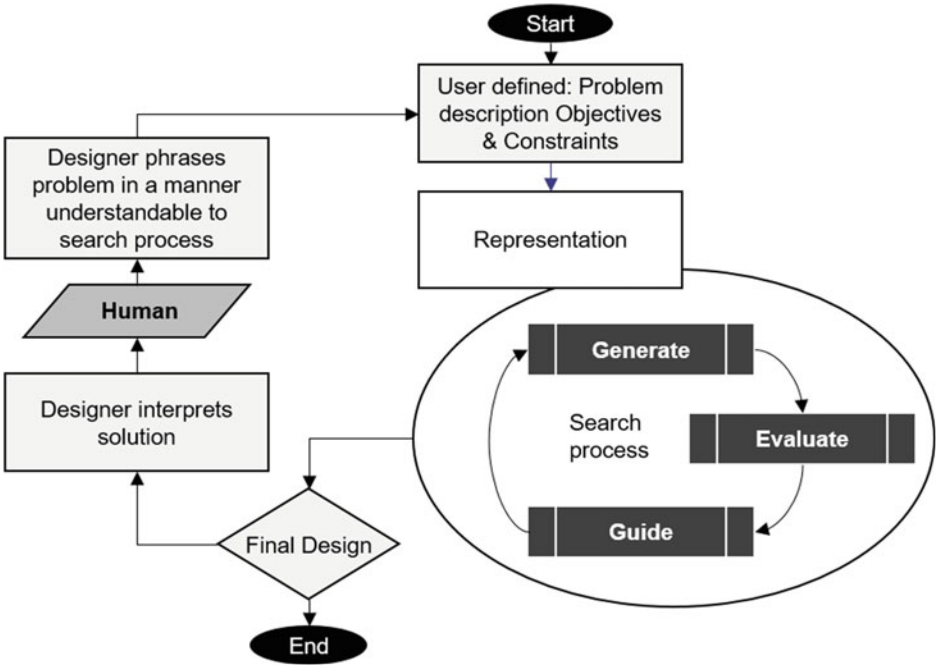

Fig. 1 The generic flowchart for the synthesis of open-ended engineering design problems based on [15]

of the solutions. The representation can therefore be represented in different ways, such as forms, functions and structures. This phase forms the foundation for all further steps and must therefore be carried out manually with considerable care. In the generative part, new solutions are synthesized computer-aided based on the representation. To evaluate the quality of the solution, the CDS method must be able to separate good solutions from bad ones. In the last step of this phase, feedback must be provided to the system describing how to proceed. Whether the next synthesis steps are triggered by using search methods, e.g. simulated annealing, or knowledge based engineering methods, such as using an inference engine, depends directly on the representation of knowledge-rewriting [15].

With the help of CDS, the potential for individualising products can be expanded. Within product individualisation, different approaches can be chosen that characterise the degree of individualisation depending on the specification and functionality. Through the CDS, these individualisation measures can be formulated as conditions and restrictions in the representation. For example, anthropometric body and bone measurements can be used as a starting point for the automated design synthesis of individualised medical products such as endoprostheses [18].

2.2 Evolutionary Multi-objective Optimization

The efficiency of CDS can be maximized with multi-objective optimizations, which are solved with evolutionary algorithms. A multi-objective optimization problem is characterized by the existence of several objective functions that must either be minimized or maximized. In addition, constraints can be formulated that must be satisfied by each possible solution. A multi-objective optimization problem can be described in its general form as follows [19]:

$$\begin{aligned} \text{minimize/maximize: } & f_m(\vec{x}), & m = 1, \ldots, M; \\ \text{subject to: } & gj(\vec{x}) \geq 0, & j = 1, \ldots, J; \\ & hk(\vec{x}) = 0, & k = 1, \ldots, K; \\ & x_i^{(L)} \leq x_i \leq x_i^{(U)}, & i = 1, \ldots, n. \end{aligned} \tag{1}$$

Here $\vec{x} = (x_1, \ldots, x_n)^T$ is the vector of design variables. It contains the decision variables that describe a solution. The variables can be formulated as continuous, discrete or binary and are each limited by a lower and an upper bound. Both conditions of inequality $g_j(\vec{x}) \geq 0$ and conditions of equality $h_k(\vec{x}) = 0$ are considered as constraints.

Constraints often reflect limited resources, user requirements or bounds on the validity of the computational model concerning the optimization problem. The solutions that satisfy both the constraints and the variable bounds together form the valid-dimensional design variable space:

$$X := \{x \in X : g_i(\vec{x}) \geq 0 \wedge h_k(\vec{x}) = 0\}. \tag{2}$$

Since the different goals are usually opposite, no optimal point exists as a single solution. The result is now a solution set. It is defined by the fact that at each point of this set, one objective function can only be improved by making another worse. Accordingly, this separation of inefficient solutions is called the Pareto front [20].

Evolutionary algorithms (EA) are stochastic and metaheuristic optimization methods that use the principles of selection, recombination and mutation, following the example of biological evolution [21]. With the help of an optimization, ideal design solutions can be found in the CDS that optimally fulfil the requirements, which are sometimes contradictory, while complying with all restrictions and limits. In this context, evolutionary computing try to minimize a fitness function, which depends on various variables, in this case genes [22]. A fitness function evaluates how close a given solution (the combination of different genes) is to the optimum solution of the desired problem. EA have a characteristic process, which is shown in Fig. 2.

Collections of individuals (or genomes) are generated through the random initial variation of genes. Each combination of genes has its fitness. The aim is to find better solutions step by step and to determine or approximate optima in this way. Each individual represents a possible solution to the optimization problem. After the individuals have been

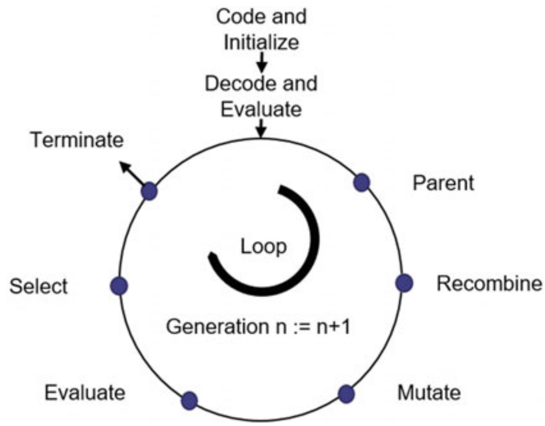

Fig. 2 Schematic structure of an evolutionary algorithm with a loop through which different generations are created based on [22]

evaluated, they are selected, recombined and mutated. Subsequently, they are again evaluated and further selected so that the maximum or minimum of the sought-after objective function can be found within several generations [21].

3 CDS of Patient-Specific Short Shaft Endoprosthesis for Maximum Bone Ingrowth

In the following Sect. 3.1, CDS is applied to the design of a patient-specific short-shaft hip arthroplasty. The multi-objective optimization of the lattice structures for maximum bone ingrowth, are presented in Sect. 3.2.

3.1 Medical Reverse Engineering and Computational Design Syntheses of a Parametric Short Shaft

The basis for the patient-specific design synthesis of the short-shaft hip endoprosthesis are computer tomographic data (CT scans) generated in reverse engineering. These CT scans can be used to segment the different tissue types, in this case, bone. To ensure complete preservation of the bone wall (cortical bone) during implantation of a short stem arthroplasty and postoperatively, only the bone marrow and the cancellous bone are segmented in medical reverse engineering. The healthy bone wall is used to create primary stability as well as bone accretion. This segmentation represents the solution space of the patient-specific short-shaft endoprosthesis.

The transformation of the design space to the desired shaft geometry is performed using a knowledge base, which is implemented in the process chain. This knowledge base is defined at a high level of abstraction by the user and mainly describes the type and location of the targeted bone anchorage. An advantage of this knowledge implementation is the possible adaptation of the solution according to the application and pathological identification.

Bone-anchored implants, such as the short-shaft hip prosthesis, must also fulfil various osteological competencies to ensure biocompatibility, primary stability, and sufficient long-term stability. Thus, a proximal bone anchorage in the metaphysis should mimic the natural biomechanical conditions of the proximal femur. Besides, stem geometry and material should have a favorable implant stiffness that allows for stretch stimuli above the threshold of activation of the mechanosensory system. Another basic osteological requirement is a preferred cancellous embedding of the implant, in addition to compact clamping, to create a rapid bone adaptive remodeling and attachment, which should ensure long-term stability and prevent stress shielding.

To move from the design space to the solutions of the targeted short shaft endoprosthesis, various steps have to be taken for mathematical identification and manipulation of the topology. For this purpose, the visual programming language Grasshopper3D is used. This enables the automated parametric design synthesis of the patient-specific short stem endoprosthesis as shown in Fig. 3.

The triangulated mesh from the segmentation of the CT scans is registered in the CDS environment. The contour is described via defined surface points and mapped by NURBS curves. NURBS curves (*Non Uniform Rational Basic Splines*) are a mathematical method for describing three-dimensional polylines. A NURBS curve is defined by the position of control points and their degree and weight values. Control points are used to define the shape of the NURBS curve. For this purpose, the weight value and the degree of each control point can be changed.

The new contour can thus be fully parameterized using the generated NURBS curves, in which prominent points of the cortical bone represent control points. An implemented

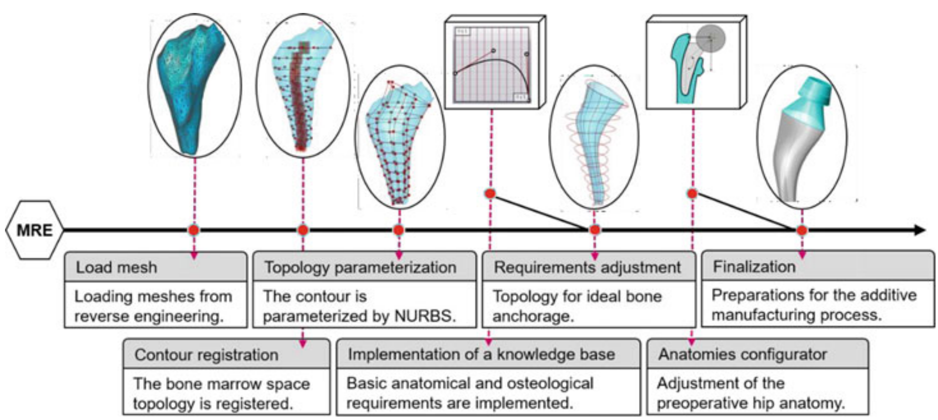

Fig. 3 Process chain for generating a patient-specific short-shaft endoprosthesis based on [18]

knowledge base adjusts the NURBS curves (in particular the position of the control points and the weights) to generate a design of the short stem endoprosthesis that meets the anatomical and osteological requirements. The knowledge base is model-based and allows the user to vary the bone anchorage by using Bézier curves. These curves describe the distance by which the NURBS curves are displaced from the outer margin to ensure an optimal fit. Subsequently, a first evaluation is already performed in this step by checking the implantability and the conical course. Finally, the head of the short stem arthroplasty is created based on the required postoperative hip anatomy.

The result of this procedure is a patient-specific short stem endoprosthesis with optimal geometry for a form fit. The geometry generated in this way is used in the following section as the basis for effect-engineering.

3.2 Effect-Engineering: Generation of a Lattice Structure for Maximum Bone Ingrowth

A bone has a non-uniform porous structure. Within the porous structure, the graded density structure grows from the inside of the bone to the edge, the bone wall. In the current researches of bone-anchored products, these graded structures are tried to imitate in order to produce various functions such as Young‘s modulus matching, stretch stimulus generation, or bone ingrowth [23, 24]. Lattice structures can perform a variety of these functions, which can maximize the efficiency of components. For example, revision rates for endoprostheses can be significantly reduced by effective bone ingrowth [25].

Since they are impossible or extremely complicated to produce using conventional manufacturing processes, the application is particularly interested in terms of additive manufacturing [5]. A lattice structure is an architecture formed by an array of the spatial arrangement of unit cells with edges and faces. The porous structure has a fully controllable pore size, pore shape, and density. The generation of the lattice structure usually goes through three phases: lattice pattern selection, lattice cell parameter set, and lattice layout determination. In this process, desired volume models are voxelized by unit cell cubes. These voxels can be uniformed or non-uniformed in the model. Afterward, these voxels are filled with the unit cells. The determining parameters are the cell shape (usually modeled on metallic crystal lattices), the cell size, and the cell thickness. Thus, each cell can be designed individually, which allows the defined control of the pore characteristic and the mechanical properties [26].

In this work, the lattice structure is intended exclusively to maximize bone ingrowth, the area of the proximal and distal metaphysis that is particularly critical for stress shielding is separated in the form of a bounding box and filled with lattice structures (cf. Fig. 4).

Studies have shown that pore sizes at approximately 650 μm promote bone ingrowth. With the help of this effect, a bony layer, in the bone-implant interface, can be created

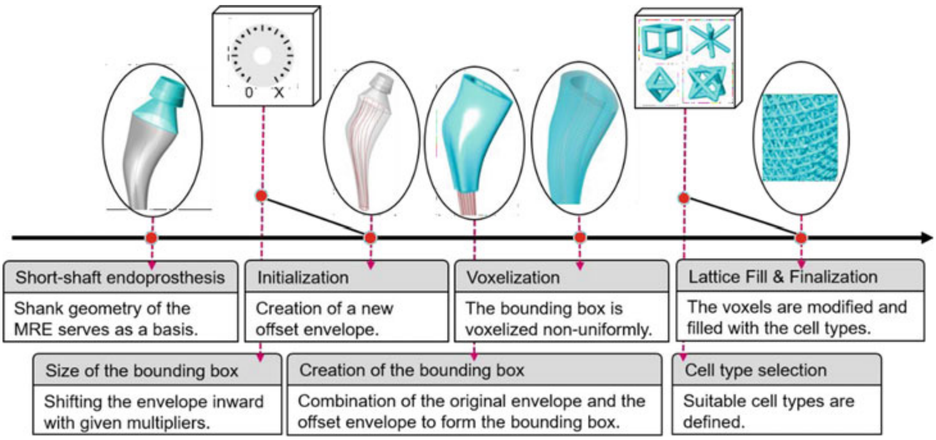

Fig. 4 Process chain for generating lattice structures in the target zone of the metaphysis or maximum bone ingrowth

that can compensate for the large differences in the Young's modulus between bone and implant, has a damping effect and equalizes the forces in the interface [27, 28]. The lattice structure is placed in the critical area of possible aseptic loosening and supports bone ingrowth.

As the lattice structure is inserted in the area of relevant mechanical loading of the metaphysis, a minimum weakening of the structure with maximum bone ingrowth at the same time should be realized in the bounding box of the grid structure. For this reason, a lattice structure is sought that has a maximum surface area and minimum volume of the bounding box.

A restriction here is the maximum pore size of 650 µm (and minimum porse size of 150 µm to ensure open cells for powder removal), as well as the manufacturing restrictions of additive manufacturing in the form of minimum wall diameter of the struts at 0.25 mm. The formulation of the multi-objective optimization becomes:

$$\begin{aligned} \text{maximize:} \quad & A_{\text{Lattice}}(\vec{x}), \\ \text{minimize:} \quad & V_{\text{BoundingBox}}(\vec{x}), \\ \text{subject to:} \quad & 150\,\mu\text{m} \le g_{\text{PoreSize}}(\vec{x}) \le 650\,\mu\text{m}, \\ & g_{\text{StrutDiameter}}(\vec{x}) \ge 250\,\mu\text{m}, \\ & g_{\text{StrutDownskin}}(\vec{x}) \le 30^\circ. \end{aligned} \tag{3}$$

The genes that define the design variable $\vec{x}$ are shown in Fig. 5.

Six genes are varied in the multi-objective optimization. To increase the performance of the multi-objective optimization, these genes were limited in intervals and the step sizes were adjusted. The gene *x*Offset-BB (G1) concerns the area offset for area B to

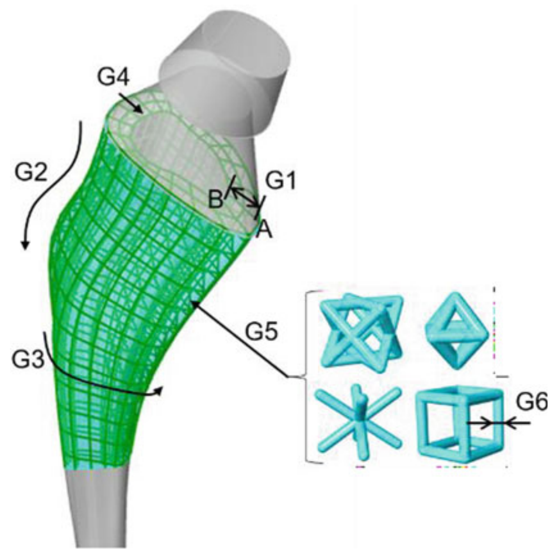

Fig. 5 Representation of all genes that are varied in the multi-objective optimization

area A, which makes up the bounding box. This parameter is the main driver for the volume of the bounding box. The gene *x*LatticeType (G2) describes the shape of the unit cell. Four different unit cells can be selected, all of which comply with the manufacturing restriction of maximum overhang angles. The genes *x*Lattice-x, *x*Lattice-y, *x*Lattice-z (G3–G5) define the number of volume subdivisions in each spatial direction between the surfaces A and B. The total volume of the bounding box is composed of these parameters. These parameters compose the total number of non-uniform voxels within the bounding box volume. The gene *x*StrutRadius (G6) describes the radius of the pipe elements with which the lattice beams are filled.

Each combination of the genes generates a complete and, based on the intervals, valid solution of the lattice structure. The analysis and evaluation of the genome is done by calculation functions. Thus, the lattice structure is meshed and the surface area of the mesh, as well as the volume of the bounding box, is calculated. During the mesh generation, it is also possible that cells are completely closed so that the surface area can decrease if the voxels are too small and the strut diameter are too large. For this reason, manual evaluation and estimation of optimal parameters is not possible. The resulting pore size is calculated as the maximum pore diameter within, or between, two adjacent cells. Since non-uniformed cells are applied in this application, this pore size is averaged for the outer layer of the voxels, the surface of the short stem endoprosthesis. Due to the ambiguous definition of the pore size for the different cell types, this formulation was done as a soft restriction. This means that results with a pore size outside the limits are also represented in the genomes.

Multi-objective optimization is performed using the Octopus tool, which enables Multi-Objective Evolutionary Optimization. It allows searching for many objectives

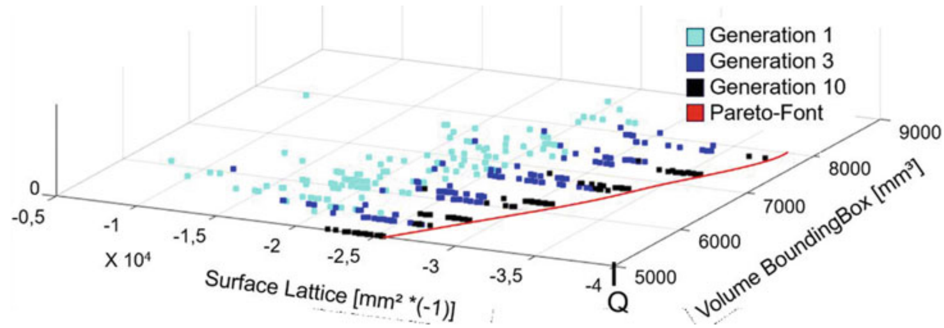

Fig. 6 Scatter plot of the multi-objective optimization. Shown are the generation 1, 3 and 10, as well as the Pareto font

simultaneously and generates a set of optimized trade-off solutions between the extremes of each objective. It introduces the Pareto principle for multiple objectives and is based on SPEA-2 and the HypE algorithm [21]. The results of the multi-objective optimization are shown in Fig. 6 by the location of the cubes in the 3D scatter plot of the objectives.

Over 10 generations, each with a population size of 100, 2.300 genomes were thus tested, selected, mutated and evaluated. Each genome represents a combination of different genes. Since the algorithm minimizes the objectives, the objective of the maximal lattice surface was negated for the algorithm. Cubes that are closer to the Coordinate intersection Q and each axis satisfy the objectives better than more distant cubes. In addition, the colors represent the different generations of multi-objective optimization. It is clear that each advancing generation satisfies the objectives better until a distinct Pareto font emerges.

The plot of Genetic distance graphs, in Fig. 7, shows the convergence behavior of multi-objective optimization. Each graph represents a genome, with the vertices representing the individual values of the respective gene. For better visualization, they have been normalized to 1. For better visualization, the numerical range of each gene they were normalized to 1. For example, a value of xStrutRadius (G5) = 0.8 in the interval of 0.125 - 0.3 mm is an actual value of 0.265 mm.

A clear increase in convergence over the generations can be detected. The genomes generated automatically in this way can then be reproduced quickly, allowing manual interpretation of the results. This procedure facilitates the search for optimal solutions. In Fig. 8, two poor solutions of the lattice structures are shown.

In a normal manual evaluation process, these solutions would not receive further attention. Instead, users would mainly interpret solutions close to the Pareto front. A pareto-optimal solution is shown in Fig. 9.

This solution is a result of multi-objective optimization, which optimally combines the objectives and the restrictions. This lattice structure can be additively manufactured and maximize bone ingrowth in the distal and proximal metaphysis.

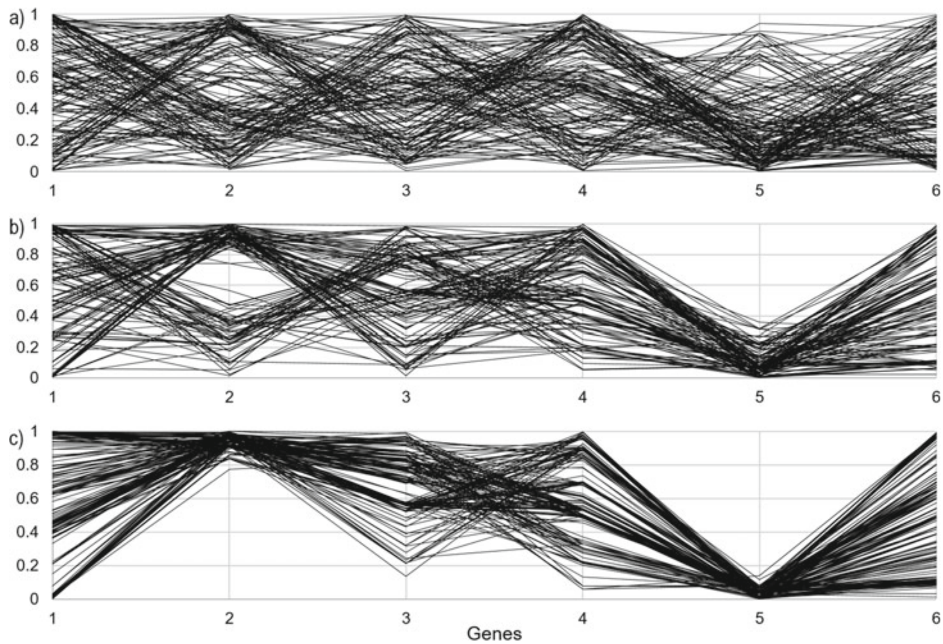

Fig. 7 Normalized parameters graph showing convergence for the six genes in **a** generation 1, **b** generation 3, and **c** generation 10

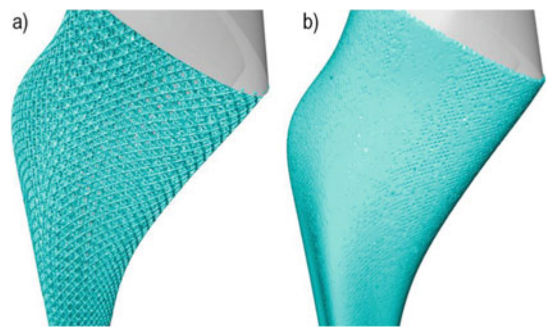

Fig. 8 A Solution with high volume and low surface area, which results in an average pore size of 1.7 mm (within the limits of the gene intervals), b) solution with low volume and low surface area, as the cells close due to the settings, which results in an average pore size of 20 μm

4 Summary and Outlook

In this work, the Design Automation of a Patient-Specific Endoprosthesis with Multi-Objective Optimized Lattice Structures in a highly integrative Computer-Aided Engineering Environment (CAEE) was presented. For this purpose, a patient-specific short-shaft endoprosthesis was generated using the methods of CDS based on CT scans. This short-shaft endoprosthesis represents the geometric basis of the subsequent effect-engineering.

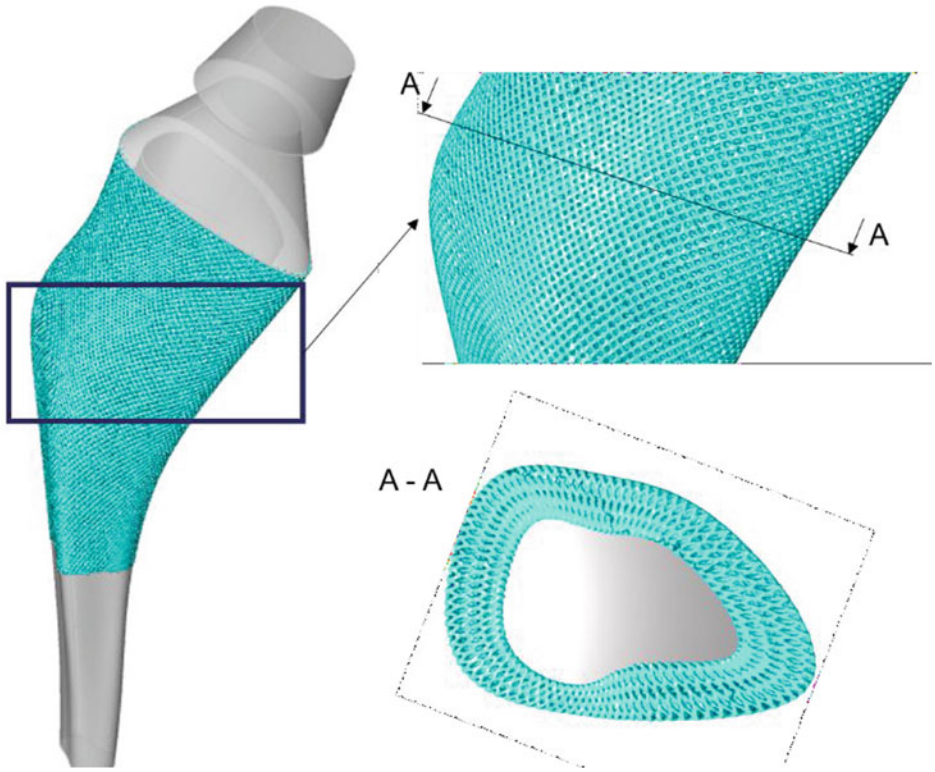

Fig. 9 Paretto-Optimal solution for maximum bone ingrowth with a large surface area and a small volume of the BoundingBox, which results in an average pore size of 0.63 mm

In this case, the effect of bone ingrowth is implemented. For this purpose, a relevant region of the short-shaft endoprosthesis was segmented and populated with parametric lattice structures. The parametric design allowed a multi-objective optimization to maximize the bone ingrowth.

A major advantage of this approach is the generic design. The CDS can work with any input mesh from reverse engineering, identify restrictions from it, and generate solutions. The stored knowledge in the CDS can be adapted and modified at any time. The subsequent multi-objective optimization can thus also be applied to any model and is not tailored to a specific prosthesis type. Here, too, the objectives, the genes, and their intervals can be adjusted at any time to produce even better results.

However, the lack of simulative validation so far, especially of the different cell structures, is critical. A validation of the mechanical parameters and a proof of stability must be carried out in order to be able to guarantee the safety of the product. The use of lattice structures often leads to increased stresses at the struts of the lattice structure, which can lead to failure. This lack of consideration of the load conditions requires further clarification. As a simplified lattice unit, the Gibson-Ashby model is widely used for the evaluation of porous structures. The model describes the mathematical relationship between the porosity and the apparent compressive strength and the elastic modulus [29]. Furthermore, other different influences, including tension–compression asymmetry, build direction dependence, and size effects, have to be considered. In addition, numerical simulations are necessary to evaluate more precisely the desired positive effect of the lattice structure on the stress shielding. Stochastic cell distributions, such as Voronoi structures, can also be used to further approximate the mechanical and osteological conditions of the bone.

The patient-specific endoprosthesis can maximize the requirements for durability, functionality, and freedom from complications compared to prefabricated prosthesis systems by ensuring that the implant matches the bone and not the other way around. The combination of the CDS and the effect-engineering to maximize bone ingrowth enable optimal positioning of the implant in the bone to ensure optimal primary and secondary stability. It also minimizes stress shielding, which is one of the main reasons for the revision of the endoprosthesis.

Acknowledgements Funded by the Ministry for Science and Culture of Lower Saxony (MWK)—School for Additive Manufacturing SAM.

References

1. Müller, P., Gembarski, P. C., & Lachmayer, R. (2021). Spezifikationen einer Entwicklungsumgebung zur synthese einer patientenindividuellen Kurzschaftendoprothese der Hüfte. In: *Stuttgarter Symposium für Produktentwicklung SSP 2021*.
2. Tusk, I. (2020). Warum individuelle Schäfte am Hüftgelenk? *Der Orthopade, 49*(5), 403–407. https://doi.org/10.1007/s00132-020-03904-w
3. Niederlag, W., Lemke, H. U., & Rienhoff, O. (2010). Personalisierte Medizin und individuelle Gesundheitsversorgung: Medizin- und informationstechnische Aspekte. *Bundesgesundheitsblatt, Gesundheitsforschung, Gesundheitsschutz, 53*(8), 776–782. https://doi.org/10.1007/s00103-010-1098-8.
4. Bondio, M. G., & Michl, S. (2010). Individualisierte Medizin: Die neue Medizin und ihre Versprechen. *Dtsch Arztebl, 107*(21).
5. Ehlers, T., Lachmayer, R., Vajna, S., & Halle, T. (2020). Producibility. In: S. Vajna (Hrsg.), *Integrated design engineering* (pp. 287–323). Springer Nature Switzerland AG 2020. https://doi.org/10.1007/978-3-030-19357-7_9
6. Chen, H., Han, Q., Wang, C., Liu, Y., Chen, B., & Wang, J. (2020). Porous scaffold design for additive manufacturing in orthopedics: A review. *Frontiers in Bioengineering and Biotechnology, 8*, 609. https://doi.org/10.3389/fbioe.2020.00609

7. Sathish, T., Vijayakumar, M. D., & Krishnan Ayyangar, A. (2018). Design and fabrication of industrial components using 3D printing. *Materials Today: Proceedings, 5*(6), 14489–14498. https://doi.org/10.1016/j.matpr.2018.03.036
8. Arjunan, A., Demetriou, M., Baroutaji, A., & Wang, C. (2020). Mechanical performance of highly permeable laser melted Ti6Al4V bone scaffolds. *Journal of the Mechanical Behavior of Biomedical Materials, 102*, 103517. https://doi.org/10.1016/j.jmbbm.2019.103517
9. Gembarski, P. C., & Lachmayer, R. (2017). Impact of rule-based systems on product complexity. *ANNALS of Faculty Engineering Hunedoara–International Journal of Engineering.*
10. Brockmöller, T., Siqueira, R., Gembarski, P. C., Mozgova, I., & Lachmayer, R. (2020). Computer-aided engineering environment for designing tailored forming components. *Metals, 10*, 1589. https://doi.org/10.3390/met10121589
11. Feldhusen, J., & Grote, K.-H. (2013). *Pahl/Beitz Konstruktionslehre.* Springer Berlin Heidelberg.
12. Chakrabarti, A., Shea, K., Stone, R., Cagan, J., Campbell, M., Hernandez, N. V., & Wood, K. L. (2011). Computer-based design synthesis research: An overview. *Journal of Computing and Information Science in Engineering, 11*(2). https://doi.org/10.1115/1.3593409.
13. Ehrlenspiel, K., Kiewert, A., & Lindemann, U. (2007). *Kostengünstig Entwickeln und Konstruieren.* Springer Berlin Heidelberg.
14. Rigger, E., Shea, K., & Stankovic, T. (2018). Task categorisation for identification of design automation opportunities. *Journal of Engineering Design, 29*(3), 131–159. https://doi.org/10.1080/09544828.2018.1448927
15. Cagan, J., Campbell, M. I., Finger, S., & Tomiyama, T. (2005). A framework for computational design synthesis: Model and applications. *Journal of Computing and Information Science in Engineering, 5*(3), 171–181. https://doi.org/10.1115/1.2013289
16. Unglert, J., Jauregui-Becker, J., & Hoekstra, S. (2016). Computational design synthesis of reconfigurable cellular manufacturing systems: A design engineering model. *Procedia CIRP, 57*, 374–379. https://doi.org/10.1016/j.procir.2016.11.065
17. Becker, J. M. J., & Wits, W. W. (2015). Enabling lean design through computer aided synthesis: The injection moulding cooling case. *Procedia CIRP, 37*, 260–264. https://doi.org/10.1016/j.procir.2015.08.057
18. Müller, P., Gembarski, P. C., & Lachmayer, R. (2021). Parametric topology synthesis of a short-shaft hip endo-prosthesis based on patient-specific osteology. In: *World Mass Customization & Personalization Conference 2021 (Accepted).*
19. Emmerich, M. T. M., & Deutz, A. H. (2018). A tutorial on multiobjective optimization: Fundamentals and evolutionary methods. *Natural Computing, 17*(3), 585–609. https://doi.org/10.1007/s11047-018-9685-y
20. Teich, J. (2001). Pareto-front exploration with uncertain objectives. In: *Evolutionary multi-criterion optimization* (pp. 314–328), Bd. 1993. Lecture notes in computer science. Springer Berlin Heidelberg.
21. Vierlinger, R., & Hofmann, A. (2013). A framework for flexible search and optimization in parametric design. In: *Design Modelling Symposium*, Berlin.
22. Dasgupta, D. (1997). *Evolutionary algorithms in engineering applications. With 61 tables.* Springer.
23. Fantini, M., & Curto, M. (2018). Interactive design and manufacturing of a Voronoi-based biomimetic bone scaffold for morphological characterization. *The International Journal on Interactive Design and Manufacturing, 12*(2), 585–596. https://doi.org/10.1007/s12008-017-0416-x

24. Gómez, S., Vlad, M. D., López, J., & Fernández, E. (2016). Design and properties of 3D scaffolds for bone tissue engineering. *Acta Biomaterialia, 42*, 341–350. https://doi.org/10.1016/j.actbio.2016.06.032
25. Warnke, P. H., Douglas, T., Wollny, P., Sherry, E., Steiner, M., Galonska, S., et al. (2009). Rapid prototyping: Porous titanium alloy scaffolds produced by selective laser melting for bone tissue engineering. *Tissue engineering. Part C, Methods, 15*(2), 115–124. https://doi.org/10.1089/ten.tec.2008.0288
26. Nagesha, B. K., Dhinakaran, V., Varsha Shree, M., Manoj Kumar, K. P., Chalawadi, D., & Sathish, T. (2020). Review on characterization and impacts of the lattice structure in additive manufacturing. *Materials Today: Proceedings, 21*, 916–919. https://doi.org/10.1016/j.matpr.2019.08.158
27. Rojekt, J., & Telega, J. J. (2001). Contact problems with friction, adhesion and wear in orthopaedic biomechanics. Part I – General developments. *Journal of Theoretical and Applied Mechanics, 39*, 655–677.
28. Deng, F., Liu, L., Li, Z., & Liu, J. (2021). 3D printed Ti6Al4V bone scaffolds with different pore structure effects on bone ingrowth. *Journal of Biological Engineering, 15*(1), 4. https://doi.org/10.1186/s13036-021-00255-8
29. Gibson, L., & Ashby, M. (1997). *Cellular solids: Structure and properties* (2nd ed.). Cambridge solid state science series. Cambridge University Press. https://doi.org/10.1017/CBO9781139878326

Design of a Thermo-Hydraulically Optimised Heat Exchanger for Production by Laser Powder Bed Fusion

Robin Kahlfeld, Ina Meyer, Stephan Kabelac, and Roland Lachmayer

Abstract

Additve Manufacturing (AM) offers the possibility to design and optimise Heat Exchangers (HX) in a completely new way, beyond the conventional types, which are limited by semi-finished products like pipes and plates. This paper starts with a short summary of the limitations of conventional Heat Exchangers along with possible solutions and potentials offered by AM of Heat Exchangers. A special focus is on the use of lattice structures to enhance heat transfer. A thermo-hydraulically optimised Heat Exchanger for AM by Laser Powder Bed Fusion (LPBF) is presented. Before designing the Heat Exchangers, considerations made are shown. This gas cooler was flow-optimised using CFD simulations and it has an internal lattice structure on the gas side. For a reference element of the structure used, the simulations show an enhancement in heat transfer between 187 and 266% compared to a plain tube. Finally, LPBF printed demonstrator Heat Exchangers and geometries are shown.

R. Kahlfeld (✉) · S. Kabelac
Institut für Thermodynamik, Leibniz University Hannover, Garbsen, Germany
e-mail: kahlfeld@ift.uni-hannover.de

S. Kabelac
e-mail: kabelac@ift.uni-hannover.de

I. Meyer · R. Lachmayer
Institut for Product Development, Leibniz University Hannover, Garbsen, Germany
e-mail: meyer@ipeg.uni-hannover.de

R. Lachmayer
e-mail: lachmayer@ipeg.uni-hannover.de

R. Lachmayer et al. (eds.), *Innovative Product Development by Additive Manufacturing 2021*, https://doi.org/10.1007/978-3-031-05918-6_9

Keywords

Additive manufacturing (AM) • Heat exchanger (HX) • Laser powder bed fusion (LPBF) • Lattice structures • CFD simulation

1 Introduction

In the course of the current ongoing climate and sustainability debates, the requirements in the field of thermal management, especially for heat exchangers (HX), have successively increased regarding efficient performance enhancement. The overriding goal is to achieve sustainable life cycles through more efficient use of resources [1]. A HX is a device in which thermal energy is transferred from one fluid flow to another. Therefore, HXs are used in a wide variety of industrial plants, such as in the energy and chemical industries, or in the heating and air conditioning of buildings and wherever machine components need to be cooled or heated. Conventional HXs consist of tubes/plates, sheets and are assembled by welding, soldering and screwing [2]. This angular construction can lead to flow maldistribution and increased pressure loss [3, 4]. To solve this problem and develop new types of heat exchangers, additive manufacturing (AM) technology is a key factor [5–9]. This allows flow optimised and customized design as well as a variety of constructive means, such as lattice structures, density gradations or bionic design, to be implemented [10, 11]. The main aim of this paper is to design a HX for LBPF printing that has an increased surface-to-volume ratio and flow-optimised geometry to generate an increase in thermal performance while maintaining or even reducing pressure drop. To demonstrate this potential a gas cooler is designed, which is flow optimised using CFD simulations and has an internal lattice structure on the gas side. This paper starts with a brief overview of conventional HXs and potentials offered by AM of HXs. The developed HX is shown and the results of the CFD simulations of both the liquid side flow and a reference element of the gas side structures are presented. Finally, an LBPF printed simplified demonstrator HX is presented.

2 Conventionally and Additively Manufactured Heat Exchanger

Depending on the application, HXs are designed to optimise the heat transfer and keep the pressure loss as low as possible while using available semi-finished products. In the following section, conventional designs are shown and relevant resulting problems will be explained. Potentials of improving heat transfer by AM will be shown and current researches is presented. A special focus will be on the use of lattice structures, which is a new method of increasing the surface for heat transfer, while being very gradable and adaptable.

2.1 Conventional Heat Exchangers and Difficulties

Inside a HX, a hot and a cold fluid, separated by a wall, pass each other in co-current, counter-current or cross-current flow, while heat is transferred from the hot to the cold fluid. These fluids can be gases or liquids, which can also condense or evaporate on their way through the apparatus. Conventional designs of HXs are strongly determined by the semi-finished products available. Tubes and plates are cut, corrugated or processed in other ways and afterwards screwed, welded or soldered together. Figure 1 shows the common types of conventional HXs, mainly categorized by the use of semi-finished products.

A common type of HX is the shell-and-tube HX, shown schematically in Fig. 2. It consists of a tube bundle with distributor and collector headers in which a fluid flows. The bundle is located in a cylindrical Shell. Another fluid flows in the space around and between the tubes. If the surface area outside a tube bundle should to be increased, fins

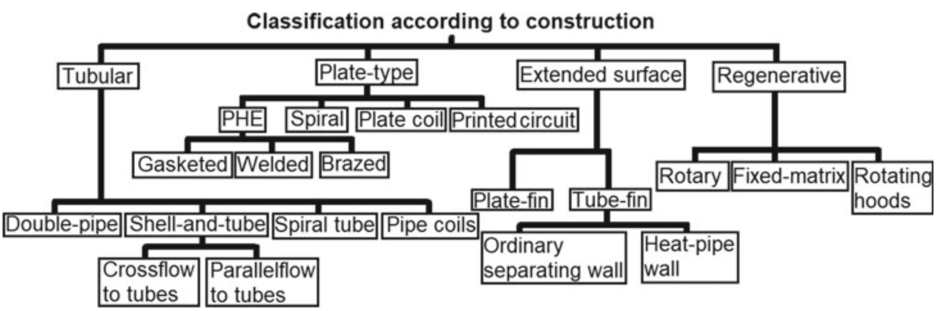

Fig. 1 Types of HXs acc. to [2]

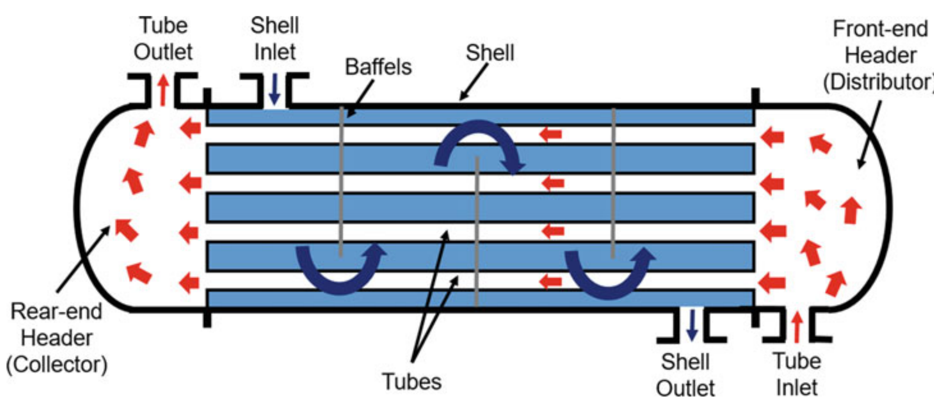

Fig. 2 Structure of a shell-and-tube HX acc. to [13]

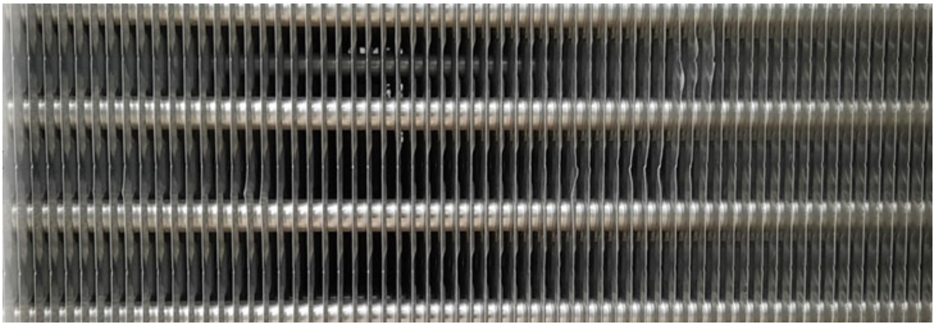

Fig. 3 Fined tubes in a HX

for instance can be attached to the tubes, as can be seen in Fig. 3. Other widely used HXs are plate HXs, in which the two fluids flow in the gaps between corrugated plates [12].

The most common problem in designing HXs is to achieve the required thermal performance while not exceeding a given pressure drop and, especially for mobile applications, minimizing the weight and size of the apparatus. Another difficulty is the design for a specific operating point which can result in poorly calculable behavior for instance in the partial load operation of a system [12]. Furthermore, the correct distribution of the fluids over the entire available flow cross-section is another problem and should always be ensured for the apparatus to work efficiently. Investigations repeatedly show the occurrence of maldistributions, as investigated and described in [3, 3].

2.2 Potentials of Additive Manufactured Heat Exchangers

AM of HXs and HX components by LPBF offers new possibilities. Flow guidance and structures are mainly free selectable, considering the design guidelines of AM using LPBF, described for example in [10, 14, 15]. These new degrees of freedom enable new approaches to solve or reduce the difficulties described at the end of the last section. Entirely new types of HXs could be developed, especially in the field of compact high-performance devices. In [6], for instance, a compact, CFD-optimised cooler for use by the *Formular Student* is presented.

In [9] many different basic geometries of inner flow guidance for AM HX are shown, visible on Fig. 4, as well as inlet and outlet geometries for example based on biometric structures. It provides a large set of those and design tools and approaches are given.

The use of complex, three-dimensional structures in HXs also represents a new approach. This includes a wide variety of lattice structures or surface functions, such as gyroids. In [5] additively manufactured HXs derived from conventional plate HXs are

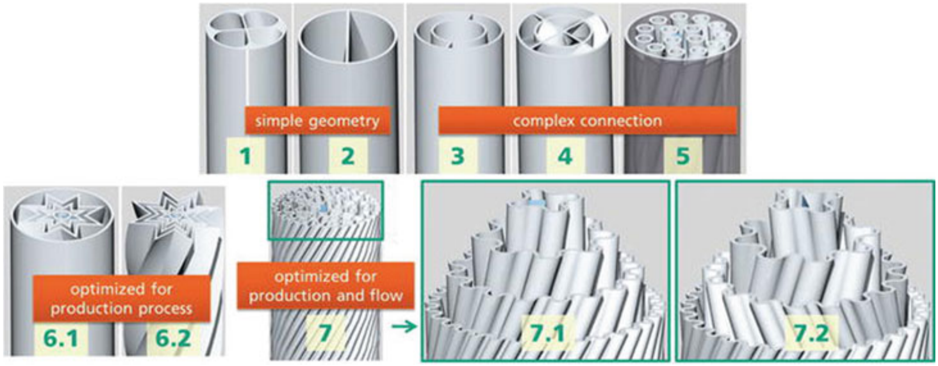

Fig. 4 Different inner flow guidance for HXs [9, Figure by R. Kordaß]

Fig. 5 Additively Manufactured HX with gyroid structure [5]

developed using such surface functions, which can be seen for example in Fig. 5. In the following section, the use of lattice structures to improve heat transfer is discussed in more detail.

Use of lattice structures for enhanced heat transfer

Wire meshes and foam structures have been used in conventional HXs for decades, even without AM. By increasing turbulence and surface area, heat transfer can be improved [16, 17]. Figure 6 shows Wire Mesh Inserts for shell and tube HXs tubes.

In conventional HXs these are retrofitted structures and therefore have limited thermal contact with the tube walls, which is disadvantageous regarding the thermal resistance. The use of such structures can also be applied and even used more efficiently by AM. On one hand, good thermal contact between the structure and other heat-conducting components of the HX is ensured, since the structure and other parts of the HX are the same component, on the other hand, the geometry, thickness and grading of the structure can

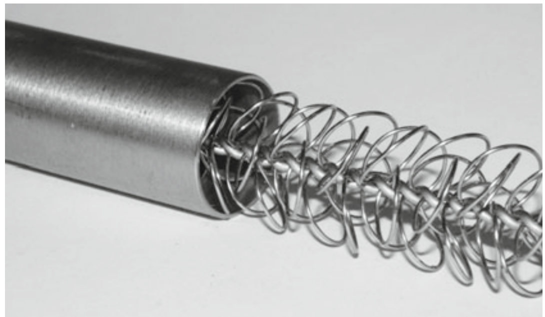

Fig. 6 hiTRAN® thermal systems technology, courtesy of CALGAVIN LTD

be selected almost free and optimised for special applications. Local change of structure, for example along the flow path, is possible to adapt to a change of fluid properties, for example in two phase flow. Ho et al. [7, 8] have already used various lattice structures consisting of polyhedrons instead of fins on the gas side of HXs, which resulted in an noticeable improvement of heat transfer. Compared to a fin-tube HX the lattice HX had a 2 times higher heat transfer coefficient.

3 Case Example: Design of a Gas Cooler for LPBF-Printing

Different approaches to use additive manufacturing for the improvement of HXs are presented in the previous section. Traditional designs of heat exchangers are often manufactured additively in modified form, for instance done in [5]. The aim for this case study is to use as many improvements offered by AM as possible to develop a new apparatus concept, which is not derived from any classical HX type. It describes the development of an additively manufactured gas cooler, which could, for instance, be used as an intercooler or for exhaust gases heat recovery. The water side of the HX is flow optimised regarding to pressure drop and distribution and is in its principle similar to the basic helical geometries presented in [9]. A conventional tube bundle HX serves as a reference component for the liquid side for CFD simulations. The gas side is filled with internal lattice structures to increase surface area and turbulence, which is also done in [7, 8]. The basic conceptual design of the apparatus as well as the improvements of heat transfer and pressure drop by using flow optimisation and lattice structures are discussed. CFD simulations are performed using the software *Ansys Fluent (2021 R1)*. At the end of the section, the AM of test geometries is described. The design restrictions for LPBF, as given in [10, 14, 15], were take into account, but are no further thematised.

3.1 Design Consideration for the Designed Heat Exchanger

In the following section, considerations, which were taken into account for the HX design are shown. The design is funded on known basics for aerodynamic design and the use of lattice structures in HXs. Prior to this section, it should be mentioned that both heat transfer and pressure loss or flow resistance typically increase with increasing turbulence of a flow, which can be seen in a large number of correlations, in [18] for instance. Following this logic, if considered uniformly for the whole apparatus, optimising the flow and reducing the pressure loss leads to a decrease in heat transfer. However, this conclusion is no longer straightforward if a closer look at the apparatus is taken. There are two reasons for this. Firstly, because heat transfer does not take place in all areas of the HX. If kinetic energy dissipates due to turbulence or frictional pressure losses in the collector and distributor areas, avoidable entropy generation occurs. Secondly, as already mentioned, a maldistribution can worsen the thermal performance of the apparatus. The goal therefore is to distribute the flow as smoothly and homogeneously as possible in the apparatus for the design point and partial load. It is important to generate the required turbulence, as well as the needed surface area, in the parts involved in the heat transfer, in this case by using lattice structures.

Flow-optimised Geometry and Flow Guidance

Flow-optimised geometries has already been a subject of intense research, for example in the aerodynamic optimisation of cars and aeroplanes [19]. The flow resistance of different body profiles depends on the direction of the flow and the shape of the body, as can be seen in the very generic Fig. 7. It is obvious that blunt edges, high cross-sectional changes and plates placed vertically in the flow cause high flow resistances and lead to turbulent stalls [20]. It is therefore advisable to avoid these structures and better use uniform flow

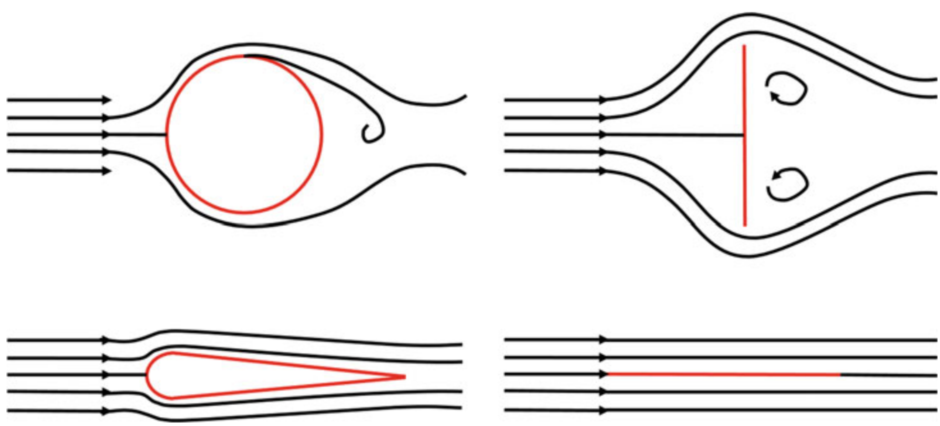

Fig. 7 Streamlines around profiles acc. to [20]

paths and continuous, slow cross-sectional changes, especially in the areas of collector and distributor section.

To evenly distribute the fluid in the HX, intelligent flow guidance can be designed, which should be more suitable than, for example, a vertical plate in the distributor and collector area of a conventional shell-and-tube HX. For this HX the undisturbed pipe flow, which should be circumferential symmetric at all flowrates, is already divided into the different channels. The distribution should therefore be even regarding the flowrate of each channel. In the collector area of the HX, the requirements are less complex; the flow should be guided out of the apparatus with as little loss of momentum as possible.

Use of Lattice Structures for Enhanced Heat Transfer

For the designed HX, the heat transfer should be enhanced further with a permissible increase in pressure loss, this can be achieved without increasing the volume of the apparatus. This is possible by adding an internal lattice structure to the HX. Generally individual lattice structures that can be adapted and graded in terms of geometry, mesh size and beam diameter are made possible by AM. Local properties can be adjusted to optimize the heat transfer for changing conditions along the apparatus. Due to the significantly lower heat transfer and pressure loss in gases compared to liquids, in this HX, the use of an internal structure is done for the gas side. The internal structures should be simulated and iterated for smaller reference elements using CFD simulations to estimating heat transfer and pressure loss, because a simulation of the whole, structured HX is not possible.

3.2 Conceptual Design of the Heat Exchanger

The size of the HX is determined by the available LPBF printers, an *EOS M280* and an *Aconity Midi+* with an *Aerosint Recoater*. The outer contour of the HX is a cylindrical body with a diameter of 93 mm and a length of 223 mm. Inside this cylinder, eight separate channels of a width of mainly 6 mm and a height of 43.5 mm are placed in a helical shape, in which the cooling water is flowing. The geometries used will be discussed in detail in the following section. The gas will flow in the space around these channels, which will be filled with a lattice structure. The HX can be operated in counterflow as well as cocurrent flow. The connecting pipes of the HX have an inner diameter of 30 mm. Figure 8 shows the transparent apparatus without the internal structure.

The HX should first be made of stainless steel, 1.4404. In order to estimate of the thermal performance, an inflow velocity of the hot gas (Air) of 18 m/s is assumed at a temperature of 400 °C, which is cooled down to 100 °C. For this case, a thermal power of about 2 kW can be assumed. In order to achieve a uniform flow with the lowest possible pressure drop, the given design recommendations described were used. The transitions between the 30 mm inlet tube to the full cross-section and the tapering to 30 mm at

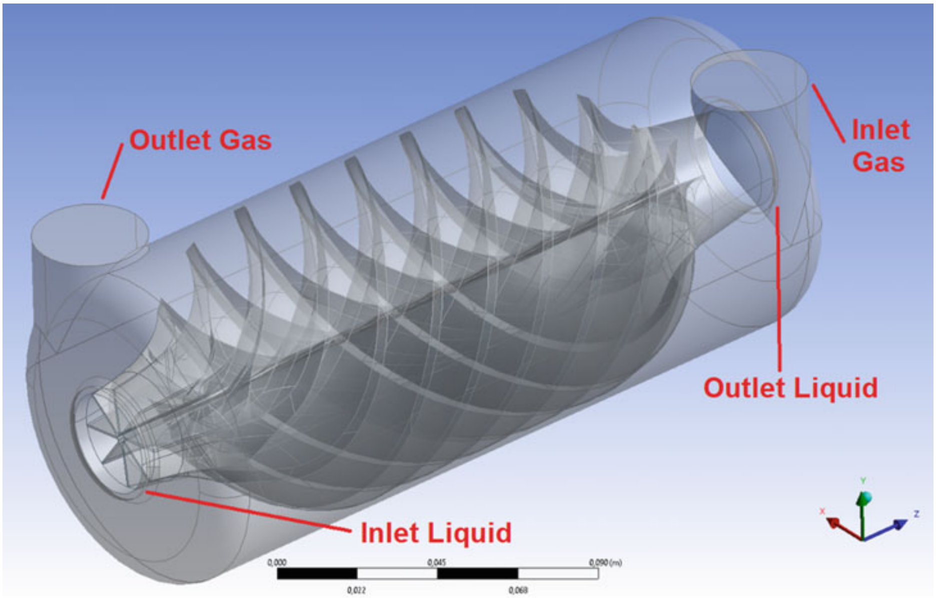

Fig. 8 Transparent HX (without structure on the gas side)

the outlet are continuous and without edges. The symmetrical pipe flow at the inlet is separated into the eight equivalent channels. Both are shown in Fig. 9.

The liquid distribution is aided by the helical type structure, since a distribution from the inside to the outside takes place due to the rotational movement resulting in a centrifugal force. Figure 10 shows the flow space of the liquid side of the flow-optimised

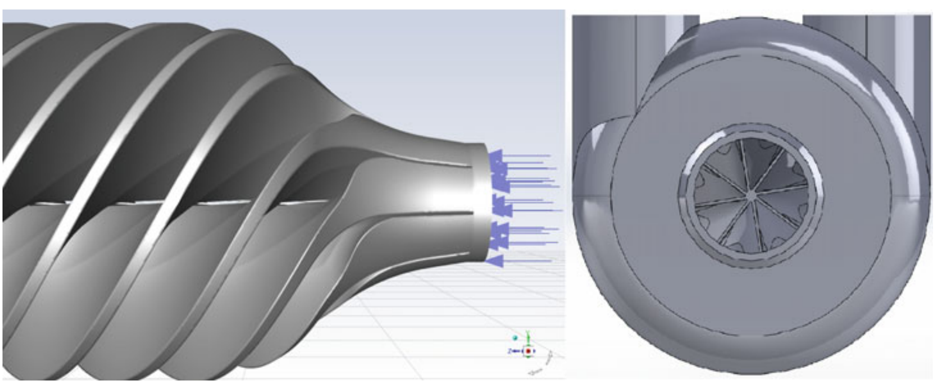

Fig. 9 Inlet area of the liquid (left) and view into the inlet tube with flow dividing ribs (right)

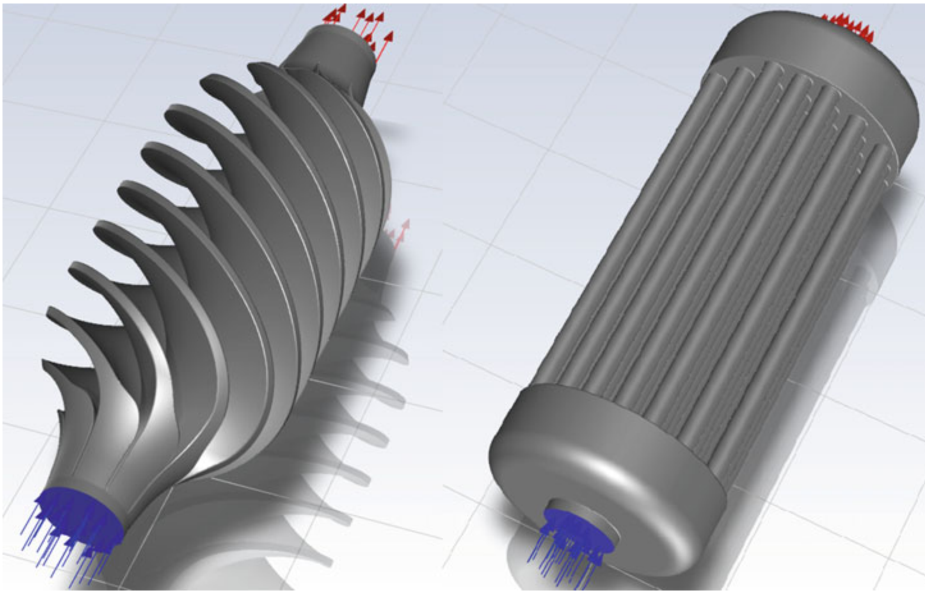

Fig. 10 Liquid flow volumes of the optimised HX (left) and the conventional tube bundle (right)

HX and a conventional tube bundle of the same size. In the following section, the flow through the AM HX and the tube bundle is simulated.

CFD Simulation of Flow and Pressure Loss

In order to determine the flow distribution and pressure loss of the geometries, an adiabatic simulation of the liquid side of the AM HX is created and compared with the tube bundle, which has the same surface area and outer geometry. Since the heat transfer on the water side is very likely sufficient to transfer the expected thermal power and the water heats up by less than 0.5 K at an inflow velocity of 2 m/s, an adiabatic simulation is permissible. The meshing of the fluid volumes of the AM HX and the reference tube bundle are generated with the settings listed in Table 1. Inflation layers were created in the areas close to the wall in order to properly represent the boundary layers. A partially cut through the meshing is shown in Fig. 11.

Table 1 Meshing settings liquid side

	Element size (mm)	Largest element size (mm)	Nodes AM HX	Nodes tube bundle
Standart meshing	0.6	3	6,467,165	4,528,150
Fine meshing	0.4	2	11,124,310	10,573,640

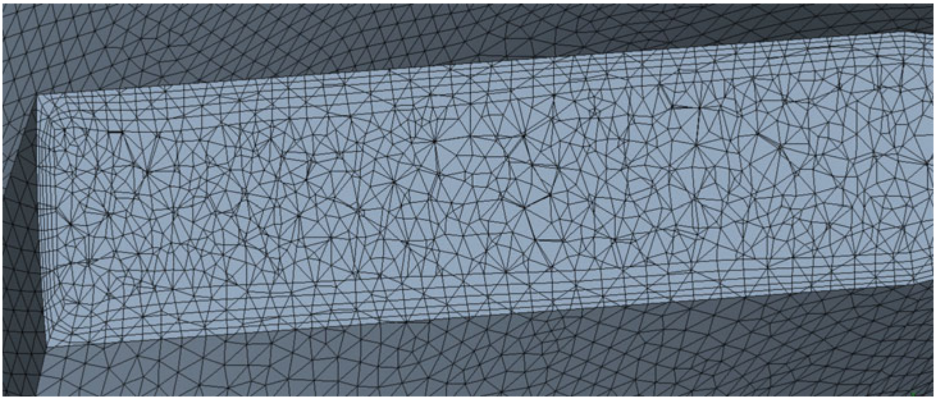

Fig. 11 Section through the mesh in a channel

The simulation is performed for an inflow velocity of 2 m/s of water at 20 °C. The k-omega-SST turbulence model was used. An investigation if the results are independent of the mesh sizing has taken place and can be confirmed. Since the continuity residuals did not converge sufficiently, transient simulations were also performed for both HXs to investigate whether there was a relevant time-dependent change in the viewed quantities, which can be negated.

For the steady-state simulations, the pressure losses and flow velocities listed in Table 2 were obtained. The optimised new geometry has a slightly lower pressure drop and a 59% higher average flow velocity, which should increase the heat transfer.

In addition to the pressure drop and the average flow velocity, the fluid distribution in the apparatus must also be investigated. This is done visually along and across the flow for both geometries. As seen in the plot of velocity magnitudes along the flow, Fig. 12, the fluid in the optimised HX is already well distributed after about 1/4 of the way through the channels. The uniform distribution is also visible in the middle cross-section of the apparatus, shown in Fig. 13 on the left. It is to be expected that also for partial loads the distribution of the total mass flux will be more or less equal. For the

Table 2 Pressure loss and mean flow velocity

	Pressure loss (Pa)	Mean flow velocity (m/s)
Conventional tube bundle	3457	0.76
AM heat exchanger	2935	1.21
	−15%	+59%

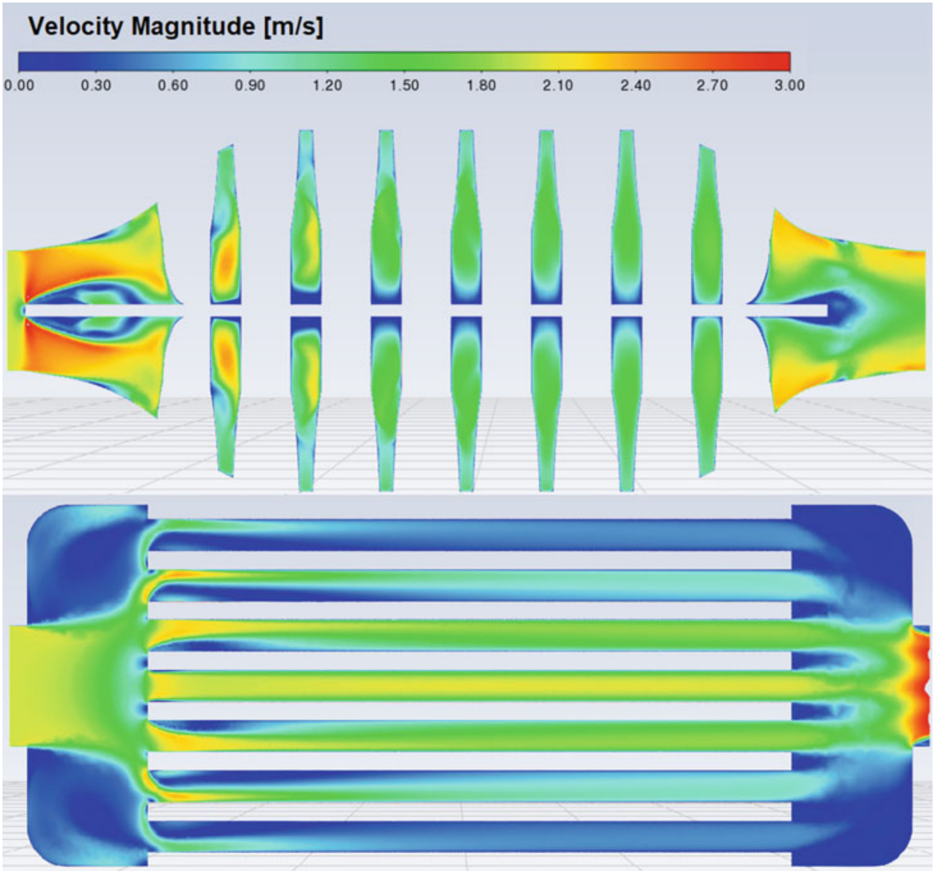

Fig. 12 Longitudinal section of the AM HX and the tube bundle

reference tube bundle, on the other hand, the maldistribution is clearly visible both in the section lengthwise through the apparatus and the cross-section. The flow velocity in the central tube rows is significantly higher and drops rapidly towards the outside.

3.3 Construction and Simulation of the Lattice Structure

The optimised HX described in the two previous sections should be filled with a lattice structure on the gas side. The improvement of the heat transfer through lattice structures is to be verified by a prior investigation. For this purpose, CFD simulations of a reference element with different beam thicknesses will be carried out.

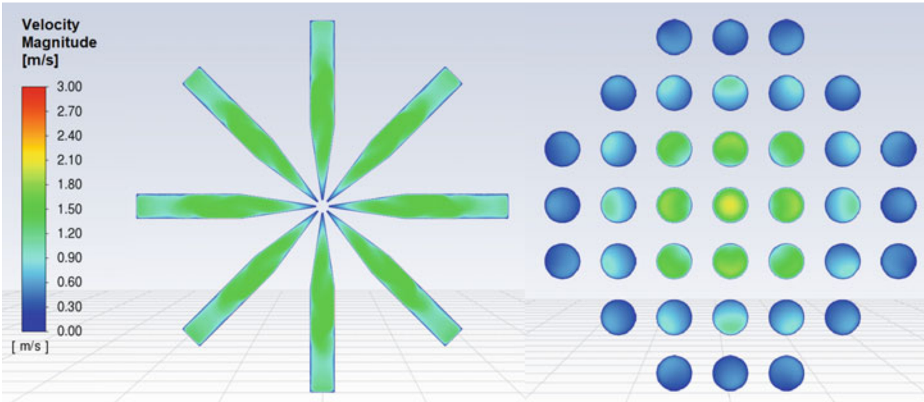

Fig. 13 Flow velocity in the middle flow cross-section

CFD Simulation of Heat Transfer and Flow of the Lattice Structure

This simulation should demonstrate the basic effect of the internal structures and determine a mesh size and beam thickness, which is generally suitable for the HX's targeted power of about 2 kW. The pressure loss should not become unacceptably high, a value of less than 5000 Pa is aimed for. The simulation is carried out for a 50 mm long reference element with a diameter of 25 mm, which is placed in a 100 mm long pipe section. The smooth 25 mm areas in front of and behind the structure serve as the inlet and outlet areas of the flow. Figure 14 shows a cut through the 3D model of a structure created for the simulation.

To generate the 3D models used in the simulation, the CAD Software tool *Creo Parametric* is used. Since polyhedron structures will be choosen in the HX, which are also used by Ho et al. [7, 8], the truncated octahedron element available in *Creo* is used for the simulation. Beam thicknesses of 1, 1.5 and 2 mm are simulated for a mesh size of

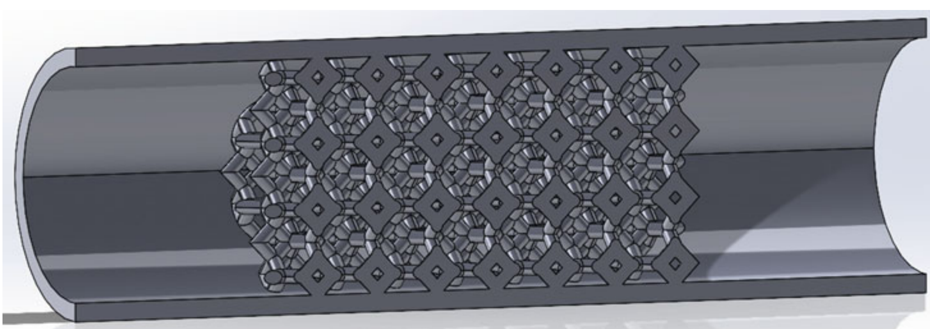

Fig. 14 Halved 3D for the CFD simulation

7 mm. The 7 mm mesh size was also studied in Hu et al. [8] for polyhedron structures and could possibly be used as a reference later. The simulation is performed for air at an inflow velocity of 5 m/s at 700 K. On the outside of the pipe, a convective heat transfer is set to model the water side with an assumed heat transfer coefficient of 1200 W/(m^2 K), which is set rather low and corresponds more to applications between free convection and slow flowing water, and a water temperature of 300 K [18, 21]. Since the material used for the first produced HX is to be stainless steel 1.4404, the thermal conductivity is given as 15 W/(m K) [22]. The air density is approximated as an ideal gas and other data is linearly interpolated between 300 and 700 K. The k-omega-SST turbulence model was used, but the influence of different models used has to be further elaborated. An investigation of the dependence of the results of the mesh sizing as well as occurring unsteady phenomena was checked and not observed. Inflation layers are generated to improve the near-wall boundary layers. Table 3 lists the meshing settings and Fig. 15 shows a longitudinal section through the meshing.

Figure 16 shows the temperature distribution in longitudinal section through the simulated structures. In Table 4 and Fig. 17, the heat flows and pressure losses are plotted. According to the results, significant improvement in heat transfer can be achieved by introducing an internal structure. Even for a beam diameter of 1 mm on half the tube length, the transferred heat increases by +187% without increasing the construction volume in any kind. It also results in an increase of pressure loss from 2 to 93 Pa, which

Table 3 Meshing settings of the lattice structure

	Element size (mm)	Largest element size (mm)	Nodes
Standart meshing	1	2	4,252,556
Fine meshing	0.7	1.4	4,387,726

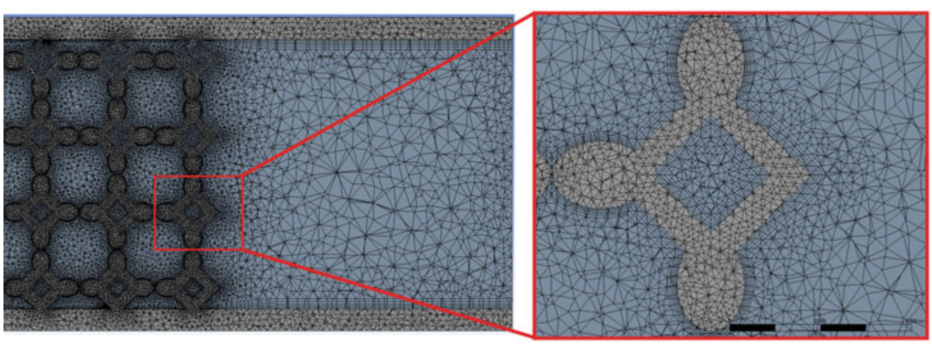

Fig. 15 Section through the meshing of a lattice structure

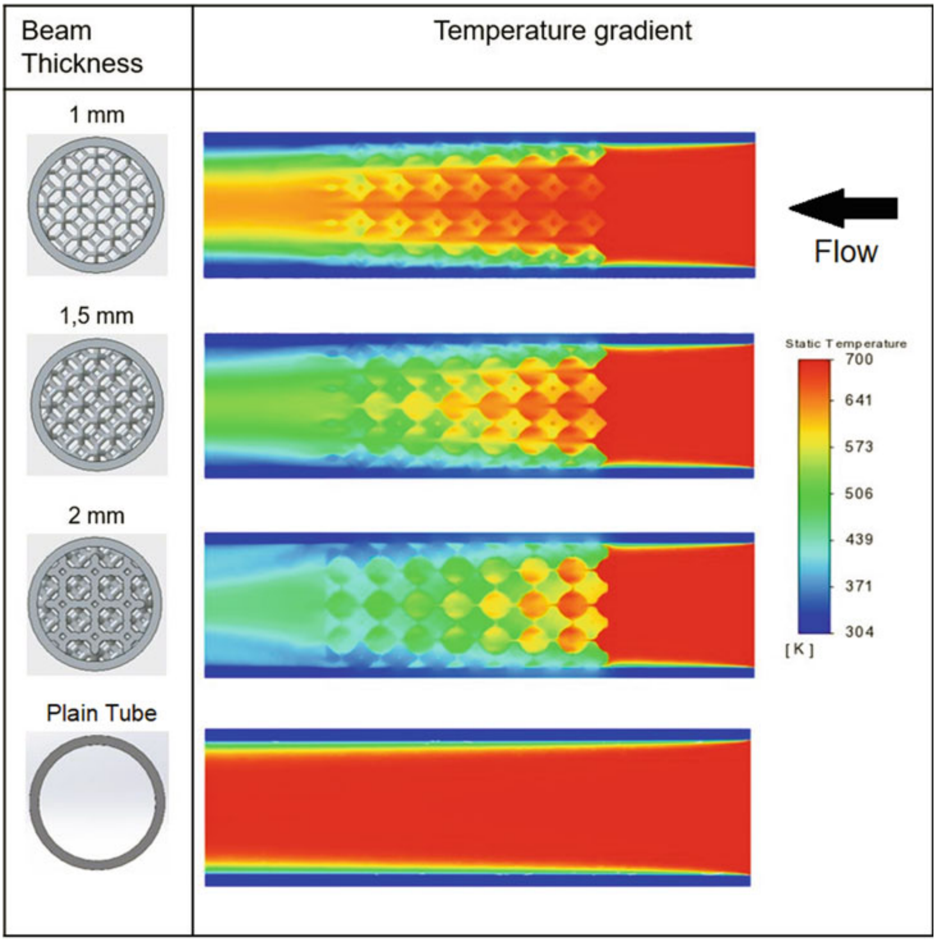

Fig. 16 Simulated temperature distribution in the structured and unstructured tubes

Table 4 Pressure loss and heat transfer of the simulated structures

	Heat flow (W)	Pressure loss (Pa)
Unstructured tube	87	2
1 mm	250	93
1.5 mm	319	227
2 mm	373	655

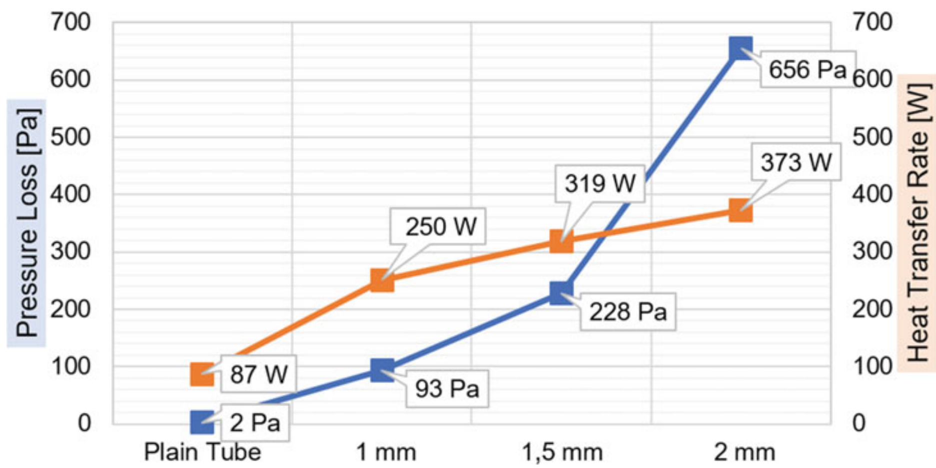

Fig. 17 Pressure loss and heat transfer of the simulated structures

is still a small value for most applications. If the beams are thickened further to 1.5 mm and 2 mm, the heat transfer improves by +266% and +328% respectively, whereby the pressure loss more than doubles and even increases sevenfold compared to the 1 mm structure.

The simulation can prove the volume-related efficiency using lattice structures. Considering this limited parameter study for the use of a polyhedron structure on the gas side of the HX, a beam thickness between 1 mm and 1.5 mm is reasonable for the mesh size of 7 mm. For 2 mm beam thickness the gain in thermal performance in relation to the increase of pressure loss is no longer within a reasonable range.

Generation of the Lattice Structure on the Gas Side of the HX

The lattice structure on the gas side of the HX is created using the software for additive manufacturing *Netfabb*, as this software is suitable for inserting it into complex internal shape of the HX. A polyhedron structure of the simulated mesh size is used. The gas side is a fully filled geometry in the CAD-model and is hollowed out. It has a wall thickness of 1.5 mm and is filled with an icosahedron-shaped polyhedron structure of a mesh size of 7 mm. In the distributor and collector areas, where the structure's function is less to enhance heat transfer and more to support the print and distribute the flow, the beam thickness is chosen to be 1 mm. In the heat exchanging areas between the water-filled channels, the thickness is set to 1.5 mm. Regarding the total pressure loss and heat transfer, it can be estimated with sufficient accuracy using the simulation results, that the concept apparatus pressure loss will be less than 5000 Pa and a thermal output of at least 2 kW will be maintained. A more precise estimation and measurement of these values will be necessary. Figure 18 shows a longitudinal section through the completely constructed HX.

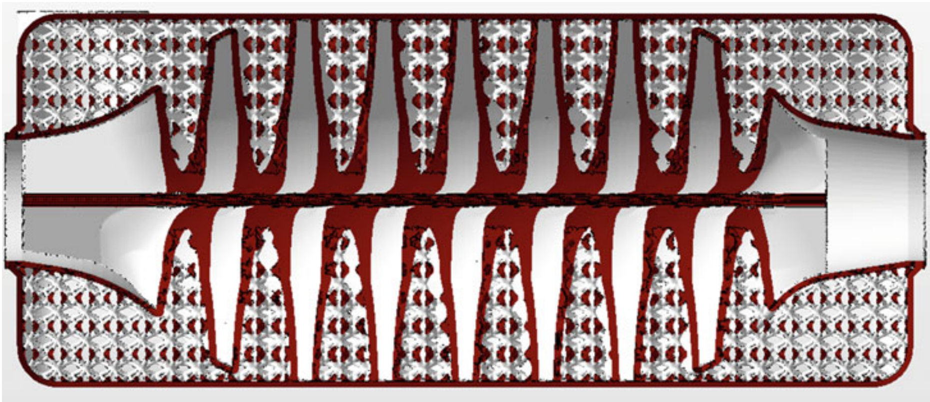

Fig. 18 Complete AM heat exchanger with inner lattice structure

3.4 Additive Manufacturing

Manufacturing of the entire HX has not yet taken place at this time. Printing on an LPBF printer made of 1.4404 is to be carried out. Smaller devices with and without internal structure were already printed. These devices are the ones shown in Fig. 19 as a 3D model.

They will be characterized experimentally in the future to validate the CFD simulations of the internal structures. Figure 20 (a) shows a complete apparatus printed in 1.2709 without internal structure, (b) a partially printed apparatus with internal structure and (c) a single cell of the structure.

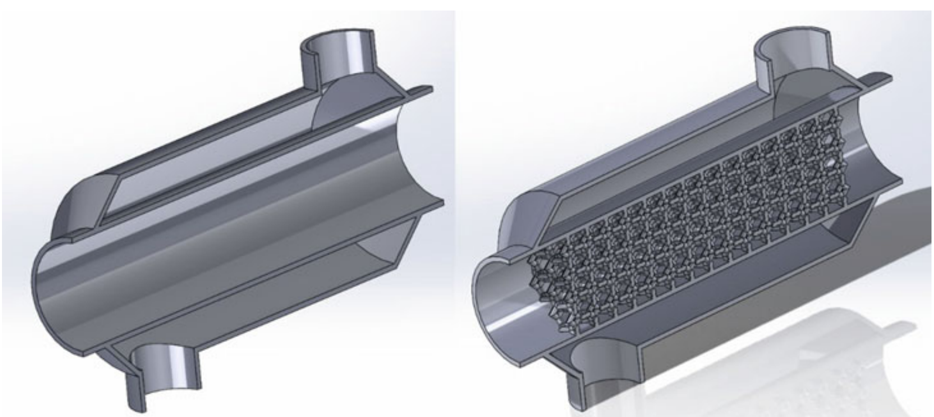

Fig. 19 HX with and without internal lattice structure

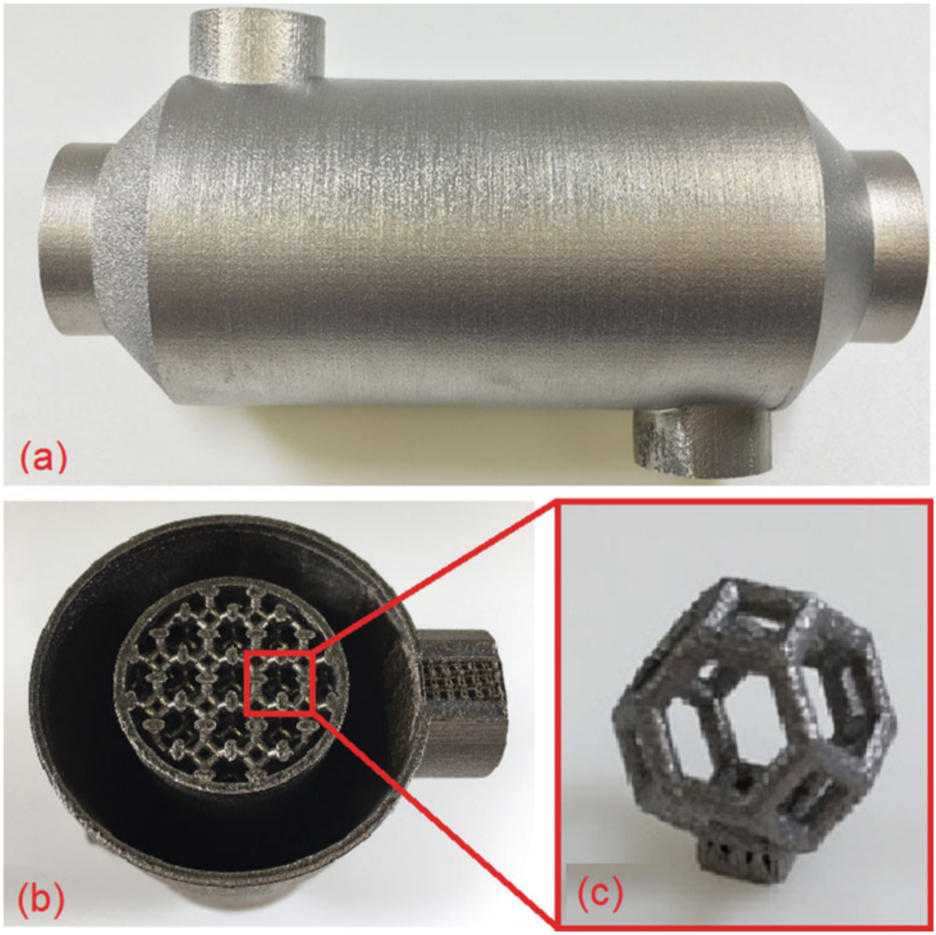

Fig. 20 LBPF-printed sample components made of 1.2709

4 Conclusion

This paper presents the development of a novel thermo-hydraulically optimised HX for LPBF printing. As a concept apparatus a gas cooler was developed. Design consideration for the flow optimised geometry and the use of lattice structures in additive manufactured HXs are shown. On the liquid side, CFD simulations showed an increase in flow velocity in the cross-section of 59% while a 15% reduction in pressure drop occurred compared to a conventional tube bundle of the same construction size. On the gas side, the apparatus was filled with lattice structure. A CFD simulation of a smaller reference element highlighted an enhancement in heat transfer by the use of lattice structures. In a limited parameter study, the use of polyhedron structure with beam thicknesses of 1 mm on half a tubes length already increased the heat transfer by 187% compared to a plain tube. Smaller internally structured HXs could already be printed. Overall, the high potential in AM of HXs mentioned at the beginning could be demonstrated again and was developed further.

The first printing of the designed HX made of 1.4404 is targeted for the near future. Heat transfer and pressure drop should be characterized by measurements. In the progress of this project, some described procedures must be further elaborated, especially a general methodical approach for additively manufactured HXs should be developed. The simulations must be validated experimentally and refined regarding to exactly fitting boundary conditions. For the lattice structures, the validation shall be done by measuring different structures in the coaxial tube HX. Extensive investigations of heat transfer and pressure drop in lattice structures will be carried out by simulations as well as by experiments. This way it should be possible to provide additively manufactured HXs with application-optimised internal structures in the future with optimised geometry, mesh and beam size as well as material with possible local property adjustments.

Acknowledgements Funded by the Ministry for Science and Culture of Lower Saxony (MWK) – School for Additive Manufacturing SAM

References

1. Skop, H., & Chudnovsky, Y. (2018). Energy efficiency and advanced heat recovery technologies. In *Handbook of thermal science and engineering*. Springer Viewig. https://doi.org/10.1007/978-3-319-26695-4
2. Chudnovsky, Y., & Sekulic, D. P. (2018). Introduction and classification of heat transfer equipment. In *Handbook of thermal science and engineering*. Springer Viewig. https://doi.org/10.1007/978-3-319-26695-4
3. Wen, J., Li, Y., Zhou, A., & Zhang, K. (2006). An experimental investigation of entrance configurationon flow maldistribution in plate-fin heat exchanger. *International Journal of Heat and Mass Transfer, 49*. https://doi.org/10.1016/j.ijheatmasstransfer.2005.10.029
4. Bobbilli, P., Sundena, B., & Dasb, S. K. (2006). An experimental investigation of the port flow maldistribution in small and large plate package. *Heat Exchangers, Applied Thermal Engineering, 26*(16). *Elsevier*. https://doi.org/10.1016/j.applthermaleng.2006.01.015
5. Kim, J., & Yoo, D. (2020). 3D printed compact heat exchangers with mathematically defined core structures. *Journal of Computational Design and Engineering*. https://doi.org/10.1093/jcde/qwaa032
6. Neugebauer, R., Müller, B., Gebauer, M., & Töppel, T. (2018). *Additive manufacturing boosts efficiency of heat transfer components*. Fraunhofer-Institute for Machine Tools and Forming Technology, Chemnitz, Germany. https://doi.org/10.1108/01445151111172925

7. Ho, J. Y., Leong, K. C., & Wong, T. N. (2020). Additive-manufactured metallic porous lattice heat exchangers for air-side heat transfer enhancement air-side heat transfer enhancement. *International Journal of Heat and Mass Transfer, 150. Elsevier*. https://doi.org/10.1016/j.ijheatmasstransfer.2019.119262
8. Ho, J. Y., Leong, K. C., & Wong, T. N. (2019). Experimental and numerical investigation of forced convection heat transfer in porous lattice structures produced by selective laser melting. *International Journal of Thermal Sciences, 137. Elsevier*. https://doi.org/10.1016/j.ijthermalsci.2018.11.022
9. Scheithauer, U., Kordaß, R., Noack, K., Eichenauer, M. F., Hartmann, M., Abel, J., Ganzer, G., & Lordick, D. (2018). *Potentials and challenges of additive manufacturing technologies for heat exchanger*. Fraunhofer IKTS, Fraunhofer, IWU,. https://doi.org/10.5772/intechopen.80010
10. Lachmayer, R., & Lippert, R. B. (2020). *Entwicklungsmethodik für die additive Fertigung*. Springer Viewig. https://doi.org/10.1007/978-3-662-59789-7
11. Lachmayer, R., Gembarski, P. C., Gottwald, P., & Lippert, R. B. (2017). The potential of product customization using technologies of additive manufacturing. In *Managing complexity* (pp. 71–81). Springer. https://doi.org/10.1007/978-3-319-29058-4
12. Mehendale, S. S. (2018). Single-phase heat exhangers. In *Handbook of thermal science and engineering*. Springer Viewig. https://doi.org/10.1007/978-3-319-26695-4.
13. Cengel, Y., Turner, R., & Cimbala, J. (2017). *Fundamentals of thermal fluid sciences* (5th ed.). McGraw-Hill.
14. Lippert, R. B. (2018). *Restriktionsgerechtes Gestalten gewichtsoptimierter Strukturbauteile für das Selektive Laserstrahlschmelzen, TEWISS*. Dissertation, Garbsen. https://doi.org/10.15488/3489
15. Lachmayer, R., & Ehlers, T. (2021). 16.13 *Gestaltung für Additive Fertigung in Pahl/Beitz Konstruktionslehre*. Springer Vieweg. https://doi.org/10.1007/978-3-662-57303-7_16
16. Sekulic, D. P. (2018). Compact heat exchangers. In *Handbook of thermal science and engineering*. Springer Vieweg. https://doi.org/10.1007/978-3-319-26695-4
17. Drögemüller, P. (2014). The use of hiTRAN wire matrix elements to improve the thermal efficiency of tubular heat exchangers in single and two-phase flow. *Chemie Ingenieur Technik*, Wiley,. https://doi.org/10.1002/cite.201400081
18. Stephan, P., Kabelac, S., Kind, M., Mewes, D., Schaber, K., & Wetzel, T. (2019). *VDI-Wärmeatlas*. Springer Vieweg, Berlin. https://doi.org/10.1007/978-3-662-52989-8
19. Kaushik, M. (2018). *The standard atmosphere in theoretical and experimental aerodynamics*. Springer Viewig.
20. von Böckh, P., & Saumweber, C. (2013). *Fluidmechanik*. Springer Vieweg. https://doi.org/10.1007/978-3-642-33892-2
21. Gnielinski, V. (2021). *G2 Wärmeübertragung bei erzwungener Konvektion: Konzentrischer Ringspalt und ebener Spalt in VDI-Wärmeatlas*. Springer Vieweg, Berlin,. https://doi.org/10.1007/978-3-662-52989-8
22. SLM Solutions Group AG: Materialdatenblatt Fe-Alloy 316L (1.4404), SLM Solutions Group AG, Lübeck

Systematic Investigations Concerning Eddy Currents in Additively Manufactured Structures

M. Haase and D. Zimmer

Abstract

Based on layer-by-layer component generation, AM offers immense freedom in terms of design and material capabilities that cannot be achieved by conventional manufacturing. AM also provides potential for guiding and influencing the electromagnetic flux. The manufacturing process allows to realize a three-dimensional iron circuit design. Air gaps or powder cavities can be specifically placed in components to minimize the circulation paths of the induced voltage and thus the resulting eddy currents. In this investigation, additively manufactured toroidal cores are tested on a self-developed testing rig with regard to the resulting magnetization losses. For the toroidal cores, an iron-silicon alloy (FeSi3%) is used under the Laser Beam Melting process (LBM). The results provide a comparison of the specific power losses between solid and thin-walled structures of the iron cross-section.

Keywords

Additive manufacturing • Electromagnetism • Eddy currents

M. Haase (✉) · D. Zimmer
Chair of Design and Drive Technology, Paderborn University, 33098 Paderborn, Germany
e-mail: michael.haase@upb.de

Direct Manufacturing Research Center/Paderborn Institute for Additive Fabrication, Paderborn University, 33098 Paderborn, Germany

R. Lachmayer et al. (eds.), *Innovative Product Development by Additive Manufacturing 2021*, https://doi.org/10.1007/978-3-031-05918-6_10

1 Introduction

Additive Manufacturing (AM), which is mostly characterized by the layer-by-layer manufacturing of components, offers many possibilities and advantages. In addition to the elimination of product-specific tools and preparations, a wide variety of structures and shapes can be manufactured. For these reasons, AM is increasingly coming into focus in industry. Due to the increasing complexity and the increased requirements for new products, its use becomes more necessary [1]. Therefore, different approaches to exploit the benefits are currently being explored. One of them focuses the area of electromagnetism. Here, eddy currents within additively manufactured toroidal cores are to be reduced by suitable cross-sectional structures. Initial investigations showed promising results. However, this topic needs to be investigated more in detail [2, 3].

Electromagnetic coils are often used in technical systems. They are always coupled with a current and a resulting magnetic flux. If an electrically conductive material is inserted into a time-varying magnetic field or is set in motion in a constant field, a current arises as a result of the induced voltage [4, 5]. These currents are called eddy currents. To reduce the eddy currents, it is necessary to divide the solid geometry of an iron circuit into cross-sections that are as small as possible and electrically insulated from each other. This is where conventional manufacturing processes reach their limits. AM processes, on contrast, allow a three-dimensional cross-sectional division due to the given design freedom. It is thus conceivable to minimize the circulation paths of the induced current by changing the cross-section design.

In this investigation, different designs of AM cores are compared regarding their electrical losses for the targeted reduction of eddy currents. The results are demonstrated on basis of simple toroidal test specimens. These are manufactured using Laser Beam Melting (LBM). The primary aim of this investigation is the reduction of electrical losses that occur as a result of eddy currents by developing suitable cross-sectional structures for AM.

2 State of the Art

2.1 Eddy Currents

When an AC voltage is applied to a coil with an iron core, losses occur that are generally mapped to remagnetization losses. These are composed of eddy current, hysteresis, excess and residual losses [6]. Since eddy current losses are of particular importance in this investigation, they are described more in detail in the following. In general, eddy currents are electric currents that are spatially generated in electrically conductive materials as a result of a change in the magnetic field. Here, eddy currents have closed current lines, similar to the magnetic field, which explains the concept of the vortex from the field theory [7]. The law of induction is valid for all electrically conducting materials. For example, if a metal plate is perpendicularly penetrated by an alternating magnetic field, the law of induction states that a vortex field with field strength *Ei* is induced around the magnetic field lines in the metal. Accordingly, the moving charges form a current flow called an eddy current. Eddy currents occur when two fundamental conditions are met. Firstly, they only form in electrically conductive materials. Secondly, eddy currents can only be generated if a change in the magnetic flux density *B* is happening. There are two possibilities for the required magnetic field change. Either the magnetic field is a time-varying field generated by alternating current (rest induction) or the electrically conducting material is moved relative to a constant magnetic field (motion induction). Motion induction is mainly used in eddy current brakes. Here, eddy currents are an active component required for the brake to work. However, this is not the case in most electrical engineering applications. In the present case, eddy currents are undesirable side effects that should be reduced. Affected are transformers as well as AC or DC machines, where eddy currents reduce the efficiency. In a transformer, eddy currents are formed in the iron core due to the time-varying magnetic flux with undesirable heat losses. To keep these losses as low as possible, the electrical resistance of the iron core in the current paths should be as high as possible. This is currently achieved by interrupting the current paths of the eddy current with insulating intermediate layers. To achieve this, the iron core is replaced with 0.1–0.3 mm thick iron sheets, which have an insulation of lacquer on one side. Furthermore, it is possible to hinder eddy currents by using powder core material or ferrites as iron core material. Ferrites are electrically non-conductive ferromagnetic materials, while powder core materials are, for example, iron powder embedded in synthetic resin with high specific electrical resistance. Eddy currents are self-contained electric currents, which is why they also form a magnetic field equal to that of a current-carrying conductor. This can be described very well by the skin effect [7], which is an effect of field displacement in the magnetic conductor. It describes the inhomogeneous current density distribution in a conductor, which is generated by alternating current flowing in the conductor itself. The current is displaced to the surface of the conductor and flows through a thin layer, while the interior of the conductor remains current-free. This is especially the case in the high-frequency range [8].

3 Derivation of Suitable Geometric Structures for Eddy Current Reduction

3.1 Purpose of the Investigation

The aim is to develop suitable cross-sectional AM-structures to reduce eddy currents in iron circuits—similar to conventionally laminated components. By combining the advantages of AM, such as functional integration and lightweight construction potential, new concepts for electric motors could be developed using freely designable stators. This would enable a stator design which allows to integrate housing functions such as cooling structures, bearing- and screw connection points in order to reduce the number of components and thus the total weight of the motor. Since, according to Adam [9], certain manufacturing restrictions have to be considered in the LBM process, at first fundamental investigations are necessary with regard to relevant design measures for reducing eddy currents, which should demonstrate the feasibility of the project.

Further on, experimental investigations are planned to determine the influences with regard to eddy current losses. The test rig setup is based on DIN EN 60404-6 [10], which describes the methods for recording magnetic properties in an alternating field on a toroidal test specimen.

3.2 Methodical Implementation

The step-by-step procedure of the method to derive suitable structures is presented below.

Step 1: Determination of target values:

The aim is the generation and investigation of geometrical structures, which cause influences on the magnetic properties, especially the eddy currents. Therefore, in addition to the hysteresis curves, the resulting specific power losses are defined as target values of the investigations.

Step 2: Identification of factors affecting remagnetization:

To understand which factors can be changed to reduce remagnetization losses in additively manufactured structures, it is first necessary to consider the associated physical laws. As mentioned, the remagnetization losses can be divide in hysteresis, eddy current and the excess or residual losses. The hysteresis losses can be described by

$$p_{hyst} \approx k_H \cdot \frac{4 \cdot H_C}{\rho} \cdot B_{\max} \cdot f \tag{1}$$

These losses result from the work necessary to shift the Weiss domains [11, 12]. The loss component is proportional to the area of the hysteresis loop in the B-H diagram. Thus, these losses depend essentially on the material and the maximum induction.

The eddy current losses, which are caused by eddy currents in the iron core or in the sheet edges of a laminated core, can be calculated directly from the material data and the geometry using the approach of the classical Maxwell equation.

$$p_w = \frac{\pi^2 \cdot \sigma \cdot d^2}{6 \cdot \rho} \cdot B_{\max} \cdot f \tag{2}$$

In addition to the electrical conductivity and the maximum induction, the eddy current losses are also dependent on the conventionally used sheet thickness of the iron circuit. Thus, a geometric factor is given, which can be changed constructively in an additively manufactured component. This formula is designed according to Maxwell's equation for iron circles with current flowing through them parallel to the direction of the sheet metal. This approach does not consider the current displacement that occurs, since conventionally the sheet thicknesses are usually so small that the effect is negligible. In the case that

$$\frac{f}{Hz} = \frac{d^2}{[mm^2]} > 70 \tag{3}$$

is exceeded, the current displacement effect must also be considered. Since the eddy current losses are caused by induction currents in the coil core, the electrical conductivity of the material and the sheet thickness are decisive. For additive components, this means that the current displacement effect must be considered with increasing frequency, since manufacturing sheet thicknesses below 0.3 mm are currently not producible using the LBM process. As a result, at high frequencies only the structures on the surface are relevant for the eddy current losses. The excess loss was first described by Bertotti [11] and can be attributed to the magnetic domain structure of the material with sliding Bloch walls. Since the Bloch walls cannot be displaced without resistance during magnetization, additional energy is required. This loss fraction depends a lot on the microscopic structure and the distribution of the magnetizable domains in the material.

$$p_{exc} = \frac{c}{\rho} B_{\max}^{1,5} f^{1,5} \tag{4}$$

The last loss fraction covers the time lag of the induction behind a preceding field change. At high flux densities, this loss component is quite small compared to the three components described above, so it is neglected in the following.

Thus, the eddy current losses are the only ones that can be reduced by design adjustments. All other effects depend on the material and are not considered in this context. Nevertheless, AM offers the possibility of processing materials that cannot be processed using conventional methods. In addition, a distinction must be made as to whether a change in the entire cross-sectional structure is necessary or whether only an adaptation in the outer edge areas is sufficient [6, 11].

Legend:

p_W:	Eddy current losses	ρ:	Density
σ:	Electrical conductivity of the sheet	$B_{\max}$:	Max. flux density
f:	Frequency	d:	Sheet thickness
p_{hyst}:	Hysteresis losses	k_H:	A form factor near 1
H_C:	Coercivity	C:	A material-specific value
p_{exc}:	Excess losses		

Step 3: Selection of relevant influencing factors from a geometric point of view:

Subsequently, the most important geometric influencing factors are selected. Within this investigation, only the change of an entire cross-sectional structure is considered. The possibility of changing only partial areas of a specimen in order to consider border areas or core areas separately is not considered in this study.

Step 4: Definition of subfunctions for selected influencing factor:

Subfunctions are defined for the selected factor to be able to investigate the sensitivity of individual design parameters of the factor. The idea regarding this classification was to find design parameters which can be varied in investigations in order to find an optimum concerning loss reduction. A decisive point of view was to divide the cross-sections into smallest possible segments in order to reduce the circulating paths of the eddy currents and thus to reduce the losses. These segments must also be fixed to each other in order to realize a single component. Which medium is located between the solid structures has an additional influence on how the eddy currents can propagate in the overall system. So, the overall function "Reduction of eddy current losses by changing cross-section structures" resulted in the three sub-functions "dividing cross-sections", "fixing cross-sections to each other" and "electrically insulating cross-sections to each other". The functional hierarchy derived from this is shown in Fig. 1.

As can be seen, different possibilities exist for dividing the iron cross-section into several smaller structures. Further on, it is possible to divide it into thin-walled structures or to fill them with unit cells. It is also conceivable to divide the cross-section with varying geometry and arrangement as presented in Fig. 2. The counterpart of this variant is the insertion of cavities with varying geometry and arrangement.

The sub-function "fixing cross-sections to each other" can be broken down into three relevant sub-functions. In the first step, a fixation element must be selected to fix the previously divided cross-section structures to each other. Then, the positions where the

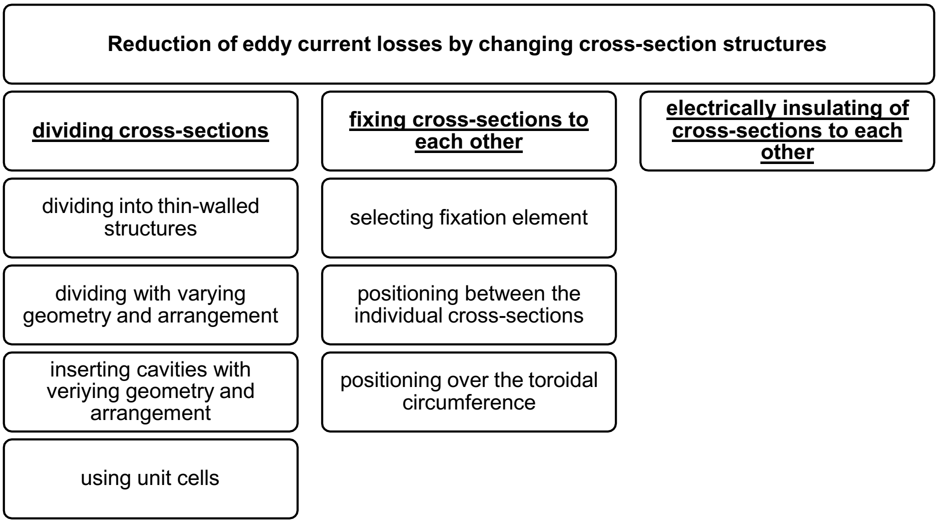

Fig. 1 Functional hierarchy of the cross-sectional structures for the toroidal test specimens

sub-function \ active principle		AP1	AP2
Dividing cross-sections	Division into thin-walled structures	vertical 	horizontal 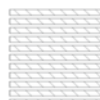
	Division with varying geometry and arrangement	square - symmetrical 	circular - symetrical 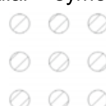
	Insertion of cavities with varying geometry and arrangement	square - symmetrical 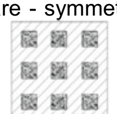	circular - symetrical 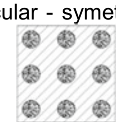
	Use of unit cells	BCC 	F2BCC 

Fig. 2 Excerpt of active principles for the defined sub-function dividing cross-section

individual cross-sections are to be fixed must be determined. Finally, it must be determined how often and in which arrangement this fixation is to be distributed over the entire toroidal circumference.

The last sub-function "electrically insulating cross-sections" results from the selected cross-section and its connecting element. Due to the structural design, it is possible to design areas with powder cavities or with air gaps. In the case of air gaps, filling with an insulating resin would be possible in the post-process, which would also mechanically reinforce the structure.

Figure 2 shows examples of geometric solutions for the above-mentioned subfunctions. As shown, the cross-sections can be divided into four different structures and arrangements. There are several solutions for each cross-section division. On the one hand, the toroidal cross-section can be divided into thin-walled structures, which can be arranged vertically or horizontally. On the other hand, the division of the cross-section with varying geometry and arrangement is possible. For example, the cross-section can be divided squarely and arranged symmetrically. In addition, cavities can be integrated into the cross-section. Hereby varying geometries and arrangements (e.g. square-symmetrical, square-offset) can be realized as well. Furthermore, it is conceivable to divide the cross-section into unit cells.

Step 5: Design and classification of test specimens:

The dimensions of the toroidal test specimens that are used for the experimental investigations are based on DIN EN IEC 60404-6 and are shown in Fig. 3.

After evaluating the geometry of the individual subfunctions, the most promising results can be combined to form active structures which ultimately define the shape of the toroidal cross-sections. For this purpose, combinations of the three subfunctions from Fig. 1 are formed. The procedure is explained by means of an example shown in Fig. 4.

In the first step, one of the cross-section divisions is selected. In the example, this is the division "Thin-walled structure in vertical direction". Then, for the sub-function

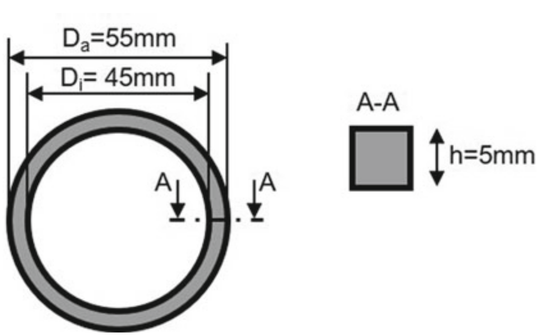

Fig. 3 Geometric envelope dimension of the toroidal test specimens to be examined

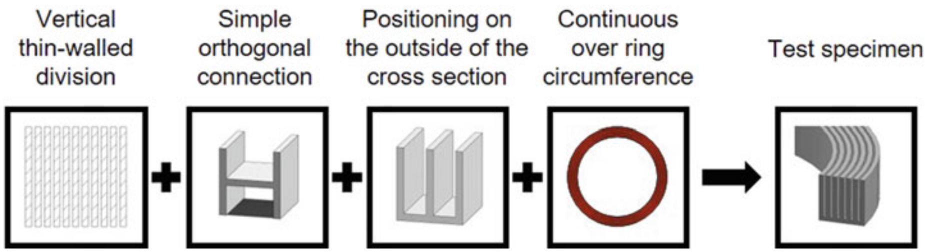

Fig. 4 Procedure for the creation of an active structure

"fixing cross-sections to each other", a suitable geometry must be selected for each sub-function. As shown in Fig. 4, the single-sided, simple orthogonal bar fixation is selected as the fixing principle, which follows the entire circumference of the toroidal. As a result, the illustrated toroidal cross-section is obtained, which will be designated in the further course with the number 1.1.1. For the sub-function "electrically insulating cross-sections to each other", air is used due to the design, since no external material is added in the post-process. This procedure can be performed for a variety of other cross-section divisions, connectors, and isolations. The cross-sections considered in this investigation are shown in Fig. 5.

Step 6: Definition of measurement method
The setup of the test rig used for the investigation of the toroidal specimens is shown in Fig. 6. The main components of the test rig are:

Toroidal core: This is wound with a primary N1 winding and a secondary N2 winding and has a square cross-section. The number of turns is 200 in each case.

Amplifier: The linear power amplifier BAA 1000 BEAK amplifies the introduced control signal in such a way that a sinusoidal current signal with a form factor of 1.11 is output at the terminal. In addition, the current signal is output in parallel via a monitor output for data backup and progress display.

NI-cRIO: The system from National Instruments is used for recording as well as for analog and digital output signals. In this case, the current waveform running in the primary winding, the induced voltage in the secondary winding and alternatively the capacitor voltage are recorded. The simultaneous recording of all measurement data must be ensured.

PC: This is used for process control by specifying frequencies and current amplitudes. Furthermore, the measurement data acquired via the cRIO system are displayed and saved.

The solid lines in the diagram indicate the currents and voltages which are conducted from the amplifier to the coil in the primary circuit and to the voltage pickup module

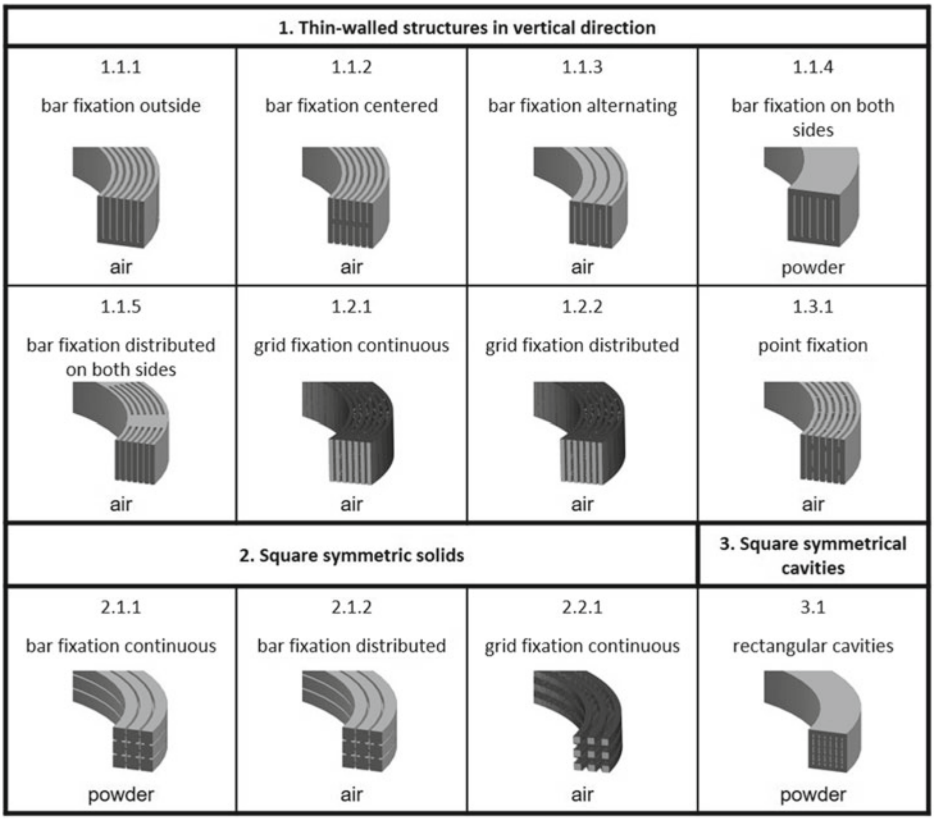

Fig. 5 Considered active structures of this investigation

in the secondary circuit. The dashed lines represent the analog measurement signal lines. The dotted lines indicate the digital communication between the cRIO system and the PC.

The measurement procedure is carried out in the following steps: First, a starting frequency must be defined. As a rule, a frequency of 50 Hz is started with, since this is usual for the measurement of conventional sheet metal, which is due to the frequency of the main voltages [5]. Then the first measuring cycle starts. The current is automatically increased until the starting value of the flux density at the secondary winding defined at the beginning is reached. As a rule, this is started at 0.2 T (T). The current curve looks as follows: According to the EN 60404-6 standard, a distinction can be made between two forms of progression. In one case, a sinusoidal current is introduced into the primary winding, whereas in the second case, an adjusted signal waveform is introduced into the primary winding, resulting in a sinusoidal voltage waveform at the output of the secondary winding. Usually, the second case is preferred for comparability. However,

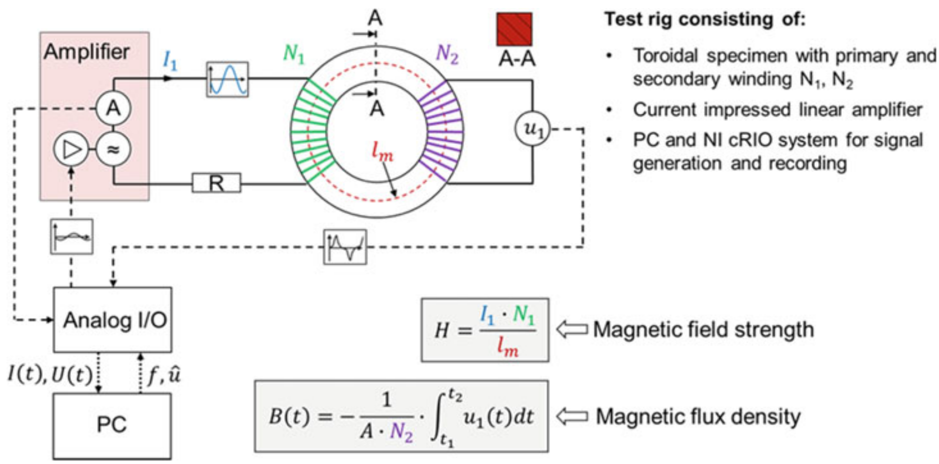

Fig. 6 Test rig setup for the examination of the toroidal test specimens

this is coupled with a complex control which was neglected for the preliminary investigations of this method development. For the long-term goal, this has to be adapted to allow a comparison with respect to conventional laminations. The voltage of the primary coil adapts according to the impedance. The voltage of the secondary coil as well as the voltage and current of the primary coil are saved for a few periods by of the measuring system. After saving data, the current is increased again until the next defined value of the flux density is reached. Depending on how accurate the commutation curve is to be, jumps in flux density of 0.05–0.2 T are usually selected. This process is repeated steadily up to the flux density of 1.5 T. The measurement cycles are then repeated for further frequencies. Usually, the first cycle is followed by the frequency of 100 Hz and is then steadily increased by 100 Hz. As the frequency increases, the remagnetization losses increase, leading to increasing current amplitudes. These reach their maximum at a certain frequency. Accordingly, the current to be introduced is the limiting factor within this measurement.

3.3 Experimental Investigation

The measurement was performed for each of the toroidal test specimens (Fig. 5) and a solid toroid at the flux densities from 0.2 to 1.5 T and frequencies of 50, 100, 200 and 300 Hz. In the context of this investigation, the hysteresis curves and the iron losses over the different frequencies are of primary importance. It is usual to state the specific power loss $P_{v,spec}$ in W/kg [5].

$$P_{v,spez} = \frac{w_{v,spez} \cdot f}{\rho} \quad (5)$$

Legend:

$P_{v,spez}$:	Specific power loss	ρ:	Density
$W_{v,spez}$:	Specific loss energy	f:	frequency

The massive toroidal test specimen is used as a starting point. For this purpose, the hysteresis curve at the power frequency of 50 Hz and a flux density of 1.5 T as well as the specific power loss over the frequencies 50, 100, 200 and 300 Hz are described. Figure 7 shows the hysteresis curve of the solid toroidal core, which was additively manufactured from an iron-silicon alloy.

The flux density B in Tesla is plotted on the abscissa and the field strength H in amperes per meter on the ordinate. It can be seen that the solid toroidal core has not yet reached saturation at a flux density of 1.5 T. This is evident from the fact that the curve flattens out with increasing flux density, but is not yet parallel to the ordinate, which would indicate saturation. In addition, the hysteresis curve of the solid toroidal test specimen is very broad, as expected, and thus exhibits high coercive field strengths, which can be attributed to the remagnetization losses. The conversion of the loss energy to the specific power loss allows to compare the specimens with regard to different densities. Figure 8

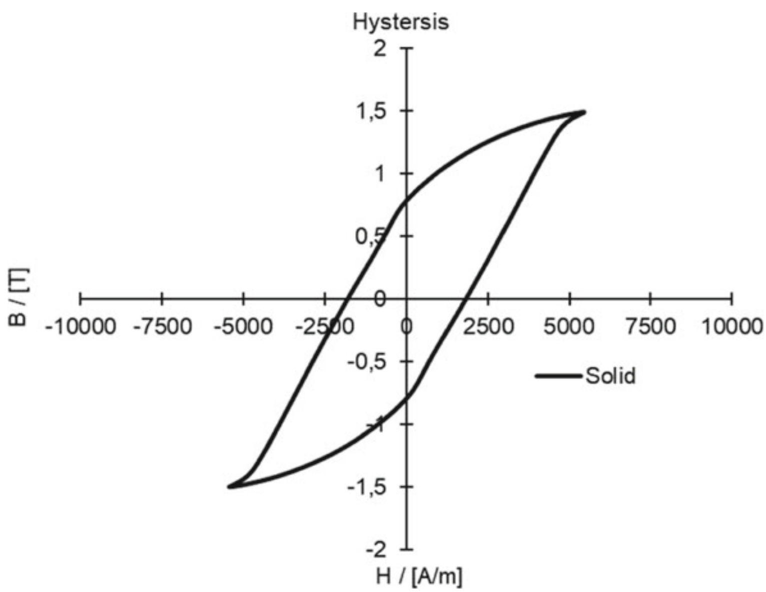

Fig. 7 Hysteresis curve of a FeSi3% toroidal core with solid cross-section

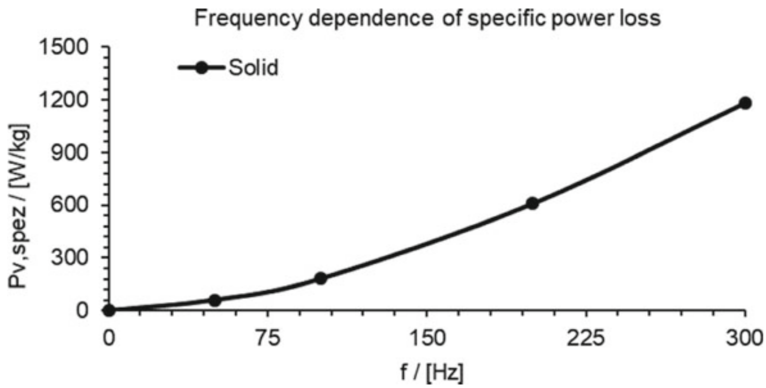

Fig. 8 Specific power loss of a FeSi3% toroidal core with solid cross-section

shows the curve of the specific power loss in relation to the remagnetization frequencies for the solid toroidal test specimen.

The frequency in Hertz (Hz) is plotted on the abscissa and the specific power loss in watts per kilogram on the ordinate. The specific power dissipation is plotted for the frequencies 50, 100, 200 and 300 Hz at the magnetic flux density of 1.5 T. The specific power loss is about 60 W/kg at a frequency of 50 Hz and 1180 W/kg at a frequency of 300 Hz.

Figure 9 shows hysteresis curves of the toroidal test specimens with the vertical thin-walled structure from Fig. 5. The hysteresis curves are here described at the power frequency of 50 Hz at a flux density of 1.5 T as well Similar to the solid specimen, Fig. 10 shows the curves of the specific power loss versus the frequencies for the toroidal test specimens with a thin-walled structure.

The hysteresis curve of the toroidal specimen 1.1.4 is significantly wider than those of the other curves, where only a small difference can be seen. This indicates that in the outer regions the eddy currents can propagate better in the relatively massive structures than in those where the fixation is distributed differently across the cross-section. In addition, there is the powder used as insulation in this test specimen. What is noticeable is that a significantly higher magnetic field strength is required to achieve a value of 1.5 T. However, this is related to the lower iron fill factor, since there is significantly less iron material for the same cross-section due to the introduced cross-sectional structures. The corresponding specific power losses are shown in Fig. 10.

This also confirms the assumptions that were indicated by the hysteresis curves. The toroidal specimen 1.1.4, which has a closed envelope and therefore uses the non-melted powder as insulation, exhibits the highest power dissipation with about 650 W/kg. Despite this, the power dissipation was reduced by almost 45% compared to the solid specimen. This is followed by specimen 1.1.5 with a specific power loss of almost 300 W/kg. The

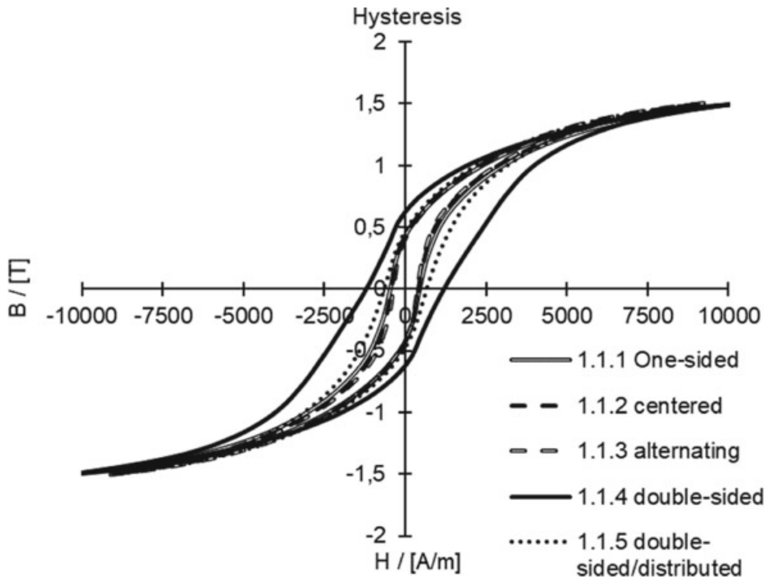

Fig. 9 Hysteresis curves of toroidal cores with thin-walled structures and different fixation

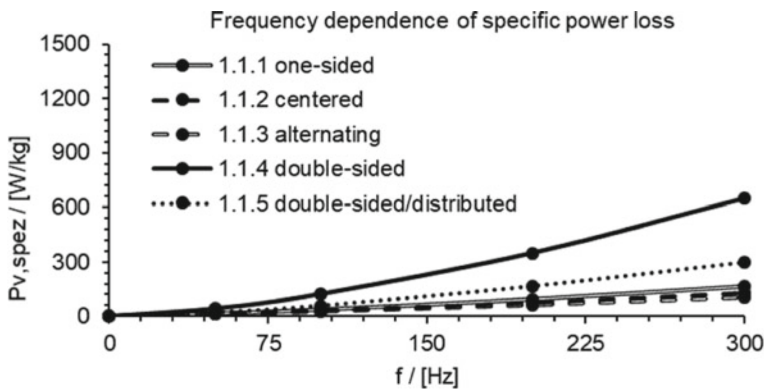

Fig. 10 Specific power loss of toroidal cores with thin-walled structures and different fixation

three other toroidal cores from this group show similarly specific power losses of about 105 to 165 W/kg.

Furthermore, the hysteresis curves were recorded for all test specimens listed in Fig. 5 and the respective specific power losses were evaluated. In addition to the values of the specific power losses, the iron filling factors of the respective test specimens are also summarized in Table 1.

The values in the table clearly show that the thin-walled structures present the lowest specific power losses. Only test specimen 1.1.4, which has powder inclusions, deviates

Table 1 Evaluated results of specific power losses and iron fill factors from the experimental investigations for the generated toroidal specimens

Toroidal core grouping	Toroidal core number	f (Hz)	$P_{v,spec}$ (W/kg)	Iron filling factor (%)
	1.1.1	300	165.53	81
Thin-walled	1.1.2	300	128.86	85.5
Structure with bar	1.1.3	300	103.67	79
Fixation	1.1.4	300	648.96	84
	1.1.5	300	299.23	78
Thin-walled	1.2.1	300	202.47	82
Structure with point	1.2.2	300	121.55	75
Fixation	1.3.1	300	161.88	81
Square symmetrical arrangements	2.1.1	300	545.59	88
	2.1.2	300	364.85	87
	2.2.1	300	211.02	63
	3.1	300	674.72	84

significantly from the average value. In this context it is also evident that all the test specimens with powder inclusions—which should act as insulation—have significantly higher specific power losses than the test specimens with air gaps. In this case, these are the test specimens 1.1.4, 2.1.1 and 3.1. A clear demarcation between the bar fixations and the point fixations for the thin-walled structures could not be observed. The fixation by lattice structures was classified as point fixation, since the fixation from the lattice structures to the walls is point-like. Test specimen 1.1.3 exhibited the lowest power loss. However, the iron filling factor of 79% was in the lower range. With regard to the iron filling factors, it is also noticeable that the first three toroidal cores differ, although they have the same values in the CAD file. On the one hand, this is due to the post-processing of the toroidal test specimens. On the other hand, the test specimens 1.1.2 and 1.1.3 have significantly more overhang areas that cannot be post-processed due to accessibility. In the overhang areas, powder adhesion is increased, since the laser energy applied penetrates deeper than just one-layer thickness into the powder bed and thus partially melts the underlying powder. In addition, certain powder residues can remain in the thin air gaps, which also leads to certain fluctuations in the values. The highest iron filling factors were achieved with the square-symmetrical arrangements. However, the greatest power losses are present in these test specimens. Test specimen 1.1.2 was defined as the optimum structure in this investigation. With a reduction of 89% of the specific power loss compared to the solid specimen and a reduction of the iron filling factor of only 14.5%, the best compromise was achieved.

4 Conclusion and Outlook

The main task of this investigation was the development of suitable cross-sectional structures to reduce eddy currents in additively manufactured toroidal cores by suitable design measures. Twelve toroidal test specimens were generated, which were derived using the elaborate procedure. They were manufactured using the LBM process. After the post-processing, hysteresis curves were recorded for the toroidal test specimens in order to quantify the magnetic characteristics with respect to eddy current losses. The results were described, evaluated and interpreted, resulting in a summary of the following findings.

Dividing the cross-section into vertical thin-walled structures proved to be most useful in this investigation. This type of cross-section division offers many different fixation possibilities for the individual cross-sections, allowing to obtain air as an insulating medium between the cross-sections. The powder, which is not melted during the process, proved to be unsuitable in this process with regard to the insulation. However, powder cavities still brought certain loss reductions compared to solid structures. In addition to the highest savings potential in terms of eddy current losses, the toroidal cores with thin-walled structures exhibited a high iron fill factor of min. 75%. Dividing the cross-section into a square-symmetrical arrangement was only useful to a limited extent. Due to the many contact points between the individual cross-sections and the many powder inclusions, the specific power losses were relatively high compared to the thin-walled structures.

With the help of the developed approach, further structures are to be worked out and examined. Since only one test specimen was manufactured and measured for each generated active structure in this investigation, it is necessary to increase the number for subsequent investigations in order to cover a statistical certainty. Besides the investigation of complete cross-sections, hybrid shapes of different materials as well as cross-sections with solid core and surface structures are conceivable. In order to enable comparability with industrially measured sheet metal materials, it is necessary to adapt the test rig or to carry out the measurement on a system designed for this purpose.

References

1. Gebhardt, A. (2016). *Additive Fertigungsverfahren – Additiv Manufacturing und 3D-Dru-cken für Prototyping – Tooling – Produktion* (5. Auflage). Carl Hanser Verlag.
2. Lammers, S., Quattrone, F., & Mrozek, R. (2016). Machbarkeitsstudie 3D Druck Elektromotoren, FVA-Heft Nr. 1189, Forschungsvereiningung Antriebstechnik e.V., Frankfurt.
3. Taube, A., Lammers, S., Urbanek, S., & Mrozek, R. (2018). Weichmagnetische Werkstoffe für die additive Fertigung von E-Motoren. FVA-Heft Nr. 1286, Forschungsvereiningung Antriebstechnik e.V., Frankfurt.
4. Frohne, H., Löcherer, K. H., Müller, H., Harriehausen, T., & Schwarzenau, D. (2008). *Moeller Grundlagen der Elektrotechnik* (21. Auflage). Vieweg + Teubner Verlag.

5. Kallenbach, E., Eick, R., Quendt, P., Ströhla, T., Feindt, K., Kallenbach, M., & Radler, O. (2012). *Elektromagnete – Grundlagen, Berechnung, Entwurf und Anwendung* (4. Auflage). Vieweg + Teubner Verlag.
6. Canders, W.-R. (2011). *Berechnung von Eisenverlusten – Physikalisch basierter Ansatz nach Bertottis Theorie*. Jahresbericht, Institut für Elektrische Maschinen, Antriebe und Bahnen, TU Braunschweig, Baunschweig.
7. Paul, R. (1993). *Elektrotechnik 1. Felder und einfache Stromkreise* (3. Auflage). Springer.
8. Bauer, D. (2019). *Verlustanalyse bei elektrischen Maschinen für Elektro- und Hybridfahrzeuge zur Weiterverarbeitung in thermischen Netzwerkmodellen*. Springer Vieweg. https://doi.org/10.1007/978-3-658-24272-5
9. Adam, G. A. O. (2015). *Systematische Erarbeitung von Konstruktionsregeln für die additiven Fertigungsverfahren Lasersintern, Laserschmelzen und Fused Deposition Modeling*. Dissertation, Universität Paderborn. Forschungsberichte des Direct Manufacturing Research Centers, Band 1. Shaker Verlag, Aachen.
10. DIN Deutsches Institut für Normung e.V. (2004). Magnetische Werkstoffe – Teil 6: Verfahren zur Messung der magnetischen Eigenschaften weichmagnetischer und pulverförmiger Werkstoffe bei Frequenzen im Bereich 20 Hz bis 200 kHz mit Hilfe von Ringproben (IEC 604046:2003), Berlin.
11. Bertotti, G. (1988). General properties of power losses in soft ferromagnetic materials. *IEEE Transactions on Magnetics, 24*(1), 621–630. https://doi.org/10.1109/20.43994
12. Halbedel, B. (2014). Magnetische Eigenschaften der Materialien, Institut für Werkstofftechnik, TU Ilmenau.

Electroplating as an Innovative Joining Method for Laser Additive Manufactured Components Made of AlSi10Mg

Kris Rudolph, Marco Noack, Maximilian Hausmann, Eckhard Kirchner, and Pedram Babaei

Abstract

Powder bed fusion (PBF) enables the manufacturing of complex structures. While part consolidation is a widespread method of utilizing the design potentials of additive manufacturing, new approaches in research suggest a systematic separation of parts. Conclusively, separated parts must be joined after the manufacturing process. In this paper, electroplating is proposed as a joining process for PBF fabricated components. The joining by electroplating process is described and successfully used to join PBF manufactured tension rods. The influence of the joining geometry on the buildup of the joint is investigated. Furthermore, tensile strength and failure causes of the joined specimens are determined. Tensile strength for nickel joined specimens is 127.4 MPa and for copper joined specimens 83.2 MPa. Causes of failure are delamination in the zinc layer and fracture of the base body. The tool-free character of the process holds potential for joining complex geometries in PBF.

Keywords

Additive manufacturing • Joining process • Electroplating

K. Rudolph (✉) · M. Noack · M. Hausmann · E. Kirchner
Fachgebiet für Produktentwicklung und Maschinenelemente, Technische Universität Darmstadt, 64287 Darmstadt, Germany
e-mail: kris.rudolph@tu-darmstadt.de

P. Babaei
Eduard-Zintl-Institut für Anorganische und Physikalische Chemie, Technische Universität Darmstadt, 64287 Darmstadt, Germany

R. Lachmayer et al. (eds.), *Innovative Product Development by Additive Manufacturing 2021*, https://doi.org/10.1007/978-3-031-05918-6_11

1 Introduction

Additive manufacturing (AM) yields several advantages compared to conventional manufacturing methods. These advantages come mainly from a great freedom in design and the possibility of mass customization through tool-less and therefore cost effective production of small quantities [7]. This results in a demand for individualized or lightweight designed products, elevating the economic importance of AM in production today due to this competitive factor. However, a broader application is lacking since only few industries are using AM for the manufacturing of end products [30].

Efforts to increase the dissemination of AM made by industry and research include the development of the AM processes through improvement of technical and economic aspects. From a product development perspective the complete development of the design potentials is another aspect. Research approaches in product development for additive manufacturing address component consolidation [11, 19] or the use of agile development methods [25]. More recent research approaches in Design for Additive Manufacturing (DfAM) address systematic component separation to exploit manufacturing advantages [24, 26, 27]. However, these approaches do not address a critical aspect: the subsequent joining of the components. In this paper, the general suitability of electroplating for joining of additive manufactured components is investigated.

2 State of the Art

In this section, the state of the art in DfAM, in joining of additive manufactured parts with a focus on powder bed fusion manufactured parts is discussed. In addition, the research gap is presented.

2.1 Design for Additive Manufacturing

In order to fully use the design potentials for the available manufacturing systems the product developer has to consider the possibilities and restrictions of the manufacturing method used. The term Design for Manufacturing (DfM) describes a group of methods to design according to these restrictions and possibilities. Due to its generative character the potentials and limits of AM differ greatly from conventional processes [7]. Thus, the set of DfM rules especially for AM is summarized in DfAM.

Research into DfAM has been growing in recent years. Some of the approaches resulted in adaptions of design process models focusing on the design of products for AM [12, 16]. In other approaches individual methods were developed. A distinction is made between restrictive and opportunistic methods [17]. Opportunistic methods such as the Design Pattern Matrix [31] extend the solution space and help the designer to discover new solutions. Furthermore, to make full use of the potentials of AM not only the design of individual parts should be looked upon. The architecture of a product, i.e., its physical and functional structure and the relations of the individual elements to each other, should also be considered [13]. The possibility of part consolidation is one major aspect of manipulation of the product architecture. By combining several individual parts to one single one with a higher complexity, the manufacturing possibilities of AM can be used to their full potential. A high degree of consolidation results in integral design while low degrees correspond to differential design. Different methods for applying part consolidation exist [11, 19].

However, from a cost perspective the optimal degree of consolidation for a part is not necessarily the highest degree. Nie et al. [19] studied the relationship of manufacturing costs to the degree of consolidation. While assembly costs decrease with increasing degree of consolidation, material costs for support material and process costs increase. The optimum is highly dependent on the geometry and the required part count [19]. This leads to the assumption that in some cases component separation or part degradation is appropriate. However, the separation of components to be manufactured additively has been dealt with much less frequently than component consolidation in the past. Generally, these approaches only addressed the separation of parts that are too large for the available build space [3, 20]. Other reasons for component separation include the reduction of the required support structure or the production of functional surfaces that would otherwise be oriented in opposite directions in the building space [24]. In current studies, Reichwein et al. [24, 26, 27] is investigating the systematic separation of components. A procedure is presented in which a separation plane is automatically determined in order to separate components to be manufactured additively with respect to various criteria. The criteria include minimization of support structures and maximization of the utilization of the available build space and thus maximization of the number of pieces that are manufactured in a single process run [27]. In addition, a product model is presented which enables an abstraction of the product components. Based on this abstraction, a consolidation and the subsequential separation can be performed. This enables a reconstruction of the product architecture with respect to functional and structural aspects [26]. In the course of this semi-automatic component separation, a wide variety of separation geometries is created. The articles provide at most superficial suggestions as to how the components are to be joined after production.

2.2 Joining of Additive Manufactured Parts

Studies on joining of additively manufactured parts can be found in literature. Metal parts made by powder bed fusion (PBF) are usually joined by welding. Common processes are laser beam welding (LBW), electron beam welding (EBW) and friction welding (FW), especially friction stir welding (FSW).

Laser beam welding can be used to successfully join PBF parts made of different metals or alloys or join additive manufactured parts with conventional manufactured parts. However, post-processing is necessary to reduce the surface roughness in the welding region as well as a higher energy input than with conventional laser beam welding [1, 29]. LBW of parts made of AlSi10Mg lead to a reduced tensile strength with 262 MPa, while tensile strength of parts made in one piece was at 441 MPa [1]. Tensile tests of the welded joint between an additively manufactured component made of Ti6Al4V with a wrought component made of the same material show that failure always occurs in the wrought component. EBW can also be used to join PBF parts. However, tensile strength is lower than LBW produced joints [28].

Friction welding is used to avoid solidification related problems like hot cracking. PBF components made of AlSi10Mg [8] and other materials can be joined by friction welding or friction stir welding. However, the tensile strength is reduced while the ductility is increased [9, 18, 22].

For non-PBF manufactured parts, mostly polymeric parts there are several studies on joining these parts. Ramirez et al. [23] present a snap-fit joint directly manufactured on the part. For fused filament fabricated parts the usage of adherents is viable [2]. However, adequate preparation of the joining surfaces is required [6]. Kuklik et al. [15] studied the usage of laser transmission welding. Pimentel et al. [21] examine the strength of threaded connections by fabricating threads directly into the component, cutting them subsequently, or inserting them as metal inserts.

2.3 Research Gap

Current research streams address the systematic separation of components for manufacturing reasons, as described in Sect. 2.1. However, the separated components must ultimately be joined to obtain the final product geometry. In literature, the suitability of different joining options for additively manufactured components is investigated. For PBF, these are mainly welding processes. However, the joining geometries investigated are very simple, e.g., the contact surface between two plates or between two cylinders. The automatic component separation from Reichwein et al. usually generates much more complex separation geometries, which can also consist of several contact surfaces [24]. This can pose a major challenge to tool guidance or to the accessibility of the joining zone in the first place.

A tool-less joining process could overcome these challenges. This would also complement the tool-less character of additive manufacturing. By means of electroplating, components can be coated almost independently of their geometry [10]. Therefore, electroplating is proposed as a joining method for additive manufacturing in this paper. The process was investigated by Dini and Johnson [5] as early as 1974 for joining tubes. Krauss et al. [14] join tungsten using brazing. The filler material is applied to the joining surfaces by electroplating before the brazing process. Further publications on joining by electroplating are not known.

3 Experimental Setup

In this section, the process of joining by electroplating is explained. Afterwards, the joining geometries investigated and the results of the tensile tests are presented.

3.1 Joining by Electroplating

Electroplating is an electrochemical process commonly used for metallic coating of substrate bodies. The basis for this is electrochemical metal deposition. When a metal object is immersed in an electrolyte, spontaneous metal dissolution can occur. In this process, metal atoms leave the metal lattice and migrate into the electrolyte in the form of positive cations. This is also called anodic metal dissolution. A negative excess charge remains in the electrode. The cations are attracted to a negatively charged electrode due to the electrostatic attraction. There, the ions discharge and the metal is deposited on the surface of the electrode. This process is called cathodic metal deposition. The result is a dynamic equilibrium, which is described in Eq. (1). Me is the metal, e is the elementary charge and z is the number of atoms per elementary cell.

$$\mathrm{Me} \rightleftharpoons \mathrm{Me}^{z+} + z \cdot e^{-} \tag{1}$$

By applying a voltage between the electrodes of an electrolytic cell, an electron flow can be generated from the anode to the cathode. This causes the cations in the electrolyte to migrate to the cathode and the anions to migrate to the anode. This process is called direct current process and is shown in Fig. 1. In this study, the workpiece to be joined forms the cathode. The anode, however, consists of the coating material and dissolves into the electrolyte during the process, regenerating the metal content in the electrolyte. The dissolved quantity corresponds to the quantity deposited on the workpiece. [10]

The process steps for joining additively manufactured components made of AlSi10Mg are listed below. Between each step, the specimens are rinsed with distilled water. One part of the samples was joined with nickel and the other part with copper, two materials commonly used in electroplating.

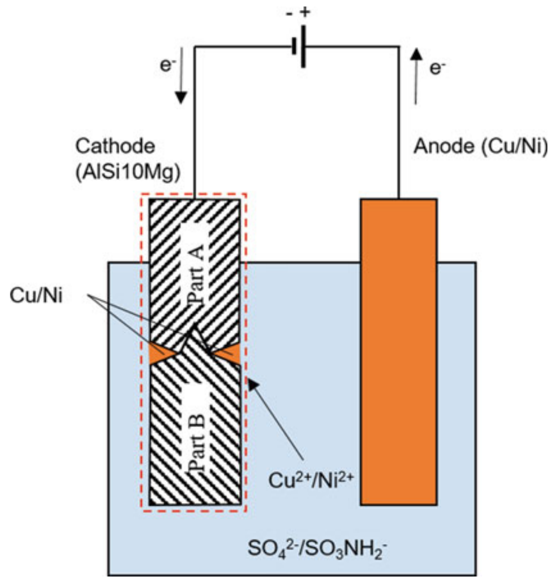

Fig. 1 Schematic of an electrolytic cell for joining components by electroplating with nickel or copper based on [10]

1. The surface morphology of the component to be coated has a major influence on the coating thickness distribution. In particular, roughness peaks can lead to non-uniformities [10]. Therefore, the surface roughness in the joining zone is reduced by grinding.
2. The oxide layer on the surface of the component is removed by bathing the component in a sodium hydroxide solution (concentration 7.5 mol/l).
3. To further remove the oxide layer and to prevent a renewed oxidation of the surface, the component is galvanized electroless using a zincate with copper content. The zincate layer also provides better adhesion of the coating material.
4. To improve the quality of the zincate coating the coating is removed with nitric acid (concentration 2 mol/l). A new zinc coating is then applied.
5. A thin layer of copper is applied to the component in an alkaline copper electrolyte. This copper layer is primarily intended to protect the zincate, which would be dissolved in the acidic milieu of the subsequent electroplating.
6. To achieve a targeted material deposition, the component is wrapped with an insulating tape. Only the joining surfaces and a small area for contact with the power source are left free. To join several components at the same time, they are placed in a fixture and connected by means of copper wire. This setup can be seen in Fig. 2.
7. The specimen are then connected to a power source and immersed into an electrolyte where the joining process takes place. The electrolytes used and the process parameters are listed in Table 1.
8. After joining, the samples are washed one last time with distilled water and milled to final geometry as shown on the right side in Fig. 2.

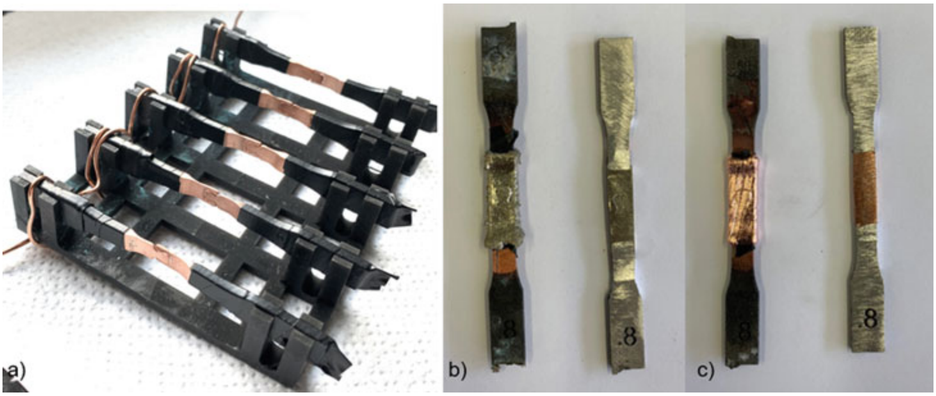

Fig. 2 **a** Specimen prepared to be plated and specimens bonded with **b** nickel or **c** copper after they have been plated (left) and after they have been milled to final geometry (right)

Table 1 Electrolytes used and their process parameters

Electrolyte	Formular	PH value	Concentration	Current density (A/dm^2)	Temperature (°C)	Duration
Copper sulfate	$CuSO_4$	8.5	unknown	2.5	20	2 min
Copper sulfate	$CuSO_4$	1	unknown	5	20	17.5 h
Nickel sulfamate	$Ni(SO_3NH_b)2$	3.5	185 g/l	5.5	60	45 h

3.2 Sample Design and Results of Joining

Since the tensile strength of the joint is being investigated, the test specimens were designed as tension rods and bars following DIN 50125 [4]. Initial joining tests were carried out with round specimens according to Form A of DIN 50125. For this purpose, however, the model of the tension rod was split in the middle. To position the halves in relation to each other, the tension rod halves were provided with either a pin or a hole, each with an additive manufactured thread. To maintain the size of the original component, material must be removed in the parting line area to make room for the filler material. This material removal is in the form of a wedge with a 30° opening angle. The dimensioning of the tensile rods can be seen in Fig. 3 on the left. The specimens are screwed together and joined according to the procedure in Sect. 3.1. The result is shown in Fig. 3 on the right. It is clearly visible that the joining zone was not completely filled, while increased material was deposited at the edges at the beginning of the joining

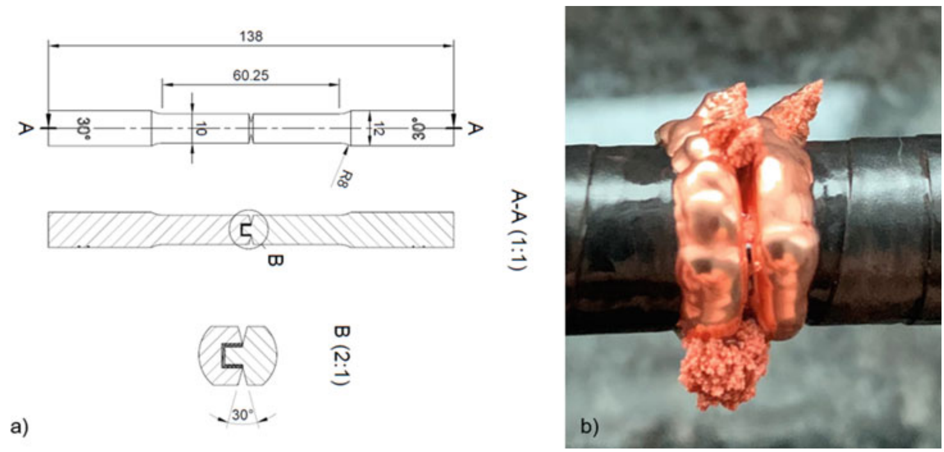

Fig. 3 **a** Technical drawing of the tension rod. **b** Joined tension rod with visible gap in the joining zone

zone. According to Kanani [10] this is mainly due to the course of the electric current lines. These generally do not run parallel, but are influenced by geometric factors and the arrangement of the electrodes. Consequently, the edge at the joining zone led to a concentration of the electric field lines towards the edge and thus to increased material deposition in this area. Nevertheless, a sufficiently strong joint was created through which relative movement with muscle force was not possible. Nevertheless, due to the visibly low degree of filling of the joining zone, no tensile tests were carried out for Form A tension rods.

The aim is to completely fill the joining zone with material. For this purpose, a new test specimen was designed with a significantly more open joining zone. In addition, the outer edges of the joining zone were made blunter to reduce material agglomeration. This time, Form E of DIN 50125 serves as the basic body. The geometric dimensions can be seen in Fig. 4. The separation geometry was chosen in the form of a jigsaw connection to allow the components to be loosely connected before electroplating. In a length of

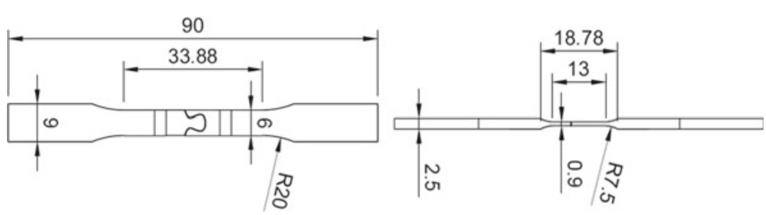

Fig. 4 Technical drawing of the tension bar

18.78 mm around the separation area, the thickness of the tension rod is reduced from 2.5 to 0.9 mm with a radius of 7.5 mm to smoothen the edges. This creates a uniform topology without sharp edges, allowing for more uniform material deposition.

As shown in Fig. 2, test specimens with this geometry could be joined. The joining zone is completely filled with material and the cladding is relatively uniform. However, material buildup again occurs at the transition to the nominal thickness, which must be removed to achieve nominal thickness by post-processing. In the context of this investigation, this step is particularly important to ensure comparability of the tension tests between the joined samples and the referenced samples. However, it is conceivable that with sufficient process control and optimized joining geometry, post-processing can be reduced or even eliminated in some cases.

All specimens were manufactured on the PBF system EOS M290 with the parameter set "direct part parameter". The material used is AlSi10Mg. The build-up direction is parallel to the tensile direction for all specimens.

3.3 Tensile Test and Discussion of Results

Tensile tests for Form E adapted specimens were carried out on a tensile compression testing machine from Zwick Roell. For each type of specimen (reference, nickel-joined and copper-joined) four specimen were tested. The average stress–strain curve of each specimen type is plotted in Fig. 5. The comparative samples reach a tensile strength of 410.5 MPa, which corresponds to literature. The joined specimens, on the other hand, have a significantly lower tensile strength. Copper-joined specimens fail at 83.2 MPa, nickel-joined specimens fail at 127.4 MPa. The curves of copper and nickel are very similar, although with different tensile stress values and strains. Both specimen types show an initial failure in the range of 0.4 and 0.6% strain with a significant decrease

Fig. 5 Stress–strain curve

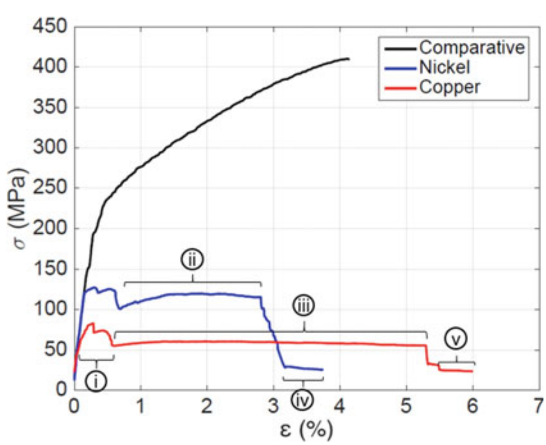

in the measured tensile stress at 0.6% strain (section i). Following, for the nickel joint, there is a renewed increase in tensile stress to approximately 94% of the maximum value (section ii). For the copper compound, there is a slight increase to approx. 72% of the maximum value (section iii). At 2.8% elongation, the nickel joint fails a second time. The stress drops to about 30 MPa and then proceeds linearly with a slight negative slope (section iv). At 3.8% elongation, the measurement is stopped because the measured stress falls below the threshold of 20% of the maximum measured tensile stress. However, the tensile bar halves are still in contact at that point, but can be separated by hand. The copper specimens fail a second time at 5.3% elongation and end up at the same stress level and curve as the nickel samples (section v). The copper test ends as soon as the tension rod halves are completely separated.

As mentioned, there are two failure modes. By looking at the destroyed specimens, exemplified in Fig. 6, the failure cases can be determined for all specimens.

One case is the fracture of one of the component halves made of AlSi10Mg, probably due to the form-fit character of the jigsaw joint. The second failure case is the detachment of the zinc layer from the substrate. However, no assignment was made as to which stress drop in the stress-strain diagram belongs to which failure case due to the ambiguous force flow in the joint. It was identified that the joint is completely separated after the second stress drop. Therefore, the last segment of each specimen at about 30 MPa can be explained by friction between AlSi10Mg and the zinc layer, since there is still contact between the loose parts.

In addition, the joined test specimens were examined for their electrical properties. For this purpose, a two-point measurement was performed using the R&S HM8118 LCR

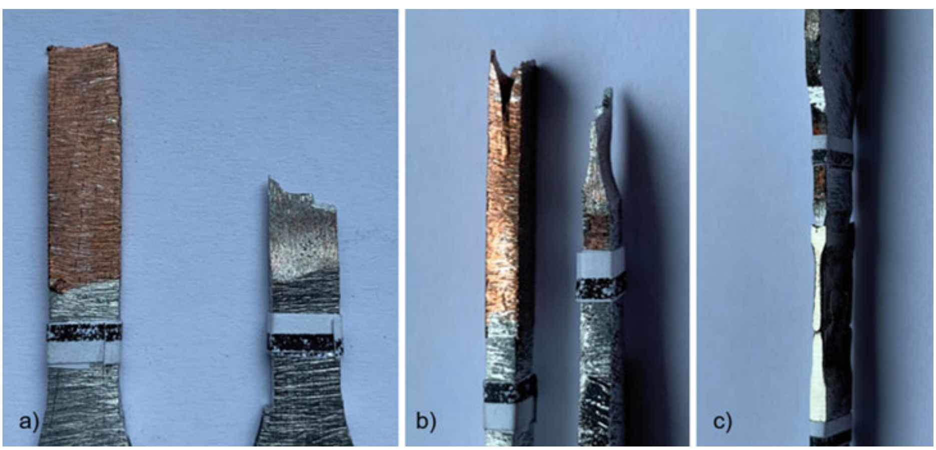

Fig. 6 Failure images: **a** and **b** copper specimens, clear separation of the component halves, crack of the AlSi10Mg and detachment of the zinc layer visible. **c** Nickel specimens, joint destroyed, but component halves still loosely in contact

measurement bridge from Rhode&Schwarz. The contact surfaces of the specimens were smoothed to minimize the effects of surface roughness. The conductivity, inductance and phase angle were measured at the frequencies from 20 Hz to 200 kHz, but no significant differences in electrical properties were found between the samples. However, this result is considered unlikely and is attributed to the method of measurement and the limited resolution of the measurement setup.

4 Conclusion and Outlook

The suitability of electroplating as a joining technology for additive manufacturing is examined. Both electroplating and additive manufacturing allow great freedom in the geometry to be processed, which is why a combination of the processes is logical. In particular, the advancing research in the field of systematic component separation in DfAM makes a largely geometry-independent joining process necessary.

Two different joining geometries are investigated. Even though a joint could be established, it was shown that narrow joining zones cannot be completely filled with material, but material accumulation occurs at the edge of the joining zone. More openly designed joining zones can be completely filled with material. But here, too, material accumulation occurs at the edges, which has to be removed during post-processing. Nevertheless, it is shown that components manufactured by PBF can be joined by electroplating.

Tensile tests show that the joined specimens have a significantly lower tensile strength than specimens manufactured in one piece or joined by laser beam or friction welding. While the nickel compound has 31% of the tensile strength of the reference specimens, components joined with copper have 20% of the tensile strength. The detected failures are cracking in the AlSi10Mg region of the specimens and detachment of the zinc layer from the base body. In order to improve the clarity of the results, it is suggested to manufacture the base bodies without a jigsaw joint but with a butt joint. Furthermore, an improvement of the quality of the zinc layer or an enlargement of the joining area is suggested to make a detachment of the zinc layer more difficult. The choice of a different base material, which forms a better bond with the zinc layer, is also suggested. In an investigation of the electrical properties, no significant differences were found between the sample types.

The basic suitability of electroplating for additive manufacturing is presented and the basis for further investigation is provided. First, the fracture structure must be investigated to gain full understanding of the failure mechanisms and locations. In addition, the wear resistance of the joint will be investigated. Then, possibilities for improving the load-bearing capacity of the compound are to be investigated. This can be achieved by optimizing the geometry of the joining zone, investigating different joining materials or improving the adhesion of the individual layers. In addition, it is planned to investigate the manufacturing of a form-fit element in the joining zone, in order to replace material closure as the main joining mechanism. Furthermore, real and complex components are to be joined. The joining capability in the real application, the necessary postprocessing and the resulting mechanical properties are to be investigated. The outcome will be used to evaluate and further develop electroplating as a joining method for PBF manufactured components. Finally, the usage of joined components as anode will be investigated under the aspects of recycling and dismantlability. In this way, components could be separated non-destructively while reusing the filler material.

References

1. Biffi, C. A., Fiocchi, J., & Tuissi, A. (2019). Laser Weldability of AlSi10Mg alloy produced by selective laser melting: microstructure and mechanical behavior. *Journal of Materials Engineering and Performance, 28*(11), 6714–6719. https://doi.org/10.1007/s11665-019-04402-7
2. Cavalcanti, D. K. K., Banea, M. D., & de Queiroz, H. F. M. (2019). Mechanical characterization of bonded joints made of additive manufactured adherends. *Annals of Dunarea De Jos University of Galati Fascicle XII Welding Equipment and Technology*, *30*, 27–33. https://doi.org/10.35219/awet.2019.04
3. Deka, A., & Behdad, S. (2019). Part separation technique for assembly-based design in additive manufacturing using genetic algorithm. *Procedia Manufacturing, 34*, 764–771. https://doi.org/10.1016/j.promfg.2019.06.208
4. DIN e.V. *DIN 50125:2016-12, Prüfung metallischer Werkstoffe_- Zugproben.* Berlin: Beuth Verlag GmbH.
5. Dini, J. W., & Johnson, H. R. (1974). Joining by electroplating. *Metals Engineering Quarterly, 14*(1), 6–12.
6. Frascio, M., Jilich, M., Pizzorni, M., Monti, M., Avalle, M., & Zoppi, M. (2019). The use of low pressure plasma surface modification for bonded joints to assembly a robotic gripper designed to be additive manufactured. *Procedia Structural Integrity, 24*, 204–212. https://doi.org/10.1016/j.prostr.2020.02.017
7. Gibson, I., Rosen, D., & Stucker, B. (2015). *Additive manufacturing technologies: 3D printing, rapid prototyping and direct digital manufacturing* (Second Edition). Springer. https://www.loc.gov/catdir/enhancements/fy1617/2014953293-b.html.
8. Gill, M., Terry, E., Abdi, Y., Hawkes, S., Rindler, J., Schick, D., Ramirez, A., & Herderick, E. D. (2020). Joining technologies for metal additive manufacturing in the energy industry. *JOM Journal of the Minerals Metals and Materials Society, 72*(12), 4214–4220. https://doi.org/10.1007/s11837-020-04441-9
9. Hassanin, A. E., Velotti, C., Scherillo, F., Astarita, A., Squillace, A., & Carrino, L. (2017). Study of the solid state joining of additive manufactured components. In *2017 IEEE 3rd International Forum on Research and Technologies for Society and Industry (RTSI)* (pp. 1–4). IEEE. https://doi.org/10.1109/RTSI.2017.8065967
10. Kanani, N. (2020). *Galvanotechnik: Grundlagen, Verfahren und Praxis einer Schlüsseltechnologie* (3., aktualisierte Auflage). Hanser.
11. Kim, S., & Moon, S. K. (2020). A part consolidation design method for additive manufacturing based on product disassembly complexity. *Applied Sciences, 10*(3), 1100. https://doi.org/10.3390/app10031100
12. Kranz, J. (2017). *Methodik und Richtlinien für die Konstruktion von laseradditiv gefertigten Leichtbaustrukturen.* Berlin, Heidelberg: Springer. https://doi.org/10.1007/978-3-662-55339-8.

13. Krause, D., & Gebhardt, N. (2018). *Methodische Entwicklung Modularer Produktfamilien: Hohe Produktvielfalt Beherrschbar Entwickeln*. Vieweg. https://ebookcentral.proquest.com/lib/gbv/detail.action?docID=5215463.
14. Krauss, W., Lorenz, J., & Konys, J. (2014). Joining of HHF materials applying electroplating technology. *Fusion Engineering and Design, 89*(7–8), 1213–1218. https://doi.org/10.1016/j.fusengdes.2014.04.042
15. Kuklik, J., Wippo, V., Jaeschke, P., Kaierle, S., & Overmeyer, L. (2020). Laser Transmission Welding of additive manufactured parts: Process modifications to reduce cavities inside the weld seam. *Procedia CIRP, 94*, 139–143. https://doi.org/10.1016/j.procir.2020.09.027
16. Kumke, M. *Methodisches Konstruieren von additiv gefertigten Bauteilen* [Dissertation]. Wiesbaden: Springer Fachmedien Wiesbaden.
17. Laverne, F., Segonds, F., Anwer, N., & Le Coq, M. (2015). Assembly based methods to support product innovation in design for additive manufacturing: An exploratory case study. *Journal of Mechanical Design*, *137*(12), Article 121701. https://doi.org/10.1115/1.4031589.
18. Moeini, G., Sajadifar, S. V., Wegener, T., Brenne, F., Niendorf, T., & Böhm, S. (2019). On the low-cycle fatigue behavior of friction stir welded Al–Si12 parts produced by selective laser melting. *Materials Science and Engineering: A, 764*, 138189. https://doi.org/10.1016/j.msea.2019.138189
19. Nie, Z., Jung, S., Kara, L. B., & Whitefoot, K. S. (2020). Optimization of part consolidation for minimum production costs and time using additive manufacturing. *Journal of Mechanical Design*, *142*(7), Article 072001. https://doi.org/10.1115/1.4045106.
20. Oh, Y., Zhou, C., & Behdad, S. (2018). Part decomposition and 2D batch placement in single-machine additive manufacturing systems. *Journal of Manufacturing Systems, 48*, 131–139. https://doi.org/10.1016/j.jmsy.2018.07.006
21. Pimentel, A., Noversa, T., Freitas, L., Nunes J. P., Brito, A. M., Lima, R., Alves, T. (2018). Mechanical joining methods for additive manufactured assembly tools. In *Proceedings of the 8th international conference on polymers and moulds innovation—PMI 2018*.
22. Prashanth, K. G., Damodaram, R., Maity, T., Wang, P., & Eckert, J. (2017). Friction welding of selective laser melted Ti6Al4V parts. *Materials Science and Engineering: A, 704*, 66–71. https://doi.org/10.1016/j.msea.2017.08.004
23. Ramírez, E. A., Caicedo, F., Hurel, J., Helguero, C. G., & Amaya, J. L. (2019). Methodology for design process of a snap-fit joint made by additive manufacturing. *Procedia CIRP, 79*, 113–118. https://doi.org/10.1016/j.procir.2019.02.021
24. Reichwein, J., & Kirchner, E. (2021). Part orientation and separation to reduce process costs in additive manufacturing. *Proceedings of the Design Society, 1*, 2399–2408. https://doi.org/10.1017/pds.2021.501
25. Reichwein, J., Vogel, S., Schork, S., & Kirchner, E. (2020). On the applicability of agile development methods to design for additive manufacturing. *Procedia CIRP, 91*, 653–658. https://doi.org/10.1016/j.procir.2020.03.112
26. Reichwein, J., Rudolph, K., Geis, J., & Kirchner, E. (2021a). Adapting product architecture to additive manufacturing through consolidation and separation. *Procedia CIRP, 100*, 79–84. https://doi.org/10.1016/j.procir.2021.05.013
27. Reichwein, J., Steffan, K.-E., & Eckhard, K. (2021b). Bauteiltrennung zur Reduzierung der Prozesszeit und—kosten in der Additiven Fertigung. In D. Roth (Chair), *Stuttgarter Symposium für Produktentwicklung SSP 2021*. Symposium conducted at the meeting of Fraunhofer—Institut für Arbeitswissenschaft und Organisation IAO, Stuttgart.
28. Tavlovich, B., Shirizly, A., & Katz, R. (2018). EBW and LBW of Additive Manufactured Ti6Al4V Products. *Welding Journal*, *97*(6), 179–190. https://doi.org/10.29391/2018.97.016.

29. Wits, W. W., & Becker, J. J. (2015). Laser beam welding of titanium additive manufactured parts. *Procedia CIRP, 28*, 70–75. https://doi.org/10.1016/j.procir.2015.04.013
30. Wohlers, T. T. (2018). *WOHLERS REPORT: 3d printing and additive manufacturing state of the industry*. WOHLERS Associates.
31. Würtenberger, J., Reichwein, J., & Kirchner, E. (2018). Using the potentials of additive manufacturing by a systematic linkage of the manufacturing process to product design. In *Design conference proceedings, proceedings of the DESIGN 2018 15th international design conference* (pp. 1465–1476). Faculty of Mechanical Engineering and Naval Architecture, University of Zagreb, Croatia; The Design Society, Glasgow, UK. https://doi.org/10.21278/idc.2018.0225.

Simulation, Validation and Quality Assurance

Additive Manufacturing of a Laser Heat Sink: Multiphysical Simulation for Thermal Material Requirement Derivation

Julian Röttger, Tobias Grabe, Max Caspar Sundermeier, Fabian Kranert, Oktay Heizmann, Tobias Biermann, Arved Ziebehl, Peer-Phillip Ley, Alexander Wolf, and Roland Lachmayer

Abstract

Heat dissipation inside diode-pumped Nd:YVO_4 laser crystals requires an efficient cooling concept to reduce heat-induced stress and thus to avoid the mechanical destruction of the laser medium. Due to a high degree of design freedom, additive manufacturing of heat sinks offers great potentials to integrate cooling channels and sensors within a single component. These advantages are associated with a reduced choice of materials. The thermal and mechanical properties of the printing material have a significant impact on the emerging stress. For a suitable choice of printing material, temperatures and stress occurring in the application of the product are calculated using a multi-physical simulation model. By coupling optical, thermal and mechanical effects within a single simulation model, the mechanical stress in the laser crystal is investigated as a function of thermal material properties. Based on this information, thermal requirements are defined to ensure a non-destructive operation of a present laser application.

J. Röttger (✉) · T. Grabe · M. C. Sundermeier · O. Heizmann · T. Biermann · A. Ziebehl · P.-P. Ley · A. Wolf · R. Lachmayer
Institute of Product Development, Leibniz University Hannover, 30823 Garbsen, Germany
e-mail: Roettger@ipeg.uni-hannover.de

J. Röttger · T. Grabe · F. Kranert · R. Lachmayer
GROTESK, 30823 Garbsen, Germany

F. Kranert
Laser Zentrum Hannover E.V, Hollerithallee 8, 30419 Hannover, Germany

F. Kranert · T. Biermann · A. Wolf · R. Lachmayer
Cluster of Excellence PhoenixD, 30167 Hannover, Germany

R. Lachmayer et al. (eds.), *Innovative Product Development by Additive Manufacturing 2021*, https://doi.org/10.1007/978-3-031-05918-6_12

Keywords

Additive manufacturing • Multiphysics simulation • Laser application

1 Introduction

Additive manufacturing offers several advantages, such as the potential to integrate multiple functions within a single component due to the high degree of design freedom. Products can thus be manufactured in almost any geometry and adapted to the expected mechanical and thermal loads. [1]

However, depending on the 3D printing process, only a limited selection of commercial materials is available. The appropriate choice of material is based on requirements that need to be defined at the beginning of the product development process. By testing the developed product in its application, thermal and mechanical loads can be identified. Based on this information, existing requirements can be refined. Thus, requirements for further developments of the product can be specified and returned in a feedback loop. According to the refined requirements, the printing material is to be chosen to consider thermal and mechanical loads in the application.

The specification process is demonstrated by developing a 3D printed crystal heat sink for a low-power laser system. In a first development loop, optical and functional requirements are defined. By using Fused Filament Fabrication (FFF), lightweight and low-cost optomechanical systems can be printed in a short manufacturing time [2]. In the next development loop, thermal and mechanical effects are considered to improve the cooling capacity of the heat sink. During the operation of the laser system heat is generated inside the crystal. By printing with copper-filled polylactide (Cu-PLA) filament, the thermal conductivity of the heat sink material is increased compared to the formerly used PLA [3].

Nevertheless, mechanical stress occurs due to thermal expansion inside the crystal. If the fracture tensile stress is exceeded, there is an increased risk that the crystal will break. In addition, the optical efficiency of Nd:YVO_4 crystals decreases with increasing temperature [4]. Therefore a certain amount of energy is to dissipate. To ensure an efficient and non-destructive operation of the laser system, thermal material requirements are derived to reduce the thermal-induced load. Limiting values are derived by calculating the occurring temperatures and stress in the crystal depending on the heat conductivity and the heat transfer coefficient.

In a laser system, optical, thermal and mechanical effects are strongly dependant on each other. Due to the complex geometry of the heat sink, an analytical calculation of the resulting temperature and stress is difficult. Therefore, a numerical multi-physical simulation model is developed to calculate the stress in the crystal depending on the thermal material parameters of the additively manufactured heat sink.

2 Laser System with Additively Manufactured Optomechanics

In this section, a laser system with additively manufactured optomechanics is introduced. First, the overall system, including optical components, their optomechanics and the laser diode is described. One of the implemented optomechanics is the 3D printed heat sink. The integrated functionalities and the used material properties are presented below. The heat sink mounts a laser crystal. Its material properties influence the generation and dissipation of heat.

2.1 Overall System

The laser system is an assembly of mainly printed optomechanics and conventional optical components enclosed in a printed housing, as shown in Fig. 1. The pump light from a fiber-coupled laser diode with an output power of 8 W and a central wavelength of 808 nm is collimated and focussed into the crystal. The resonator consists of a high and a partially reflective mirror for the laser wavelength of 1064 nm. All optomechanical parts are printed via PLA-based filaments. Thereby, the adapter for the pump fiber, the lenses, the laser crystal, and the resonator mirrors are imprinted directly into the optomechanics, leading to a firm and stress-free fixation. [2]

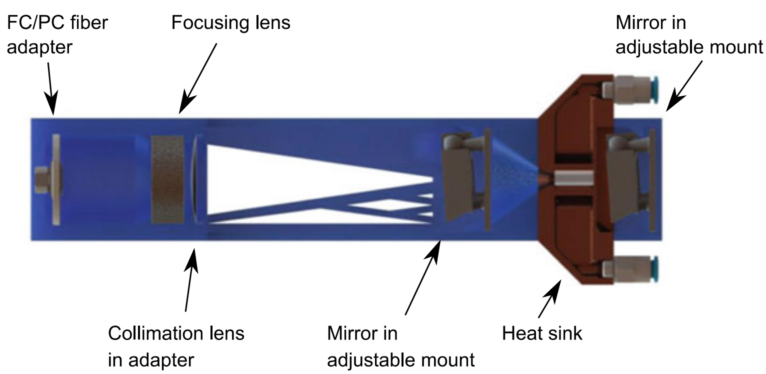

Fig. 1 Design of the laser system with 3D-printed optomechanics

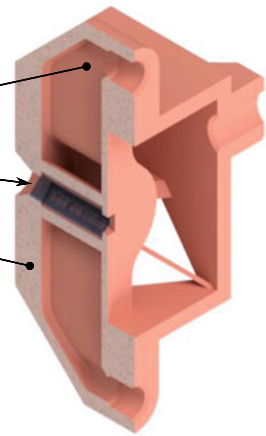

Fig. 2 CAD model of the function integrated heat sink

2.2 Crystal Heat Sink

For cooling the laser crystal, the possibilities of additive manufacturing were exploited to obtain a highly integrated functional unit, where the cooling channels and water connections are integrated directly into the design. Furthermore, a thermal resistance detector (RTD) and the laser crystal are embedded directly into the heat sink.

In their research, Grabe et al. [5] investigate the influence of the thermal bonding between a crystal and an additively manufactured heat sink on the resulting temperature. These studies demonstrate that a linear decrease in the heat transfer coefficient is accompanied by an exponential temperature increase in the crystal. In contrast, the geometry of the cooling channels was found to have only a minor influence on the cooling performance [5]. For this reason, the geometry of the cooling channels is not optimized for cooling performance but adapted to be manufactured without support structures while maintaining high surface qualities. The sectional view of the function integrated heat sink is shown in Fig. 2. A composite Cu-PLA filament, which is gravimetrically filled with 80% copper powder, is used to increase the thermal conductivity [6]. Due to the low thermal conductivity of the copper-PLA filament $k_{\mathrm{Cu-PLA}} = 0.25$ W/(m · K) in comparison to conventionally used copper $k_{\mathrm{Cu}} = 240 - 380$ W/(m · K), only a low cooling capacity could be achieved [7, 8]. In Table 1, the material properties of the filament used are listed, according to the manufacturer.

2.3 Laser Medium

The laser medium is a Neodymium doped YVO4-crystal (CASIX, China) with the dimensions $3 \times 3 \times 11$ mm^3, whereby the first 2 mm are undoped and the residual 9 mm are

Table 1 Material properties of Cu-PLA [6]

Parameter	Symbol	Value
Young's modulus	$^{E}\mathrm{CuPLA}$	4210 MPa
Tensile strength	$^{R}\mathrm{m,CuPLA}$	18.3 MPa
Density	$^{\sigma}\mathrm{CuPLA}$	3400 kg/m^3
Thermal conductivity	$^{k}\mathrm{CuPLA}$	0.25 W/(m · K)
Softening temperature	$^{T}\mathrm{max,CuPLA}$	66 C
Elongation at break	$^{A}\mathrm{CuPLA}$	4.5%

Table 2 Material properties of Nd:YVO$_4$ [9, 10]

Parameter	Symbol	Value
Young's modulus	E_{YVO4}	133 GPa
Poisson ratio	ν_{YVO4}	0.33
Refractive indices	n_{a}; n_{c}	1.9573; 2.1652
Thermal expansion coefficients	a_{a}; a_{c}	$4.43 \cdot 10^{-6}\ \mathrm{K}^{-1}$; $11.37 \cdot 10^{-6}\ \mathrm{K}^{-1}$
Thermal conductivity	K_{a}; K_{c}	5.1 W/(m · K); 5.23 W/(m · K)
Convective heat coefficient of air	h_{air}	27.5 W/(m^2 · K)
Fracture tensile stress	$\sigma_{\mathrm{max,YVO4}}$	53 MPa
Melting point	$T_{\mathrm{max,YVO4}}$	1810 C

doped with a concentration of 0.27 at%. The c-axis of the crystal is aligned parallel to the optical z-axis of the diode laser and is located at a distance of $z = 154$ mm to the laser source. Table 2 summarises the mechanical properties of the Nd:YVO$_4$-crystal. The data shows the anisotropic material behavior in terms of thermal expansion and thermal conductivity.

3 Additive Process Chain Feedback Loop

The development process of the heat sink can be methodically analyzed with the schematic representation of the additive process chain according to DIN 3405, as shown in Fig. 3 [11]. The development of an additively manufactured product is based on initial requirements, which are used to design a CAD model. In a pre-, in- and post-processing step, the designed component is prepared, printed and reworked. The manufactured component is inserted into the application to prove the fulfillment of the defined requirements. In addition, new requirements can be identified from the application of the product, or

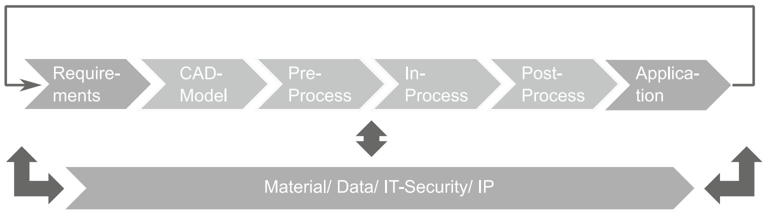

Fig. 3 Schematic representation of the process chain for the development of additive manufactured components

existing requirements can be refined. New requirements are returned to the developing process in a feedback loop. As illustrated in Fig. 3, an interaction between all process steps and the printing material is to be considered.

With the design, manufacturing and testing of the heat sink, the additive process chain was completed once. By integrating the system into the application, an increased temperature is detected. Furthermore, a negative impact on the efficiency of the laser system is analyzed [12]. These findings must be applied to further developments of the heat sink through a feedback loop. Therefore the defined optical, mechanical and functional requirements need to be supplemented by thermal requirements. More precisely, the specification of the thermal conductivity and the heat transfer coefficient for the crystal/heat sink pairing needs to be quantified.

4 Theoretical Simulation Approach

In the laser system, optical, thermal and mechanical effects interact with each other. Therefore, a multiphysics simulation model is built to analyze the influence of the printing material's heat conductivity on the resulting temperature and stress distribution.

In a multi-physical simulation model, single simulation models are linked to each other in order to represent either unidirectional or bidirectional connections. The optical simulation model is combined with the thermal model via the intensity profile of the laser beam at the position of the laser crystal. When the crystal is irradiated, a part of the induced energy is converted into heat. The propagation of this heat in the crystal and heat sink is calculated using the thermal simulation model. By integrating the Computational Fluid Dynamics (CFD) simulation, the convection of the heat energy through the water is calculated. The thermal gradient causes an expansion of the materials, which results in mechanical stress. To calculate the expansion and the resulting stress a mechanical simulation model is developed.

4.1 Optic Simulation

The optical simulation model is integrated into the multi-physical simulation model to determine the intensity distribution of the laser beam inside the crystal. By evaluating beam profile measurement results along the optical path, a Gaussian beam distribution has been identified. For the beam profile characterization, the beam radius on the surface of the crystal is to be determined. Therefore, a ray transfer matrix analysis is developed. The geometry and the position of the optical components are implemented as matrices in the analysis. A measured beam quality of $M^2 = 52$ and a waist radius of $\omega_0 = 52.5$ μm are taken into account to calculate the beam radius as a function of the optical path z. From the simulation, a beam radius of $\omega_p = 182$ μm is derived at the position of the crystal face.

According to Lambert-Beer's law, the intensity of light decreases exponentially depending on the absorption coefficient of the medium through which it propagates [13]. By calculating the effective absorption coefficient α_{eff} the overlap between the narrow emission spectrum of the laser diode, which is shown in Fig. 4 (right) and the absorption coefficient of the crystal is considered [14].

$$\alpha_{\text{eff}} = \frac{\int_0^\infty \alpha(\lambda) \cdot p(\lambda) d\lambda}{\int_0^\infty p(\lambda) d\lambda} = \frac{1}{p} \int_0^\infty \alpha(\lambda) \cdot p(\lambda) d\lambda \tag{1}$$

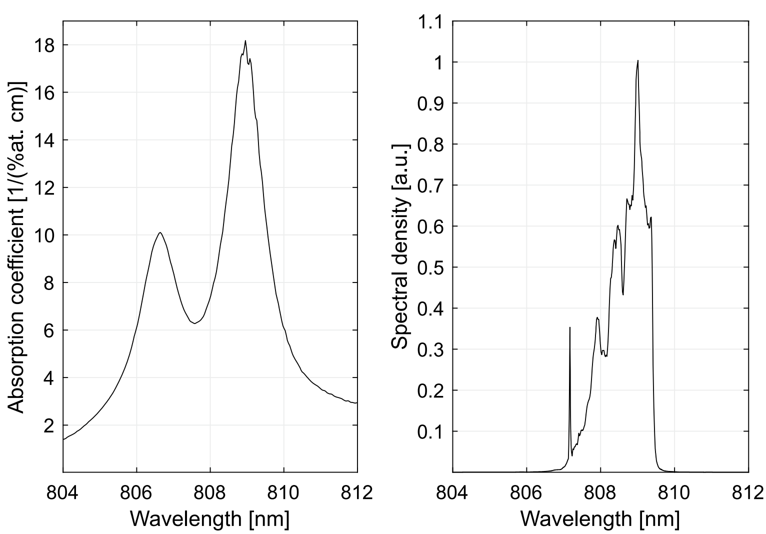

Fig. 4 (Left) Normalized absorption coefficient of Nd:YVO_4; (Right) Spectral density of the pump laser

According to Chen et al., the absorption coefficient of Nd:YVO_4, pumped with a center wavelength of 808 nm, is linear depending on its doping concentration [15]. By multiplying the resulting effective absorption coefficient with a factor of 0.27, according to its doping concentration (0.27 at%), the absorption coefficient of $\alpha = 3.54\ \text{cm}^{-1}$ can be determined.

4.2 Thermal Simulation

The thermal simulation model serves to calculate the heat distribution inside the crystal and the heat sink. First, a heat source is implemented to the model to calculate the generated heat. Furthermore, heat conduction, heat transfer and heat convection are considered to calculate the steady-state heat gradient. Due to the resulting temperature gradient, the heat is conducted through the material of the crystal. Heat is transferred from one component at the interface between the crystal and the heat sink. Inside the heat sink, heat is conducted through the printing material towards the cooling channel. The heat energy convects to the water inside the cooling channel.

Heat Source

When the laser crystal is irradiated, a part of the energy introduced into the laser crystal is converted into heat. The heat generation inside the pumped Nd:YVO_4 crystal can be related, among other things, to the quantum defect, the quantum efficiency, quenching and excited-state absorption [16]. According to Xiong et al. [17], the thermal efficiency of Nd:YVO_4 crystals is dominated by the quantum defect, which can be calculated using Eq. (2).

$$\eta_h = \left(1 - \lambda_{\text{pump}}/\lambda_{\text{Lasing}}\right) \tag{2}$$

To describe the heat generation inside the laser medium, Xiong et al. neglect other absorption mechanisms due to a low doping concentration of <0.5 at% [10]. This assumption will be adopted to implement a heat source since the crystal used has a doping concentration of 0.27 at% heat generation will only be considered for the doped part of the composite crystal.

The total heat load Q results from the proportional relationship between the output power of the laser diode and the thermal efficiency, as shown in Eq. (3).

$$Q = P_{\text{in}} \cdot \eta_h \tag{3}$$

The heat density $q(r, z)$ is described by the heat generation inside the crystal volume. The radial distribution of the induced heat inside the crystal is based on the assumption of a Gaussian intensity profile of the laser beam [18]. The beam radius $\omega_p = 182\ \mu\text{m}$, which is calculated in the optical simulation model, will be inserted in the Eq. (3).

$$q(r,z) = \frac{2Q\alpha}{\pi\omega \mathrm{p}^2}\left(1 - e^{-al}\right)e^{\frac{-2\mathrm{r}^2}{\omega \mathrm{p}^2}}e^{-\alpha l}\ \left[\mathrm{W/m^3}\right] \tag{4}$$

The heat distribution inside the crystal and inside the heat sink can be analyzed by implementing the heat density into the stationary heat transfer Eq. (5). A direct dependency exists between the heat distribution in the system and the heat conduction coefficient, as shown in Eq. (6) [19].

$$\rho C_{\mathrm{P}} u \cdot \nabla T + \nabla \cdot q = Q \tag{5}$$

$$q = -k \cdot \nabla T \tag{6}$$

Heat Transfer

The direct application of the printing material on the surface of the crystal is intended to improve the thermal transition between the two materials. Imperfections, like air pockets or the detachment of printed material, decrease the heat transfer. Grabe et al. show in their research a high impact of the heat transition coefficient on the cooling performance of the heat sink [3]. In order to investigate the influence of the coefficient on the resulting temperature and mechanical stress, the value is iteratively increased in a parameter study to identify limit values for the non-destructive operation of the laser system.

Heat Convection

To reduce the generated heat inside the heat sink water with a temperature of $T = 18$ °C flows through the cooling channel. A computational fluid dynamics simulation model is implemented to represent the heat convection in the cooling channel. To characterize the fluid flow, the calculation of the Reynolds number is required. Therefore, the mean flow velocity $v = 0.97\ \mathrm{m \cdot s^{-1}}$ is calculated, considering the inner diameter of the connected tube and the measured flow rate. By inserting the water density of $\rho = 997\ \mathrm{Kg \cdot m^{-3}}$ the dynamic viscosity $\eta_{\mathrm{H2O,18°C}} = 1.0087$, the diameter of the tube and the flow velocity to Eq. (7), the Reynolds number can be calculated to

$$\mathrm{Re} = \frac{\rho \cdot v \cdot d}{\eta} = \frac{999\frac{\mathrm{Kg}}{\mathrm{m^3}} \cdot 0.97\frac{\mathrm{m}}{\mathrm{s}} \cdot 4 \cdot 10^{-3}\mathrm{m}}{1.0087} = 3827 \tag{7}$$

The critical Reynolds number is approximately $Re_{\mathrm{krit}} = 2300$ [20]. As the Reynolds number exceeds the critical Reynolds number, turbulent flows are more likely to occur.

4.3 Solid Mechanic Simulation

The crystal is mounted approximately stress-free in the heat sink. Due to the introduced energy, a temperature gradient is formed, which results in an expansion of the material. The anisotropic expansion of Nd:YVO_4 is characterized by the coefficients αexp,a = $4.43 \cdot 10^{-6} \cdot K^{-1}$ and $\alpha_{exp,c} = 11.37 \cdot 10^{-6} \cdot K^{-1}$ [17]. The thermal expansion and thus the strain inside the crystal is implemented into the simulation model by using Eq. (8) [19].

$$\varepsilon_{th} = \alpha_{exp}(T - T_{Ref}) \tag{8}$$

By printing the filament onto the crystal, a form-fitting connection can be achieved. Due to the thermal expansion, a pressure load is expected between the surface of the crystal and the heat sink. Thus, no relative displacement between the two components is assumed.

4.4 Model Validation

The multi-physical simulation model is based on a link of individual simulation approaches, which contains assumptions and simplifications. Therefore a validation is required to prove the accuracy of the model and the simulation results.

The heat density approach presented is based on a model developed by Xiong et al. [17] using the software ANSYS [17]. For the comparison of both numerical solutions, the parameters and material properties of Xiong et al. model are adopted to the developed simulation model. In Xiong et al. simulation model, the composite crystal is analyzed in isolation. The boundary condition of constant temperature of $T_0 = 20$ °C on the crystals surface substitute a water-cooled heat sink [17]. The composite Nd:YVO_4/YVO4 crystal Xiong et al. simulate measures $3 \times 3 \times 10$ mm^3 including a 4 mm undoped endcap and is loaded with 5 W of heat.

Figure 5 shows the results of Xiong et al. simulation model and the remodeled simulation model results using the same boundary conditions. The deviation of the calculated maximum temperatures corresponds to approximately 4 %. The deviation at the position $z = 0$ mm is even smaller. However, higher deviation can be found in the range between $z = 6 - 8$ mm. With regard to the calculation of the maximum temperatures and the resulting stress, the temperatures agree with reasonable accuracy.

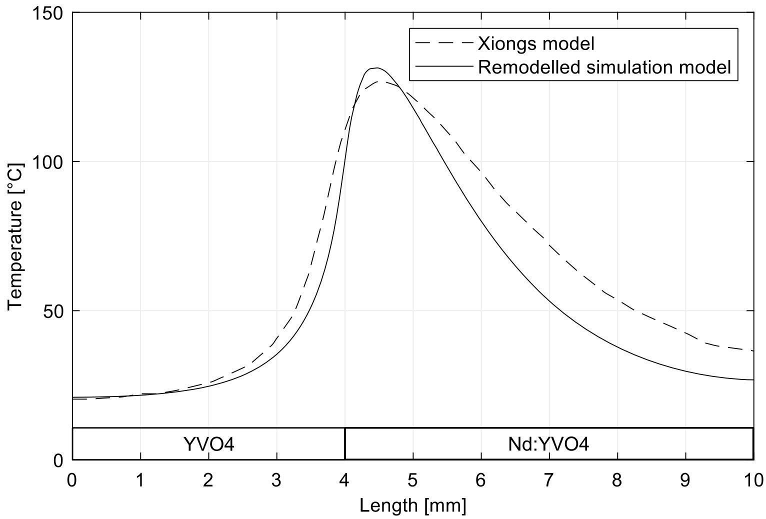

Fig. 5 Stationary studies of longitudinal heat distribution with solid lines for the remodelled simulation model and dashed lines for simulation results by Xiong et al.

5 Simulation Results

To define thermal material requirements for the heat sink, the maximum temperatures in the heat sink are analyzed. In addition, the maximum mechanical stress in the crystal is considered for the derivation of material requirements. Therefore, two parameters are iteratively changed. These are the heat transfer coefficient and the thermal conductivity between the crystal and the heat sink. A parameter study is made in a range of 50 $W/(m^2 \cdot K)$ and 2000 $W/(m^2 \cdot K)$ with a step size of $\Delta h = 50$ $W/(m^2 \cdot K)$.

5.1 Temperature Study

Due to the Gaussian intensity distribution of the laser beam emitted by diode pump laser, the maximum temperature occurs in the center of the crystal. As shown in Fig. 5, the highest temperature along the optical axis occurs shortly after the transition between the end cap and the doped crystal. In Fig. 6, the temperature is shown in dependence on the two investigated parameters. Since the heat source is located in the crystal, the temperature gradient starts from the crystal and goes towards the cooling channel. The highest temperature in the heat sink is at the boundary between the crystal and the heat sink. The calculated maximum heat sink temperature is shown Fig. 6 in dependence of the heat transfer coefficient and the heat conductivity.

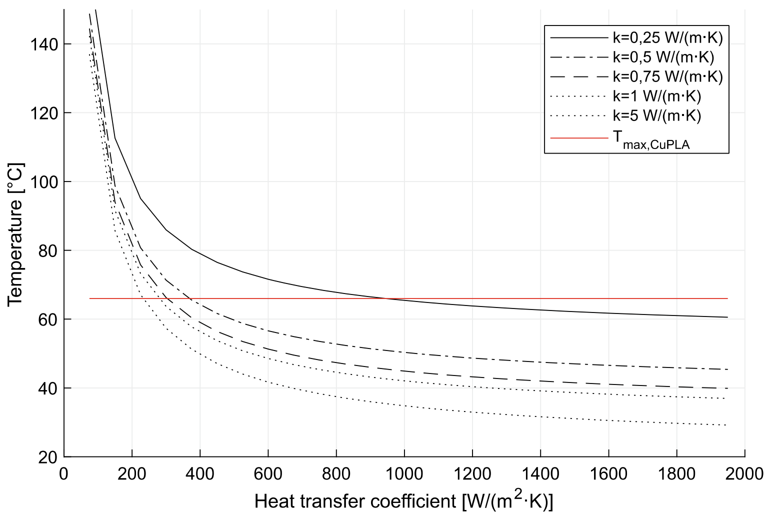

Fig. 6 Thermal simulation results of the parameter study

The softening temperature of the filament $T_{\text{max,CuPLA}} = 66$ °C, given by the manufacturer, defines the permitted maximum temperature of the heat sink material (Table 1). If the temperature is exceeded, a safe fixation of the crystal in its position can no longer be ensured of the crystal cannot be ensured. Permissible parameters can be derived from Fig. 6 taking into account the softening temperature.

5.2 Mechanical Stress Study

The temperature gradient in the crystal causes thermal expansion in the material and thus mechanical stress. Figure 7 shows the maximum stress inside the crystal in dependence on the investigated parameters.

The maximum permitted stress of Nd:YVO_4 crystal is $\sigma_{\text{max,YVO4}} = 53$ MPa (Table 2). If this limit is exceeded, there is an increased risk that the crystal will fracture. Permissible parameters can be derived from Fig. 7.

6 Discussion

6.1 Interpretation of Simulation Results

The simulation results identified a strong influence of the investigated parameters on the mechanical stress and the occurring temperatures. From the data obtained, it can

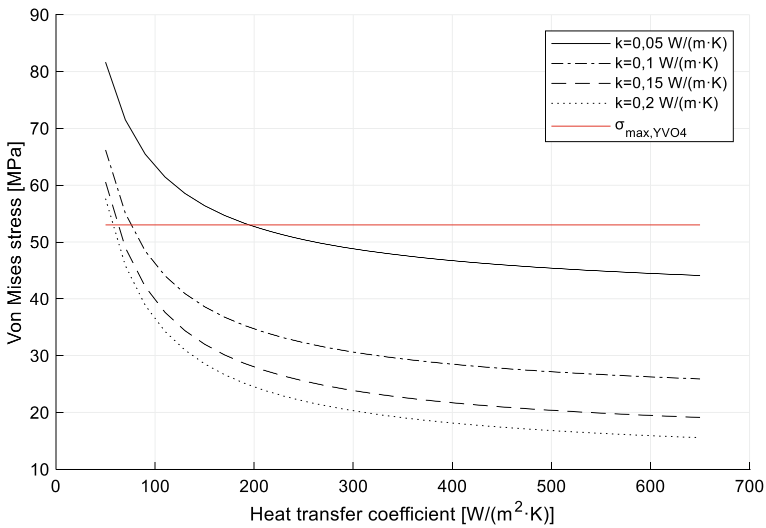

Fig. 7 Solid mechanical simulation results of parameter study

be deduced that the mechanical stress increases exponentially with decreasing thermal conductivity. Similar behavior is observed for the heat transfer coefficient. From the simulation results, a permissible material parameter space can be identified in which softening of the print material and fracturing of the crystal can be prevented.

According to the results of the temperature study, the formerly used copper-filled PLA with $k_{CuPLA} = 0.25$ W/(m $\cdot$ K) is critical for the investigated application. If the heat transfer is smaller than $h_{\min} = 1000$ W/(m^2 $\cdot$ K) the printing material of the heat sink softens due to the resulting temperatures. When using CuPLA, there is also the risk that the crystal will break if the heat transfer falls below $h_{\min} = 90$ W/(m^2 $\cdot$ K). In the temperature study and the mechanical stress study limiting values are derived separately. The limit values from the temperature study determine the required thermal material properties due to their minor magnitude. The requirements defined in this paper must be taken into account when developing printing materials for the laser application described.

In addition to the investigated thermal conductivity, the coefficient of expansion of the printing material and the modulus of elasticity also influence the resulting stress. A factor could be derived from the ratio of these three parameters whose influence on the stresses should be considered in future work.

6.2 Potential for Simulation Model Improvement

By coupling multiple physical effects within one simulation model, the attempt is made to describe the thermal effects comprehensively. Nevertheless, some assumptions were made when building the simulation model. For example, the absorption coefficient was simplified not to be temperature-dependent. Furthermore, saturation effects in the Nd:YVO_4 crystal were not considered when calculating the absorption coefficient. Increasing the level of detail could improve the accuracy of the simulation model.

6.3 Simulation Model Improvements to the State of the Art

In the simulation model, Xiong et al. described the heat distribution inside a composite Nd:YVO_4/YVO4 crystal was calculated. Therefore the simulation model is simplified by isolating the crystal from the heat sink. To consider the cooling capacity, Xiong et al. implemented constant room temperature on the surface of the crystal as a boundary condition. Xiong's approach was adopted and expanded in the multiphysics simulation model by considering the heat transfer through an implemented heat sink. Thus, heat dissipation can be modeled more accurately.

The simulation model described by Grabe et al. [5] provides the possibility to investigate the mechanical stress inside the crystal in dependence on the cooling channel geometry. Also, a strong influence of the heat transfer coefficient was highlighted. Moreover, the simulation model presented in this paper provides the possibility of considering the mismatch between the spectral absorption coefficient of the Nd:YVO_4 and the emitted spectrum of the diode laser. Furthermore, it is possible to implement composite crystals with an undoped endcap.

7 Conclusion and Outlook

7.1 Conclusion

By developing the simulation model for a specific application, a solution space for possible combinations of printing material properties was determined. The influence of thermal conductivity and the heat transfer coefficient on the resulting maximum temperature in the heat sink and the maximum stress in the Nd:YVO_4 crystal are investigated. Taking into account the new material requirements, non-destructive operation of the laser system with printed optomechanics becomes possible.

7.2 Outlook

With the development of the simulation model, the physical interactions in the laser crystal and thus the resulting thermal and mechanical loads can be calculated. In order to fully exploit the possibilities of the simulation model, it is advantageous to apply the method presented to the other additively manufactured optomechanics of the laser system. A general validity of the simulation model could thus be proven. Furthermore, the reliability of the system could be increased with a suitable selection of the printing materials individually adapted to the thermal and mechanical loads that occur in the application.

Acknowledgements This research has been funded by the Deutsche Forschungsgemeinschaft (DFG, German Research Foundation) under Germanys Excellence Strategy within the Cluster of Excellence PhoenixD (EXC 2122, Project ID 390833453), funded by the Ministry for Science and Culture of Lower Saxony (MWK)—School for Additive Manufacturing SAM and funded by EFRE—Nbank within the project GROTESK—Generative Fertigung optischer, thermaler und struktureller Komponenten (ZW6-85018307, ZW6-85017815, ZW6-85017913, ZW6-85018048).

References

1. Lachmayer, R., & Lippert, R.B. (2020). *Entwicklungsmethodik für die Additive Fertigung*. Springer.https://doi.org/10.1007/978-3-662-59789-7.
2. Kranert, F., Budde. J., Neef, P., Bernhard, R., Lammers, M., Rettschlag, K., Grabe, T., Wienke, A., Neumann, J., Wiche, H., Wesling, V., Ahlers, H., Lachmayer, R., & Kracht, D. (2020). 3D-printed, low-cost, lightweight optomechanics for a compact, low-power solid-state amplifier system, p. 4.
3. Kranert, F. (Hrsg). (2021). Thermische und strukturelle Analyse von Polymermaterialen in generativ gefertigten Optomechaniken für den Einsatz in der Laserentwicklung, Bd. 10.
4. Délen, X., Balembois, F., & Georges, P. (2011). Temperature dependence of the emission cross section of Nd:YVO_4 around 1064 nm and consequences on laser operation. *Journal of the Optical Society of America B: Optical Physics, 28*(5), 972. https://doi.org/10.1364/JOSAB.28.000972
5. Grabe, T., Budde, J., Kranert, F., Wienke, A., Neumann, J., Kracht, D., & Lachmayer, R. (2020). Kühlkörper-Designansatz für einen in AlSi10Mg eingebetteten YAG-Laserkristall, S 159– 175. https://doi.org/10.1007/978-3-662-61149-4.
6. Formfutura Datasheet Classic Copper MetalFil
7. Bargel, H.-J., Schulze, G., & Hilbrans, H. (Eds.). (2008). *Werkstoffkunde* (10th ed.). Springer.
8. Elkholy, A., Rouby, M., & Kempers, R. (2019). Characterization of the anisotropic thermal conductivity of additively manufactured components by fused filament fabrication. *Progress in Additive Manufacturing, 4*(4), 497–515. https://doi.org/10.1007/s40964-019-00098-2
9. Wang, Y., Yang, W., Zhou, H., Huo, M., & Zheng, Y. (2013). Temperature dependence of the fractional thermal load of Nd:YVO_4 at 1064 nm lasing and its influence on laser performance. *Optics Express, 21*(15), 18068–18078. https://doi.org/10.1364/OE.21.018068
10. Peng, X., Asundi, A., Chen, Y., & Xiong, Z. (2001). Study of the mechanical properties of Nd:YVO_4 crystal by use of laser interferometry and finite-element analysis. *Applied Optics, 40*(9), 1396–1403. https://doi.org/10.1364/AO.40.001396
11. VDI-Gesellschaft Produktion und Logistik. (2020). Additive manufacturing—Legal aspects of the process chain. VDI-Gesellschaft Produktion und Logistik
12. Kranert, F., Budde, J., Hinkelmann, M., Wienke, A., Neumann, J., Kracht, D., & Lachmayer, R. (2021–2021) Quasi-monolithic laser system based on 3D-printed optomechanics, S. 19.

13. Träger, F. (Ed.). (2007). *Springer handbook of lasers and optics*. Springer.
14. Schöne, W. (1998). *Theoretische und experimentelle Untersuchung thermischer Effekte in diodengepumpten Hochleistungs-Nd:YAG-Stablasern.* Universität. https://doi.org/10.15488/5716
15. Chen, Y.-F. (1999). Design criteria for concentration optimization in scaling diode end-pumped lasers to high powers: Influence of thermal fracture. *IEEE Journal of Quantum Electronics, 35*(2), 234–239. https://doi.org/10.1109/3.740746
16. Blows, J. L., Omatsu, T., Dawes, J., Pask, H., & Tateda, M. (1998). Heat generation in Nd:YVO 4 with and without laser action. *IEEE Photonics Technology Letters, 10*(12), 1727–1729. https://doi.org/10.1109/68.730483
17. Xiong, Z., Li, Z. G., Moore, N., Huang, W. L., & Lim, G. C. (2003). Detailed investigation of thermal effects in longitudinally diode-pumped Nd:YVO/sub 4/lasers. *IEEE Journal of Quantum Electronics, 39*(8), 979–986. https://doi.org/10.1109/JQE.2003.814371
18. Pfistner, C., Weber, R., Weber, H. P., Merazzi, S., & Gruber, R. (1994). Thermal beam distortions in end-pumped Nd:YAG, Nd:GSGG, and Nd:YLF rods. *IEEE Journal of Quantum Electronics, 30*(7), 1605–1615. https://doi.org/10.1109/3.299492
19. Lienhard, J. H. (2011). *A heat transfer textbook* (4th ed.). Dover Publ.
20. Spurk, J. H. (2004). *Strömungslehre* (5th ed.). Springer.

Investigation of Powder Bed Topography by Fringe Projection for Determining the Recoating Process and Powder Bed Quality

D. Jutkuhn, V. Müssig, and C. Emmelmann

Abstract

The quality of the powder layer is a decisive factor for the stability of powder bed fusion processes. Stereo-vision in-situ monitoring based on two high-speed cameras in combination with fringe projection is used to investigate the 3D topography of the powder bed in the L-PBF process. This paper proposes a method to determine the powder layer quality, by developing a powder bed quality factor from the so obtained data of the layers' depth map. The proposed method is evaluated in the course of an empirical investigation, which consists of thirty-six experiments. In a quantitative evaluation, separated aspects of the analysed height data are combined to a powder bed quality factor in order to be able to compare the powder bed quality for different parameter sets. The focus of this analysis is on levelness and reproducibility, compared between layers within one experiment as well as the layers between experiment iterations.

Keywords

Powder bed quality • In-situ monitoring • Laser powder bed fusion

D. Jutkuhn (✉) · V. Müssig
Fraunhofer Research Institution for Additive Manufacturing Technologies IAPT, Hamburg, Germany
e-mail: dennis.jutkuhn@iapt.fraunhofer.de

C. Emmelmann
Institute of Laser and System Technologies, Hamburg University of Technology, Hamburg, Germany

R. Lachmayer et al. (eds.), *Innovative Product Development by Additive Manufacturing 2021*, https://doi.org/10.1007/978-3-031-05918-6_13

1 Introduction

Additive manufacturing has been successfully used in series production for years, yet these processes continue to be restricted by inconsistency in manufacturing quality. Major causes are the nonexistence of universally applicable process parameters and the untracked changes of process conditions leading to process instabilities. In addition, transferability of process parameters between manufacturing machines and parts to be built might not be given. Data and in-depth knowledge regarding the processes could be used, to find parameters for each individual case. Also, process parameters that guarantee long-term robustness during production are an actual challenge [1]. To overcome these limitations, technical solutions like in-situ monitoring systems in combination with intelligent data processing are needed that would allow for the permanent monitoring and consequently for the assurance of the process parameters. To ameliorate systemic limitations of additive manufacturing, various measurement techniques allowing for the direct or indirect measurement of different process parameters have been researched in previous work.

Moreover, integrated stereo camera systems have promising potential to research various process parameters and to provide effective in-situ process monitoring capabilities. In this paper, a method is proposed to measure the stability of the recoating process in Laser Powder Bed Fusion (L-PBF) by quantification of the powder bed quality. The powder bed topography is quantified for applied powder layers by a processing chain that is executed on depth data acquired by a high precision stereo camera system. The qualification method is then empirically tested and evaluated in the experimental phase. From the achieved results a powder bed quality factor (PBQF) is determined to assess the layerwise quality and reproducibility of the recoating process.

2 Powder Bed Quality Assessment by 3D Topography Measurement

The aim of the assessment of the recoating process is to increase the productivity, process stability and product quality of an L-PBF system. In this paper, the powder recoating process is investigated by experimental parameter variation. The focus is on the recoating time and quality of the applied powder layers. The quality and reproducibility of the recoating process and resulting powder layer can be determined from the provided depth map generated by an in-situ powder bed monitoring system. The data analysis is focused on the powder layer thickness, levelness and homogeneity in every single layer and for all layers applied for a specific parameter set.

3 Methodology

This section describes the complete process from data acquisition, over data processing to data evaluation. Additionally, the measurement hardware and its operating principle are being elaborated.

Acquisition of three-dimensional topography data. The depth data used to quantify the topography of the powder layer is acquired by a stereo camera system developed by Hexagon Technology Center GmbH in cooperation with Fraunhofer IAPT. It consists of two high resolution monochrome cameras (7,920 × 6,004 pixels) with Scheimpflug adapter and a mechanical slide projector. Fringe projection is used to reconstruct a three-dimensional scene of the build plane [2, 3]. By using two cameras and a combination of projected stripe patterns, redundant measurement data is collected to fully construct the depth information of the build plane, which has a size of 170 × 170 mm. Prior calibration is used to ensure a high level of precision.

During three-dimensional scene reconstruction, the system produces a three-dimensional triangle mesh with 32 Mio. polygons. However, such high resolution is not required to employ the assessment method of the powder bed quality proposed in this paper. Therefore, the triangle mesh is resampled into a uniformly structured depth map of 2,000 × 2,000 pixel resolution. The ability to deploy the method on the resampled resolution offers multiple advantages: the execution of the data processing runs at higher speed and the decreased amount of data allows for long-term storage to build up an extensive process knowledge database.

The layers' depth map provided by the structured light system has a lateral resolution of 40 µm and a depth variance σ^2 of 3.76 µm. The 95th percentile interval of the random error is bounded at 8.45 µm.

Processing of three-dimensional topography data. An evaluation analysis is required to obtain evaluable data from the measured height profile. Due to the optical setup of the structured light system, calibration and the complex, irreversible processing chain of the height data generation there is a gradient in the height profile of the powder bed that is not related to the orientation of the build plane. For this correction purpose, a height normalization of the acquired data set is carried out first. This is performed in MATLAB, the output data for each measurement is a 2,000 × 2,000 px matrix of the layers' depth map.

First, the original matrix is reduced to a square area of the building platform (1,539 × 1,539 px). The matrix is then subdivided into 9 × 9 areas and the average value of each area is determined. The result is the middle profile k, which is smoothed with a two-dimensional Gaussian filter (sigma 125) to achieve an compensation profile g for the optical correction of the data set.

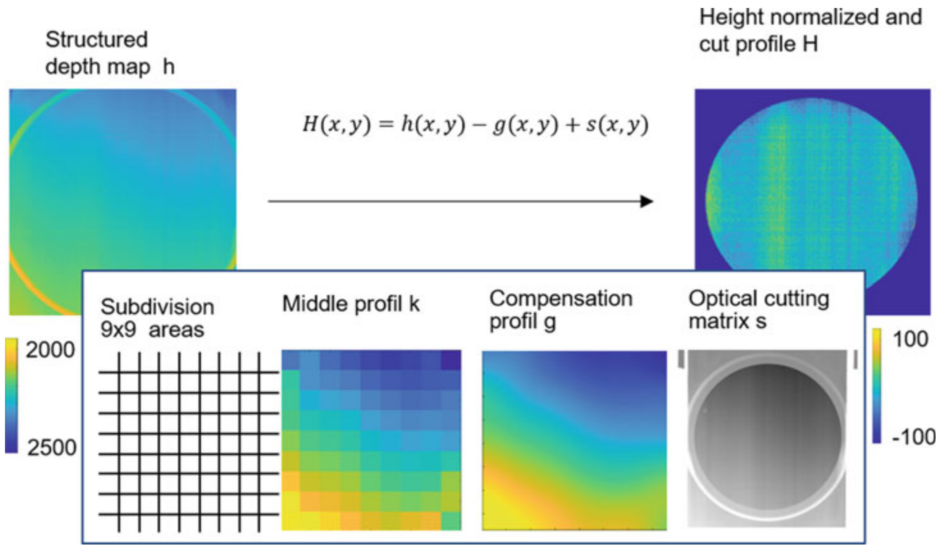

Fig. 1 Data processing chain

For segmentation of the region of interest, the area of the round building platform (170 mm in diameter) is determined with an optically defined cutting matrix s. The diameter of the segmented area is reduced then by 9% to exclude the influence of edge effects of the build platform in the evaluation (see Fig. 1).

In order to be able to compare the layers' depth maps with each other, a reference layer must be reproducible selected for each experiment. For this layer a height normalization is performed and the compensation profile g is applied on all other layers in one experiment. To determine the reference layer, each experiment is evaluated twice. In the first evaluation run, it is assumed that the first evaluated powder layer (layer #30) is the reference layer. A height normalization is carried out for layer #30 and applied to all layers of the experiment. The height mean value M and the height standard deviation σ of each layer are determined and the average ØM and Øσ are determined from them. The layer whose mean value and standard deviation are closest to the average mean value and the average standard deviation ØM and Øσ is assumed to be the final reference layer. For this selected reference layer, the height standard deviation σ is calculated and the height normalization is carried out again and applied to all other layers. In this way, all layers of an experiment are referred to the same reference and thus comparable in the evaluation.

Determination of powder characteristics. A particle analysis is carried out to determine the powder properties. The powder material AlSi10Mg is used in virgin condition (particle size distribution 20–63 µm) and the same powder but already in used/processed condition (sieved with mesh size 100 µm). The CAMSIZER from Microtrac Retsch GmbH is used to examine the particle size, symmetries, sphericity, and the length–width ratio of

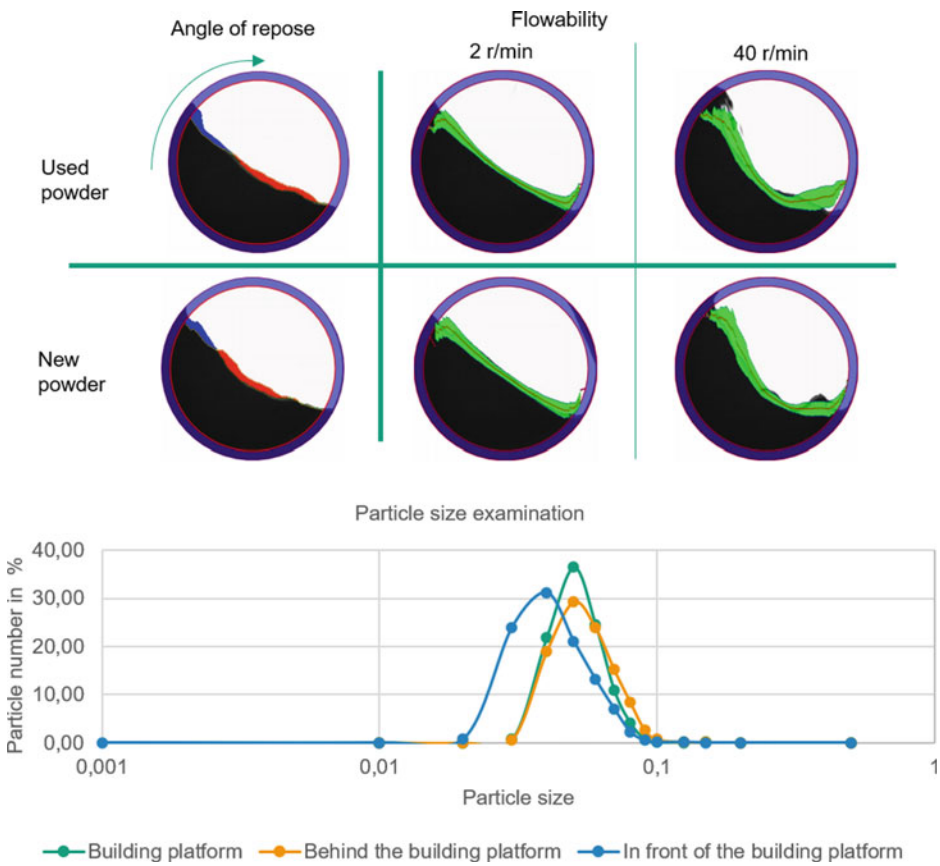

Fig. 2 Determination of powder properties with Granudrum and Camsizer

a particle sample. These samples were taken during the recoating experiments in front of, on and after the build platform from the powder coating. The GRANUDRUM from Granutools is used to measure the flowability and cohesion of the powder. The angle of repose and a cohesion number are determined at different rotational speeds (see Fig. 2).

4 Experimental and Empirical Validation

All tests are carried out on the L-PBF machine AconityLAB from Aconity3D. The powder is shifted from a powder supply through a perforated plate in front of the recoater, which is located in the build chamber. The supplied powder is collected by the recoater and is applied in front of, on and after the build platform. Excess powder is transported over the build platform to a powder overflow. Laser exposure does not take place during the tests.

The variable parameters are:

- Recoater blade type (rubber blade hard, rubber blade soft, carbon brush)
- Recoating speed (50 mm/s, 150 mm/s, 200 mm/s, 250 mm/s, 350 mm/s)
- Layer thickness (30 μm, 60 μm)
- Off-set; lowering of the build platform during recoater return (0.50 mm, 0.25 mm, 0.00 mm)
- Powder characteristics (AlSi10Mg virgin powder 20–63 μm, AlSi10Mg used powder, sieved, mesh size 100 μm)

In each experiment, the powder layers #30 to #60 are examined and the experiment is repeated five times. A total of thirty-six different parameter combinations are investigated. The main effects of all parameter settings are determined in preliminary tests with the aim of identifying and excluding non-target parameters. The aim is on the assessment of the quality criteria powder levelness and layer homogeneity for all single layers and layer batches of all chosen parameter combinations. The identification of a parameter combination with higher quality and at the same time lowest powder application time concludes the investigation.

For the evaluation only the applied layers from #30 to #60 were used due to a transient phase of the layer formation in the recoating process. Initial layers that are applied on a solid surface like the build platform is one are not representable for the recoating quality and of no interest for the investigation of the influence of chosen process parameters. The first twenty-nine layers were applied with corresponding recoating parameters, but the acquired data was not processed.

Qualitative Evaluation. In the qualitative evaluations, the depth maps are visually examined and conclusions are drawn from observed effects. Known effects are identified and can be displayed in high resolution (e.g. trenching in the powder bed for carbon brush). In the following, new effects in the powder bed are presented.

Horizontal height profile of the building platform. The following diagram shows the average height of the different coating blades. The average mean value for the vertically cut segments is shown (see Fig. 3). Experiments with strong outliers or deviations are not considered here.

Different behaviors and height gradients are observed when using different coating blades. A possible cause for this effect is that the coater blade is deformed when clamped in the holder. In experiments with elastomer blades or carbon brush, different vertical height gradients are identified in the powder bed. From the results of the experiments is suggested that the deformation or local deviation of the coater blade during machine setup influence the horizontal shape across the width of a powder bed. The embossing of the underlying coating element is demonstrably established by the examinations.

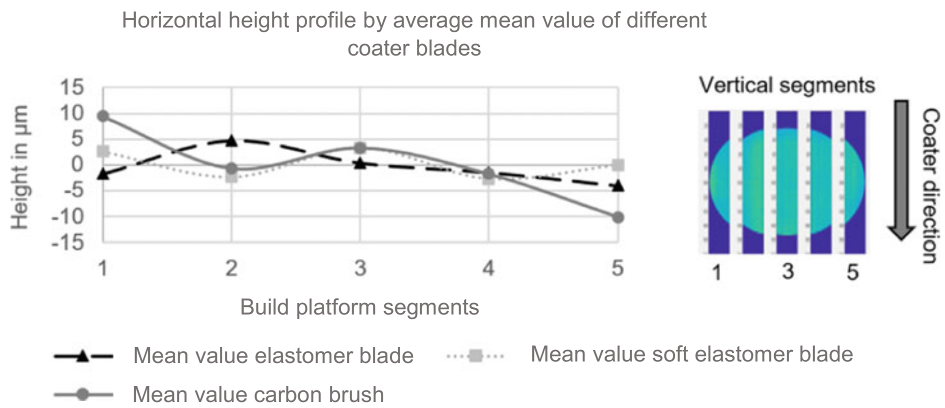

Fig. 3 Average vertical mean curve of different coater blades

Powder flips. On all measurements, more or less deep powder trenches or chatter marks parallel to the coater blade are observed (see Fig. 3). Observed chatter marks in direction of the recoating indicate a vibration of the coater blade. It is suggested that a stick–slip effect occurs on the coater blade during powder spreading. The yielding edge of the coater blade deforms elastically until the elastic energy and the translational kinetic energy exceed the adhesive resistance and the powder flows. The spring energy discharges and causes the coater blade to vibrate. This repetitive effect causes a powder flip and results in the observed chatter marks of the powder bed.

Powder overdosage seems to lead to particularly deep and wide chatter marks. Higher speeds lead here to a larger number of chatter marks (see Fig. 4). A possible explanation for this observation is that the elastic energy of the coater blade is not completely discharged due to the higher coating speed. The coater blade can only vibrate with a small amplitude but at higher frequency.

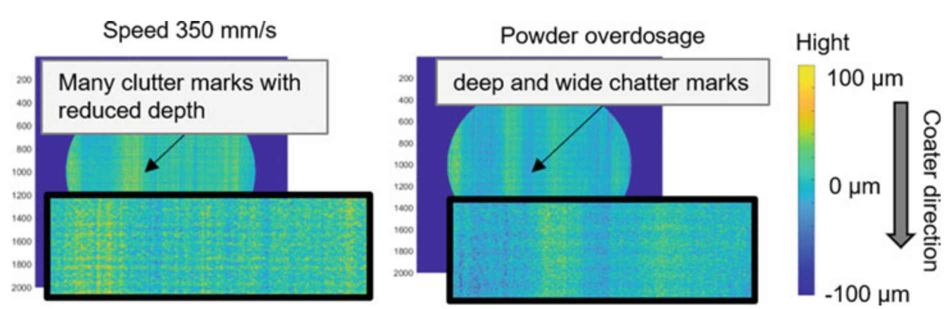

Fig. 4 Chatter marks at higher speed coating and powder overdosage

Regardless of the parameters, chatter marks appear on all scans, especially in the end area of the build platform in coating direction (see Fig. 4). There is a natural segregation process of the particle sizes in the powder when powder is applied and spread over a surface [4, 5]. Small particles are therefore deposited at the beginning of the coating process, while larger particles are usually transported further. This is confirmed by a particle examination with the Camsizer X2 from Microtrac MRB inspired by ISO 13322-2 in areas in front of, on and behind the building platform (see Fig. 4). With a changed particle size distribution, the local flowability of the powder usually changes as well. This results in a locally different load on the coater blade. The resulting vibrations lead to the formation of local chatter marks, which can raise in its intensity with the coating distance.

Vertical powder trenches. In the case of elastomer blades, powder trenches occur, some of which are constant in location over several test series but differ in intensity. Between parameter combinations without cleaning, trenches mainly occur with similar or increasing intensity. Therefore, it can be assumed that the trenches are related to the condition of the coater blade. Occasionally, a powder trench is clearly visible at the beginning of the building platform coating. The trench ends in the middle of the build platform with a powder elevation (see Fig. 5). This indicates that the trenches may be caused by powder adhesion or powder clumping to the coater blade. External effects or the weakening of the adhesion mechanisms often cause the powder deposit to detach from the rubber blade again. As trenches recur at the same locations, it can be assumed that powder accumulation is favoured at said areas of the coater blade. One possible reason for this is that these trenches can be attributed to abrasion effects of the coater blade. Due to the elastic nature of the coater blade, particles can be pressed into the material during the coating process, the so-called “primary particles”. The resulting unevenness of the coater blade causes further particles to adhere in front of and to the primary particle, so that the trenches are

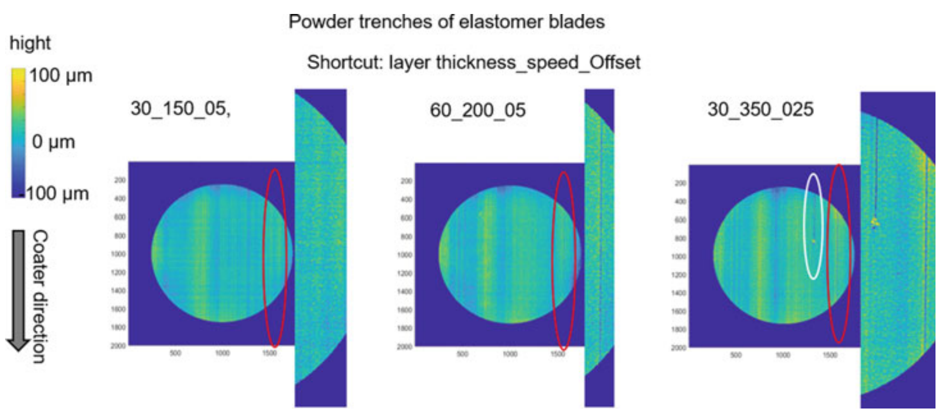

Fig. 5 Powder trenches in different variations of intensity

intensified as the coating process progresses. The pressing in of particles causes lasting damage to the elastomer blade. New particles can be pressed into the damaged area with less resistance after cleaning the blade or detaching the particles. For this reason, the trenches appear mainly in the same areas. [6]

During periodic cleaning, the coater blade is inspected visually without any aids. Irregularities such as deformations cannot be detected at any time. It is possible that wear effects cannot be identified without optical aids.

Vertical Height Profile. A height gradient develops along the powder coating application (see Fig. 6). In the area that the coater reaches first, the average mean value of the powder layer height is below 0 µm (between −1.42 and −16.43 µm). In the back area of the build platform, the average mean value of the powder layer height is above 0 µm (between 0.22 and 13.18 µm). It can be noted that slower coater speeds lead to smaller deviations between these areas, while higher speeds lead to larger deviations. In addition, thicker powder layers are more susceptible to strong variations. Reasons for this are possibly segregation effects during powder application [5]. The powder weight and the decrease of the powder weight over the coating distance could also be causes for this effect.

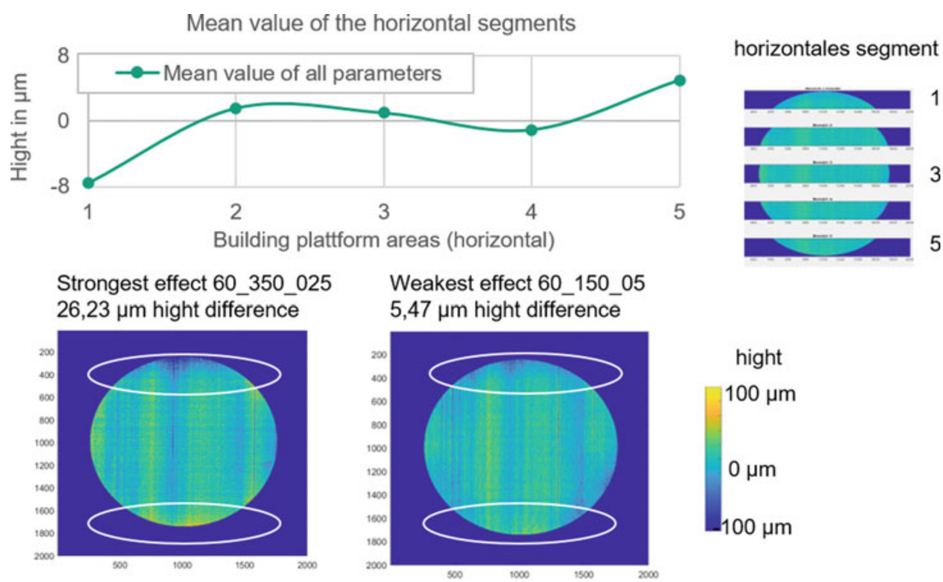

Fig. 6 Analysis of powder bed segments in recoating direction

5 Discussion of Results and Conclusion

The following powder bed effects can be identified in the course of the experiments carried out:

- Parallel to the coater blade: a height gradient can be seen in the powder bed. This is probably caused by deformations of the coater blades.
- Parallel to the coater blade: clatter marks are visible. This is probably caused by oscillation of the coater blade. High powder quantities and high coater speeds intensify this oscillation effect.
- In the direction of the coater: a height gradient occurs. This is probably due to powder segregation and weight loss of the powder during application.
- In the direction of the coater: constant powder trenches can be observed when coating with elastomer blades. This is possibly due to particles digging into the elastomer blade. This probably results in a wear effect that is intensified with the coating distance and amount of applied layers.

Powder bed quality factor PBQF. A powder bed quality factor is being developed to quantitatively express and compare the height data of all experiments. The focus of the PBQF development is on the layer thickness, levelness and homogeneity of the powder layers for different parameter combinations. The development of the PBQF is based on the procedure of the multi-criteria decision analysis. The height properties are weighted and off-set added to the height data. In the process, all height data are related to the standard parameters on a percentage basis in order to exclude unwanted weightings.

The powder bed quality factor consists of three partial factors. The absolute value factor: Here, the absolute height data are entered. The layer consistency factor indicates the susceptibility to variation within a test (layer #30 to #60). It describes how consistent a single experiment can be performed. The reproducibility factor describes the reproducibility between the individual experimental repetitions for a parameter combination. Combined, these factors result in the powder bed quality factor.

The powder bed quality factor shows that layer thickness of 30 µm tend to exhibit higher powder homogeneity. Layer thickness of 60 µm show a higher reproducibility. (see Fig. 7).

Quantitative Evaluation. In a quantitative evaluation, test settings susceptible to variation are quantitatively identified. A variance analysis and a residual analysis are performed and the confidence interval is determined. Test results that deviate strongly from the results of the standard parameters are classified as susceptible to variation. In a process parameter window, the powder bed quality factor and the quantitative evaluation are combined.

With a combined evaluation of the powder application time and the powder bed quality factor, the efficiency of a test can be shown. Here, the parameter combination (layer

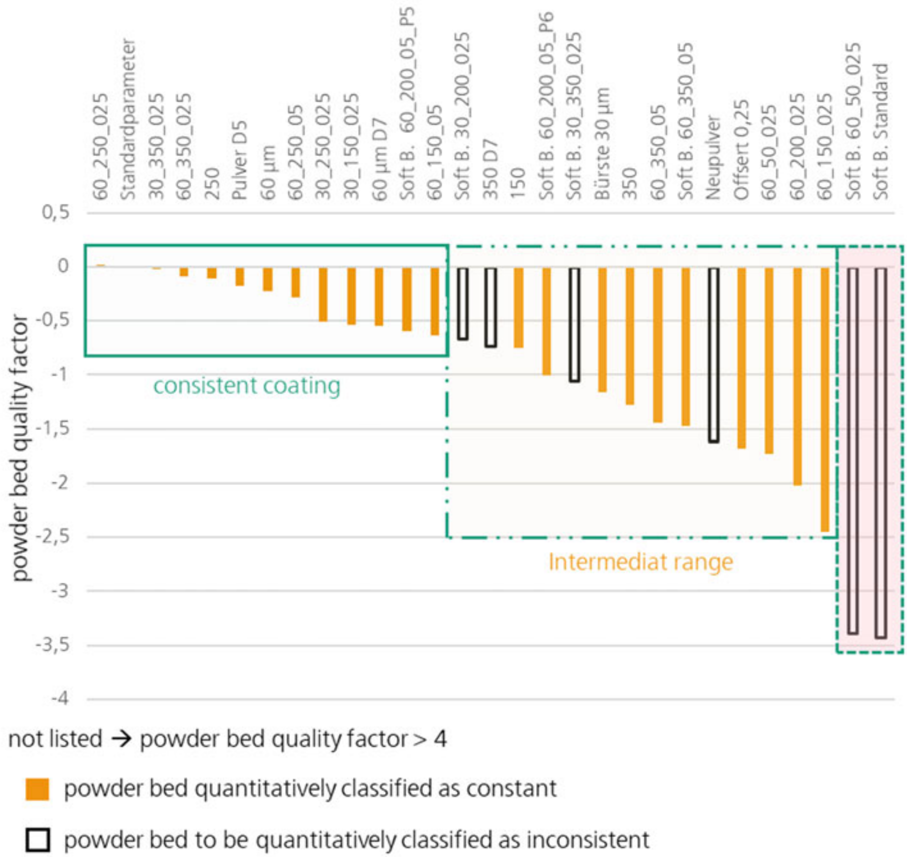

Fig. 7 Evaluation of powder bed quality factor for experimental investigated parameter combinations

thickness: 60 µm, coating speed: 200 mm/s, Off-set: 0.25 mm, AlSi10Mg used powder) achieved both a higher powder bed quality factor and a lower coating application time.

6 Future Work

This paper presents a first approach for the quantitative assessment of powder bed quality. The underlying experiments form a data basis for the analysis of powder bed quality based on height data provided by the measurement system structured light 3D. Further analysis is needed to verify the causes of the qualitative effects. By means of parameter variation, a significant process window for coating application with AlSi10Mg was covered but not investigated in depth. Future work will have to extend this process window and investigate it in more depth in order to provide a more meaningful basis for the determination, selection and weighting of criteria in the assessment of powder bed quality factor. Furthermore, the transferability to other materials as well as different coating application principles need be investigated in further experiments. The validity and applicability of the PBQF also needs to be proofed according to the resulting process and part quality.

References

1. Munsch, M., Schmidt-Lehr, M., & Wycisk, E. (2019). AM power: Metal additive manufacturing market report 2019. https://am-power.de/reports
2. Zhang, B., Ziegert, J., Farahi, F. & Davies, A. (2016). In situ surface topography of laser powder bed fusion using fringe projection. *Additive Manufacturing, 12,* 100–107. https://doi.org/10.1016/j.addma.2016.08.001.
3. Land II, W. S., Zhang, B., Ziegert, J., & Davies, A. (2015). In-situ metrology system for laser powder bed fusion additive process. *Procedia Manufacturing, 1,* 393–403. https://doi.org/10.1016/j.promfg.2015.09.047.
4. Seyda, V., Herzog, D., & Emmelmann, C. (2017). Relationship between powder characteristics and part properties in laser beam melting of Ti–6Al–4V and implications on quality. *Journal of Laser Applications, 29,* 022311. https://doi.org/10.2351/1.4983240.
5. Seyda, V. (2018). *Werkstoff- und Prozessverhalten von Metallpulvern in der laseradditiven Fertigung*. Dissertation. Springer Vieweg, Berlin, Heidelberg. https://doi.org/10.1007/978-3-662-58233-6.
6. Xiang, Z., Zhang, M., Yan, R., Yin, Q. & Zhang, K. (2021). Powder-spreading dynamics and packing quality improvement for laser powder bed fusion additive manufacturing. *Powder Technology, 389,* 278–291. https://doi.org/10.1016/j.powtec.2021.05.036.

Normalization Matrix for Sustainability Assessments Considering the Laser Powder Bed Fusion Process

Johanna Wurst, Iryna Mozgova, and Roland Lachmayer

Abstract

The sustainability assessment of a product and the related process chain is the result of balancing influencing factors. Using different methods, such as life cycle assessment according ISO14040/44, it is possible to determine the ecological impact based on an evaluation of various influencing factors. For being able to identify and validate the potential of laser powder bed fusion process compared to conventional processes, a standardised approach is required. Following the "technical–economic evaluation" as defined in VDI2225 and the basics of the utility value analysis, objectives and evaluation criteria must be established and combined in a methodical approach. In this paper, a possibility to standardise the various influencing factors of additive and conventional manufacturing processes by a developed normalization matrix is presented. The effects of this norming are validated and discussed regarding their applicability based on the process chain of a demonstrator.

Keywords

Life cycle assessment • Laser powder bed fusion • Normalization

1 Introduction

Regarding the continuing trend of the sustainability movement, the question increasingly arises what impact the current activities have on the ecosphere over which time period. As

J. Wurst (✉) · I. Mozgova · R. Lachmayer
Institute of Product Development, Leibniz University Hannover, An der Universität 1, 30823 Garbsen, Germany
e-mail: wurst@ipeg.uni-hannover.de

R. Lachmayer et al. (eds.), *Innovative Product Development by Additive Manufacturing 2021*, https://doi.org/10.1007/978-3-031-05918-6_14

the focus in this case is often on the selection of a better or, in this case, ecologically more sustainable alternative, the impact can be assessed on the basis of decision problems.

One possibility to evaluate the ecological dimension of processes and products is the methodical procedure of the Life Cycle Assessment (LCA) according to the ISO 14040/44 standard. This approach aims to initially record the exchanged elementary flows between the ecosphere and technosphere in a inventory and to subsequently evaluate the ecological impact in a Life Cycle Inventory Assessment (LCIA). In order to be able to formulate a valid result for the solution of the underlying decision problem following this LCIA, the comparability of the results must be ensured.

Normalization is an optional step of the LCA to improve the understanding of the relevant relationships within the results [1]. Moreover, this screening for inconsistencies is covered in ISO 14042 under the title "Preparation for further additional procedures, such as grouping, weighting, and life cycle interpretation".

In this paper, the various challenges of Life Cycle Assessments are first examined in more detail and the relevance of a targeted normalization is highlighted. Following, various assessment and standardized normalization approaches will be presented and a hybrid normalization methodology will be formulated on the basis of these. The study continues with a case study of product manufacturing using laser powder bed fusion, investment casting and milling. In a final paragraph, the findings are discussed and an outlook is presented.

2 Research Background

2.1 Life Cycle Assessment

The ecological sustainability analysis contains the collection and systematic analysis of the ecological impacts of products during their entire life cycle. These environmental impacts include those that occur during the production, use phase and end-of-life phase of a product, as well as upstream and downstream processes [2]. The traditional life cycle assessment according to the ISO 14040 ff. series of standards includes four phases, the "goal and scope definition", the "life cycle inventory analysis", the "life cycle impact assessment" and the "interpretation" of the results (see Fig. 1) [2, 3].

Within the first phase, the scope and the objectives of the analysis are defined, to be able to capture all inputs and outputs of this analysis in a life cycle inventory during the second phase [3]. These inputs are those resources, like raw materials, energy and water. The outputs are resulting emissions in air, soil and water [2, 4, 5]. In the subsequent phase the LCIA, the environmental impacts are calculated based on the results of the previous LCI and classified and interpreted in the final phase [3].

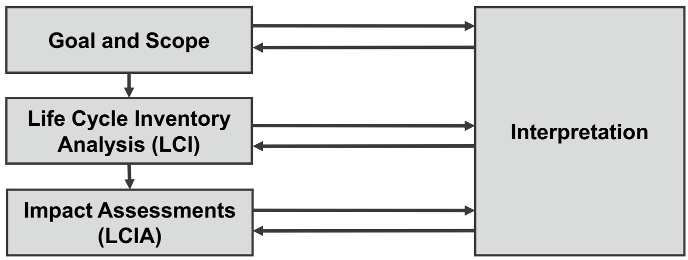

Fig. 1 Components of a life cylce assessment according to ISO 14040 [2]

With regard to the entire ISO 14040ff. series of standards, the principles of implementation and the characteristics of a life cycle assessment are defined. These five principles also serve as requirements for the application of a (holistic) life cycle assessments [2]:

- The analysis must have a relative character, which is defined, for example, by the definition of the functional unit and by the use of results from other methods.
- There is a direct dependency between the level of detail, the period under consideration and the scope of the assessment as well as the related objectives.
- During the preparation of a life cycle assessment, it is not only possible to use one single method, but a variety of different methods, which allow a high degree of interpretation.
- During the evaluation, links between the LCA and other environmental management methods can be identified.
- There is no scientific basis for dealing with the results of LCAs that can summarize these results in an overarching numerical order or numerical single value.

The last point forms the basic motivation for the consideration to develop a methodical procedure, as the quantification of sustainability on the basis of concrete results represents one of the largest gaps and questions within the sustainability assessment.

2.2 Life Cycle Inventory Assessment

Within the phase of the LCIA, the aggregated results of the generated Life Cycle Inventory are evaluated with reference to their impact by various categories [6]. Each of these categories can be calculated by different methods. In the scope of this paper, the focus is on the ReCiPe method, as it includes a variety of different categories and indicators for the holistic coverage of environmental sustainability aspects [7]. Further, a distinction between midpoint and endpoint approaches within this method can be made enabling both problem (midpoint) and damage (endpoint) oriented assessments to be made [7].

Table 1 Categories and indicators of the "ReCiPe"-method [5]

LCIA-categories	Unit	LCIA-indicators	Unit
Land occupation (urban/ agri.)	m^2a	Occupation	m^2*yr
Climate change	kg CO_2-Eq.	Infra-red radiative forcing	W*(yr/m^2)
Freshwater eutrophication	kg 1,4-DCB-Eq.	Hazard-weighted concentration	m^2*yr
Human toxicity	kg 1,4-DCB-Eq.	Hazard-weightes dose	–
Marine ecotoxicity	kg 1,4-DCB-Eq.	Hazard-weighted concentration	m^2*yr
Ozone depletion	kg 1,4-DCB-Eq.	Stratospheric ozone concentration	ppt*yr
Terrestial ecotoxicity	kg CFC-11-Eq.	Hazard-weighted concentration	m^2*yr

A summary of the calculable LCIA categories and indicators of the problem-oriented ReCiPe method are shown in Table 1 [5].

Each of the different categories is represented by different equivalents of substances, which are calculated on the basis of method-specific indicators (see Table 1). The outcomes of the diverse methods, such as the popular CML2001 or the IMPACT2002+, allow for a wide range of different calculation and evaluation approaches [8].

One aim of a successful LCA is to represent the actual environmental mechanisms and interdependencies as close to reality as possible [6]. Therefore, Frischknecht et al. (2019) recommend the use of normalization steps to specifically minimize uncertainties [6].

2.3 Normalization Methods

Normalizing data from a LCA, besides weighting, is a way to generate aggregated results which are directly associated to various references. Generally, a normalization is the calculation of the amount of a result in relation to one or more reference values, these methodological procedures can be clearly distinguished from a following weighting [4, 9]. Using a normalization is subject to different objectives in accordance to the assumptions of Pizzol et al. (2017) [10, 11]. Helias et al. (2021) summarizes these goals, as follows: Results, values are to be compared and plausibility checked. In addition, communication should be facilitated and at the same time a uniform metric for the classification of results should be usable [10, 11].

In order to separate the concepts of normalization and weighting, a temporal distinction can be made [11]. Normalization is a preparation for the weighting step, because the results are combined on one scale, which are relevant for a concluding evaluation

[11]. Moreover, the knowledge regarding the similarity of considered alternatives can be included to the weighting and deviations can be compensated [9].

Myllyviita et al. (2014) deals with the comparison of the two methodological approaches in the context of an LCA of buildings and how far a normalization and/or weighting significantly influences the quality of the results. Within the normalization methods, a distinction can be made between internal and external normalization. An internal normalization refers to the comparison on models with interval scales and definition of the extreme values that can be derived from the considered alternatives [12]. According to Pizzol et al. (2016), the step of internal normalization allows the avoidance of major macroscopic biases consisting strong deviations in the estimation of the range of values [11]. However, this procedure is limited in its applicability, because several alternative solutions must already be given at the beginning of the LCA in order to be able to create an internal ranking [11]. In cases of proportional scales, the results can be evaluated by summing the total results to the value "1".

As an external normalization, the magnitude of the impacts is sorted into a superordinate context, which, for example, a product causes in relation to a reference value in a certain period of time [12]. Such reference system enables a transformation of the LCIA results to meaningful comparative values, which are mostly adapted to certain geographic areas [12]. The application of an external normalization step, in contrast to the internal normalization, finds a high degree of popularity [11]. In this context, it is possible to determine a statement regarding the plausibility of the calculated results for a reference region or a reference system. According to Predo et al. (2017), externally normalized values are also used to check whether the various aggregate results are consistent, as a linear functional correlation is presumed [13].

Seel et al. (2007) describe the systematic comparison of a process or product with a reference system as a possibility to constantly "check whether a reference model is in conformity with the current reality of the company" [14]. Based on the definition of alternatives, metrics must be defined for the evaluation, which can subsequently be weighted. On this basis, these key figures have to be calculated for each alternative before being evaluated [14].

3 Method

The previously described components of a life cycle assessment according to ISO 14040ff. a temporal order of the normalization step is given.

As shown in Fig. 2, the normalization step follows the calculation of the LCIA categories. In addition to these values, requirements for the normalization can already be taken from the first phase of the "Goal and Scope", such as the time frame of the reference system or the lengths of the process chains for each alternative considered. The

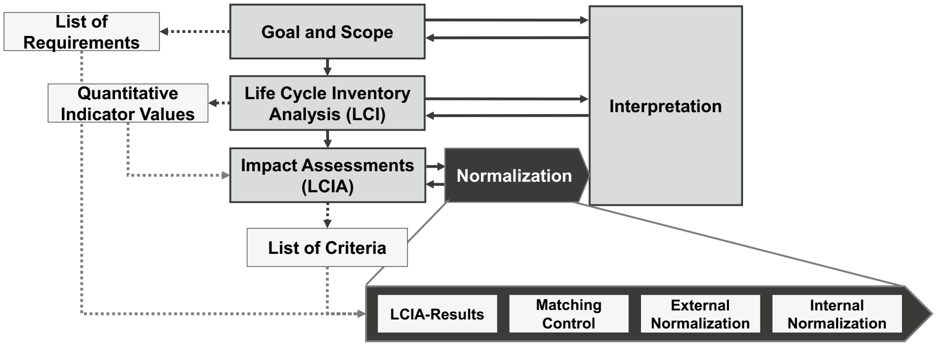

Fig. 2 Integration of the methodical approach for the internal and external normalization within a LCA framework

normalization itself, as a hybrid normalization consisting an external and an internal normalization step, is embedded before the result interpretation (see Fig. 2). This is intended to achieve the aim of providing results that are as meaningful, unbiased and close to reality as possible.

3.1 External Normalization

In the course of the external part of the normalization, first the values of the LCIA categories in the reference system are used as the calculation basis. These calculations cannot be made if either no values are available in the examined reference system or the units of the values differ from another. If these requirements are satisfied, the externally normalized values can be calculated for the results of the LCIA in each case [12]:

$$h_{i,j,E} = S_{i,j} * \frac{h_{i,j,O}}{(a_i * h_{i,R})} \quad (1)$$

For the calculation of the externally normalized values "$h_{i,j,E}$", for all "j" alternatives and for each "i" LCIA category considered. According to the assumptions of Myllyviita et al. (2014), the quotient of the original LCIA value and the category-specific reference value must be formed [12, 13]. In addition, an adjustment factor "a_i" is introduced, which reflects the development of the reference system, so that an adaptation of the available values to current conditions is possible. Furthermore, a component of the utility value analysis in the form of the degree of goal fulfillment "$z_{i,j}$" is added in order to capture information regarding the politically or economically targeted goal systems as well [15]. Depending on the amount of deviation of the LCIA categories from the aimed value, the factor varies from 0 to 4, so that 4 indicates an agreement of more than 60% and 0 an agreement of less than 10%.

3.2 Internal Normalization

In the second normalization step, the alternatives are compared with each other for each LCIA category. Following the internal normalization according to Myllyviitta et al. (2014), the category-specific extreme values are formed as minimum "$h_{i,Min}$" and maximum "$h_{i,Max}$" [12]. Extending the approach, not the original values are used for this calculation, but the results of the previously performed external calculation step "$h_{i,j,E}$".

$$h_{i,j,I} = \frac{\left(h_{i,j,E} - h_{i,Min}\right)}{\left(h_{i,Max} - h_{i,Min}\right)} \tag{2}$$

Since values which are already adapted to the examined reference system are set in relation to each other, the dimensionless internally normalized results allow statements which are directly adapted to the goals and the scope of the LCA.

Following this internal normalization step, a weighting of the results is optional. This weighting aims to show the individual relevance of the diffrent LCIA categories for the scenario considered. Using this weights, different scenarios can be examined and an optimized decision between the alternatives can be made. The dimensionless results, which can be summarized in one scale, allow statements regarding the relevant sustainability potentials as well as the levers regarding the different LCIA categories. Following Ehlers et al. (2020), such sustainability potentials are multidimensional and have several direct dependencies to each other [16]. Through this approach, it is possible to identify connections between the sustainability orientation and actual impacts in the ecosphere [16]. This evaluation, as well as the previous calculation steps, are combined in an MS Excel matrix, requiring only the manual addition of the weights. For the collection of the original LCIA data, "Live-Links" are used as a direct connection between the sustainability assessment software "Umberto LCA+", allowing changes in the process chain and the resulting life cycle inventory as well as LCIA to be automatically adapted to the normalization.

4 Case Study: Laser Powder Bed Fusion, Investment Casting and Milling

For validating the assumed normalization of the LCIA results, a LCA of a product with low complexity was chosen. This approach allows defining the functional unit of the LCA as the "functional volume of the component made of steel that leaves the manufacturing process", which minimizes the scope of the analysis. The time period analyzed in the LCA covers the phases of the product life cycle from raw material extraction to the end of production and can therefore be classified as a "cradle-to-gate" approach. The alternatives considered concern the various manufacturing processes used to produce these components and differ as follows: A (laser powder bed fusion), B (investment casting) and C (milling). For each of these three manufacturing processes, process chains for

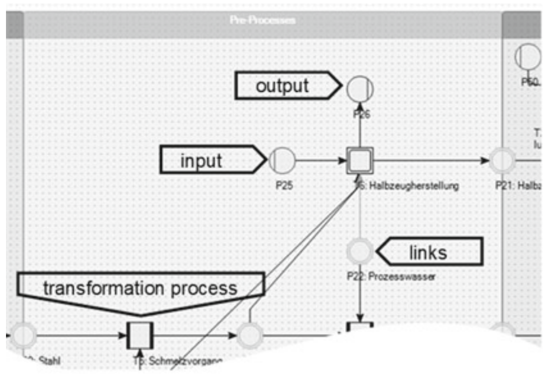

Fig. 3 Detail of the process chains from Umberto LCA+ showing the components of the Petri nets used

the relevant time period were modeled using Petri nets in the sustainability assessment software “Umberto LCA+”, then filled with data and calculated as an LCI. Modeling the processes as Petri nets allows a detailed mapping of the predefined process chains for the different manufacturing processes using inputs, outputs, links and transformation processes (see Fig. 3).

In addition to this model of the process chains, the reference flow forms the basis of the LCIA-calculation defined as a component volume of 0.0012 m^3 manufactured using a basic tool steel, such as 1.2709. In addition to the primary collected data of the production phase, secondary data from comparable case studies as well as data sets of the ecoinvent database are added in preceding process phases.

The goal of these expansions of existing primary data is to modify the level of detail for the process chain to be able to make a valid comparison according the principles of LCA. Regarding the ReCiPe method evaluated in this paper, seven different LCIA categories are identified (see Table 2).

The results shown in Table 2 reveal a wide range between the calculated data of the individual categories as well as the different alternatives. For the example of the “land occupation” category, a value four times higher than alternative A is calculated for alternative C, so there is a high level of variance in the LCIA results even at this early point and a need for normalization. In addition to these calculated values and as a basis for the following first step of the hybrid normalization in form of an external normalization, the data of the reference system is listed. Published values from the Institute for Environment and Sustainability of the Joint Research Centre of the European Commission from 2014, referring to average LCIA factors of the year 2010, serve as the reference system. The values are calculated per person of the approximately 499 million inhabitants of the EU-27 states and are also shown in a cumulative way [17].

The LCIA categories highlighted in grey cannot be used in the following analysis because the reference system either does not provide any reference values or the units differ from each other, which excludes a normalization (see Table 2). Due to this limitation, the remaining four LCIA categories of “climate change”, “ozone depletion”,

Table 2 Results of the LCIA for the three alternative manufacturing processes calculated in accordance to the "ReCiPe (H)" method by Umberto LCA+

						External normalization step		
Method	LCIA categories	Unit	A (LPBF)	B (Casting)	C (milling)	Reference unit	System ILCD sum	EU-27 per person and year
ReCiPe MP (H)	Land occupation	m^2a	95.57	109.29	465.47	kg C deficit	4.06E+10	8.22E+04
	Climate change	CO_2-Equ.	5.44627	10.72499	90.13547	CO_2-Eq.	4.60E+12	9.22E+03
	Human toxicity	1,4-DCB-Equ.	5.96757	5.71856	81.06080	CTUh	1.84E+04	3.96E−05
	Ozone depletion	CFC-11-Equ.	1.65E−04	4,58E−04	2.19E−03	CFC-11-Eq.	1.08E+07	2.16E−02
	Terrestial ecotoxicity	1,4-DCB-Equ.	0.88	2.41	1.27	–	–	–
	Ionising radiation	U235-Eq.	980.23	1.20521	15.61399	U235-Eq.	5.64E−11	1.14E+03
	Fresh water eutrophication	P-Eq.	6.62	6.09	132.17	P-Eq.	7.41E+08	1.76E+00

LCIA-categories	unit	reference system		C (milling)			Internal normalization step reference: external normalized values A (LPBF)	B (casting)	C (milling)
		$h_{i,R}$			$h_{i,j,E}$				
climate change	CO2-Eq.	$h_{1,R}$	9,22E	9,01E+04	$h_{1,3,E}$	9,78	2,36E+00	3,49E+00	0,00E+00
ozone depletion	CFC-11-Eq.	$h_{2,R}$	2,1	2,19E-03	$h_{2,3,E}$	0,10	3,06E-02	4,24E-02	0,00E+00
ionising radiation	U235-Eq.	$h_{3,R}$	1,1	1,56E+04	$h_{3,3,E}$	13,70	3,44E+00	4,23E+00	0,00E+00
freshwater eutrophication	P-Eq.	$h_{4,R}$	1,7	1,32E+02	$h_{4,3,E}$	75,11	1,50E+01	1,38E+01	0,00E+00

Fig. 4 Section of the normalization matrix showing the results of the external normalization step

"ionizing radiation" and "freshwater eutrophication" are normalized first externally and then internally.

4.1 External Normalization Step

In the first step of this methodological approach, the available reference values from 2010 are adapted to the developments of the last 10 years in order to minimize a bias of the results already in this step. Assuming that the reference values have decreased by 0.02% in the last years, the reference values of the individual categories are respectively modified. As introduced in the previous section, the externally normalized values are calculated for the relevant LCIA categories and alternatives according to formula (1). Since the ratio to the higher-level reference system is evaluated in this step, the results are dimensionless and serve as a basis for the following step of internal normalization between the investigated alternatives. In addition, the results from Fig. 4 can be classified into a scale with a positive value range from 0 to 4.5 (see Fig. 4).

4.2 Internal Normalization Step

During the second, internal normalization step, the minimum and maximum values of the considered alternatives are calculated based on the results of the external normalization. Via the quotient of the differences from the external results and the minimum values and the difference from the maximum and minimum values of the LCIA category considered indicates a direct dependency between the results of the alternatives.

In this example, only three alternatives were calculated and compared with each other, therefore the scale range from 0 to 1, if alternative C is neglected, is only filled in a value range from 0.68 to 1 (see Fig. 5). The values shaded in grey are those results that are obtained from a calculation of the differences from alternative A and B without

LCIA-categories	unit	reference system: externa values			
		A		B	
		$h_{i,j,E}$		$h_{i,j,E}$	
climate change	CO2-Eq.	$h_{1,1,E}$	2,36	$h_{1,2,E}$	3,4
I) ozone depletion	CFC-11-Eq.	$h_{2,1,E}$	0,03	$h_{2,2,E}$	0,
ionising radiation	U235-Eq.	$h_{3,1,E}$	3,44	$h_{3,2,E}$	4
freshwater eutrophication	P-Eq.	$h_{4,1,E}$	15,05	$h_{4,2,E}$	13

results: external and internal normalized values							
	A			B			C
I			$h_{i,j,I}$			$h_{i,j,I}$	
$,I$	0,68	0,00	$h_{1,2,I}$	1,00	1,00	$h_{1,3,I}$	0,00
$,I$	0,72	0,00	$h_{2,2,I}$	1,00	1,00	$h_{2,3,I}$	0,00
$1,I$	0,81	0,00	$h_{3,2,I}$	1,00	1,00	$h_{3,3,I}$	0,0
$1,I$	1,00	1,00	$h_{4,2,I}$	0,92	0,00	$h_{4,3,I}$	0,0

Fig. 5 Section of the normalization matrix showing the results of the internal normalization step

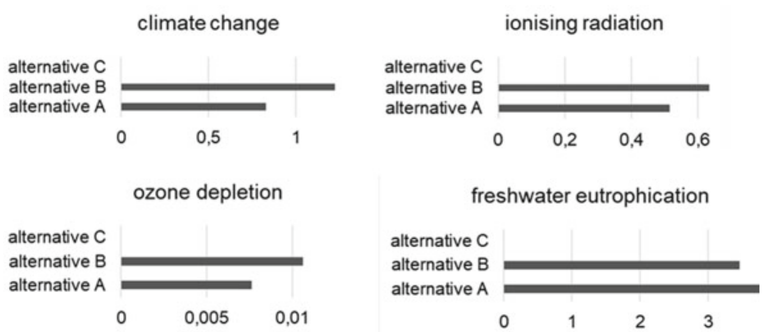

Fig. 6 Internal and external normalized values for each analyzed alternative and LCIA-category

considering the other alternative C. Because of the high differences of the externally normalized values, these results are negative and outside the scale interval, therefore these values are not evaluated further.

After this internal normalization step, the results are calculated with the predefined weights, so that the individual perception regarding the significance of the impacts on the various ecosphere segments is captured. The resulting total hybrid normalization results, which are analyzed in the final fourth step of results interpretation, are shown in Fig. 6.

4.3 Results

The aim of this normalization matrix in form of transforming the original values into dimensionless metrics, allowing comparative statements and serving to solve decision problems, was tested on an exemplary product. The results of the four calculated LCIA results shown in Fig. 7 in relation to the identified reference values of the ILCD can be allocated to a quantifiable unit in the form of substance equivalent values. For the example of the LCIA category "ozone depletion", CFC-11 equivalents are calculated.

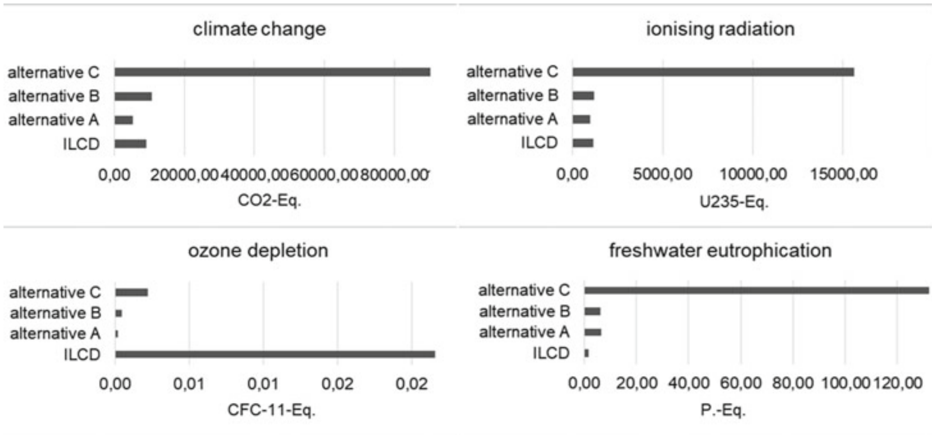

Fig. 7 Original values for each LCIA-category considered in comparison to the ILCD reference system

This calculation of the equivalent therefore shows that CFC emissions are responsible for more than 60% of the ozone depletion [18]. It is a characteristic value for the LCIA category, which has a direct relation to the resulting impact in the ecosphere.

In this example, the "ozone depletion" is the only LCIA category whose ILCD value significantly exceeds those of the analyzed alternatives (see Fig. 7). Therefore, it is questionable if this category is of high significance for the investigated conventional or additive manufacturing processes. This suggestion of minor relevance is further demonstrated by the overall weighted results. As shown in Fig. 6, all compared manufacturing processes for this LCIA category have metrics in the range of 0–0.0122 only. In contrast to the original equivalent-based scales, low values do not reflect a low impact but a low sustainability potential, so this assumption can be strengthened by normalization (see Fig. 6).

For the results of the LCIA categories "climate change" and "ionizing radiation", the highest sustainability potentials can be identified for alternative B, investment casting. The corresponding value ranges of 0–1.24 for "climate change" and 0–0.62 for "ionising radiation" are significantly higher than the range for "ozone depletion" (see Fig. 6). In contrast, the potential of alternative A, the additive LPBF process, dominates the alternative B value bin the LCIA category of "freshwater eutrophication." Consequently, it must be considered how to deal with a high single potential compared to a variety of lower ones of other alternatives during the final interpretation of the whole LCA. For the comparison of the manufacturing processes, the "freshwater eutrophication" forms a leverage, which suggests a positive development tendency.

The strong differences within the LCIA results of alternative C, investment casting, and the other manufacturing processes need to be considered individually. According to Pizzol et al. (2016), such discrepancies in values can occur more often if, for example, the alternatives were not analyzed using a consistent framework or analysis method [11]. Furthermore, incompleteness within the life cycle inventories lead to further biases in the results [1, 11]. It is necessary to look further into whether such errors caused these variations, and to what extent, based on the calculation of further LCAs of various demonstrator products.

In addition, the question remains if the validity of the results can be increased with a higher number of alternatives by comparing further manufacturing processes, other material compositions or by adding and/or changing steps of the process chain.

5 Conclusion and Outlook

Based on the results of this case study and the strong variance between the alternatives of additive manufacturing, investment casting and, in contrast, milling, the question must be answered how to minimize the bias of the LICA-values. Although supporting data sets were used for the calculation of the LCIA categories, the investigated process chain does not pretend to be complete. Thus, the continuing use of these normalized data is subject to an error that should not be ignored in the documentation. In order to handle this challenge of cross alternative data quality and availability, further case studies and evaluation iterations are needed to validate as well as extend the data sets and process chains. However, since one of the principles of building an LCA is to have a comparable level of detail for the alternatives studied, these attempts must be equally pursued for both additive and conventional manufacturing processes, and various demonstrators must be manufactured and analyzed. In addition, the question remains regarding where and how the sensitivity of the results can be ensured [19]. The possibilities of setting up an LCA are too large and the obligatory specifications defined in the ISO 14040ff. series of standards too limited.

Ackknowledgement This research has been funded by the Ministry for Science and Culture of Lower Saxony (MWK)—School for Additive Manufacturing SAM.

References

1. Heijungs, R., Guinée, J., Kleijn, R., Rovers, V. (2007). Bias in normalization: Causes, consequences, detection and remedies. *The International Journal of Life Cycle Assessment, 12,* 211–216. https://doi.org/10.1065/lca2006.07.260
2. International Standard Organization. (2021). *Umweltmanagement—Ökobilanz—Grundsätze und Rahmenbedingungen (ISO 14040:2006 + Amd 1:2020).* Deutsches Institut für Normung e.V. Beuth Verlag GmbH.

3. Johanning, A., & Scholz, D. (2013). A first step towards the integration of life cycle assessment into conceptual aircraft design. In: Deutscher Luft- und Raumfahrtkongress 2013 (DocumentID: 301347)
4. Yang, W.-C., Chon, S.-H., Choe, C.-M., & Yang, J.-Y. (2021). Materials selection method using TOPSIS with some popular normalization methods. *Engineering Research Express, 3*(1). https://doi.org/10.1088/2631-8695/abd5a7 .
5. Acero, A. P., Rodriquez, C., & Ciroth, A. (2015). LCIA methods: Impact assessment methods in life cycle assessment and their impact categories. Green Delta, openLCA.
6. Frischknecht, R., & Jolliet, O. (2019). Global guidance on environmental life cycle impact assessment indicators—Volume 2. United Nations Environment Programme. Life Cycle Initiative.
7. Huijbregts, M. A. J., Steinmann, Z. J. N., Elshout, P. M. F., Stam, G., Verones, F., Viera, M., Zijp, M., Hollander, A., & van Zelm, R. (2016). ReCiPe2016: A harmonised life cycle impact assessment method at midpoint and endpoint level. *The International Journal of Life Cycle Assessment, 22,* 138–147. https://doi.org/10.1007/s11367-016-1246-y .
8. Allacker, K., Souza, D., & Sala, S. (2014). Land use impact assessment in the construction sector: an analysis of LCIA models and case study application. *The International Journal of Life Cycle Assessment, 19,* 1799–1809. https://doi.org/10.1007/s11367-014-0781-7 .
9. Suarez-Alvarez, M. M., Pham, D.-T., Prostov, M. Y., & Prostov, Y. I. (2012). Statistical approach to normalization of feature vectors and clustering of mixed datasets. *Proceedings of the Royal Society A: Mathematical, Physical and Engineering Sciences, 468,* 2630–2651. https://doi.org/10.1098/rspa.2011.0704 .
10. Helias, A., & Servien, R. (2021). Normalisation in LCA: How to ensure consistency?. *The International Journal of Life Cycle Assessment, 26,* 1117–1122. https://doi.org/10.1007/s11367-021-01897-y .
11. Pizzol, M., Laurent, A., Sala, S., Weidema, B., Verones, F., & Koffler, C. (2016). Normalisation and weighting in life cycle assessment: quo vadis? *The International Journal of Life Cycle Assessment, 22,* 853–866. https://doi.org/10.1007/s11367-016-1199-1 .
12. Myllyviita, T., Leskinen, P., & Seppälä, J. (2014). Impact of normalisation, elicitation technique and background information on panel weighting results in life cycle assessment. *The International Journal of Life Cycle Assessment, 19,* 377–386. https://doi.org/10.1007/s11367-013-0645-6 .
13. Prado, V., Wender, B. A., & Seager, T. P. (2017). Interpretation of comparative LCAs: External normalization and a method of mutual differences. *The International Journal of Life Cycle Assessment, 22,* 2018–2029. https://doi.org/10.1007/s11367-017-1281-3 .
14. Seel, C., & Loos, P. (2007). Controlling konfigurativer Referenzmodelle. In: J. Becker, P. Delfmann, & T. Rieke (eds.), *Effiziente Softwareentwicklung mit Referenzmodellen* (pp. 77–106). Physica-Verlag HD. https://doi.org/10.1007/978-3-7908-1994-6_6 .
15. Lindemann, U. (2016). *Handbuch der Produktentwicklung.* Hanser. ISBN 978-3-446-44518-9.
16. Ehlers, T., Wurst, J., & Lachmayer, R. (2020). Bewertung der ökologischen und ökonomischen Nachhaltigkeit in der Additiven Fertigung. In: *In Konstruktion für die Additive Fertigung 2019* (pp. 177–199). Springer Vieweg. https://doi.org/10.1007/978-3-662-61149-4_12 .
17. Benini, L., Mancini, L., Sala, S., Manfredi, S., Schau, E. M., & Pant, R. (2014). Normalisation method and data for Environmental Footprints. In: JRC Technical Reports (Vol. Report EUR 26842 EN). European Commission. Joint Research Centre. Institute for Environment and Sustainability. https://doi.org/10.2788/16415 .
18. Sleeswijk, A. W., van Oers, L. F. C. M., Guinée, J. B., Struijs, J., & Huijbregts, M. A. J. (2008). Normalisation in product life cycle assessment: an LCA of the global and European

economic systems in the year 2000. *The Science of the Total Environment, 390,* 227–240. https://doi.org/10.1016/j.scitotenv.2007.09.040 .

19. Benini, L., & Sala, S. (2016). Uncertainty and sensitivity analysis of normalization factors to methodological assumptions. *The International Journal of Life Cycle Assessment, 21,* 224–236. https://doi.org/10.1007/s11367-015-1013-5 .

Specifications, Potentials and Solution Finding

Additive Manufacturing of 3D Multilayer Devices

Ejvind Olsen, Keno Pflieger, Andreas Evertz,
and Ludger Overmeyer

Abstract

This article presents the design potential of a novel additive manufacturing process for three-dimensional (3D) multilayer devices with vertical interconnect accesses (VIA). The technical approach is based on multilayer printing of alternating metal-containing and insulating ink layers on 3D component surfaces. Additional laser ablation of the insulating coating creates VIA cavities, and the laser structuring of the metal ink sinters the conductive traces. Digital processing with a laser enables high variability in the generation of multilayer circuits. In particular, this enables the specific design of fully additively manufactured components with highly integrated electric circuits, including micro-VIA and fine-pitch contacts for area-array chip packages. An illustrative layout of a fully additive manufactured 3D multidirectional illumination device for customized and controllable lightning of test specimens shows the new freedoms in design that the process provides.

Keywords

Laser ablation • Laser sintering • Conductive traces • Vertical interconnect accesses • Mechatronic integrated devices • Multilayer devices • Multilayer printing

E. Olsen (✉) · K. Pflieger · A. Evertz · L. Overmeyer
Institute of Transport and Automation Technology, Leibniz University Hannover, An der Universität 2, 30823 Garbsen, Germany
e-mail: ejvind.olsen@ita.uni-hannover.de

R. Lachmayer et al. (eds.), *Innovative Product Development by Additive Manufacturing 2021*, https://doi.org/10.1007/978-3-031-05918-6_15

1 Introduction

The increasing demand for highly integrated electronic systems has affected all levels of the production chain. In addition to the progressive high integration of microprocessors (Moore's law) with smaller transistors each year, the ongoing miniaturization also includes packaging and interconnect technologies. Printed circuit boards (PCBs) are the primary circuit carriers for networking electronic components in electronic devices. High-density integrated (HDI) PCBs are realized by increasing the number of conductor layers, reducing the pitch, and implementing vertical interconnect access (VIA). Similar increases in integration as in HDI-PCBs never occurred for spatial circuit carriers of mechatronic integrated device (MID) technologies. The existing MID processes are predominantly substrate-bound and are thus mostly limited to single-layer conductive track circuits. There by, the applications for MID components are characterized by low complexity, e.g., simple circuits, sensor technology, or radio frequency identification (RFID) antennas [1]. In the laser direct structuring (LDS) MID process, the substrate is created by injection molding, patterned by a laser, and chemically metalized [2]. Therefore, metallization is limited to the substrate surface. Only overmolding with an additional LDS layer makes multiple conductive trace layers possible on the MID component surfaces. However, overmolding is only suitable for a small number of additional layers to be produced [3]. Another technology for additive generation of 3D multilayers is directly printing the traces during 3D printing [4]. However, scaling to mass production and generating traces on large-scale components are problematic for technical reasons.

This article presents a novel multilayer printing (MLP) technology for generating conductive traces and VIA directly on free-form spatial surfaces. MLP technology produces hybrid electromechanical 3D multilayer devices (MLDs) and extends the existing 3D MID technology field. Increasing integration is expected to assist future developments in product miniaturization through the direct manufacturing of electronic functional elements (e.g., capacitors and coils [5]) and assembling fine-pitch components on 3D components (e.g., housings [1, 6]). The MLP technique combines alternating insulating and metal nanoparticle ink coatings on a component surface with local laser processing. Laser ablation of the insulator generates VIA cavities, and laser sintering of the metal ink generates conductive structures. The coating with insulating and metal-containing inks can be realized using such application techniques as full-surface and local processes.

The technology field of printed electronics offers a wide range of commercially available functional inks and additive manufacturing technologies for electronic conductors. However, printed structures, e.g., RFID transponders, light-emitting diodes (LEDs), or solar cells [7–9], have been primarily applied to 2D surfaces. Moreover, it is possible to print planar multilayer functional elements [10, 11] and VIA [12]. Because printed electronics require no chemical metallization baths, they are promising to reduce the environmental impact [13]. The recently introduced priming technology for conductive trace generation on additive manufactured and thermally sensitive components makes the

MLP process applicable to various 3D components [6, 14]. This enables to advance the integration density of MID [15] to the current requirements of applications and achieve a more compact product design through the direct routing of complex circuit layouts.

There is still a significant application potential for MID technologies owing to the unique properties resulting from the combination of electronic and mechanical tasks in one component. A recent trend is the increasing need for highly variable production in technology fields driven by individualization, such as biomedical applications [16, 17]. Mass customization and rapid prototyping require supply chains with small batch sizes and short product cycles. Moreover, additive processes make demand-driven manufacturing possible, avoid cost-intensive warehousing, and reduce technical complexity. Conventional MIDs are severely limited in their geometric adaptability owing to the molding process. Some MID technologies (LDS ProtoPaint [18] and additive manufacturing [19]) already have shorter MID product cycles and higher substrate variability for prototype designs [20]. However, all LDS technologies still rely on chemical metallization baths that require complex infrastructure, costly maintenance, and the procurement and environmentally friendly disposal of chemical components. Thus, there is a demand for new MID technologies applicable to various base materials, reduced requirements for costly equipment, and to address customization.

The compatibility of MLP with additively manufactured components and digital laser processing results in high variability. MLP technology is also suitable for prototyping and could become a niche technology for small companies. At the same time, this process can be used with a series of high-volume applications. For example, highly integrated and customized products [21] can be manufactured in the future. Further advantages are the low number of process steps in the process chain and transferability to large-scale components. The production of multilayer MIDs represents a technology that can create a significant competitive advantage in the market. The avoidance of chemical metallization processes and the possibility of shorter logistics chains can positively impact environmental protection. This results in further relevance of the technology for the society and environment.

2 Multilayer Printing (MLP) Approach

The MLP process chain is described in detail in Sect. 2.1. The fundamental approach in this study is based on the alternating printing of functional coatings and local laser processing. Section 2.2 provides an overview of the possible printing techniques, and then the laser processing for sintering (Sect. 2.3), ablation (Sect. 2.4), and cleaning (Sect. 2.5) is discussed.

2.1 Process Chain

The MLP process is presented schematically in the following figures. These schematic illustrations use copper ink as the conductive layers. Nevertheless, conductive inks from different materials are also compatible. Figure 1 schematically illustrates the concept of an MLD component using a mirror-symmetric grid of nine contact pads in a 3 × 3 array. A small number of only nine pads is presented, but, in reality, the number of contact pads can be scaled to an arbitrary complexity of the high-density circuit layout. Even ball grid arrays (BGAs) with 100 contacts (10 × 10 contact arrays) or more are possible.

The dashed black line indicates the mirror plane and the cross-section plane for the following schematic figures. Copper ink is nonconductive after coating and becomes conductive after sintering. Thus, the insulating brown copper ink area seperates the sintered copper areas (orange). The green layer is an insulator material that enables the separation between the conductive layers. The challenge for contacting fine-pitch BGA packages has already become evident with the nine contact pads on the 3D surface. The link to the contact pad with the number 5, or a short circuit between contact pads 3 and 9, can only be realized through the first layer. In addition, the first layer makes routing from contact pads 1 and 7 easier. Highly integrated fine-pitch BGA chips typically have more than 100 contacts (e.g., 10 × 10 arrays), requiring multiple metallization layers and VIA for full routing. Figure 2 illustrates the entire MLP process chain step by step in the cross-section side view (A–A).

The requirements for the 3D substrate (Fig. 2a) are low roughness, high heat stability, and small fillet radii. An optional pretreatment with a primer can achieve reduced roughness and higher heat stability [1]. A full-surface copper ink coating (Fig. 2b) provides nanoparticles for the generation of copper traces. Local laser sintering (Fig. 2c) generates conducting traces by scanning the laser spot across the 3D surface. The processing of another layer is prepared using an insulator coating (Fig. 2d). Laser ablation (Fig. 2e)

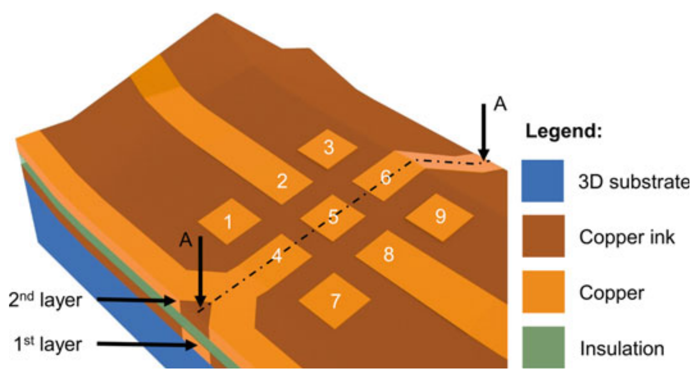

Fig. 1 Schematic of an MLD component with a contact pad array for BGA assembly

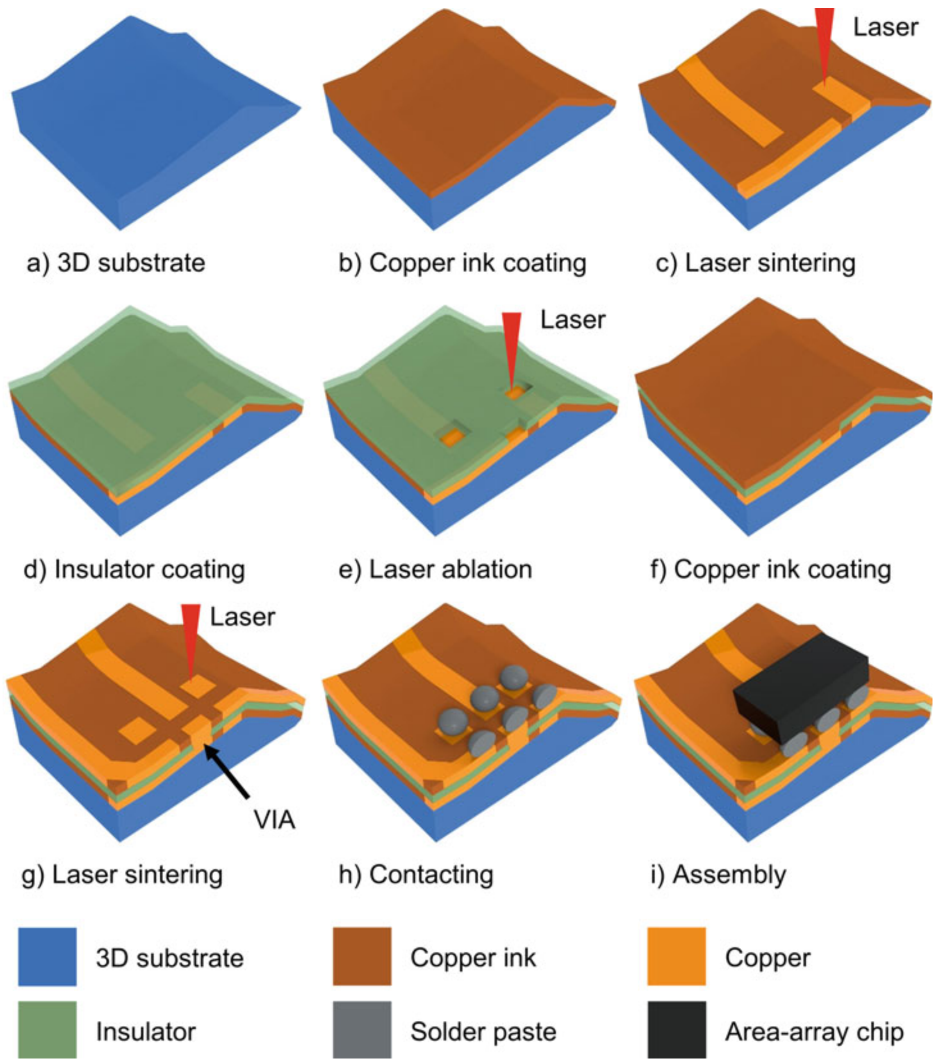

Fig. 2 MLP process diagram, A–A view

of the insulator coating creates cavities for VIA. Another copper ink coating (Fig. 2f) fills the VIA and provides copper nanoparticles for VIA and second-layer sintering. Laser sintering of the second layer (Fig. 2g) sinters the VIA and conductive traces in the same step. The process of applying insulating and copper ink layers (steps d–g) can be repeated multiple times depending on the required complexity of the circuit and the number of layers. Finally, the process chain ends with contacting (Fig. 2h) by solder paste or conductive adhesive and assembly with electric components (Fig. 2i).

Table 1 Overview of the printing processes compatible with the MLP approach. Advantageous properties are indicated by a plus sign, whereas a minus sign indicates disadvantageous properties. Zero stands for neutral

	Speed	Accuracy	Material efficiency	Process complexity	Investment costs
Ink jet [26]	–	–	+	0	0
Aerosol jet [17]	–	0	+	–	+
Spraying [27]	0	–	0	+	–
Dipping [14]	+	0	–	+	–

2.2 Printing of Coatings

Printing with metal and insulating ink plays an essential role in the proposed approach. A wide range of conductive (e.g., copper, silver, carbon nanotube, or platinum) [8] and dielectric (e.g., UV-curing epoxy [14], thermal-curing epoxy [22], zirconium silicate [23], barium titanate [24], or hexagonal boron nitride [25]) inks are available. Table 1 provides a summary of the general advantages and disadvantages of the available printing processes.

The local printing processes (ink jet [26] and aerosol jet [17]) are particularly resource-efficient but slow. In contrast, full-surface processes (spraying [27] and dip coating [14]) offer higher through put but have a higher material consumption. After the inks with conductive ingredients are applied, the sintering process creates conductivity (e.g., thermal, chemical, electrical, or photonic/laser). A full-surface dip or spray coating is preferred for fast throughput and rapid adaptability. However, a local laser sintering process is required if a full-surface coating is applied to the metal ink. Sintering in parallel using a flash lamp is only compatible with local ink deposition processes. The focus of this study was on full-surface ink deposition by dip coating and local laser processing. Nevertheless, the described layer formation is also transferable to more material efficient local coating techniques.

2.3 Laser Sintering

An essential advantage of the presented full-surface coating and local laser sintering process is its flexibility because it is 100% compatible with 2D and 3D surface layer generation at the same time. The laser processing of 3D components requires a optical scanner that includes three optical axes (x, y, and z) to move the laser spot along the surface. Commercial laser systems already offer this hardware combined with customized control software. A short energy input combined with fast cooling rates is one of the main advantages of pulsed laser sintering. This makes the electrical functionalization of temperature-sensitive components (e.g., polymers) possible. Laser sintering on 2D surfaces has been extensively researched for metal-containing coatings with silver [28] and copper [29–31]. Because copper is less expensive than silver with similar electrical conductivity, there are evident economic advantages for the laser sintering of copper. Furthermore, rapid cooling circumvents the oxidation of copper during laser sintering. The single-layer generation of conductive copper traces on additive manufactured primer-pretreated 3D surfaces has reached 10% of the conductivity of elemental copper [14]. The resolution of the conductive traces depends mainly on the adjustable focus diameter.

2.4 Laser Ablation

The first production step for VIA is the generation of a cavity. As shown in Fig. 2e, the ablation of the VIA in the MLP process is also carried out using a laser. In contrast to mechanical drilling, laser ablation of cavities can result in smaller VIA diameters [32]. Because the VIA size mainly depends on the spot diameter, laser ablation has a high potential for miniaturization. The typical producible VIA diameters of standard laser systems for ablation in electronics range from approximately 100 µm (CO_2 laser [12]) and 25 µm (UV laser [33]) to less than 10 µm (ultrashort pulsed laser [34]). The ablation must result in a VIA shape that makes the following two steps of the process chain possible: VIA coating (Fig. 2f) and sintering (Fig. 2g). Therefore, lower aspect ratios and a tapered sidewall are preferable. Recently, it was shown that ablation of epoxy insulating layers with a CO_2 laser results in a desirable parabolic-like sidewall shape. A special feature of the CO_2 laser is that it can be used for ablation and sintering [12].

2.5 Laser Cleaning

Optional laser cleaning can remove residual copper ink using a higher laser power and fast structuring speed [6]. Figure 3 shows the resulting process schematic diagram without (Fig. 3a) and with (Fig. 3b) additional cleaning steps between the additive multilayer process steps.

Cleaning results in a more homogeneous layer system consisting of only sintered conductive tracks and dielectric insulator material. Thus, residual copper ink removal can have a positive effect on the electrical characteristics and mechanical stability.

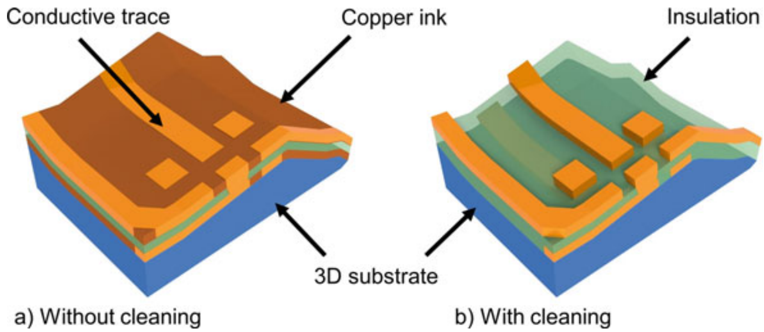

Fig. 3 Effect of residual ink cleaning on the MLP process result

3 Practical Demonstration

In the following subsections, the results from three test results are presented to demonstrate the practicability of the MLP approach in different aspects. The results in Sect. 3.1 show a printed double layer on a planar surface. In Sect. 3.2, a multilayer printed conducting layer on a 3D component is presented. Finally, a printed VIA between a PCB and printed copper layer is shown in Sect. 3.3.

3.1 Printed Double Layer

The printed double layer was generated on a 3D printed (Stratasys, Enden260 VS) 2D polymer substrate (vero blue). The resulting top view after the processing of both layers is shown in Fig. 4a. A polished cross section (Fig. 4b) shows a clear separation of the two layers (approximately 200 μm). The insulation layer is variable regarding the layer thickness. Smaller layer thicknesses are just as possible as larger ones.

Dip coating with copper ink, drying with a heat gun [14], and subsequent CO_2 laser sintering (laser cutter—Epilog Fusion 32 M2 Dual, same parameters as in a previous report [12]) created the first layer with conductive traces (red area). The copper ink used was DM-CUI-5002 (Dycotec Materials Ltd.). An epoxy-based insulating layer (orange area)—DM-INI-7003 insulator ink (Dycotec Materials Ltd.)—was then applied by hand and cured with a broadband UV lamp (BlueWave 50 UV). The insulator was applied by hand with a pipette to keep the ends of the traces of the first layer free to check the conductivity later. Subsequently, another copper ink coating by hand with a pipette and CO_2 laser sintering was used to create the second layer (green area). Resistance measurements proved that no current flowed through the insulating layer, and the top layer

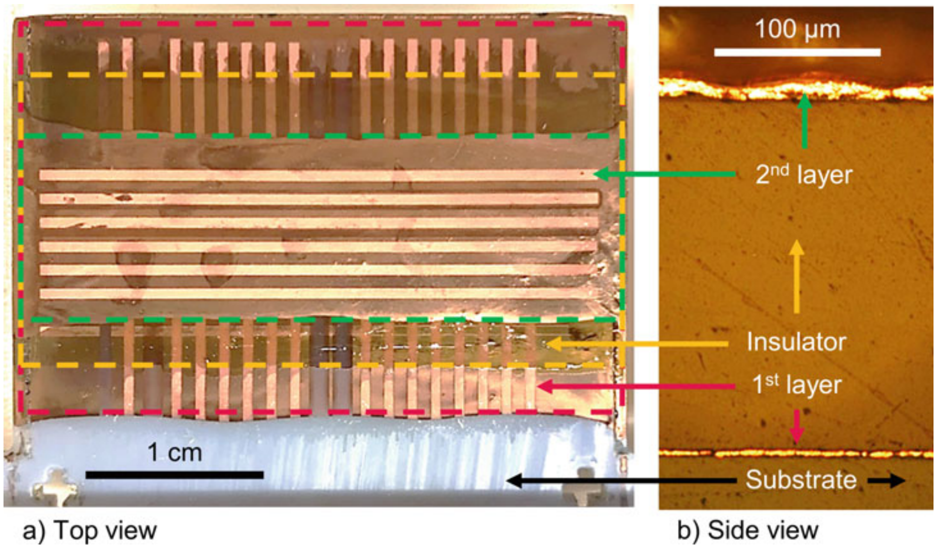

Fig. 4 Printed double layer on a 2D surface

sintering did not negatively affect the first layer. This proves the general producibility of a planar double layer using the presented MLP approach. Recent results [12] have already shown that stacking five or more layers is possible by repeating the approach multiple times.

3.2 3D Multilayer Device (MLD) Component

Next, the compatibility with 3D surfaces was tested. Figure 5 shows a 3D MID hearing aid component before (Fig. 5a) and after (Fig. 5b) printing an additional insulation and copper layer. The applied processing steps and parameters are similar to the previous section, except for the insulator coating thickness (approximately 20 µm) and laser processing. Laser sintering was performed with an Nd:YAG laser system (LPKF 160i) that includes three optical axes (*x*, *y*, and *z*) to adjust the spot to the 3D surface. The sintering parameters were the same as reported in [14].

As in the previous section, the second layer's printing did not negatively impact the first layer. The dielectric strength measurement showed a value well above 10 kV/mm. The successful generation of the 3D multilayer device demonstrated the transferability of the MLP process to 3D surfaces.

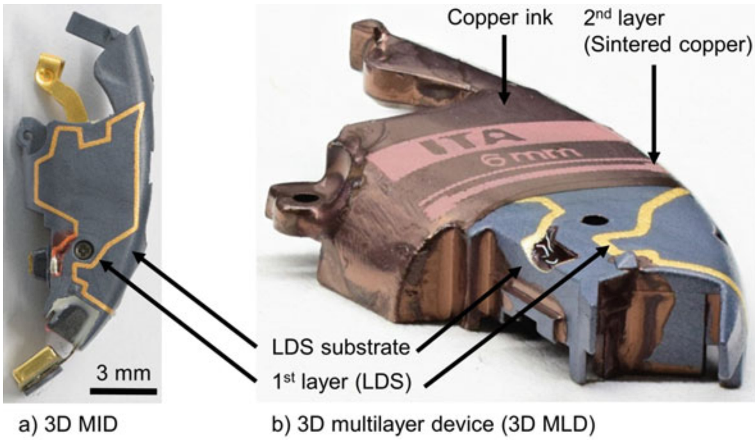

Fig. 5 First practical demonstration of a real 3D MLD

3.3 Vertical Interconnect Accesses (VIA)

The following figure show two cross-sectional views of a PCB (first layer) with a second printed insulator and a copper layer on top. The applied processing is similar to the first double layer in Sect. 3.1, except that the first layer is copper from an FR4 PCB. Figure 6a shows the resulting double layer with a printed insulation layer between the PCB copper and printed copper. As shown in Fig. 6b, the insulator was removed by an additional local CO_2 laser ablation (corresponding to Fig. 2e) before the copper ink coating to generate a VIA cavity filled with copper ink. As shown in Fig. 2g, VIA sintering was performed during the processing of the conductive trace of the second layer.

The VIA from the cross-sectional view in Fig. 6b has a resistance of 6 Ω. In the case of an underlying PCB layer, ablation is highly selective for the insulation material. However, creating a VIA on top of a printed copper layer with a thickness lower than 5 µm is more demanding, but it has already been achieved by Overmeyer et al. in 2021 [12]. The experiments resulted in a working VIA ratio greater than 99%. The additive manufactured

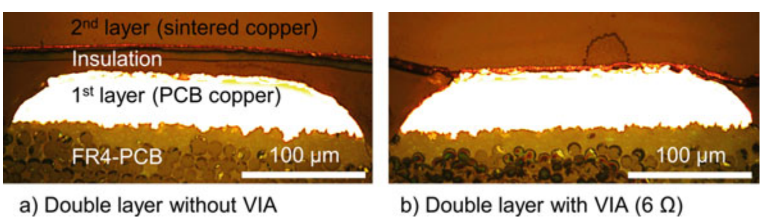

Fig. 6 Printed VIA on a PCB (first layer)

copper VIA reached a mean internal VIA resistance of 1 Ω. Further improvement of the VIA process should make even lower resistance possible in the future. Sintering of the conductive layers and VIA in one process step (corresponding to Fig. 2g) creates beneficial synergy effects.

4 Product Design

The MLP approach results in new possibilities for product design. This section presents an illustrative MLD demonstrator of a controllable 3D LED array on a freeform surface. The function of this device is adjustable multidirectional illumination of test specimens. Consequently, the shadow cast by an undercut can be circumvented. A multilayer structure is required to integrate the densely packed LED and control electronics, including fine-pitch BGA packages. Therefore, the proposed design includes four printed copper ink layers. The fully additive process chain (3D printing of the substrate and consecutive MLP process) enables the customization of the shape of the 3D LED array for possible test specimens. The multilayer on the 3D component surface connect the control electronics on the convex component top side with the LED on the concave component bottom side. The spatial view of a sample design is depicted in Fig. 7 including two additional enlarged views.

Depending on the test object, the 3D LED array component could contain more than 100 individual LEDs, controlled independently by a microcontroller and several LED drivers. The LEDs are mounted very closely together to achieve as many illumination angles as possible. The other components required are LED drivers and a supply circuit (not included in the schematic diagram). A possible application of the 3D LED array could

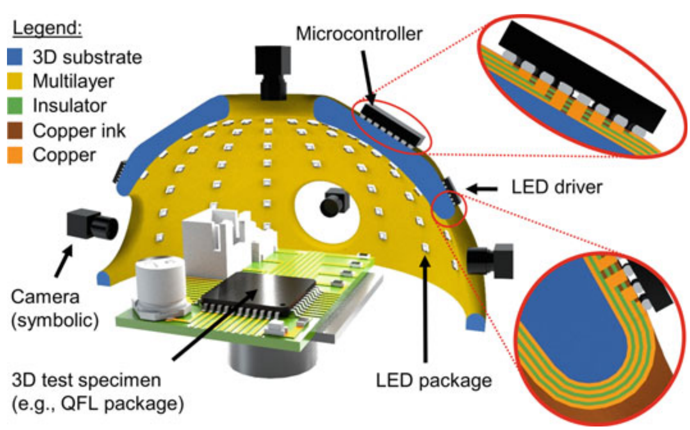

Fig. 7 MLD 3D LED array for controllable 3D illumination

be automated optical inspection. The presented product type (3D MLD with more than four conductive trace layers on the surface) cannot be manufactured using technologies other than MLP.

5 Conclusion

The novel MLP approach presented for manufacturing multilayer conductive structures on 3D spatial surfaces represents a new multilayer MID technology. This process can potentially assist the continuing miniaturization of smart devices by substituting HDI-PCB boards with integrated multilayer circuits on the component surface. One benefit of the current technology is the versatility of the gemeotrie. As shown in this study, the proposed method is suitable for 2D and 3D surfaces. The process exhibits high variability because different conductive inks, insulators, and substrate materials can be used for the MLP technique. Finally, the described controllable 3D LED array on a freeform surface shows the new degree of freedom that can be achieved with the described approach. The study of the feasibility of the presented design is the focus of our future research.

Acknowledgements The authors would like to thank the German Federal Ministry of Economics and Energy (BMWi) for funding the project "3D-MLD" (21780 N/1) based on a resolution of the German Bundestag and the German Research Foundation (DFG) for funding the Cluster of Excellence PhoenixD (EXC 2122, Project ID 390833453) within Germany's Excellence Strategy.

References

1. Dao, Q. H., et al. (2016). Novel design concept of an optoelectronic integrated RF communication module. *Procedia Technology, 26*, 245–251. https://doi.org/10.1016/j.protcy.2016.08.033
2. Laur, V., Mattei, J.-L., Vérissimo, G., Queffelec, P., Lebourgeois, R., & Ganne, J.-P. (2016). Application of molded interconnect device technology to the realization of a self-biased circulator. *Journal of Magnetism and Magnetic Materials, 404*, 126–132. https://doi.org/10.1016/j.jmmm.2015.12.021
3. Leneke, T., Hirsch, S. A., & Schmidt, B. (2008). A multilayer process for fine-pitch assemblies on molded interconnect devices (MIDs). In *2008 2nd electronics system-integration technology conference* (pp. 663–668). https://doi.org/10.1109/ESTC.2008.4684430
4. Lehmhus, D., Busse, M., von Hehl, A., & Jägle, E. (2018). State of the art and emerging trends in additive manufacturing: from multi-material processes to 3D printed electronics. *MATEC Web Conferences, 188*, 3013. https://doi.org/10.1051/matecconf/201818803013
5. Wurz, M. C., Bengsch, S., Roesener, B., & Beringer, S. (Eds.), (2018). Concept for using MID Technology for Advanced Packaging. https://doi.org/10.1109/ECTC.2018.00143
6. Olsen, E., & Overmeyer, L. (2021). Printing of laser-generated conductive copper tracks on 3D components. In *2021 14th international congress Molded Interconnect Devices (MID)*, Amberg, Germany (pp. 1–6). https://doi.org/10.1109/MID50463.2021.9361618

7. Yang, L., Rida, A., Vyas, R., & Tentzeris, M. M. (2007). RFID tag and RF structures on a paper substrate using inkjet-printing technology. *IEEE Transactions on Microwave Theory and Techniques, 55*(12), 2894–2901. https://doi.org/10.1109/TMTT.2007.909886
8. Kamyshny, A., & Magdassi, S. (2014). Conductive nanomaterials for printed electronics. *Small (Weinheim an der Bergstrasse, Germany), 10*(17), 3515–3535. https://doi.org/10.1002/smll.201303000
9. Roberts, R. C., & Tien, N. C. (2013). Multilayer passive RF microfabrication using jet-printed au nanoparticle ink and aerosol-deposited dielectric. In *Transducers & Eurosensors XXVII: The 17th international conference on solid-state sensors, actuators and microsystems*, Barcelona, Spain, 16–20 June 2013 (pp. 178–181). https://doi.org/10.1109/Transducers.2013.6626731
10. Hübler, A. C., Schmidt, G. C., Kempa, H., Reuter, K., Hambsch, M., & Bellmann, M. (2011). Three-dimensional integrated circuit using printed electronics. *Organic Electronics, 12*(3), 419–423. https://doi.org/10.1016/j.orgel.2010.12.010
11. Cai et al., F. (2014). Aerosol jet printing for 3-D multilayer passive microwave circuitry. In *Microwave conference (EuMC), 2014 44th European* (pp. 512–515). Rome. https://doi.org/10.1109/EuMC.2014.6986483
12. Overmeyer, L., Olsen, E., & Hoffmann, G.-A. (2021). Additive manufacturing of copper vertical interconnect accesses by laser processing. *CIRP Annals*. https://doi.org/10.1016/j.cirp.2021.03.006
13. Nazli Altay, B., Bolduc, M., Cloutier, S. G. (2020). Sustainable advanced manufacturing of printed electronics: An environmental consideration. In E. Hwa Yap & A. Huey Ping Tan (Eds.), *Green energy and environment*. IntechOpen. https://doi.org/10.5772/intechopen.91979
14. Olsen, E., & Overmeyer, L. (2021). Laser sintering of copper conductive traces on primer pre-treated additive manufactured 3D surfaces. *Flexible and Printed Electronics, 6*(1), 15006. https://doi.org/10.1088/2058-8585/abdbfd
15. Fischer, C., Franke, J., & Feldmann, K. (2010). Two approaches for the design of molded interconnect devices (3D-MID). In J. Kacprzyk, G. Q. Huang, K. L. Mak, & P. G. Maropoulos (Eds.), *Advances in intelligent and soft computing, vol. 66, Proceedings of the 6th CIRP-sponsored international conference on digital enterprise technology* (pp. 67–78). Springer. https://doi.org/10.1007/978-3-642-10430-5_6
16. Inzelberg, L., & Hanein, Y. (2018). Electrophysiology meets printed electronics: The beginning of a beautiful friendship. *Frontiers in Neuroscience, 12*, 992. https://doi.org/10.3389/fnins.2018.00992
17. Overmeyer, L., Hohnholz, A., Suttmann, O., & Kaierle, S. (2019). Multi-material laser direct writing of aerosol jet layered polymers. *CIRP Annals, 68*(1), 217–220. https://doi.org/10.1016/j.cirp.2019.04.115
18. Kanthamneni, A., Brose, A., Majcherek, S., Brinkhues, S., Aman, A., & Schmidt, B. (2016). Characterization of ultrasonic wire bonding for LDS MID prototyping. *IEEE Transactions on Components, Packaging and Manufacturing Technology,* 6(11), 1703–1710. https://doi.org/10.1109/TCPMT.2016.2617080.
19. Hemmelgarn, F., Ehlert, P., Mager, T., Jurgenhake, C., Dumitrescu, R., & Springer, A. (2021). Evaluation of different additive manufacturing technologies for MIDs in the context of smart sensor systems for retrofit applications. In *2021 14th international congress Molded Interconnect Devices (MID)*, Amberg, Germany (pp. 1–8). https://doi.org/10.1109/MID50463.2021.9361628
20. Eberhardt, W., Buckmüller, P., & Kück, H. (2014). MID Prototyping. In J. Franke (Ed.), *Three-dimensional molded interconnect devices (3D-MID)* (pp. 201–215). Hanser. https://doi.org/10.3139/9781569905524.007

21. Machiels, J., Verma, A., Appeltans, R., Buntinx, M., Ferraris, E., & Deferme, W. (2021). Printed electronics (PE) as an enabling technology to realize flexible mass customized smart applications. *Procedia CIRP, 96*, 115–120. https://doi.org/10.1016/j.procir.2021.01.062
22. Sanchez-Romaguera, V., Madec, M.-B., & Yeates, S. G. (2008). Inkjet printing of 3D metal–insulator–metal crossovers. *Reactive and Functional Polymers, 68*(6), 1052–1058. https://doi.org/10.1016/j.reactfunctpolym.2008.02.007
23. Varghese, J., Teirikangas, M., Puustinen, J., Jantunen, H., & Sebastian, M. T. (2015). Room temperature curable zirconium silicate dielectric ink for electronic applications. *Journal of Materials Chemistry C, 3*(35), 9240–9246. https://doi.org/10.1039/C5TC01388G
24. Siponkoski, T., Nelo, M., Peräntie, J., Juuti, J., & Jantunen, H. (2015). BaTiO3–P(VDF-TrFE) composite ink properties for printed decoupling capacitors. *Composites Part B: Engineering, 70*, 201–205. https://doi.org/10.1016/j.compositesb.2014.11.017
25. Kim, K. K., et al. (2012). Synthesis and characterization of hexagonal boron nitride film as a dielectric layer for graphene devices. *ACS Nano, 6*(10), 8583–8590. https://doi.org/10.1021/nn301675f
26. Ahmadloo, M., & Mousavi, P. (2013). A novel integrated dielectric-and-conductive ink 3D printing technique for fabrication of microwave devices. *IEEE MTT-S International Microwave Symposium Digest (MTT), 2013*, 1–3. https://doi.org/10.1109/MWSYM.2013.6697669
27. Casaluci, S., Gemmi, M., Pellegrini, V., Di Carlo, A., & Bonaccorso, F. (2016). Graphene-based large area dye-sensitized solar cell modules. *Nanoscale, 8*(9), 5368–5378. https://doi.org/10.1039/c5nr07971c
28. Balliu, E., Andersson, H., Engholm, M., Öhlund, T., Nilsson, H.-E., & Olin, H. (2018). Selective laser sintering of inkjet-printed silver nanoparticle inks on paper substrates to achieve highly conductive patterns. *Science and Reports, 8*(1), 1–9. https://doi.org/10.1038/s41598-018-28684-4
29. Yu, J. H., Jung, H. S., Jeong, J. K., & Kang, K.-T. (2019). Sintering behavior of copper nanoparticle ink by laser in air. *Journal of Nanoscience and Nanotechnology, 19*(3), 1261–1268. https://doi.org/10.1166/jnn.2019.16233
30. Yu, J. H., Kang, K.-T., Hwang, J. Y., Lee, S.-H., & Kang, H. (2014). Rapid sintering of copper nano ink using a laser in air. *International Journal of Precision Engineering and Manufacturing, 15*(6), 1051–1054. https://doi.org/10.1007/s12541-014-0435-5
31. Ryu, J., Kim, H.-S., & Hahn, H. T. (2011). Reactive sintering of copper nanoparticles using intense pulsed light for printed electronics. *Journal of Electronic Materials, 40*(1), 42–50. https://doi.org/10.1007/s11664-010-1384-0
32. Kenney, A. L., Dally, J. (1988). Laser drilling of very small electronic via holes in common circuit board materials. https://www.semanticscholar.org/paper/Laser-Drilling-of-Very-Small-Electronic-Via-Holes-Kenney-Dally/34d7224c472171ef4bd442fab616fbf891ad2acd
33. Lei, W., & Davignon, J. (2003). Micro-via drilling applications with solid-state harmonic UV laser systems. In *International congress on applications of lasers & electro-optics*, Jacksonville, Florida, USA, M403. https://doi.org/10.2351/1.5060121
34. Zhao, W., & Wang, L. (2018). Microdrilling of through-holes in flexible printed circuits using picosecond ultrashort pulse laser. *Polymers, 10*(12), 1390. https://doi.org/10.3390/polym10121390

Automated Identification of Geometric Structures with Potential for Functional Integration

Marcel Winkler, Georg Jacobs, Philipp Jonas Fastabend, and Christian Konrad

Abstract

This study presents an automated approach that identifies suitable geometric structures in CAD-data for functional integration. Assemblies are processed and analysed in conjunction with a product's ERP data through filtering processes and classification algorithms. The main focus is on classifying parts regarding their degree of freedom to identify those that allow or restrict relative movement. With this information, the developed approach can recognize static associations of parts without relative movements via modularity optimization. The automated recognition of these static part groups creates starting points for the development of functionally integrated parts for Additive Manufacturing. Finally, it is shown that Additive Manufacturing can be beneficial for the economic production of these parts.

Keywords

Additive manufacturing • Functional integration • Part consolidation

1 Introduction and Motivation

Constantly increasing complexity due to rising performance requirements in the development of new products requires a focus on the function-optimized design of parts. With

The original version of this chapter was revised. Incorrect figures 2 and 4 has now been corrected. The correction to this chapter can be available at https://doi.org/10.1007/978-3-031-05918-6_21

M. Winkler (✉) · G. Jacobs · P. J. Fastabend · C. Konrad
Institute for Machine Elements and Systems Engineering, Schinkelstraße 10, 52062 Aachen, Germany
e-mail: marcel.winkler@imse.rwth-aachen.de

R. Lachmayer et al. (eds.), *Innovative Product Development by Additive Manufacturing 2021*, https://doi.org/10.1007/978-3-031-05918-6_16

its ability to produce complex part geometries, Additive Manufacturing (AM) can play a vital role in the future. Parts can increasingly be designed towards their optimal functional fulfilment due to the increased design freedom and fewer manufacturing restrictions compared to conventional manufacturing processes. This applies not only to individual parts but also to entire assemblies, which can be redesigned regarding the integration of additional functions or the consolidation of adjacent parts. Goals such as higher performance, reduced material usage or a reduction in the number of parts are often at the centre of this functional integration (FI) design process. A reduction in the number of parts can help to cut assembly costs and benefit processes alongside production, thus also offering economic advantages for companies [1–3]. The integration of industrial additive manufacturing processes in production facilities is tied to high investment costs. Therefore, the selection of suitable use cases in the product portfolio of a company represents a fundamental challenge and a necessity for the economic incorporation of AM processes.

2 State of the Art

For the detection of use cases for AM different methods can be applied in practice nowadays. The majority of approaches are highly part-focused and aim to assess various part-specific metrics in a rule-based way to derive potential for AM. Further, knowledge-based data science methods such as machine learning (ML) are increasingly gaining popularity in automated analyses and optimization of parts for AM [4]. However, methods for identifying use cases for FI are not yet fully mature, so that it is often only carried out on small scale or at great effort. Required competencies for a holistic view are often still unavailable in many small and medium-sized companies in mechanical engineering [5, 6]. In the following, a brief overview is given of current data-based identification methods and how initial approaches to identifying potential for FI have been derived.

2.1 Approaches of Part Identification for Additive Manufacturing

The selection of parts to be manufactured by AM is a non-trivial and often tedious process due to the quantity and variety of available data in product development [7–9]. Many approaches to portfolio screening for use cases specialize in part-specific indicators such as size or material [10, 11].

In a recent review, Bracken et al. examine ten commonly used part screening methods for an AM use case identification in industry. A gap in the current state is revealed regarding a holistic view that goes beyond a mere consideration of part parameters. The examined methods each only consider subsets of central criteria regarding part identification. FI is mostly considered as secondary objective and its potentials are not explored extensively. Further, the described approaches need to be carried out under manual supervision. Therefore, getting started with AM is still difficult and uneconomical for many companies. Future research activities are envisioned in the area of automation in part selection through algorithms and ML [12].

This is also supported by Langefeld in a study on the application possibilities of AM [7], as well as in the roadmaps towards automation in the AM sector by the VDMA [8, 9]. The summarised goal is described as solution for companies to quickly find economic use cases in portfolios without having to rely on individual expert knowledge.

In this context, interdisciplinary research initiatives are increasingly focusing their work to develop data-based methods in the field of part identification for AM. Published research approaches of applying artificial intelligence (AI) have already demonstrated promising results. ML approaches can successfully classify 3D geometries based on their complexity to identify parts to be considered for AM [13]. Furthermore, restrictive indicators for AM can also be determined based on 3D geometric data and used for potential ML applications. The "AMFI – Additive Manufacturing Feasibility Indicator" enables the evaluation of the manufacturability of parts and its potential usage as data-label for AI application [14]. The measure can also be integrated into state-of-the-art model-based development processes [15].

As interim conclusion, it becomes clear that approaches to finding individual parts for AM can be successful and well automated with the support of emerging AI methods. However, most approaches described primarily search for individual parts and consider potentials for groups of parts merely as accessory.

2.2 Identification of Use-Cases for Functional Integration

Examination of the state of the art regarding approaches that specifically seek potential for FI reveal a more concise number of available studies. Literature often refers to part consolidation in context of FI – both terms are mostly considered synonymous in literature and also for this study.

The early approach by Reiher et al. addresses the issue of part consolidation checks in assemblies. A part is selected for AM based on other potentials like described above and adjacent parts to this initial part are evaluated for FI [16]. Currently, approaches like this are most prevalent in practice of FI since the primary evaluation of potentials for FI is a rather complex problem. In industrial practice, no ready-to-use procedures have been established yet.

However, approaches in research state are already developing first solutions. The research team of Yang et al. present an approach [17] that uses a graph-based property network utilizing part properties and contact properties between adjacent parts to analyse potentials for FI systematically. Criteria such as build space, material, electric function, expected lifetime, mountability and degrees of freedom are allocated to parts

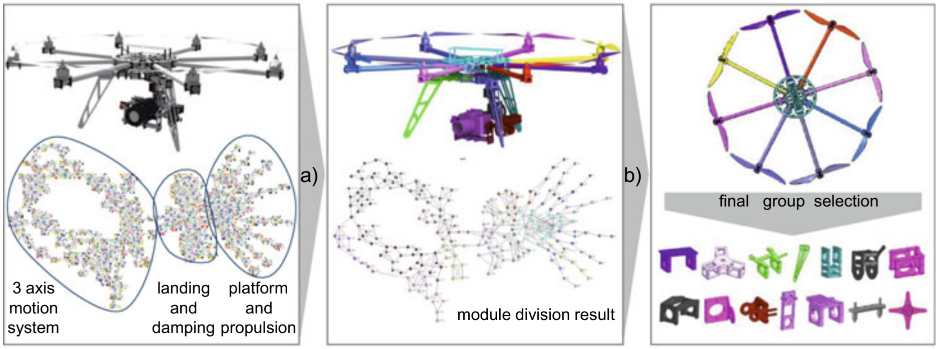

Fig. 1 Approach of finding candidates for AM part consolidation by **a** applying modularisation algorithm and **b** property- based division into groups regarding feasibility [18]

and their contacts. Individual parts and connections that are unsuitable for FI are detected and removed within the scope of the property network. Finally, only well-suited parts for FI remain in the solution space. The estimation of properties like lifetime or mountability is effortful and the whole process is rather complex and time-consuming for huge assemblies. For this reason, a modularity-based decomposition is used to separate complex products into modules potentially suitable for consolidation [18]. The modularity analysis realises a preselection of part groups with probability for FI use cases. The process is shown in Fig. 1.

3 Need for Research

The presented state of the art indicates the need for further research into methodological approaches to support identification of use cases for FI that might be suitable for AM. Developing a generally applicable method in a constantly evolving field of technology such as AM is a challenging task.

The procedure of Yang et al. [17, 18] already provides promising first steps for the systematic identification of use cases. However, there is still opportunity for improvement to provide an efficient foundational approach. The presented method mostly depends on implicit, individual knowledge of engineers who are aware of the functional and technical context of focused products. The required effort to generate a property network is time-consuming. Additionally, parts are usually redesigned when AM is used, so that implemented properties such as material might be changed. Therefore, neglecting parts for FI on the basis of such properties limits the solution space inadmissibly. Also, modularity is not always suitable for pre-selection of assemblies, as it does not necessarily represent the functional relationships within a product.

To conclude, there is a need for an enhancement for the identification of part groups for AM. In order to provide a robust approach, a method is proposed in this study that operates on the basis of geometric properties and the degrees of freedom (DoF) of parts. DoF play a fundamental role in deciding whether two parts can be combined into a solid unit. Consolidating two parts with different relative motion is rarely technically expedient, which is why DoF serve as a more robust criterion compared to modularity. Further, changes in DoF occur only rarely when a functional redesign of products is pursued. In addition, the criterion enables the division of a data set into small groups that can be considered in isolation with regard to additional factors. This reduction of the solution space efficiently supports a subsequent evaluation of the groups for FI.

The *research hypothesises* of the study therefore claims that parts holding a static bond with other parts within an assembly of a product, and accordingly have no relative degrees of freedom to each other, are suitable use cases for FI and can be considered for optimization and manufacturing using AM.

Thus, the *aim of the study* is to develop an identification method of part groups in CAD datasets that are in a static association and therefore potentially suitable for functional integration. Thereby it is intended to provide support for the essential identification of AM use cases.

The main *research question* arises from the hypothesis and goal statement and is divided into three sub-questions to be answered in this study.

- How can part groups with potential for functional integration be identified by the degrees of freedom in their connection in CAD assemblies?
  - Which elements are restrictive for a static connection between parts or favour it?
  - According to which criteria is it possible to classify these elements into groups?
  - How can static part groups be identified in the classified data set?

4 Methodical Approach and Materials

The starting point of the data-based process for evaluating FI as shown in Fig. 2, is formed by the CAD- and ERP- data of a technical product. The process is divided into four steps described in this section.

At first, the entire product is analysed to identify assemblies that are most likely to contain suitable use cases for FI due to the geometric proximity of parts. Afterwards, the identified assemblies are filtered by connecting the ERP-data with the CAD-files. Subsystems, mainly supplier parts such as electric motors, hydraulic pumps or other closed purchase units that are unattractive for FI in this context are identified and removed from the product structure (PS). This step facilitates the evaluation of the remaining assembly in terms of relative movements.

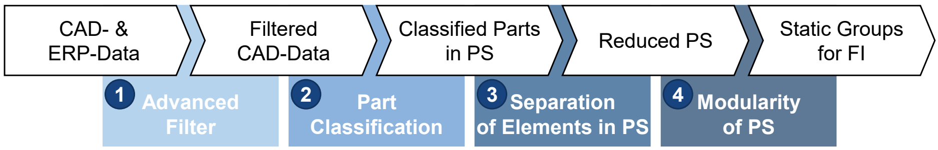

Fig. 2 Methodical approach for the identification of part groups with potential for functional integration

The approach of this study differs from existing approaches, since DoF are assigned a fundamental importance for the recognition of static groups and their automated analysis. To achieve this, parts are classified in terms of their DoF as next step. This involves defining groups of parts that typically have *internal* or *external* DoF, or which fulfil a connecting function and thus *restrict* DoF. From the collected information in CAD and ERP data, products can be analysed according to these specifications and the information about the part classes can be integrated into the graph of the PS.

The graph of the PS can be separated at the corresponding joints where relative movements occur in the third step, when the part classification is complete. Thus, the PS is further reduced and broken down into groups without relative movements.

By performing a modularity analysis in the fourth step, the static groups can be output in the data. Finally, proposed part groups can be reviewed with regard to further functional and technical criteria for AM application.

The methodological approach is conceptualized to ensure applicability to a wide range of industrial data sets. The main focus is primarily on technical products from small and medium-sized mechanical and plant engineering companies. In the following, the example of a gearbox is used for illustration and an example from an industrial project is used to validate the approach capabilities. Internal data of the company is presented in an alienated form for data protection. The application of the method requires two data sets: the CAD data of the product under consideration and related information from ERP data. The data format used in this study is the commonly used STEP AP 214 exchange format for CAD-files. Data from the ERP system associated with the product is used as Microsoft Excel sheets to ensure broad usability of the approach.

4.1 Advanced Filter Structure for Preselection of Suitable Assemblies

The automated preselection of suitable assemblies for FI aims to reduce the amount of initial data to simplify subsequent process steps. Selection criteria used for preselection build on geometric factors aiming for relevant AM part properties. A formal definition of an optimization function J for preselecting CAD-assemblies is intended. Due to the high costs and the limited build space of AM-processes, small parts with low volumes are particularly favourable for AM. For this reason, (1) part volume, (2) bounding box volume and 3) arithmetic distance to adjacent parts are used as cost criteria for a first delimitation of the considered part spectrum. Further criteria can potentially be integrated into the function likewise, however the ones mentioned are assessed as sufficient for the objective. To increase the assessment of FI, the degree of cross-linking is defined as part property and represents the number of parts that one part is connected to. This parameter represents a suitable criterion, because larger numbers of connected parts increase the probability for suitable parts for FI. Conversely, the degree of cross-linking is insufficient as cost criteria, because unsuitable parts for AM like large sheet metal parts can own a high degree of cross-linking as well. Therefore, it is used as weight factor. The optimization function J (1) accordingly consists of the cost criteria Ck and one combining weight factor G.

$$J_k = \frac{1}{\sum G_i^2} \sum_{i=1}^{n} G_1^2 C_{k,i} \tag{1}$$

For a combination of the values Jk the 2-Norm is used. Technical products typically consist of different kinds of assemblies. There are assemblies consisting of only few parts with large dimensions, as well as assemblies containing many small parts with compact distribution. Due to present limitations of the dimensioning of AM parts, compact groups are primarily focused. To address this aspect, the term of J is divided by the total number of parts n (2).

$$J = \frac{1}{n}\sqrt{J_1^2 + J_2^2 + J_3^2} \tag{2}$$

For any given dataset, J can be calculated for each assembly and the results can be presented as shown in Fig. 3 in the left diagram. The parts of the whole product can additionally be represented as digital points for a visual support of the user in CAD.

Overall, the minimization of J leads to an identification of assemblies with a great accumulation of small parts in small building volumes. ASM_1 has the lowest values for J and a high density of small parts. By focusing on individual assemblies in this way, the

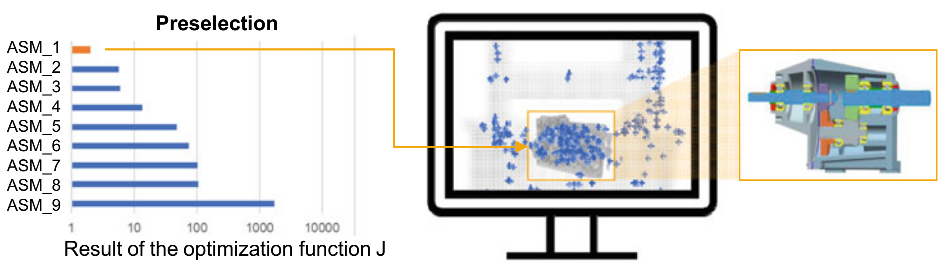

Fig. 3 Schematic procedure for pre-filtering to find assemblies of focus like the gearbox [19] shown as example

subsequent process steps can be carried out more efficiently. The presented preselection approach based on mentioned criteria is primarily suitable regarding capabilities of today's industrial AM systems. The following consideration regarding DoF for FI on the other hand, are independent of manufacturing processes.

4.2 Part Classification According to Degrees of Freedom

The classification of parts according to specific part properties plays a major role in the evaluation of FI. It is easy to examine numerical properties like size or part volume directly from the datasets. More challenging is the extraction of information that is implicit. For example, the distinction whether a part is manufactured in-house or procured usually cannot be extracted from CAD files. The same applies to knowledge about product functions, like existing relative movements between parts. Two approaches are discussed to obtain such tacit information:

1. Artificial Neural Networks
2. Semantic investigation of the part names

In general, it is possible to train neural networks with labelled CAD or ERP data to extract tacit knowledge like it is done in [13] for a single part analysis in terms of AM. But it is required to train a neural network for each identification process separately. For this reason, the effort is exceptionally high for a collection of identification processes such as would be needed in this approach.

Therefore, a semantic investigation is further exploited in this study and relates to the naming of parts and the tacit knowledge contained therein. Typically, part numbers and names are assigned in most companies to allocate parts in ERP data. Also, parts can be designated with prefixes that reveal information about certain part properties (e.g. ASM—Assembly, SP—Standard Part, EL—Electric Part). When company-specific designations are derived, knowledge about the functional context can be gained. In this way, parts of special interest groups can be recognised in ERP and linked to CAD data.

As stated before, the DoF is an elementary part property in the application of FI. Two parts that perform relative movement to each other cannot be consolidated in a static group. Static groups are considered as collections of parts that are connected in the PS and perform the same movement. For example, a shaft, a gear and a feather key can be part of the same static group.

Three major part groups are defined as relevant for the classification regarding the DoF (see Fig. 4). In principle, separating or connecting functions of parts represent the central criterion for classification. The group of separating parts is further divided into parts with *internal* DoF and *external* DoF. Part groups with an internal DoF like bearings, springs or dampers typically appear as single part in the product data and cause a relative movement

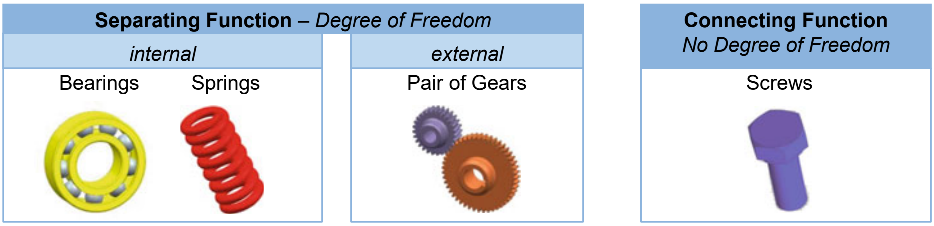

Fig. 4 Overview of different part classification groups with examples

between two (or more) connected parts. In contrast, parts with external DoF occur as a pair, like gears that exhibit a relative movement to each other. In addition, parts *restricting* DoF such as screws are considered as third classification group.

4.3 Separation of Elements in Product Structure

By correctly assigning all characteristic parts, the assembly can be separated into static groups and considerations in terms of FI can be focused on identified groups. For this separation, characteristic parts with relative motion can be removed from the PS because they cannot be assigned to a static group. The process is visualized in Fig. 5. The procedure is automated via the NXopen API in the CAD-Software Siemens NX. Algorithms are implemented to obtain the PS automatically and transfer it as adjacency matrix to Excel for further processing. Subsequently, the extracted matrix is processed in the open-source graph analysis tool Gephi. Gephi provides methods to visualize, analyse and process graphs [20]. In the graph of the PS parts are represented as nodes and the connections between parts as edges. The model and the PS of the gearbox is given in Fig. 5a.

The presented characteristic parts with internal DoF are drawn from ERP data and the knowledge is transferred into the graph. Looking into the example, the only relevant term for parts with internal DoF is "bearing". Other part classes with external relative movement like "radial shaft seal" can be processed in an equivalent manner. In the example,

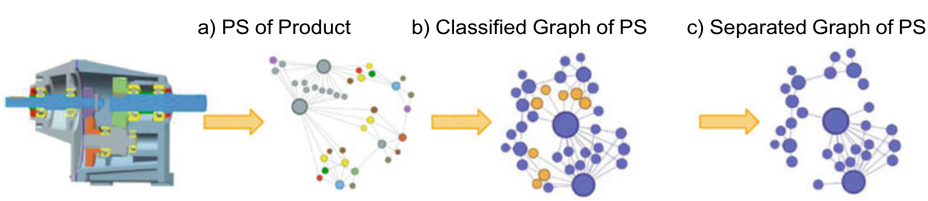

Fig. 5 Derivation of the **a** product structure with **b** representation of the classified parts and **c** unravelled PS

part names are determined by semi-automatic analysis of the assembly data. With regard to analyses of larger amounts of data is beneficial to create a standardised list of the characteristic terms from ERP data for classification.

Characteristic parts with internal DoF are removed in the graph of the PS when classification is complete. The effect is shown in Fig. 5b, c. Similarly, edges between two parts with external DoF can also be removed.

4.4 Modularity of Product Structure to Find Static Groups

Even though the removal of the identified parts might not lead to a complete partitioning of the assembly into static groups, the linkage between different static groups is weakened. The separation of all pairs of parts with external relative movement theoretically leads to the definition of static groups. Nevertheless, it can be assumed that not all characteristic parts can be found. On the one hand, no integrity can be assumed for the collection of part names used, and on the other hand, the CAD data occasionally contains errors. However, the topology of the graph of the PS generated in Fig. 5c is well suited to support automated identification of static groups by a modularity analysis. The Louvain-algorithm for extraction of communities from networks, available in Gephi, is used to achieve the separated outcome of the PS highlighted in Fig. 6a.

Static groups with potential for FI can be found in the present product for example in the yellow marked gear shaft group (see Fig. 6b). The part shown in Fig. 6c illustrates an example how a FI variant of a gear shaft can be designed. Parts like shaft and gearwheel are integrated into one single part, alongside with channels for the supply of lubricant [21].

5 Results

As result of this study, following aspects can be stated regarding the developed approach. Products can be pre- filtered solely on the basis of geometrical information in CAD data

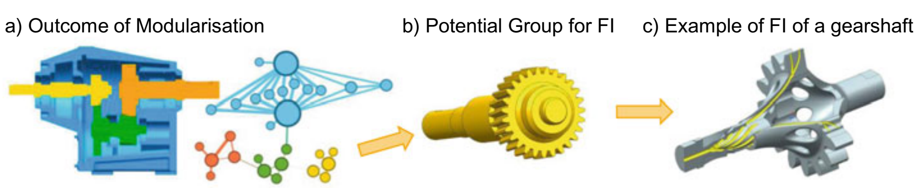

Fig. 6 Workflow after performing **a** modularisation algorithm on reduced PS to **b** select potential parts for FI to **c** develop an exemplary part using FI [21]

to focus the scope of consideration to relevant assemblies. The classification of parts according to their DoF is *expedient* to narrow the dataset for the identification of static groups with suitability for FI. For the separation, the assignment of parts into characteristic groups with fixational function and internal or external DoF is favourable. The division can be automated by classification algorithms that draw information from the part designations in ERP lists. The result of the classification can be mapped to the graph of the PS to support visual traceability of the separation of the graph at nodes (parts with internal DoF) or edges (connections between parts with relative DoF). Static part groups can successfully be identified in conclusion by modularity in the PS graph and visualised in CAD.

The algorithm successfully provides a basis for identifying possible use cases for FI by dividing the entire solution space into isolated part groups. Whether identified groups are ultimately suitable for FI needs to be further evaluated from a technical and economic point of view.

In the following, the application of the developed approach will be validated based on an industrial example and the result will be discussed.

5.1 Validation and Discussion

The company's internal data for validation will only be presented in an alienated form for reasons of data protection. For the identification of AM use cases, CAD datasets as well as the associated ERP data are provided to perform the method flow presented in Fig. 2.

Company-specific prefixes are considered when classifying the parts to ensure correct allocation. The result of the method application is shown in form of the classified graph of the PS after modularisation in Gephi in Fig. 7a. Static groups only consisting of parts

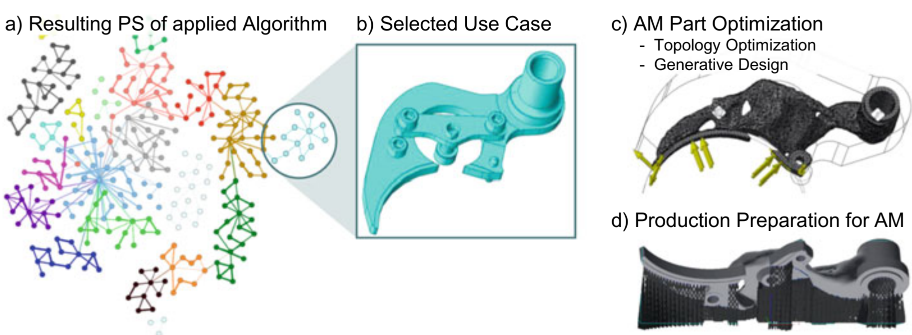

Fig. 7 **a** Application of the developed approach to an industrial project example with the **b** subsequent use case selection, **c** part optimization using functional integration and **d** production preparation for AM

without relative movement are visibly separated by the algorithm to support use case selection. The use case shown in Fig. 7b is chosen for optimization regarding FI for AM. Various optimization workflows can be carried out at this point, such as topology optimization or a complete redesign by generative design, based on active surfaces and load cases. After production preparation in manufacturing specific software, the cost for AM can finally be estimated.

In the example, savings in manufacturing cost of 43% can be achieved compared to conventional manufacturing. Besides a technical improvement, the redesign of the part utilizing FI combines eight of the previous parts into one single part. This also raises potential to save costs in terms of storage, logistics or overhead. However, it needs to be noted that the presented cost comparison cannot be seen as generally valid, but always needs to be determined on a company-specific basis. There are many internal factors like existing process capabilities or hourly rates that can vary greatly among industries.

6 Summary and Outlook

To summarize, a methodical approach is presented that enables use case identification for functional integration to support design optimization with regard to AM. The analysis of CAD and ERP data sets with respect to the degrees of freedom of parts plays a fundamental role. Based on the classification of parts, CAD assemblies and their product structure can be processed via modularisation to unveil part groups that can be combined as static compound. The validation further reveals that these part groups are suitable as starting point for optimization processes regarding functional integration and AM can be beneficial from a technical and economic point of view. Looking ahead, possibilities for refinement of the presented approach appear. For example, part classification purely on geometrical data basis is conceivable to reduce the dependency on fully maintained ERP data. For this purpose, part classification methods need to be enhanced. In the future, fully automated classification by more capable ML algorithms is envisaged. Those can be trained to recognise characteristic part classes and integration into the presented approach is designated. Furthermore, it can be helpful to re-evaluate used data types. For example, the STEP AP 242 as standard for model-based product development offers more extensive analysis options. This way contextual information about connections like tolerances could be considered. In general, advances in digital tools are needed to support the process of redesigning parts and assemblies for AM. Besides methods for evaluating feasibility which can be applied in subsequent process steps (see Sect. 2.1), there is a lack of time-efficient and accurate cost forecasts tools to additionally incentivise the consideration of AM already in early stages of product development.

References

1. Ziebart, J. R. (2012). Ein konstruktionsmethodischer Ansatz zur Funktionsintegration. Ph.D. Thesis, Technische Universität Braunschweig, Braunschweig.
2. Wagner, C. (2018). Funktionsintegration im Rahmen einer fertigungsgetriebenen Produktentwicklung. Ph.D. Thesis, Technische Universität Darmstadt, Darmstadt.
3. Campbell, I., Diegel, O., Kowen. J., Mostow, N., & Wohlers, T. (2021). *Wohlers Report 2021: 3D Printing and Additive Manufacturing Global State of the Industry*. WOHLERS Associates, Fort Collins (Colorado).
4. Ellsel, C., Werner, S., Göpfert, J., & Stark, R. (2021). Evaluation of design support tools for additive manufacturing and conceptualisation of an integrated knowledge management framework. In *DS 111: Proceedings of the 32nd Symposium Design for X*. *Proceedings of the 32nd Symposium Design for X. 27 and 28 September 2021: The Design Society*. https://doi.org/10.35199/dfx2021.17
5. Caviezel, C., Grünwald, R., Ehrenberg-Solies, S., Kind, S., Jetzke, T., & Bovenschulte, M. (2017). Additive Fertigungsverfahren (3-D-Druck)—Innovation analyse. Büro für Technikfolgen-Abschätzung beim Deutschen Bundestag (TAB), Berlin.
6. Karevska, S., Steinberg, G., Müller, A., Wienken, R., Kilger, C., & Krauss, D. (2019). *3D-Printing: Hype or game changer?: A global EY Report 2019*. EYGM Limited.
7. Langefeld, B. (2020). *De-risking your supply chain in times of the coronavirus—How a digital inventory and additive manufacturing can mitigate risks*. Roland Berger GmbH.
8. VDMA Arbeitsgemeinschaft AM (2018). *Additive Manufacturing Metall-Pulverbett Automatisierungs Roadmap: SMART FACTORY*. VDMA, Frankfurt.
9. VDMA Arbeitsgemeinschaft AM (2020). *Additive Manufacturing Kunststoff Pulverbett Automatisierungs Roadmap: SMART FACTORY*. VDMA, Frankfurt.
10. Lachmayer, R., & Lippert, R. B. (2020). Entwicklungsmethodik für die Additive Fertigung. *Springer Vieweg, Berlin, Heidelberg*. https://doi.org/10.1007/978-3-662-59789-7
11. Klahn, C., Meboldt, M., Fontana, F. F., Leutenecker-Twelsiek, B., & Jansen, J. (2021). Entwicklung und Konstruktion für die Additive Fertigung. Vogel Communications Group, Würzburg.
12. Bracken, J. E., McComb, C., Simpson, T. W., & Jablokow, K. W. (2020). A review of part filtering methods for additive manufacturing. In *46th Design Automation Conference (DAC) [V11AT11A030] (Proceedings of the ASME Design Engineering Technical Conference; Vol. 11A-2020). American Society of Mechanical Engineers (ASME)*. https://doi.org/10.1115/DETC2020-22448
13. Winkler, M., Jacobs, G., Stürmer, S., & Konrad, C. (2020). Application of data mining for the identification of parts for additive manufacturing. In *2020 International Conference on Intelligent Engineering and Management (ICIEM),* (pp. 281–288). https://doi.org/10.1109/ICIEM48762.2020.9160307.
14. Winkler, M., Stürmer, S., & Konrad, C. (2021). Evaluation of the additive manufacturability of CAD-parts for initial data labelling in AI-based part identification. In *IOP Conference Series: Materials Science and Engineering, 1097*, 012020. https://doi.org/10.1088/1757-899X/1097/1/012020.
15. Winkler, M., Jacobs, G., Spütz, K., & Konrad, C. (2021). Evaluation of parts for additive manufacturing utilizing system models of AM plants. In *IOP Conference Series: Materials Science and Engineering*, *1097*, 012022. https://doi.org/10.1088/1757-899X/1097/1/012022.
16. Reiher, T., Lindemann, C., Jahnke, U., Deppe, G., & Koch, R. (2017). Holistic approach for industrializing AM technology: From part selection to test and verification. *Progress in Additive Manufacturing 2*, 43–55. https://doi.org/10.1007/s40964-017-0018-y.

17. Yang, S., Santoro, F., & Zhao, Y. (2018). Towards a numerical approach of finding candidates for additive manufacturing-enabled part consolidation. *Journal of Mechanical Design*, *140*(4). https://doi.org/10.1115/1.4038923.
18. Yang, S., Santoro, F., Sulthan, M. A., & Zhao, Y. (2019). A numerical-based part consolidation candidate detection approach with modularization considerations. *Research in Engineering Design*, *30*(3). https://doi.org/10.1007/s00163-018-0298-3.
19. Wünsch, A., Pilz, F., & Vajna, S. (2020). *Siemens NX für Einsteiger—Kurz und bündig*. Springer Fachmedien.
20. Bastian M., Heymann S., & Jacomy M. (2009). Gephi: an open source software for exploring and manipulating networks. In *International AAAI Conference on Weblogs and Social Media*. https://doi.org/10.13140/2.1.1341.1520.
21. Katrodiya, Y. (2018). Functionally Integrated Shaft and Gear. In *Design for Additive Manufacturing —Challenge 2018*. Fraunhofer IGCV, Augsburg.

Microfluidic Flow Rate Control Device: From Concept to Product Through Additive Manufacturing

Alberto Bernaldo de Quirós, Miguel de las Heras, and Alberto E. Quintero

Abstract

Recent growth of the microfluidics technology field and its applications demands more modular, flexible, reliable, easy to use and complete solutions. One key component in a microfluidic system is the section in charge of propelling and controlling flow through the microfluidic chip, this consists mainly of an impulsion (actuator) part, a sensor to read a signal and feed it to the actuator which modifies flow, and a closed control loop to set the desired operating point. Present solutions are not completely integrated as a final product to the user, but merely as a group of components which need to be coupled. The approach presented here provides one single plug and play device for liquids. Users only have to connect it to the hydraulic circuit of their microfluidic system and define a flow rate set point to start their experiments, thus avoiding setup difficulties. This microfluidic flow rate control device consists mainly of an electronics control board and a fluidic section composed of sensors and actuators. For the latter component, DLP 3D printing process of additive manufacturing was used

A. B. de Quirós · M. de las Heras · A. E. Quintero (✉)
R&D Department, Micro Electrochemical Technologies S.L, Móstoles, Madrid, Spain
e-mail: alberto.quintero@b5tec.com

A. B. de Quirós
e-mail: alberto.bernaldo@b5tec.com

M. de las Heras
e-mail: miguel.delasheras@b5tec.com

A. B. de Quirós
Centro de Electrónica Industrial, Universidad Politécnica de Madrid, Madrid, Spain

M. de las Heras · A. E. Quintero
Dept. de Ingeniería Térmica y de Fluidos, Universidad Carlos III de Madrid, Leganés, Spain

R. Lachmayer et al. (eds.), *Innovative Product Development by Additive Manufacturing 2021*, https://doi.org/10.1007/978-3-031-05918-6_17

as a rapid prototyping tool, going from conceptual design to a final product in a few months. Feedback between real performance and numerical modelling allowed operation improvements in the equipment thanks to fast prototyping and testing capacity. Finally, a fully integrated plug and play system which controls flows in a range of 10–1000 μL/min with a ± 1 μL/min resolution and easily coupled to microfluidic lines is obtained. In summary, additive manufacturing contributes not only as a tool to build new ideas, but also to optimize an already designed device, thanks to reduced costs and simplified fabrication processes for complex three-dimensional structures.

Keywords

Microfluidics • Vat photo polymerization • Microfabrication

1 Introduction

Microfluidics applications in research areas, requires precise and reliable control systems able to reach a flow rate setpoint rapidly and maintain stable behavior during operation. A plethora of applications require flow control solutions in microfluidic systems. Those related with synthesis of new pharmaceutical compounds [1] involve specific flow rates in the order of microliters per minute to obtain the higher efficiencies and purities. Some others as rare earth elements recovery by liquid-liquid extraction processes [2], some of which can even avoid the use of a membrane as a physical separator between liquids [3, 4] provided a stable flow rate is achieved in order to prevent multiphase flow due to interface collapse. Biological applications such as dynamic cell culture to understand bone regeneration processes [5] demand specific flow control to avoid cell cluster disintegration due to high shear stress, others such as flow cytometry need stable flows to ensure proper functioning of the sensors in charge of detecting physical and chemical characteristics of the cells or particles [6]. Although not exhaustive, this list provides a flavor of what is expected of microfluidic control systems and how these requirements may evolve in the near future.

Microfluidic control systems are mainly composed of an actuator impulsing the fluid integrated with a sensor monitoring the fluid in real time (e.g. flow rate) and feeds that information to the actuator in order to adjust its operation parameters. This process is iterated until the sensed value and the setpoint defined by the user match within a given tolerance. In present available commercial solutions, actuator and sensor are usually not integrated. While there are easily integrable commercial sensors at the microscale (e.g flow meters or pressure sensors), this is not the case for most actuator pumping systems.

Some of the fluidic pumping systems commonly used in microfluidics applications are those resorting to the principle of pressure driven flow [7]. While exhibiting a high level of flow rate control, these are very bulky and require special valve configurations in the system to operate in closed loop due to the pressurized inlet tank, which increases size and programming complexity. In the classical approach for pumping systems in microfluidics, syringe and peristaltic pumps are employed. These are able to provide higher flow rates, but their sizes are still large, with great miniaturization and portability difficulties, and fluidic pulses are inescapable [8, 9]. Some solutions such as electroosmotic pumps [10] or magnetohydrodynamic pumps [11] are limited in their application owing to the properties of the fluids that may be used. More compact and versatile solutions for microfluidics are high frequency piezoelectric pumps [12, 13], their main advantages are low energy consumption, low cost, and easy integration in line on chip scale.

Despite its novelty as a technological field, spanning just two decades of truly relevant advances, microfluidics has demonstrated its potential and advantages mainly in analysis of samples, allowing small quantities of samples and reagents with high resolution and sensitivity, low cost, and fast processes [14]. The most common approach for the manufacturing of microfluidics devices has been similar to that followed in the microelectronics industry, mainly photolithography and associated technologies as e-beam evaporator, plasma etching, chemical etching, among others. However, these techniques are best suited for two dimensional designs with relatively low aspect ratio, thus posing significant limitations in the three dimensional structures that can be built. To build multilayer devices that enable more complex three dimensional structures have been done previously to overcome this drawback [15]. Recent advances in 3D printing technology, especially those related to vat photopolymerization as Digital Light Processing (DLP) and Stereolithography (SLA), has allowed direct generation of monolithic, enclosed microfluidics complex structures thanks to improved resolutions in manufacturing devices. Nowadays, these have become a more common approach to manufacture microfluidics components, at least at the prototype level [16, 17].

The aim of the present work is integration of commercially available piezoelectric pump and flow sensor components through a software embedded control, and the improvement of performance by adding a so called variable resistor built by additive manufacturing process of DLP 3D printing. The paper is organized as follows. In Sect. 2, the initial stage of the conceptual design for the microfluidic flow rate control device and manufacturing methods to develop it are introduced. In Sect. 3, integration of the commercially available components without the variable resistor is tested, followed by addition of the variable resistor to compare the performance, finally a model to characterize structural behavior is developed and used to generate a new optimal design for the variable resistor with the desired performance. In Sect. 4, the final product is manufactured and its response compared with other commercially available common solutions for microfluidics control to demonstrate its improvement. In Sect. 5, the main conclusions of the analysis are presented.

2 Conceptual Design and Manufacturing

2.1 Fluidic System

Fluidic system is the hardware component of the equipment in direct contact with the fluid. It consists of the components shown in Fig. 1, involving for the final setup a piezoelectric micropump propelling the fluid at an initial gross flow rate near the desired value, a variable resistor to fine tune it through a controlled pressure drop in the fluid, a flowmeter which senses and feeds the information to the control system in charge of varying actuator operation parameters (i.e. micropump and variable resistor) through the electronics to reach the setpoint defined by the user, and a pressure sensor providing additional pressure drop data in the fluid line.

Piezoelectric micropump and flowmeter are commercially available and directly integrated in the fluidic system. For the fluidic connector of the pressure sensor, the variable resistor, and the scaffold structure for all the fluidic system components, 3D printing vat photopolymerization additive manufacturing was performed, specifically a DLP printer Asiga MAX X27 with an XY pixel resolution of 27 µm and a minimum resolution in the Z direction of 15 µm was used. Two different commercially available resins were used to build the fluidic system structure shown in Fig. 2, Moiin Tech Clear transparent resin (Moiin, Germany), and Excellent Resins Lightning Gray (Litholabs, Germany).

Details of the variable resistor are shown in the left hand side image of Fig. 2. It is a typical quake valve design as the original one presented by Unger et al. [18], but with improvements in the design and manufacturing process. The classical approach to build

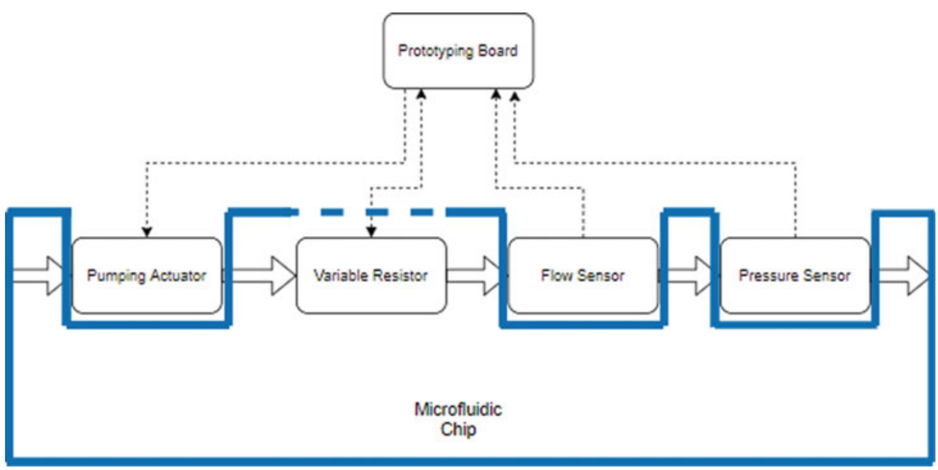

Fig. 1 Conceptual design of the fluidic system where the microfluidic chip (blue color line) containing all connections between elements and the variable resistor are integrated

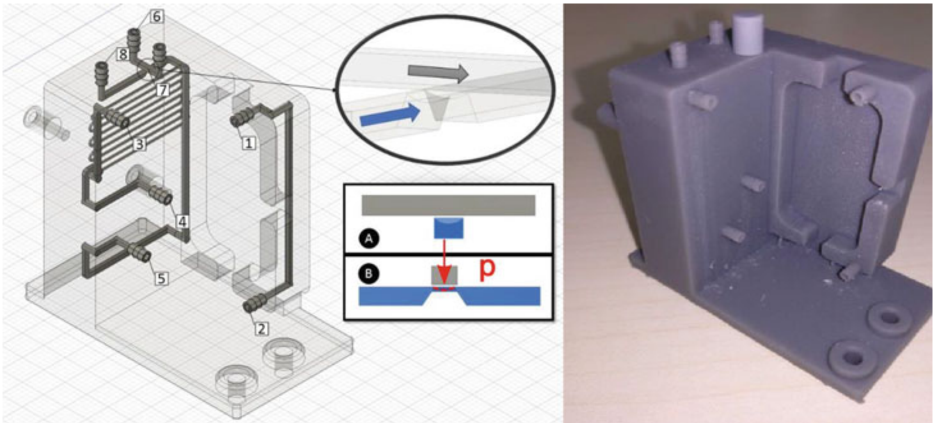

Fig. 2 CAD design (left hand side image) with labels for the different connection ports and details of the variable resistor: (1) fluid inlet, (2) micropump inlet connection port, (3) micropump outlet connection port, (4) micro flowmeter connection port, (5) micropump outlet connection port, (6) micro compressor connection port, (7) variable resistor detailed in the circle image with the fluid indicated by blue arrow and air indicated by grey arrow, (8) fluid outlet, image (**a**) is a front view of fluid line in blue color with a lateral view of compressed air line in grey color, image (**b**) is a lateral view of fluid line in blue color with a front view of compressed air line in grey color. Final 3D printed microfluidic chip (right hand side image)

microfabricated devices as the one presented here involves different processes such as UV Lithography and PDMS replica molding to obtain layers that must be stacked later in order to obtain the final product. Precise layer alignment in these methods introduces a great deal of complexity as well as the challenge of obtaining leakage free sealings and the requirement of remarkable lifetimes from the thin layers of elastomer if long term usage is intended. A more industrial scale approach such as micro injection molding avoids alignment and sealing difficulties, but it also adds the expensive costs of generating molds for structures that are but mere prototype iterations. All these drawbacks can be overcome through using DLP 3D printing, which generates a monolithic variable resistor, while allowing for the generation of many different testing prototypes in a short period of time. It also reduces investment costs thanks to the low price of raw materials and the inherent maskless, mold-free nature of this technology.

The operation principle of the variable resistor requires a compressed air line connected to a control micro channel which is orthogonal to the fluidic channel, both are separated through a small membrane in the order of 100 μm at their contact point. Increasing air flow rate in the line leads to increased air pressure inside the control micro channel, thereby deflecting the membrane and reducing fluidic line cross section, ultimately increasing the pressure drop across the fluidic channel. In the present research, variable resistor geometry is the one presented in Fig. 2. Membrane thickness is optimized to obtain the desired flow control device performance through the process explained in Sect. 3.3.

2.2 Electronics and Control System

Electronics were designed to control the microfluidic response based on the active elements, sensors and other fluidic elements previously mentioned. Active elements and sensors of the system need dedicated electronics for its use, and its integration with the Microcontroller Unit (MCU) by different interfaces. Single drivers were designed for each element and tested individually. Initial designs were prototyped decoupled from the rest of the electronics and directly operating with the single element, an approval test of the driver with a reference MCU was performed. These electronics were evaluated, redesigned and iterated at convenience, and initial calibration parameters were obtained for further use in the set integration.

After all elements were tested with the reference MCU individually, final MCU requirements for the complete integration were defined based on a computational cost estimation of control algorithms, signal treatment, and filtering; a new MCU, RAM memory and flash ROM memory were selected. Finally, interface architecture was defined, containing digital and analog input/output pins, drivers for embedded systems communication protocols (such as I2C, UART or SPI) and a driver for serial USB communication with an external computer. With all the hardware defined, a complete electronic board was designed following the scheme shown in Fig. 3. Considering this structure, the elements layout, electric connection schematics and other drawings were generated for board manufacturing.

Regarding the embedded software, its control algorithms and data filtering, the iterative process is similar to the hardware one described. When testing and iterating the individual drivers some control or calibration parameters are obtained with partial adequacy. After the hardware of the board is manufactured and the electric response validated, the software is developed with a first version using parameters from the individual tests. Concerning sensor data filtering, values of these parameters are still optimal since the integration does not introduce any change in the response of the signal. Nevertheless, control algorithms and parameters of the actuators need to be readjusted for the combined dynamic response of the system, and because the control algorithm is redefined. Other parameters needed such as some drivers adjustment of the control variables can still be used with the same previous values.

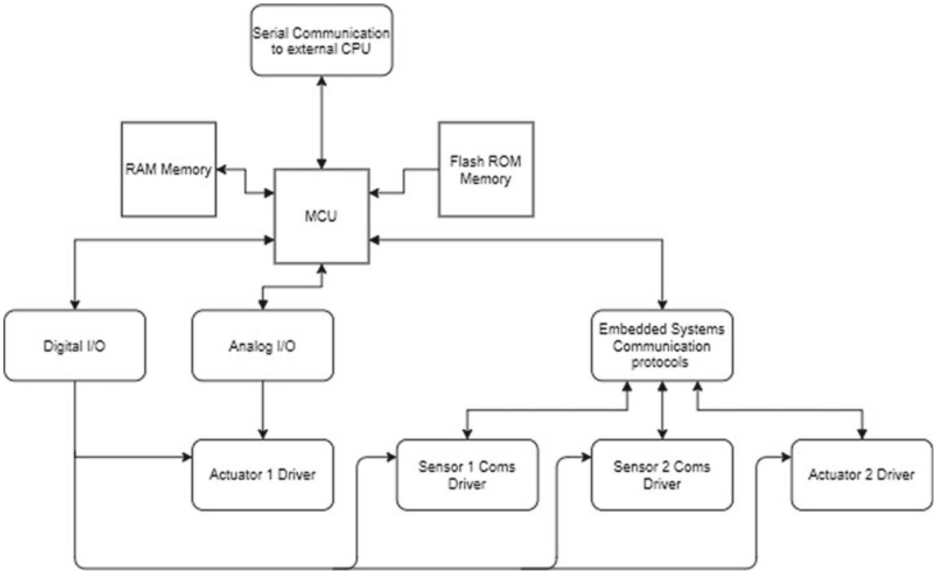

Fig. 3 Conceptual design of the electronic elements of the board and its relations (Arrows indicate information flows)

3 Integration, Testing, and Optimization

3.1 Initial Setup

The initial setup involved only integration of commercially available elements (i.e. piezoelectric micropump, flowmeter, and pressure sensor), not including the variable resistor later built by additive manufacturing. The idea of using a piezoelectric micropump to propel the liquid and closing the control loop with the information from a flowmeter sensor is shown in Fig. 4. Active pumping actuator (i.e. piezoelectric micropump) and sensors were tested individually and connected between them through flexible tubing, a prototyping board was adapted for the control and regulation of the actuator and filter of the read data (Fig. 4).

Performance was evaluated, obtaining a behavior not compliant with the requirements needed for most applications in microfluidics. Fig. 5 shows a flow rate sweep between the minimum and maximum flow rate corresponding to this initial setup without the variable resistor. Some drawbacks of this configuration are significant flow pulsation for a fixed value of flow rate, flow rate range unsuitable for common limits in microfluidics applications, with maximum values superior to the typical 1000 μL/min, and unsatisfactory flow rate resolution, with actuator step changes of around 10 μL/min instead of the desired 1 μL/min. Hysteresis processes may be ascertained by inspecting flow rate range, minimum

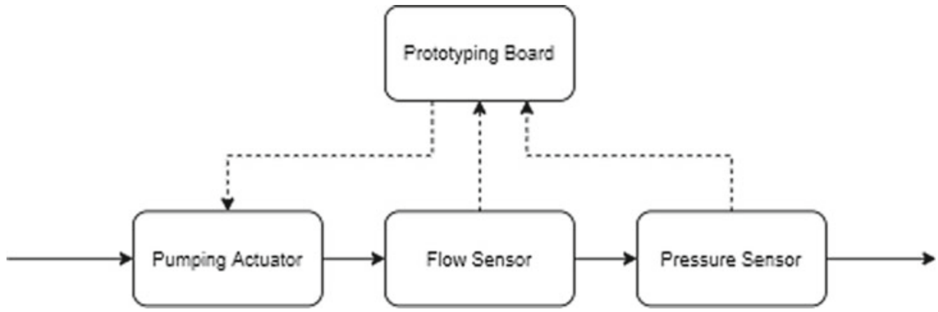

Fig. 4 Conceptual design of the initial setup

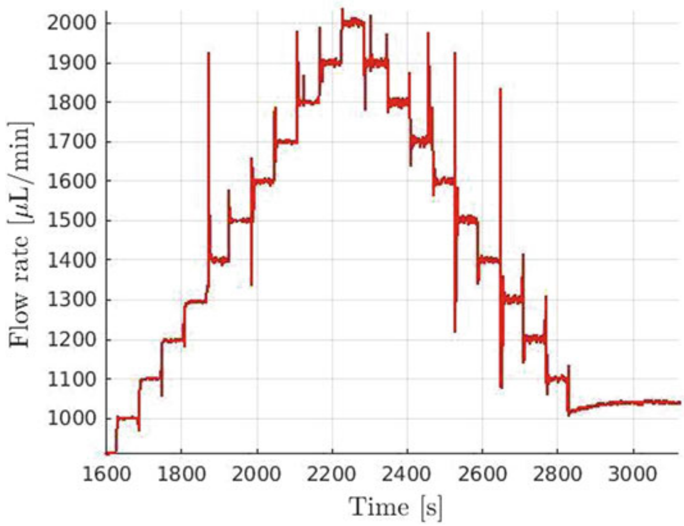

Fig. 5 Full range test control at different setpoints for the initial setup

flow rate value is below 1000 μL/min with the minimum pumping power at the beginning of the process, but it increases after reaching the maximum flow rate value and returning to the minimum pumping power, leading to a value which is above 1000 μL/min.

3.2 First Prototype

In order to sort out the problems present in the initial setup, a microfluidic chip was manufactured using DLP 3D printing additive manufacturing. It incorporates a second regulating actuator called variable resistor to adjust the flow rate range to the desired one and increase flow rate resolution. New fixed microfluidic connections inside the scaffold of the fluidic chip, specifically adapted to the elements of the microfluidic control device, constitute a major upgrade with respect to the initial setup, thereby preventing changes in circuit pressure losses and mitigating hysteresis processes. More stability is achieved in actuators and sensor response, since the design of this fluidic circuit is adjusted to reduce pulsation of the liquids after the pumping section.

The variable resistor is actuated by a commercial compressor allowing to generate a micro airflow at a desired pressure. This pressure is used to reconfigure the internal shape of the resistor, and subsequently change the pressure drop and flow rate across the liquid circuit. The complex structure of the variable resistor is manufactured by 3D DLP printing technique, not only because it introduces high precision and low tolerance, but because it has internal 3D conduits that other precise manufacturing methods such as UV lithography are not able to produce in one single enclosed piece.

It can be seen in Fig. 6 that some drawbacks of the initial setup have been improved. Flow is more stable and regulation more precise, with evident reduction in fluctuations around the flow rate setpoint with respect to those previously detected in the initial setup. Flow rates range from 100 to 500 μL/min, which is more common in microfluidics applications, although still not the required one with full range from 100 to 1000 μL/min. Nevertheless, this first prototype shows how introduction of a variable resistor allows to modify and adjust flow rate range. Further improvements in the electronics in charge of feeding actuators and PID control allow increased flow rate resolution, achieving variations of order 1 μL/min as may be ascertained by observing the reduced oscillations for

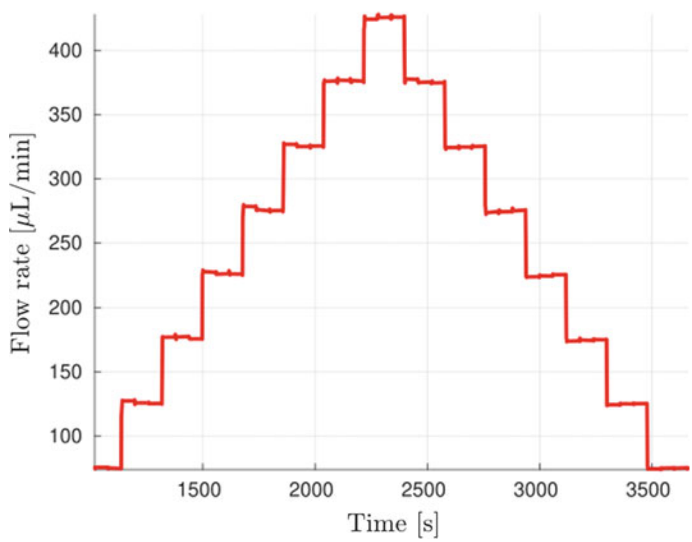

Fig. 6 Full range test control at different setpoints for the first prototype

a fixed setpoint. Finally, the hysteresis processes present in the initial setup are overcome in the first prototype. It is readily checked how the shape of curve in Fig. 6 is more symmetrical around the maximum setpoint, and in particular it is able to replicate the initial value below 100 μL/min corresponding to minimum pumping power at the end of the sweep.

3.3 Prototype Optimization

Although improvement has been achieved with the first prototype after introducing a variable resistor in the initial setup, the flow rate range is still unsatisfactory. Through order of magnitude estimation of resin properties based on prototype dimensions and performance, a first computational model is developed to better understand the interaction between resin features and microfluidic operation. Afterwards, parametric studies are carried out to calculate the Young modulus relating prototype configurations and experimental measurements, such as pressure drops and flow rates in the hydraulic circuit. All the experiments have been conducted at constant temperature, with long enough times to reach steady states in the system and homogeneous conditions. This characterization is useful for design optimization leading to a second prototype, as exposed in the next paragraph.

Variable resistor design is optimized resorting to the knowledge of resin properties acquired during device simulations with the first prototype. Figure 7 depicts all three

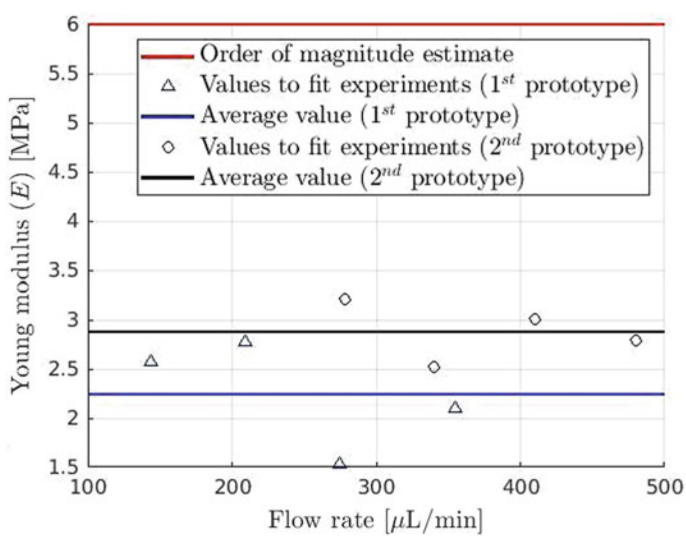

Fig. 7 Young modulus (E) calculations from computational model verifying experimental data

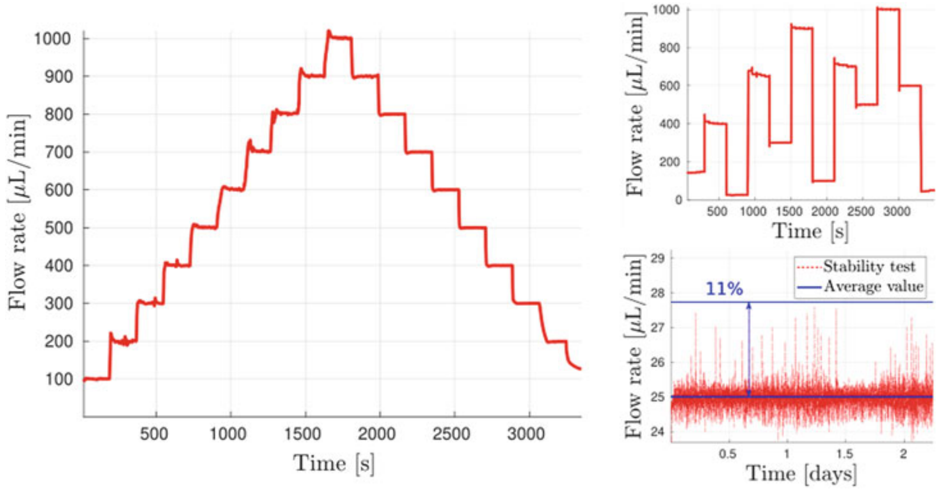

Fig. 8 Full range test control at different setpoints for the optimized prototype (left hand side), variations of flow rate setpoint (right hand side upper part), and stability test (right hand side lower part)

stages leading to the final product. A first order of magnitude estimation based on device geometry, structural deflections as well as data from similar resins [19] is employed as a first guess to adjust membrane width in the quake valve, leading to the initial prototype geometry. Experimental measurements at different operation conditions are replicated by the numerical model, providing different estimates of the Young modulus of the resin. Its new value is then approximated by the average over all experimental conditions replicated by the model and used as an input to generate an improved second prototype with increased thickness membrane. Since less oscillations are present in this second, more accurate and precise device (see Fig. 8), numerical simulations provide less scattered estimates of the Young modulus. Although the process could have been carried out to develop a third prototype, device performance is already satisfactory at this stage, and the refinement process to characterize the resin would have yielded smaller increments in the estimate of structural properties, thus leading to diminishing returns in optimization.

In summary, initial estimates and experimental data coupled to the numerical model have proven their usefulness in terms of design improvement, consolidating as a viable approach to achieve further optimization in future design iterations. Through classical manufacturing process of stacking PDMS structures obtained through replica of UV Lithography molds, the accuracy and precision required for feedback between numerical model and experimental data may be compromised due to errors in the positioning and sealing of the different layers. More disruptive methods such as micro injection molding increase the cost of prototype manufacturing significantly. In conclusion, 3D DLP additive manufacturing suits as the perfect candidate for initial stages of research that require accuracy and precise iterations at low cost.

After the optimization process carried out previously through the computational model, and ensuring that flow rate range fits the desired one as shown in the left hand side of Fig. 8, microfluidic flow rate control device response is optimized by new regulation algorithms in the software. Since there are two actuators (i.e. piezoelectric micropump and variable resistor), two coupled control PIDs are designed. PID control parameters are calculated in real time by a fuzzy logic selector based on laws from empirical knowledge of the system in terms of the variables (flow and pressure) at the working range. Using this fuzzy logic adjustment of the parameters, non- linearities of the system are better handled, and dynamic response is enhanced. This is shown in Fig. 8 right hand side upper part where more aggressive regulation steps are made in all of the range and clean and fast response is obtained. Finally, operation during long periods of time is evaluated and presented in the lower right hand side of Fig. 8, it can be seen that during a couple of days of operation with a predefined setpoint of 25 µL/min, extreme deviations (occurring up to 10 times a day) are smaller than 11% of the predefined value, the envelope for the rest of deviations being 2% of the setpoint.

4 Final Product

For the final product, a new electronic board is developed, designed to integrate all third-party hardware components, the microprocessor, additional elements for inputs and outputs, and power electronics. This board runs the embedded software of the control algorithms and user interface functionalities. Final product operation can be done through a USB connection with a computer by means of software able to store logs of all the operation variables, or directly selecting a setpoint with the buttons displayed in the menu of the LCD screen and starting the operation.

The upper left hand side of Fig. 9, presents a CAD design of the final product, including the electronic board, the final optimized design of the fluidic system, a battery to enable autonomous operation, an LCD screen that shows requested and actual flow rate during operation, and buttons that allow to configure the microfluidic flow rate control device through a menu shown in the LCD screen. The lower left hand side of Fig. 9 presents a comparison between the classical syringe pump approach, more recent pressure driven flow systems, and the novel microfluidic flow rate control device presented here, operating for a predefined flow rate of 80 µL/min. It can be seen that syringe pumps oscillations are mitigated in systems such as pressure driven flow and the one presented here. However, intrinsic obstacles to generate fluid recirculation in the former setup are overcome by the approach presented here thanks to the absence of pressurized feeding

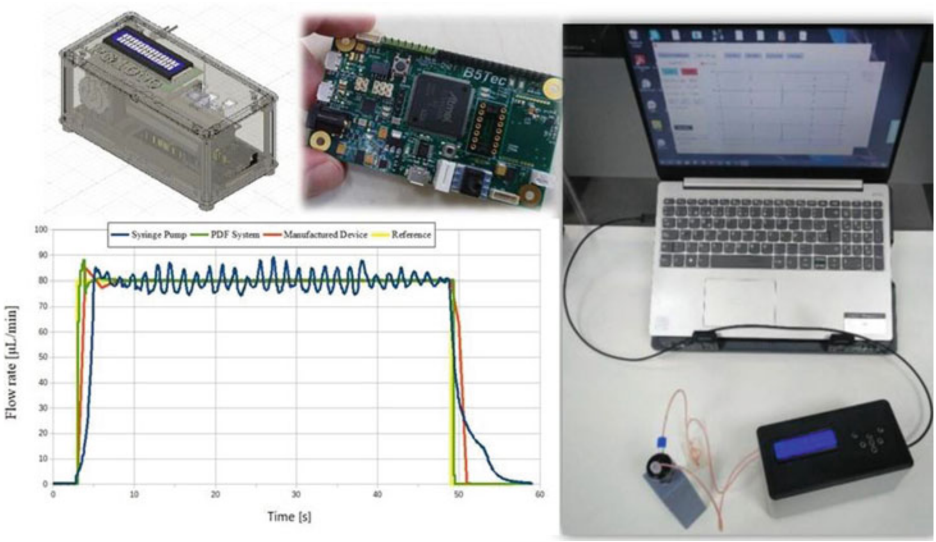

Fig. 9 CAD design of the final product and final PCB (left hand side upper part), comparison of performance between different commercial solutions and the microfluidic flow rate control device presented here (left hand side lower part), and final product operating to feed a microfluidic chip (right hand side)

tanks. Finally, the right hand side of Fig. 9 shows the compactness of a typical microfluidic experiment setup with the developed flow rate control device. Only an USB cable plugged to the computer, two fluid connections for the microfluidic chip, and the tank are necessary.

5 Conclusions

3D DLP printing additive manufacturing method has been demonstrated as an optimal approach for developing and improving prototypes from conceptual designs in the field of microfluidic applications. Integration of commercially available components has been tested and drawbacks identified. Using 3D DLP printing, a component called variable resistor has been manufactured and integrated allowing to overcome the drawbacks of the initial setup. Redesign of the variable resistor yields improved performance. This is achieved via an optimization process that involves taking experimental measurements from an initial prototype with the variable resistor and a numerical model. This information is used to estimate the order of magnitude of the Young modulus, thereby improving designs in every successive iteration. A fully plug and play final product is obtained, including the software for setpoint setting and manually fine tuning the PID. Product performance is compared with other typical solutions for microfluidics flow rate control, such as syringe pumps and pressure driven flow systems, showing superior performance and versatility. The presented micro flow controller offers steadier flow rates than typical syringe pumps, while also preventing tank pressurization and recirculation difficulties inherent in pressure driven flow systems. In this manner, trivial liquid recirculation in an accurate, low pulsation regime is achieved in the context of a fully integrated device.

References

1. Coliaie, P., Kelkar, M. S., Langston, M., Liu, C., Nazemifard, N., Patience, D., & Singh, M. R. (2021). Advanced continuous-flow microfluidic device for parallel screening of crystal polymorphs, morphology and kinetics at controlled supersaturation. *Lab on a Chip*. https://doi.org/10.1039/D1LC00218J
2. El Maangar, A., Theisen, J., Penisson, C., Zemb, T., & Gabriel, J. C. P. (2020). A microfluidic study of synergic liquid- liquid extraction of rare earth elements. *Physical Chemistry Chemical Physics, 22*(10), 5449–5462. https://doi.org/10.1039/C9CP06569E
3. Priest, C., Zhou, J., Sedev, R., Ralston, J., Aota, A., Mawatari, K., & Kitamori, T. (2011). Microfluidic extraction of copper from particle-laden solutions. *International Journal of Mineral Processing, 98*(3–4), 168–173. https://doi.org/10.1016/j.minpro.2010.11.005
4. Kikutani, Y., Mawatari, K., Hibara, A., & Kitamori, T. (2009). Circulation microchannel for liquid-liquid microextraction. *Microchimica Acta, 164*(3–4), 241. https://doi.org/10.1007/s00604-008-0065-7
5. Mestres, G., Perez, R. A., D'Elía, N. L., & Barbe, L. (2019). Advantages of microfluidic systems for studying cell- biomaterial interactions-focus on bone regeneration applications. *Biomedical Physics & Engineering Express, 5*(3), 032001. https://doi.org/10.1088/2057-1976/ab1033
6. Gong, Y., Fan, N., Yang, X., Peng, B., & Jiang, H. (2019). New advances in microfluidic flow cytometry. *Electrophoresis, 40*(8), 1212–1229. https://doi.org/10.1002/elps.201800298
7. Gao, R. Z., Hébert, M., Huissoon, J., & Ren, C. L. (2020). μPump: An open-source pressure pump for precision fluid handling in microfluidics. *HardwareX, 7*, e00096. https://doi.org/10.1016/j.ohx.2020.e00096
8. Lake, J. R., Heyde, K. C., & Ruder, W. C. (2017). Low-cost feedback-controlled syringe pressure pumps for microfluidics applications. *PLoS ONE, 12*(4), e0175089. https://doi.org/10.1371/journal.pone.0175089
9. Xiang, J., Cai, Z., Zhang, Y., & Wang, W. (2016). A micro-cam actuated linear peristaltic pump for microfluidic applications. *Sensors and Actuators A: Physical, 251*, 20–25. https://doi.org/10.1016/j.sna.2016.09.008
10. Gao, Y., Hu, G., Lin, F. Y., Sherman, P. M., & Li, D. (2005). An electrokinetically-controlled immunoassay for simultaneous detection of multiple microbial antigens. *Biomedical microdevices, 7*(4), 301–312. https://doi.org/10.1007/s10544-005-6072-0
11. Pamme, N. (2006). Magnetism and microfluidics. *Lab on a Chip, 6*(1), 24–38. https://doi.org/10.1039/B513005K
12. Ma, H. K., Chen, R. H., Yu, N. S., & Hsu, Y. H. (2016). A miniature circular pump with a piezoelectric bimorph and a disposable chamber for biomedical applications. *Sensors and Actuators A: Physical, 251*, 108–118. https://doi.org/10.1016/j.sna.2016.10.010

13. Shabanian, A., Goldschmidtboeing, F., Vilches, S., Phan, H. H., Kashekodi, A. B., Rajaeipour, P., & Woias, P. (2016). A novel piezo actuated high stroke membrane for micropumps. *Microelectronic Engineering, 158*, 26–29. https://doi.org/10.1016/j.mee.2016.03.016
14. Whitesides, G. M. (2006). The origins and the future of microfluidics. *Nature, 442*(7101), 368–373. https://doi.org/10.1038/nature05058
15. Glick, C. C., Srimongkol, M. T., Schwartz, A. J., Zhuang, W. S., Lin, J. C., Warren, R. H., & Lin, L. (2016). Rapid assembly of multilayer microfluidic structures via 3D-printed transfer molding and bonding. *Microsystems & Nanoengineering, 2*(1), 1–9. https://doi.org/10.1038/micronano.2016.63
16. Bhattacharjee, N., Urrios, A., Kang, S., & Folch, A. (2016). The upcoming 3D-printing revolution in microfluidics. *Lab on a Chip, 16*(10), 1720–1742. https://doi.org/10.1039/C6LC00163G
17. Ho, C. M. B., Ng, S. H., Li, K. H. H., & Yoon, Y. J. (2015). 3D printed microfluidics for biological applications. *Lab on a Chip, 15*(18), 3627–3637. https://doi.org/10.1039/C5LC00685F
18. Unger, M. A., Chou, H. P., Thorsen, T., Scherer, A., & Quake, S. R. (2000). Monolithic microfabricated valves and pumps by multilayer soft lithography. *Science, 288*(5463), 113–116.
19. Zhakeyev, A., Leung, D. Y., & Xuan, J. (2019). GO-modified flexible polymer nanocomposites fabricated via 3D stereolithography. *Frontiers of Chemical Science and Engineering, 13*(4), 736–743. https://doi.org/10.1007/s11705-019-1836-x

Experimental Investigation of Additive Manufacturing of Fused Silica Fibers for the Production of Structural Components in the Laser Glass Deposition Process

Khodor Sleiman, Katharina Rettschlag, Peter Jäschke, Stefan Kaierle, and Ludger Overmeyer

Abstract

Additive manufacturing is an established technique in much of industry for manufacturing complex structures from polymer and metal materials. The additive manufacturing of glass materials is a very young process, which is based on through various approaches. For example, such processes are based on a glass powder bed or the layer-by-layer deposition of viscous glass from a crucible. In the Laser Glass Deposition process (LGD), a fused silica glass fiber (0.43 mm) is additively deposited onto a fused silica substrate by CO_2 laser irradiation. In order to form structural components from complex contours, or solids, experimental investigations on the printing of homogeneous layers were carried out in this paper. The main focus of the investigations is the influence of the laser power, the printing speed and the line spacing of single tracks and single layers on the deposition morphology. The results were used to realize multilayer complex structures with more than 300 layers.

Keywords

Additive manufacturing • Laser glass deposition • Fused silica glass fibers

K. Sleiman (✉) · K. Rettschlag · P. Jäschke · S. Kaierle · L. Overmeyer
Laser Zentrum Hannover e.V., Hollerithallee 8, 30419 Hannover, Germany
e-mail: k.sleiman@lzh.de

S. Kaierle · L. Overmeyer
Institute of Transport and Automation Technology, Leibniz University Hannover, An der Universität 2, 30823 Hannover, Germany

R. Lachmayer et al. (eds.), *Innovative Product Development by Additive Manufacturing 2021*, https://doi.org/10.1007/978-3-031-05918-6_18

1 Introduction

Additive manufacturing (AM) is widely established in industry and research for polymer and metallic materials [1], while the AM of glass materials represents a novel manufacturing technology. Silicate glasses are characterized by high optical transparency, chemical and thermal stability [2]. Fused silica is used in chemical and medical apparatus engineering, as well as in optics and semiconductor technology, because of its low thermal expansion coefficients and high thermal shock resistance [3]. On the other hand, fused silica is challenging to manufacture since its working temperature is about 2000 °C. To date, the majority of complex fused silica components are manufactured by conventional manual manufacturing. This is associated with high scrap rates and low reproducibility, which is avoided with additive manufacturing.

There exist several approaches to additive manufacturing for glass materials. Among them are glass extrusion process [4], sintering process [5], stereolithography [6] and glass fiber/rod based additive manufacturing [7, 8]. In the glass fiber and rod-based manufacturing techniques, the glass filament is heated to a processable state over 1700 °C by a CO_2 laser [9]. These processes are referred to as Laser Glass Deposition (LGD). Here, with lateral fiber feeding, the laser irradiates either perpendicularly to the substrate surface [10], or laterally to the contact surface between the glass fiber and the substrate [11]. Similarly, a coaxial laser beam irradiation approach has been developed, where the glass fiber is fed perpendicularly to the substrate surface and the laser is delivered in a coaxial manner [12].

In the investigations of Witzendorff et al. [8] concerning the deposition of single fibers, a direction dependence of the deposition morphology was observed. This prevents the deposition of homogeneous layers in a closed contour. The present publication presents a methodology and demonstration for the printing of homogeneous layers in closed contours in lateral fiber deposition. In this sense, parameter studies are carried out on the deposition of single fibers and surfaces in order to find suitable parameters for printing complex contours and solids.

2 Methods

The experimental setup (Fig. 1) consists of a CO_2 laser (Rofin DC045, Coherent Inc.) with a maximum power of 4.5 kW. This output power is attenuated by 50% beam splitters, so that a power range of 50–500 W is introduced into the heating zone. The laser radiation is guided through a lens with 190 mm focal length onto a glass substrate. A defocused spot diameter of 5 mm is achieved there. The laser beam penetrates the fused silica substrate (100 × 100 × 3 mm^3, Schröder Spezialglas GmbH) perpendicularly, which has a thickness of 3 mm.

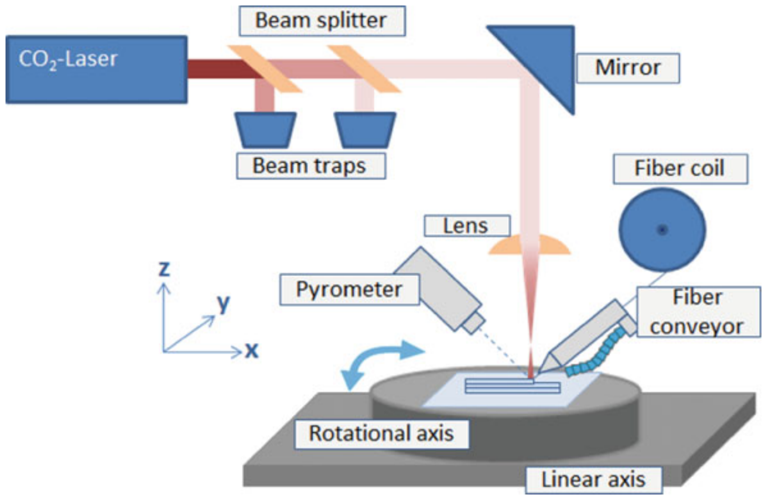

Fig. 1 Experimental setup for the laser glass deposition process

A fused silica fiber (OPTRAN®, Ceram Optec SIA, light-guiding fiber) with a diameter of 424 µm is fed with a feeding rate v_F of 0–600 mm/min laterally at an angle of 45° into the heating zone via a conveyor unit and is deposited on the glass substrate. After entering the laser beam, the coating is burned off during the feed, so that no contamination of the glass melt occurs [13].

The average temperature of the process zone is measured by a pyrometer (1 mm spot diameter, KTRD 1550-1, Maurer GmbH), which is designed for CO_2 laser processing of fused silica and measures a temperature range of 300–2500 °C at a measuring wavelength of 5 µm.

The substrate is located on a rotating base plate which can also be translated in one direction by a linear axis. The laser beam source and the fiber conveyor can move perpendicular to the base plate and in height via linear axes. The linear axes can each move at a speed v_A of 0–600 mm/min and the ratio of the velocities v_{Rel} is defined as $v_{Rel} = v_F/v_A$. An overview of the process parameters is shown in Table 1. By rotating the base plate, a preferred direction for depositing the fibers can be set so that complex contours can be applied regardless of the direction. If a rotation is performed, the linear axes must compensate for this rotation so that the fiber continues to be deposited in the same direction. The necessary compensation arc is calculated by a coordinate transformation. A rotation of the rotation axis transforms the original coordinate system K into a coordinate system K' which has been rotated by an angle α. The coordinates in the system K' can be calculated via a multiplication of the coordinates in K with the rotation matrix.

This makes it possible to implement a continuous printing process that eliminates the need for cutting and repositioning fibers, which is associated with measurement and

Table 1 Overview of process parameter ranges for laser glass deposition setup described here

Parameter	Value range
Laser power P_L	10–250 W
Axis velocity v_A	0–600 mm/min
Fiber feed rate v_F	0–600 mm/min
Velocity ratio v_{Rel}	1–7
Track distance d	0.6–1.5 mm
Laser spot diameter	5 mm
Angle of fiber conveying	45°
Temperature measurement range	300–2500 °C

contour errors. This process stability enables consistent track heights, even with flexible contours and sharp corners. Rotationally asymmetric contours can also be realized by suitable coordinate transformations. The path height of the original layer is set as a benchmark for the height change in order to obtain the same conditions at any layer height, and the width of the original path is used as a benchmark for forming a surface. Thus, process stability depends on maintaining the degree of fusion. To accurately determine the degree of fusion using specific process parameters, parameter studies were conducted with respect to the deposition morphology of the fiber tracks.

The deposition morphology can also be described by the contact angle of the fiber to the substrate. The contact angle α is defined as the angle spanned by the height h and width w of a weld in relation to the substrate surface. This is shown as a sketch in Fig. 2. Accordingly, a high contact angle represents a weak fusing and a low contact angle a strong fusing of the fiber onto the substrate. The height and width are measured

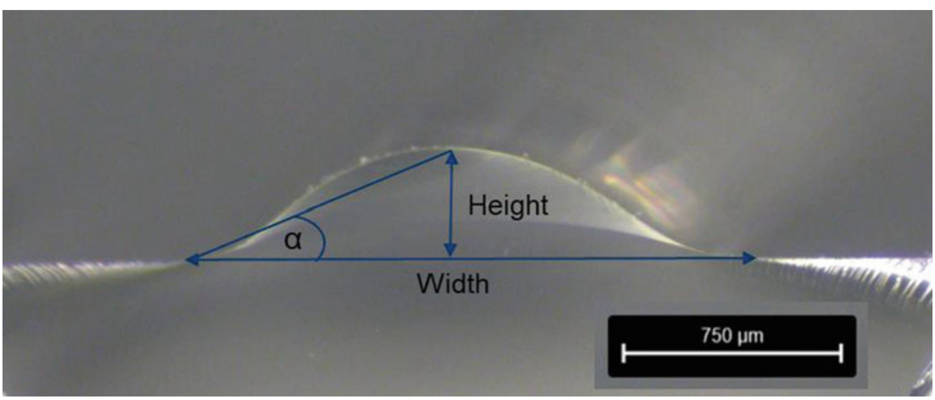

Fig. 2 Sketch of the cross section of a deposited fiber. The height h, width w and contact angle are drawn

by a tactile profile measuring instrument MarSurf LD 130, Mahr GmbH. This scans the surface of a deposited fiber horizontally, whereby the contact angle of the fiber must not exceed the angle of the stylus, otherwise measurement errors will occur. In this case, the width of a deposited fiber was remeasured with a caliper gauge.

3 Results

Contour structures

For the precise selection of the printing parameters and to ensure a stable printing process, the deposition morphology was first investigated with regard to the axis speed v_A and fiber feed rate v_F, as well as the laser power P_L. For this purpose, 80 mm individual tracks were deposited at varying speeds v_F and v_A with a speed ratio $v_{Rel} = 4$ in dependence of the laser power (Table 1). The width and height were investigated, as well as the print stability and transparency of the deposited fibers from a qualitative point of view. The results can be observed in the following graphs in Fig. 3.

It can be observed from the measured values that the height decreases and the width increases with increasing laser power, since the heat input to the glass filament increases with increasing laser power, which reduces the viscosity and causes the glass material to melt. It is also observed that for small values of v_A, a much larger interval of deposited fibers can be realized within the process limits. For example, height for $v_A = 22.5$ mm/min ranges from 0.15 to 0.59 mm for widths from 2.40 mm to 1.31 mm. At the highest speed $v_A = 112.5$ mm/min, height ranges from 0.26 mm to 0.42 mm at w of 1.82 mm to 1.49 mm. In addition, an estimate of material loss can be made from the profile data if the theoretical cross-sectional area is compared with the real profile cross-sectional area, which was interpolated. The corresponding ratios are shown graphically in the following Fig. 4 (left).

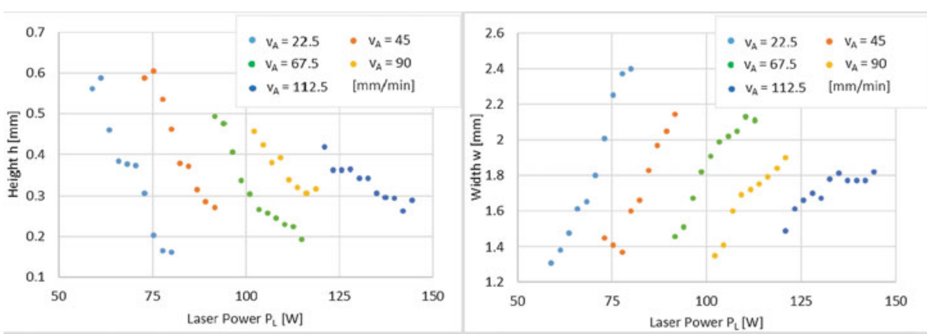

Fig. 3 Left: Graphical representation of the dependence of the height of fiber tracks on laser power. Right: Graphical representation of the dependence of the width of a fiber track on the laser power

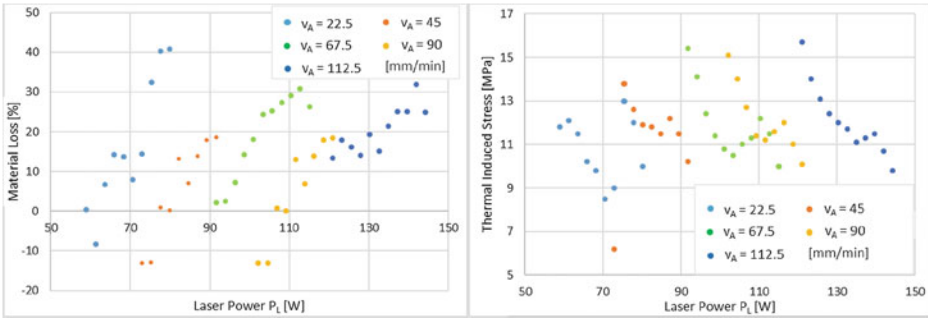

Fig. 4 Left: Graphical representation of the material loss as a function of the laser power. The negative values arose due to the inaccuracy in the interpolation of the fiber cross-section. Right: Graphical representation of thermally induced stresses in the center of a deposited fiber track as a function of laser power

It becomes clear that higher material losses are caused both during deposition with increasing laser power P_L and with low axis speed v_A, because this increases the heat input into the material, which leads to evaporation of the material. This is also manifested by the formation of bubbles in the individual paths, which are caused by the trapping of gases (air, process gas), or evaporated glass. Since glass has an amorphous lattice structure, despite the average material loss of 10–20 %, the fiber binds well, since not all lattice bonds have the same binding forces, and thus most of the melt remains in a processable viscosity range.

Further analysis of the individual tracks was performed by polarimeter measurements. This involves determining the thermally induced stresses in the glass. The respective stresses in the center of a fiber track are shown graphically in Fig. 4 (right). A general decreasing trend of the stress with increasing laser power can be observed, because with stronger fusion a larger bonding area between substrate and fiber is created on which the stresses can be distributed. In contrast to a weak bonding, which causes a point-like bonding on which the stresses are concentrated. The same observation is made for increasing axis speed v_A, at the same laser powers. It can be observed that the thermal stresses increase for higher v_A due to the weak bonding. On average, stresses between 10 and 16 MPa can be observed, which is very low compared to the facture strength of bulk fused silica of 50 MPa. However, there were isolated cracks on the fiber tracks as shown in Fig. 4 (right) for example at $P_L = 72$W and $v_A = 45$ mm/min. It can be seen that this fiber track has low degree of fusion to the substrate, which decreases the fracture strength. The relationship between contact angle and fracture strength of printed structures will be the subject of future investigations.

Based on these tests, various contours were printed in multiple layers. As an example, Fig. 5 shows an “ellipse” contour. This was printed with the parameter set $v_A = 67.5$ mm/min, $v_F = 270$ mm/min, $P_L = 95$ W and a track height of $h_z = 0.23$ mm. For this

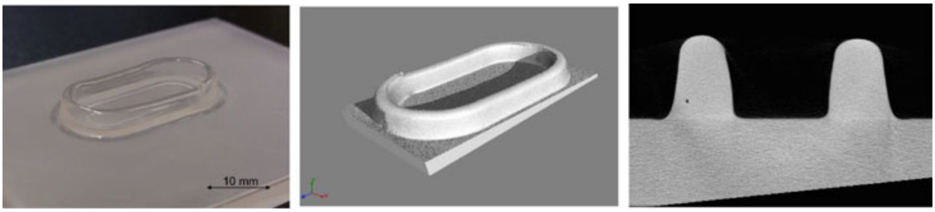

Fig. 5 Left: Real representation of a printed "ellipse" contour. Parameters used: $P_L = 95$ W, $v_A = 67.5$ mm/min, $v_F = 270$ mm/min. Middle: Overall representation of the CT model of the printed structure. Right: cross-sectional view of a section. The section shows the only bubble that could be found in the printed material

purpose, the substrate plate was rotated two times by 90° at each of the curve portions, while the linear axes were moved with a circular motion to the target position in the rotated coordinate system. This avoided a change in direction of the laterally fed fiber. The printed product shows transparent walls and was also analyzed for porosity by computer tomography. The analyses can be seen in Fig. 5 (middle, right) and show only isolated bubbles in the microstructure. Similarly, analyses of the chemical constituents show that only fused silica is present in the printed structure, thus ensuring that no components of the polymer coating are present in the printed structure.

In another example, a cone structure was printed by applying, in addition to the height shift, an overhang in the form of a shift of the fiber nozzle along the printing direction with each new layer. This is shown schematically in Fig. 6 (left). The maximum possible overhang depends on the width of the base layer. In our example, the base layer had a width of 1.2 mm. A maximal overhang of 1.5 mm (12.5% of the total width) was achieved. A single cone is shown in Fig. 6 (middle) and consists of about 60 layers. In Fig. 6 (right), the cone structure was printed several times inverted on top of each other, so that the following structure of about 300 layers could be realized. In contrast to the elliptical contour, boundary layers between the fibers can be recognized here. This indicates that the inside of the cone is not completely fused by the overhanging fiber.

A different application of the presented printing technology is the printing of free-form structures into the "air". In this case, after initial bonding of the fiber to the substrate, the fiber nozzle was pulled into the air, causing the fiber to solidify in the air and a free form could be printed. Due to the low mass of the fiber, it cooled very quickly despite the high temperatures and solidified into a solid form. This was exemplified in Fig.7 (left) in the form of a spring and in Fig. 7 (right) in the form of an individual bar. Combining such flexible structures with the solid structures, opens the possibilities to novel mechanical and optical structural parts and components made of glass.

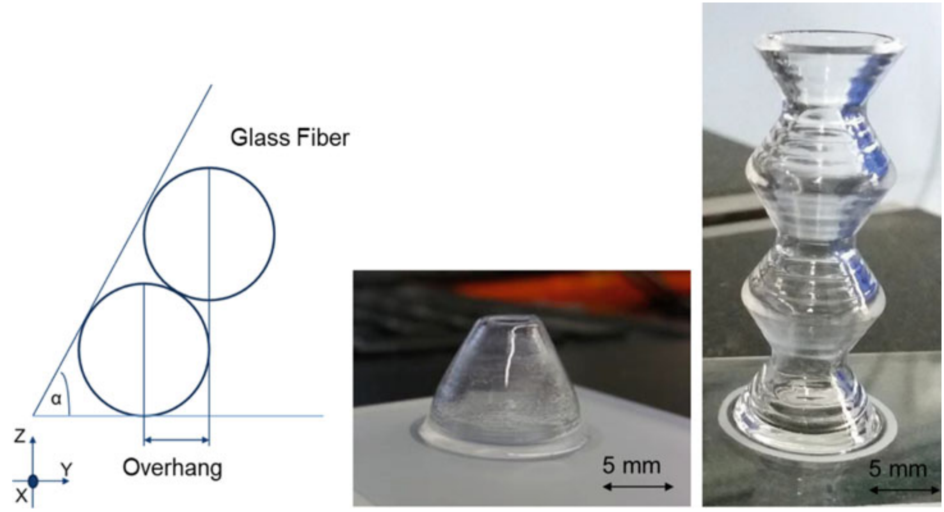

Fig. 6 Left: Sketch illustrating the printing process of a cone with the overhang drawn in. Middle: Real representation of such a printed cone. Isolated bubbles and fiber interfaces are visible. Right: Real representation of a printed multi-cone. The cone structure was printed multiple times, reversing on top of each other, in about 300 layers

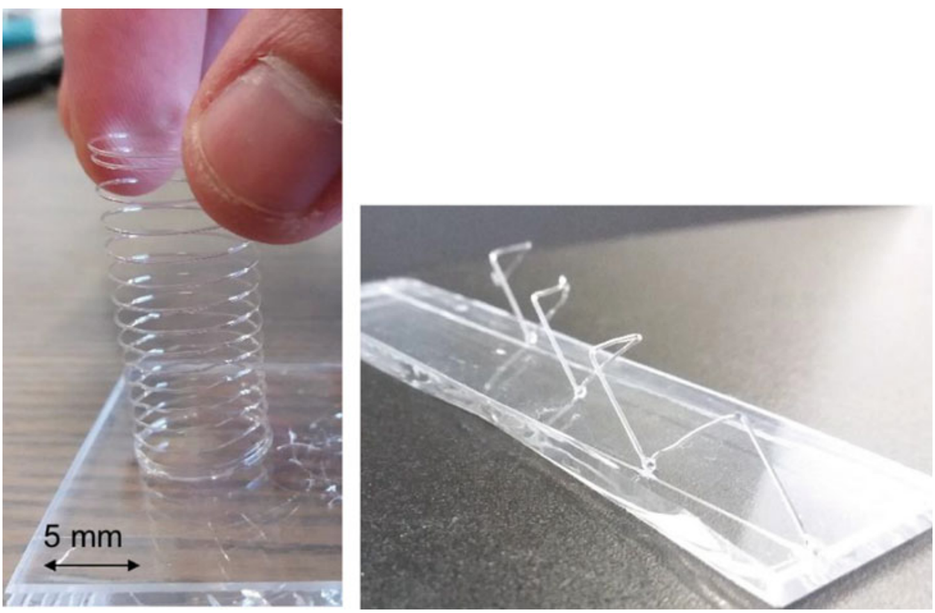

Fig. 7 Left: Real representation of a printed glass spring, which can elastically open and close. Right: Real representation of a printed free-form structure in the form of an individual bar

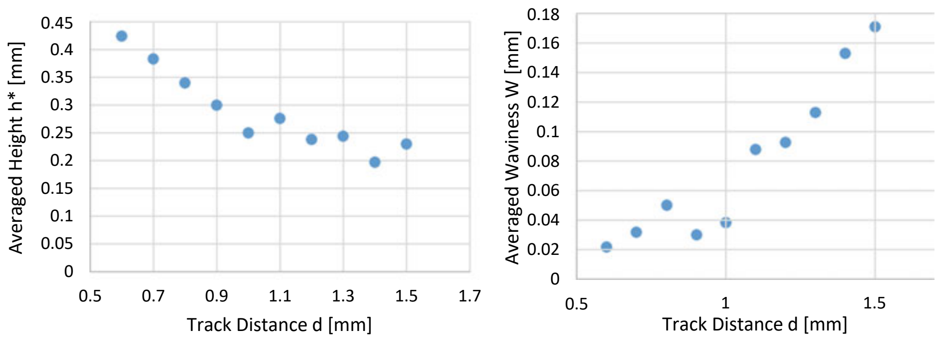

Fig. 8 Left: Graphical representation of the averaged height of a fiber layer as a function of the track spacing of the individual fibers. Right: Graphical representation of the averaged waviness of the surface of a fiber layer as a function of the track spacing. Print parameters: $P_L = 116$ W, $v_A = 67.5$ mm/min, $v_F = 234$ mm/min

Volumetric Structures

For printing a solid glass surface, the individual fibers were deposited in a meandering manner in a continuous process without cutting off the fiber. The surface finish depends on the deposition morphology of the individual tracks and their distance d from each other. In these tests, individual layers with an area of 20×20 mm^2 were deposited with varying track distances d = [0.6 – 1.5 mm] apart. The following parameters were used: A feed rate of $v_F = 234$ mm/min, an axis speed of $v_A = 67.5$ mm/min and a laser power $P_L = 116$ W. The surfaces of the individual layers were measured by means of tactile profile measurement. This resulted in the averaged height h* of the layer profile and the waviness W. The waviness was defined as the average of all differences between wave crests and troughs. The results are shown in Fig. 8.

In Fig. 8 (left), it is observed that the height decreases continuously with increasing orbital distance up to d = 1 mm. From d > 1 mm, the change is smaller and starts to stagnate, indicating that the track spacing has become too large to produce significant merging of the adjacent tracks. The initial decreasing profile height is explained by the decreasing overlap of the two orbits, which decreases the mutual merging. This is also evident in Fig. 8 (right). There, the change in waviness with increasing track spacing is shown graphically. For d < 1mm, the waviness (0.02 mm – 0.05 mm) increases only slightly, and the fibers can be well bonded together to produce a homogeneous surface. For d >1mm, the waviness increases abruptly, as already indicated in Fig. 8 (left). The overlap of the tracks is too small to ensure significant fusion. The individual layers showed no significant formation of bubbles, or sublimation. To illustrate the transparency, a barcode under a single layer is shown in Fig. 9. The barcode is very well visible, only the waviness of the glass surface distorts the image.

Fig. 9 Real representation of a printed single fiber layer for a track distance d = 1 mm. The fiber layer is transparent, but distorts the pattern due to the waviness. Left: Barcode pattern without 3D printed layer on top. Right: Barcode pattern with 3D printed layer on top

In the following, a cuboid was applied on the basis of the previous investigations. At the end of each layer, the fiber nozzle was raised while a 90° rotation was performed. As a result, the fibers were continuously printed orthogonally to each other without separation. Cuboids with a maximum of 21 layers were printed. An example of a cuboid is shown in Fig. 10. The printed cuboids show a high transparency in the top view, but a large number of bubbles can be seen. Increased homogeneity and transparency could be achieved with active laser power or feed rate control, as this would allow precise control of the deposition rate.

Besides the increased bubble appearance, a fine lattice structure can be observed in the volume of the cuboids. To investigate this, cross-sections of the cuboids were generated and analyzed under the microscope. The cross-section of a cuboid example is shown in Fig. 10 (down). The individual fiber tracts can be clearly seen, indicating no complete fusion. However, it was suspected that the refractive index gradients in the glass fiber filament caused these artifacts. Therefore, the cross sections of deposited fibers with and without a photoconductive core were compared. These cross sections are shown in Fig. 10 (up-right), and only for the fiber with a light guiding core do they show the previously observed interfaces. For the other fiber, complete fusion appears to have been realized. This suggests that the different refractive indices create an interface with the adjacent track. This effect could be used to realize novel optical components. To test this hypothesis, the refractive index curves in the glass volume have to be investigated in future studies.

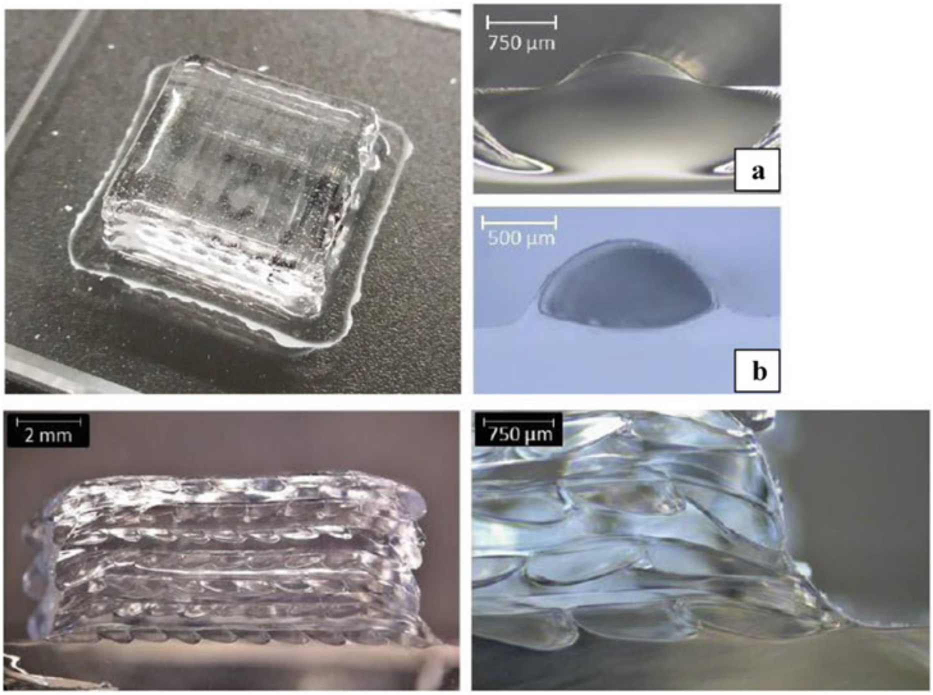

Fig. 10 Top left: Real representation of a printed cuboid with 14 layers and an edge length of 10 mm. Top right: Comparison of two fiber cross sections: **a** fiber has no light guiding core. **b** Fiber has a light guiding core. Bottom: Cross-sectional view of the printed cuboid. The interfaces of the individual fiber paths can be clearly seen

4 Conclusion

A rotary axis was integrated into the printing process to apply homogeneous fiber layers. This enabled the fiber to be deposited independently of direction, resulting in high process stability even in higher numbers of layers. Using the new setup, the printing of structural and volume elements was investigated. From initial parameter studies for the deposition of single fibers, parameter pairs were selected for the printing of the other elements. For the structural elements, the following parameters were used: $P_L = 95$ W, $v_{Rel} = 4$ with $v_F = 270$ mm/min and $v_A = 67.5$ mm/min. For the volume elements, the parameters were slightly adjusted with a $v_{Rel} = 3.5$: $P_L = 116$ W, $v_F = 234$ mm/min and $v_A = 67.5$ mm/min. Different contours were realized to demonstrate feasibility and process stability. On the one hand, cone shapes with overhangs between 1 and 1.5 mm were printed, which were applied periodically in the form of hourglass shapes in up to 300 layers, and on the other hand, free-form structures, such as the elastic spring and the bar. Combining such flexible structures with the solid structures, opens the possibilities to novel mechanical and optical structural parts and components made of glass. By printing an ellipse contour, it was shown that the printed products do not contain any residual coating. Due to the low bubble density, the ellipse contours exhibited high transparency. For volume elements, investigations were first carried out on individual layers in order to realize optimum parameters for printing surfaces with the lowest possible waviness. Track spacings of d < 1 mm were found to yield the lowest possible average waviness of 0.02–0.05 mm. Consequently, cuboids could be printed in 21 layers with the max. dimensions $14.8 \times 14.8, \times 9.4\ mm^3$. The printed solid elements showed a high transparency with isolated bubble inclusions in the top view and in the cross section, however, the boundary layers of the individual fibers could be observed. This artifact was not observed in printing with coreless glass fibers and suggests a refractive index gradient in the printed cuboid. Targeting this effect could be used to print novel optics. Future studies will analyze the material properties of the printed products.

Acknowledgements Parts of the experiments were conducted within the framework of the project "SmQL—Selbstlernende mehrstufige Qualitätsüberwachungsverfahren für die Lasermaterialbearbeitung" funded by AIF/IGF—FQS: 20419N. Also this research has been funded by the Deutsche Forschungsgemeinschaft (DFG, German Research Foundation) under Germany's Excellence Strategy within the Cluster of Excellence PhoenixD (EXC 2122, Project ID 390833453). The authors thank Sebastian Böhm and Rabeeh Ahammad Kallara Kallatummal for experimental support.

References

1. Gibson, I., Rosen, D., & Stucker, B. (2015). Additive Manufacturing Technologies, Springer-Verlag. *New York*. https://doi.org/10.1007/978-1-4939-2113-3
2. Scholze, H. (1988). Glas: Natur, Struktur und Eigenschaften. Springer-Verlag, 3. Version, Berlin, Heidelberg, New York, London, Paris, Tokyo.
3. Nürnberg, F.; Kühn, B.; Rollmann, K.: Metrology of Fused Silica, SPIE Laser Damage, 2016, Boulder, Colorado, United States https://doi.org/10.1117/12.2242487.
4. Klein, J., Stern, M., Franchin, G., Kayser, M., Inamura, C., Dave, S., Weaver, J. C., Houk, P., Colombo, P., Yang, M., & Oxman, N. Additive manufacturing of optically transparent glass. *3D Printing and Additive Manufacturing 2*(3).
5. Fateri, M., Gebhardt, A., Thuemmler, S., Thurn, L. (2014). Experimental investigation on selective laser melting of glass. *Physics Procedia 56*.
6. Kotz, F., Arnold, K., Bauer, W., Schild, D., Keller, N., Sachsenheimer, K., Nargang, T. M., Richter, C., Helmer, D., & Rapp, B. E.: Three-dimensional printing of transparent fused silica glass, *Nature 544*, 337–339.
7. Luo, J., Gilbert, L., Qu, C., Wilson, J., Bristow, D., Landers, R., & Kinzel, E. (2015). *Wire-Fed Additive Manufacturing of Transparent Glass Parts, ASME 2015 Int*. Manuf. Science and Engineering Conf.
8. Von Witzendorff, P., Pohl, L., Suttmann, O., Heinrich, P., Heinrich, A., Zander, J., Bragard, H., & Kaierle, S. (2018). Additive manufacturing of glass: CO_2-Laser glass deposition printing. In Conference on Photonic Technologies.

9. Sleiman, K., Malek, T., Hohnholz, A., Dittrich, M., Jäschke, P., Kaierle, S., Denkena, B., & Overmeyer, L. (2021). Investigation on the temperature dependent morphology of deposited fibers for laser based glass additive manufacturing, Engineered Transparency.
10. Rettschlag, K., Kranert F., Hohnholz, A., Wienke, A., Suttmann, O., Neumann, J., Kracht, D., Lachmayer, R. (2019). Laser deposition of fused silica coreless fibers to generate functional waveguides. In Laser in Manufacturing Conference.
11. Capps, N., Goldstein, J., Rettschlag, K., Sleiman, K., Jäschke, P., Kaierle, S., & Kinzel, E. Digital Glass Forming of Transparent Borosilicate Structures, Manufacturing Letters
12. Grabe, T., Lammers, M., Wang, S., Wang, X., Rettschlag, K., Sleiman, K., Barroi, A., Biermann, T., Ziebehl, A., Röttger, J., Ley, P.-P., Wolf, A., Jäschke, P., Hermsdorf, J., Kaierle, S., Ahlers, H., Lachmayer, R. (2021). Additive manufacturing of fused silica using coaxial laser glass deposition: Experiment, simulation, and discussion. In Proceedings Volume 11677, Laser 3D Manufacturing VIII; 116770Z. https://doi.org/10.1117/12.2577205.
13. Pohl, L., von Witzendorff, P., Chatzizyrli, E., Suttmann, O., & Overmeyer, L. (2018). CO_2 laser welding of glass: numerical simulation and experimental study. *The International Journal of Advanced Manufacturing Technology*

Multi-Functional Parts—Increase Functionality of Semi-Finished Parts by Additive Manufacturing

Christian Schmid, Markus Ehrlenbach, Christoph Herden, and Thomas Schmiedinger

Abstract

Additive manufacturing is a versatile fabrication technology for many different applications. The flexibility of additive manufacturing opens a wide range of design opportunities. Contrary, due to the single material approach in additive manufacturing, the functional application of these objects is limited by the material's parameter. An approach to overcome this limitation are multi-functional objects, which combine different materials. The combination of different materials with specific parameters enables the generation of parts with tailor-made functionality. The paper aims to investigate the approach of multi-functional objects to be used with semi-finished parts (e.g. tubs, rods, formed sheet structures). The additional functional elements are deposited on the semi-finished parts by a wire-based additive manufacturing process. Materials like wood and thermoplastics have been selected for characterizing the adhesional properties and the requirements in designing the interfaces. Mechanical properties of the joints will be presented in dependency on material combination and surface preparation.

Keywords

Multi-functional parts • Additive manufacturing • PMMA • PLA

C. Schmid (✉) · M. Ehrlenbach · T. Schmiedinger
Fachhochschule Kufstein Tirol Bildungs GmbH, University of Applied Sciences, Andreas Hofer Str. 7, 6330 Kufstein, Austria
e-mail: christian.schmid@fh-kufstein.ac.at

C. Herden
Institute of Polymer Materials and Plastics Engineering, TU Clausthal, Agricolastr. 6, 38678 Clausthal, Germany

R. Lachmayer et al. (eds.), *Innovative Product Development by Additive Manufacturing 2021*, https://doi.org/10.1007/978-3-031-05918-6_19

1 Introduction

1.1 Relevance of Multi-functional Parts—Material Extrusion on Semi-Finished Parts

Material extrusion is one of the most widely used additive manufacturing processes and offers many possibilities for various applications in the areas product development and production. The extensive material possibilities span a range from simple thermoplastics of different properties to filled thermoplastics with fibers and particles made of organic, ceramic or metallic materials, which can be used directly or further processed by a post-process to a metallic body, for example.

This variety of different materials results in a wide range of design options for the designer. The possibilities are expanded by combining different materials into hybrid, functional groups. This can be achieved by combining different materials such as polylactic acid (PLA) as structurally stable components with a permanently elastic thermoplastic polyurethane (e.g. for applications as a wheel-tire combination to meet various requirements). Organic materials can also be used as substrate materials, such as wood in combination with PLA or other materials.

A major disadvantage of material extrusion is the increased production time in comparison to subtractive fabrication methods like milling. Especially the fabrication of flat objects requires more time when compared to other production approaches (e.g. cutting). Consequently, the usage of semi-finished objects (e.g. plates, tubes, profiles, etc.) as substrate for additive manufacturing may overcome the production time issue of purely additive manufacturing. Thus, in combination with additive processes, semi-finished products can be expanded in multi-functional components. An example for a multi-functional object is shown in Fig. 1.

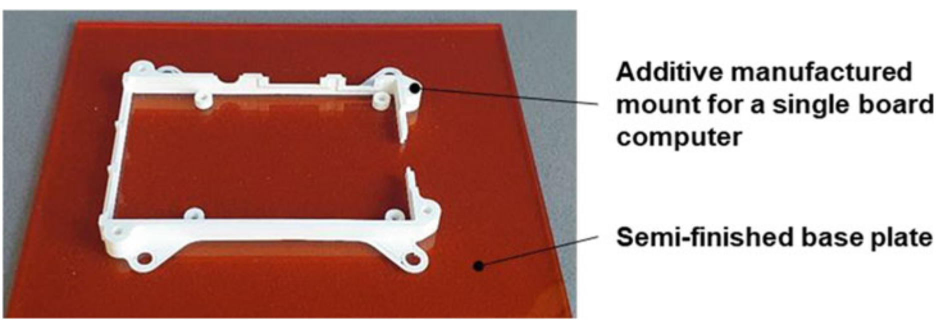

Fig. 1 Example for a multi-functional object which combines an additive manufactured mount for a single board computer and a semi-finished base plate

1.2 Hybrid Design Approach

A mandatory prerequisite of multi-functional objects is the design of the joint between the 3D printed object and the substrate. Thus, the paper aims to investigate the design parameters to define a hybrid design approach. As a long-term goal, the knowledge of the hybrid design approach can be used for the fabrication of multi-functional objects with the following characteristics: tool-free assembly, mounts for various mechatronic components, and integration of seals and interfaces.

As an example, the hybrid design approach will be described for a sensor box and for fused filament fabrication (FFF) desktop printers: The hybrid design approach starts with the assembly of the semi-finished products. These substrates will be equipped with necessary trimmings and openings. The first production step is realized by milling or cutting technologies. In the next step, the mounts for the mechatronic components will be fabricated directly onto the substrates by additive manufacturing. Finally, structures for sealing and closing will be fabricated at the edges of the semi-finished plate. These structures are responsible for secure closure and a tight-sealing of the sensor box. Additionally, the closing structures will be designed to enable the assembly without the requirement of additional tools or materials.

Another possible application of the hybrid design approach is the fabrication of low- to medium-priced FFF desktop printers. At the moment, companies like Prusa or Airwolf produce parts of the FFF desktop printers in printer farms. By using semi-finished products, the production time of these systems might be reduced significantly. In this case, the design of the housing might incorporate plates. Mounts for the required mechatronic components will be printed on the plates. The printer is assembled by inserting purchased components with almost no tools or mounting material. An additional benefit arises from the fact that the components can be easily detached and replaced without the need of additional tools.

A possible design of structures for sealing and closing is shown in Fig. 2. The connector consists of two parts which will be directly printed on the substrates. To guarantee

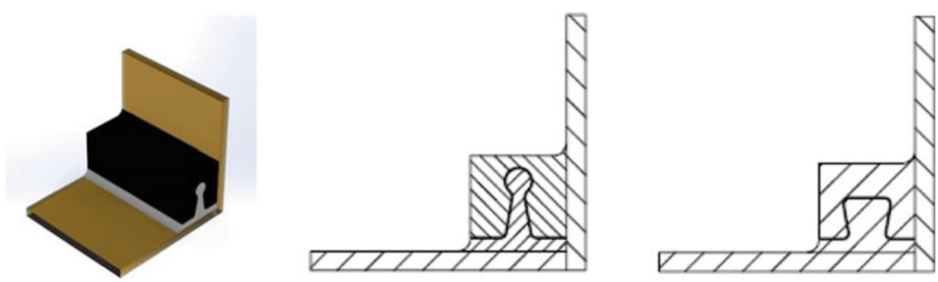

Fig. 2 Basic principle of the hybrid design system

a stable joint between the additive manufactured objects and the substrates, the design of the interface has to be optimized.

2 Problem and Objectives

Essential prerequisites for the realization of the hybrid design approach are: (a) the creation of standardized and parameterized features that can be integrated and scaled into the design, (b) optimized surface structure of the interface to ensure the adhesion of different material pairings, and (c) process parameters for the fabrication of the multi-functional objects.

At first, experimental tests with polymethyl methacrylate (PMMA) as substrate and polylactic acid (PLA) as thermoplastic for the additive production process were conducted. These experiments focused on the relevant conditions, which are necessary to achieve optimal adhesion between the substrate and the 3D printed object.

In addition to the printing on unstructured surfaces, adhesion tests with laser engraved surfaces were also carried out. Since the laser is used as a cutting tool in the fabrication of the semi-finished plates anyway, it is also possible to use it as a tool for structuring the surface of the substrate with the goal to increase the bonding strength.

The aim was to define the requirements for the substrate surfaces and the FFF printing process. According to the aim, two research questions were stated:

Which conditions in the contact zone between semi-finished product (PMMA plate) and 3D printing are decisive for maximum adhesion?

Do structures processed by laser ablation have an effect on improving adhesion?

3 State of Knowledge

3.1 Hybrid Structures by 3D-Printing

Fused filament fabrication (FFF) 3D printing is one of the most widely used additive processes. In most cases, components are made of one or a maximum of two different materials by means of material extrusion. Hybrid approaches expand the possibilities and properties of printed structures. Wimmer et al. [1] described the possibilities of filaments enriched with wood particles for the production of wood-like structures, also in combination with colored plastics. However, the use of prefabricated elements of the same or other materials in combination with 3D printing offers some additional advantages to improve productivity, increase the variety of materials, and expand the design possibilities. Mathias et al. [2] showed the possibilities of hybrid components of semi-finished products with 3D-printed structures using the combination of Lego building blocks and 3D printing.

3.2 Principles of Joining with 3D-Printing

The possibility of producing hybrid structures from different materials depends crucially on the establishment of a solid bond. The process of printing PLA on PMMA is formally equivalent to an adhesive bonding process. The substrate (PMMA) is placed on the build plate of the 3D-printer followed by deposition of the filament directly on the substrate. During the deposition process, only the filament is heated. Although, the build plate is heated, the temperature of the build plate does not exceed the plasticization temperature of the substrate. Thus, the PLA solidifies on the PMMA surface without realizing a material mixing compound.

Major influencing factors of the bonding process are the effects of adhesion and cohesion, which determine the bonding strength of the two components [3, 4]. Cohesion describes the interatomic and molecular binding forces acting in the "adhesive", in this case, the printed PLA. Adhesion, on the other hand, defines the bond to the substrate (PMMA).

The adhesion of strands applied in the shift process is the subject of some scientific work. The vast majority of investigations related to the adhesion between the individual layers of a component made of a homogeneous plastic. In his work, Butzke [5] investigated the fundamental relationships between layer adhesion in fused filament fabrication and presents approaches for improving adhesion to joints with similar material. Kneidinger [6] investigated the system of wood and polymer to determine the main adhesion effects.

Coogan and Kazmer [7] showed the direct relationship between the transferable force and the connecting surface. It is emphasized that "activating" processes on the surface, for example, by plasma treatment [8] or by gas-phase fluorination [9], generate a positive adhesion effect. Sapkal [10] shows that the thickness of the first layer has a decisive influence on the strength of PLA structures.

Meyer et al. [11] investigated the deposition of PLA on textiles by FFF. They showed that a pre-treatment of the textiles by a PMMA coating significantly increased the adhesion of PLA.

The deposition of PLA on polyamide (PA) was investigated by Sanatgar et al. [12]. As a result of investigating the influence of process parameters like extruder temperature, build plate temperature, and print speed on the adhesion, a set of optimal parameters could be defined. The bonding strength was tested by a standard test according to SS-EN ISO 1139:2010. The results of the experiments showed, that the extruder temperature and build plate temperature were directly proportional to the bonding strength of the PLA/PA compound.

The foundation of the hybrid design approach relies on the hypothesis that a surface enlargement by vertical area fractions by macroscopic and microscopic effects in the form of macroscopic grooves and microscopic surface roughness has a significant effect on the resilience of the connections. If a separation, i.e. a crack, occurs, it can be observed in preliminary tests that almost without exception, a separation occurs in the interface between the two materials. Rarely do individual material components of the printed PLA stick to the surface. The fracture can thus be characterized as an adhesion fracture, in a few cases as a mixed fracture [13].

4 Material and Methods

4.1 Test Object for Contact Zone Experiment

A specific 3D printed test object has been designed to investigate the influence of the contact zone onto the bonding strength of the multi-functional parts. The design of the object was optimized to achieve a distributed load in the contact zone preventing stress peaks. The 3D printed test object consisted of a square base plate at the interface with a side length of 15 mm and a thickness of 0.4 mm. The cross-section merged into a circular section with a diameter of 5 mm. To provide a stable connection between the 3D printed object and the different loads, the upper part of the object was widened, enclosing a drop-like hole (see Fig. 3).

The fabrication process was accomplished with a desktop FFF printer (Ultimaker 2+; Ultimaker). The G-code was prepared by the slicing software Cura (v4.9.0; Ultimaker). The fabrication parameters were set to 0.2 mm layer height and 0.4 mm layer width. The infill was set to 100%. The temperature of the nozzle was set to 200 °C, and the build plate temperature was set to 60 °C.

The PMMA substrates were placed directly on the build plate. A frame ensured a defined position of the samples during the printing process. The vertical position of the print nozzle was referenced relative to the frame. After loading the samples into the desktop FFF printer, the fabrication process was started.

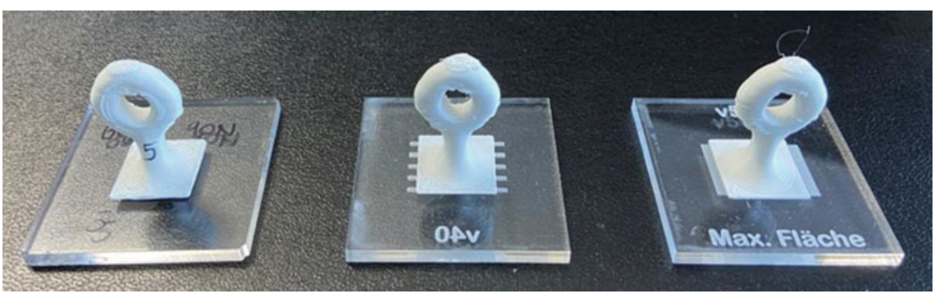

Fig. 3 The 3D printed test object consisted of a square base plate, a circular intermediate section, and an enclosed drop-like hole, which served as the attachment point for the experiments. On the left, the unstructured substrate is shown. The semi- structured substrate is shown in the middle. The structured substrate is shown on the right

4.2 Substrate-Surface-Structure Test Object

A test object for tensile lap-shear strength experiments was designed to investigate the influence of different surface structures on bonding strength. The design was optimized to achieve a solid adhesion of the initial PLA layer on the PMMA substrate (see Fig. 4). The dimensions of the sample is based on the definitions of the standard EN 1465:2009 with the two differences: (1) thickness of the PMMA substrate was 1.8 mm and (2) thickness of the PLA substrate was 3.8 mm. The differences resulted from the fabrication process of the test object.

The fabrication process was accomplished with a desktop FFF printer (Ultimaker 2+; Ultimaker). The G-code was prepared by the slicing software Cura (v4.9.0; Ultimaker). The fabrication parameters were set to 0.2 mm layer height and 0.4 mm layer width. The height of the initial layer was set to 0.1 mm for achieving a solid adhesion of the first layer on the PMMA substrate. The infill was set to 100%. The temperature of the nozzle was set to 230 °C, and the build plate temperature was set to 60 °C.

The fabrication process started with printing the PLA until reaching a height of 1.7 mm. At this height, the process paused and the PMMA substrate was inserted. The production process resumed and the initial layer of PLA on the PMMA substrate was deposited. Due to the height difference of 0.1 mm between the PLA and the PMMA substrate, the print nozzle was pressed on the PMMA substrate, thus a solid bonding of the initial PLA layer was achieved.

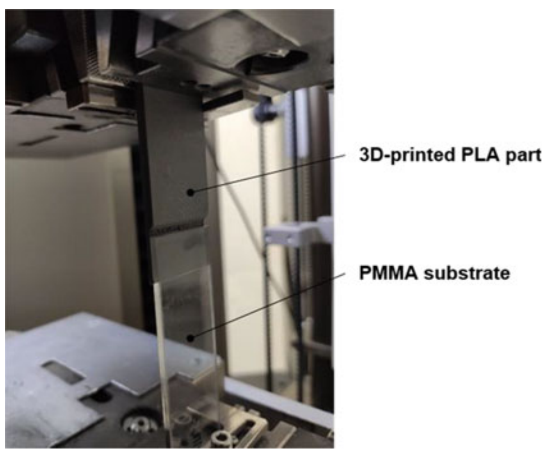

Fig. 4 The test object for assessing the influence of substrate structure onto adhesion was designed according to the standard EN 1465:2009. The thickness of the PMMA and PLA part was 1.8 mm and 3.8 mm, respectively

4.3 Preparation of PMMA Substrates

For the contact zone experiments, PMMA substrates with a side length of 40 mm were prepared. The thickness of the substrates was 3 mm. The substrates for the substrate-surface-structures experiments exhibited a length of 100 mm and a width of 25 mm. The thickness of these substrates was 1.8 mm. A laser engraver equipped with a CO_2 laser (Speedy 100; Trotec) was used for the cutting of the substrates.

The surface-structure of the substrates was either unstructured, structured, or semi-structured. Unstructured samples were defined as the original state of the untreated substrate. Semi-structured surfaces exhibited a periodic pattern consisting of engraved lines with a width of 1 mm and a distance between the lines of 2 mm. The depth of the engravements were 0.16 mm and 0.34 mm. Structured surfaces were fabricated by a complete engravement of the substrate surface (see Fig. 3). The samples were cleaned by isopropyl alcohol prior to the printing process.

4.4 Measurement of Bonding Strength

The bonding strength for investigating the influence of the contact zone onto bonding was assessed by applying static loads ranging from 20 N (0.09 MPa) to 420 N (1.87 MPa). The direction of the load was perpendicular to the interface. The point of force application was the center of the 3D printed test object (see Fig. 3). Static loads were evenly increased until sample fracture. Based on the load, the maximal bonding strength was calculated by dividing the force by the interface area (225 mm^2).

4.5 Assessment of Initial-Layer Structure After Failure

The surface structure of the interface of the 3D printed test object after failure was assessed by optical means. The surface of the interface on the 3D printed test object was assessed by optical scanning (3D structured light scanner Pro S3; HP). Test objects were fixated on a rotary base. Recorded point clouds were fused to one scan based on ten optical scans, which are evenly distributed over a full rotation. Final images were prepared with the software blender (v2.93.0).

Roughness (Rs) of the surface was determined according to El-Soudani [14]. The coefficient Rs was calculated by dividing the actual area by the nominal area. The nominal area of the samples was defined as the interface area of the plane PMMA substrate and the PLA test object. The surface of the engravements in the case of the semi-structured substrates was excluded. Thus, the focus remained on the initial layer between the test object and the substrate. The determination of the surface areas was accomplished with the software blender (v2.93.0). The analysis of the parameters was done with the software MATLAB (R2021a).

4.6 Measurement of Lap-Shear Strength

Tensile lap-shear strength of substrates with different surface-structures was determined according to EN 1465:2009. The experiments were conducted on a universal testing machine (BZ2-MM100TL.ZW01, Zwickl). For each substrate-surface-structure, six probes were tested. Measurement parameters were force and elongation. Tensile lap-shear strength was calculated based on the force and the bonding area of each probe. Strain was expressed in percent relative to the free length of the probe (112.5 mm) at the beginning of the experiment.

The values of the tensile lap-shear strength from each substrate-surface-structure group were tested ($n = 6$) upon normal distribution by applying the Anderson–Darling test (significance level 5%). Outlier in the sample group were identified based on the distance of the measurement point to the median value. The distance was set to three scaled median. Statistically significant differences between the samples was determined by paired-sample t-test. The significance level was set to 5%. Statistical analysis were accomplished with the software MATLAB (R2021a).

5 Results and Discussion

5.1 Influence of Contact Zone Structure onto Bonding Strength

The experiments revealed that the bonding strength was indirect proportional to the roughness of the surface. An increase of the surface roughness caused a decrease of the tensile strength (see Fig. 5). This relationship was observed for all three substrate-surface-structures. The highest values for the tensile strength at failure were reached by the semi-structured substrates. The roughness may play a role in establishing a solid bonding in- between the engravement, nevertheless, the engravement itself may also positively influence the bonding strength. As a consequence, the semi-structured substrates may benefit from surface roughness and the engravements.

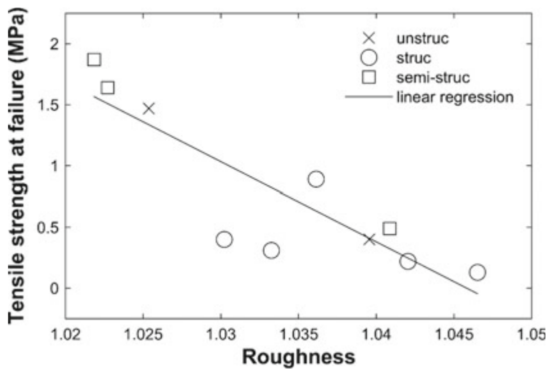

Fig. 5 The tensile strength at failure correlated with the roughness of the surface of the test object. Three different substrate- surface-structures were tested. Unstructured surfaces (unstruc) are marked with a “x”, structured surfaces are highlighted with a “o”, and semi-structured surfaces (semi-struc) with a engravement depth of 0.34 mm are displayed as squares. The R-value of the linear regression between tensile strength at failure and roughness of all samples was 0.76

The roughness parameter Rs describes the relationship between actual area and the nominal area. Rough surfaces exhibit a higher actual area compared to plane surfaces. For absolute plane surfaces, the parameter Rs reaches a value of one. The surface scan of semi-structured surfaces with different roughness parameters is shown in Fig. 6. A surface with a low roughness value was characterized by non-visible filament strands. In comparison, the filament strands were visible on surfaces with a greater roughness value. Visible filament strands may indicate an incomplete filling of the first layer. This is probably caused by a too low extrusion rate. The required extrusion rate is calculated based on parameters like layer height, nozzle diameter, filament diameter, and print speed. In the case of differences between the expected and real values (e.g. greater distance between nozzle and substrate), the calculated extrusion rate differs from the required extrusion rate. This difference can finally cause an incomplete filling of the layer.

Prior to the printing process of the test samples, the print nozzle was levelled to the frame, which was used to position the individual samples on the print bed. Measurements of the samples showed, that the thickness of the samples differed from the thickness of the frame. Samples with a lower thickness compared to the thickness of the frame resulted in an increased distance between nozzle and substrate. As a consequence, the calculated extrusion rate was lower than the required extrusion rate which resulted in an incomplete filling of the initial layer.

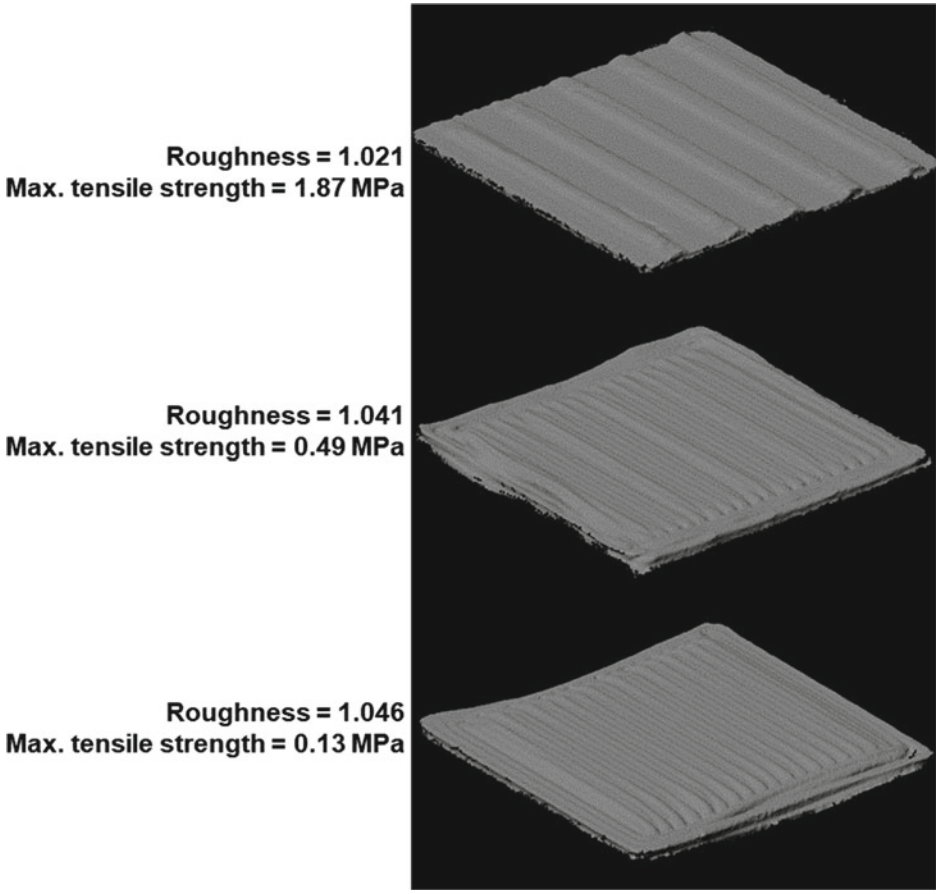

Fig. 6 The surface scans of three different substrates with the corresponding roughness parameter and maximum tensile strength at failure are shown

5.2 Influence of Substrate Surface Structure onto Bonding Strength

Structured surfaces exhibited a statistically significant higher tensile lap-shear strength compared to unstructured surfaces (p-value = 0.0052; see Fig. 7). Thus, the resulting surface after a complete structuring by a laser engraver caused an increase in the tensile lap-shear strength compared to the unstructured surface. One of the probes of with a structured surface reached a high value of lap-shear strength (2.7 MPa). Based on the pre-defined criterias for outlier detection, the value was identified as an outlier. As a consequence, the value was replaced by the median value for the following analysis.

Two different semi-structured substrates were tested to investigate the influence of the depth of the engravements onto bonding strength. Semi-structured substrates with a depth

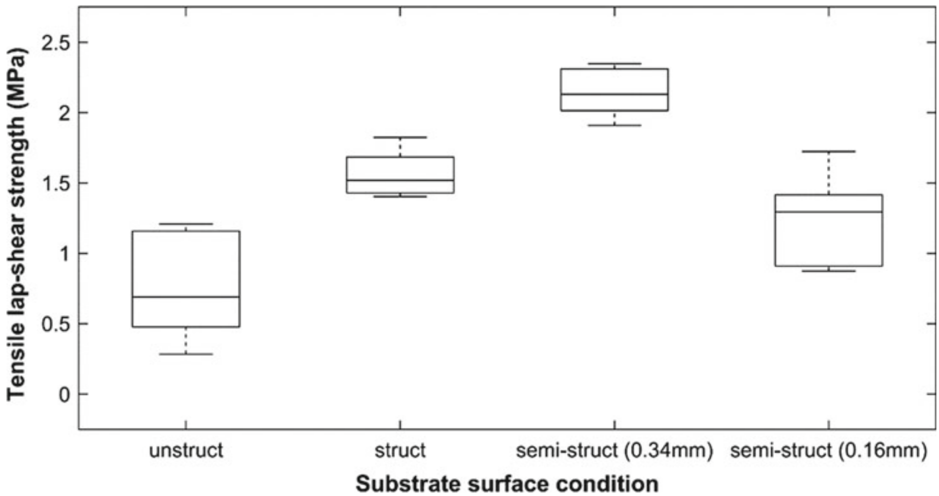

Fig. 7 The substrate-surface conditions influenced the maximum tensile lap-shear strength. Four different substrate- surface-structures have been tested: unstructured (unstruct), structured (struct), and two semi-structured (semi-struct) surfaces with different depths of engravements. The depth of the engravement is shown in brackets. For each substrate-surface- structure, six samples have been tested. The central mark of the box plot displays the median of the samples. The bottom and top edge of the box indicate the 25th and 75th percentiles, respectively. The whiskers represent the most extreme data points, which have not been labelled as outliers

of 0.34 mm reached the highest tensile lap-shear strength of all samples (see Fig. 7). The increase in strength relative to unstructured surfaces was statistically significant (p-value = 0.0037). Semi-structured engravements with a depth of 0.16 mm displayed no statistically significant increase in tensile lap-shear strength compared to unstructured surfaces (p-value = 0.0716; see Fig. 7).

By laser structuring, the resulting surface may exhibit an increased total surface area, which provides a larger bonding area than unstructured surfaces. Therefore, the bonding strength of structured substrate-surfaces withstands higher stress values than unstructured surfaces.

Semi-structured surfaces can increase the bonding strength of PLA/PMMA hybrid structures in the case of engravements with a depth of 0.34 mm. The engravements, which were normal to the load direction, might enabled an additional force flux through the lateral faces of the engravement. This additional force flux may positively affect the bonding strength of the hybrid structured.

Semi-structured surfaces with a depth of 0.34 mm exhibited a statistically increased tensile lap-shear strength compared to structured surfaces (p-value = 0.0037). In contrast to the microscopic structure of the engravement process in the case of structured surfaces, the increase in bonding strength of semi-structured surfaces may arise from the macroscopic design of the engravements.

The stress–strain behavior of the samples differed in dependency to the surface structure. Unstructured surfaces exhibited multiple stress-declines in the stress–strain curves (see Fig. 8a). Substrates with a structured surface displayed a uniform behavior of the stress–strain behavior. At higher strengths (>1.2 MPa), stress-declines were visible (see Fig. 8b). The behavior of semi-structured substrates depended on the depth of the engravements. Semi-structured substrate with depths of 0.16 mm exhibited a higher number of small stress-declines compared to unstructured substrates (see Fig. 8c). In the case of

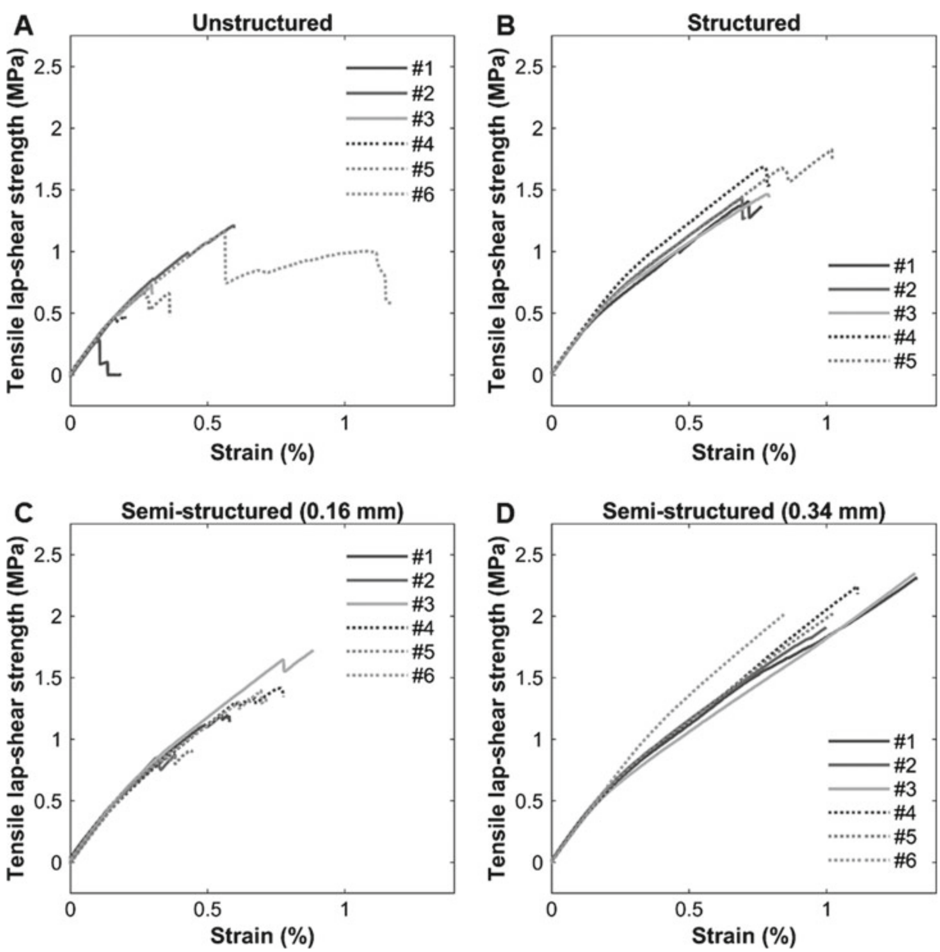

Fig. 8 Strength-strain curves of the four different substrate-surface conditions. For each surface conditions, six samples were tested. In the case of structured substrate surface, five samples were included into the analysis

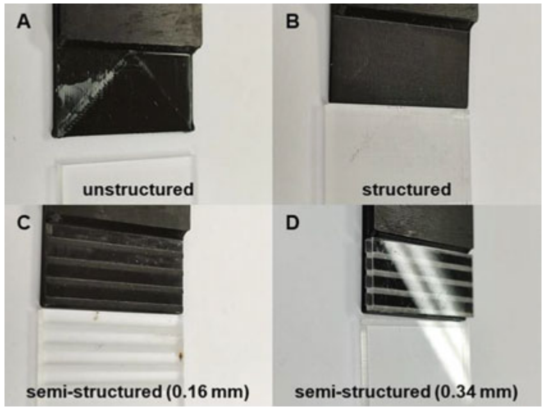

Fig. 9 Images of the probes after testing revealed the mode of failure. Unstructured, structured, and semi-structured (0.16 mm) were characterized by interfacial bond failure. Semi-structured substrates (0.34 mm) exhibited the failure in the PMMA substrate. The fracture face was in plane with the sidewall of an engravement indicating, that the engravement induced a crack, which finally led to failure

semi-structured substrates with an engravement depth of 0.34 mm, the stress–strain curves exhibited no declines compared to the other samples (see Fig. 8d).

The observed mode of failure of unstructured, structured, and semi-structured (0.16 mm engravement depth) substrates was interfacial bond failure (see Fig. 9a–c). The PMMA and PLA substrates remained intact. The mode of failure of semi-structured substrates with an engravement depth of 0.34 mm was classified as failure in the PMMA substrate. In this case, a crack may have been induced by the engravement which led to the failure (see Fig. 9d).

Unstructured substrates may gradually fail by partial detachment of the PLA part from the PMMA part. The behavior differed between the probes, which indicates a certain randomness of failure behavior. This randomness may be caused by different parameters originating from the substrate itself (e.g. unevenness of the substrate) or from the printing process (e.g. imperfections of the filament, local weak points). The individual stress–strain curves of the probes of structured surfaces was more similar compared to the unstructured surfaces. The structuring process may increase the roughness of the substrate surface, which causes an increase in the total contact area. The resulting microstructure may also act like a micro-serrating which increases the bonding strength.

The resulting uniform surface structure may led to a uniform behavior of the samples. The semi-structured substrates with 0.16 mm engravements exhibited small stress-declines, which may indicate a partial failure of the bonding. In this case, the partial failures may occur at the engravements. In comparison to the unstructured substrates, the engravement enabled a more comparable behavior of the different probes. Semi-structured surfaces with an engravement depth of 0.34 mm displayed a steady stress–strain curve without the occurrence of stress- declines. The engravement may act as interlocking connections providing an additional bonding mechanism between the PMMA and PLA parts. To the contrary, the engravement facilitated crack formation, which might led to the final failure.

6 Conclusion

Hybrid design approaches for multi-functional parts open up great potential for new designs of components. The integration of semi-finished products such as plates and profiles enables a significant reduction in 3D printing process times and costs. In addition, it is possible to combine different materials without the use of additional assembly tools. Essential boundary conditions for the profitable use of this hybrid technology are the production of well-adhering connection zones between semi-finished products and 3D printed structures. As part of the project, the influencing variables for maximum bonding were therefore investigated for the material connections between PMMA (substrate) and PLA (3D printed test object). In addition to untreated plate surfaces, laser- structured surfaces were also examined with regard to their influence on adhesion.

Tensile strength experiments revealed that the surface roughness of the 3D printed part influences the bonding strength of PLA/PMMA hybrid parts. Maximum bonding strength was reached for printed surfaces with a low roughness value. Beside roughness, the engravements of semi-structured substrates increased the bonding strength too.

To investigate the influence of substrate-surface-structure onto bonding strength, tensile lap-shear strength was measured. The standardized experiment method showed, that periodic engravements can increase the bonding strength of PLA/PMMA hybrid parts.

Finally, the research questions can be answered as follows:

Which conditions in the contact zone between semi-finished product (PMMA plate) and 3D printing are decisive for maximum adhesion?

It could be shown that the thickness of the first layer, often due to insufficiently levelled print beds, is decisive for good adhesion. In addition, the size of the connecting surface plays a significant role. A suitable measurement parameter for the quality of the initial layer is the roughness, which indicates the filling grade of the initial layer. Due to the deviation of planned and real distance between the nozzle and the substrate, the calculated extrusion rate was too low resulting in visible filament strands in the contact zone. The roughness of these structures is higher than the roughness of proper filled initial layers. It could be shown that the roughness is negatively proportional to the bonding strength. To conclude, a smooth surface of the initial layer is mandatory to provide maximum adhesion.

Do structures processed by laser ablation have an effect on improving adhesion? Laser-structured surfaces, even with vertical surface components, can increase the load-bearing capacity of the connection if the grooves are fully penetrated and no gaps have arisen. Furthermore, the depth of the engravements plays a significant role in improving adhesion. As it has been shown, engravement with 0.34 mm depth provided a higher adhesion than engravement with a depth of 0.16 mm. On the contrary, deeper engravement can weaken the substrate by facilitating crack induction.

Further experiments are required to study the influence of macroscopic and microscopic structures onto the bonding strength of multi-functional parts. Structured substrate have been produced by a defined set of fabrication parameters, however, a variation of these processing parameters might generate different microscopic structures which exhibit different bonding strengths.

The combination of microscopic structures with macroscopic structures has to be investigated to identify optimum combination of both effects to achieve a high bonding strength. Engravement patterns and the direction of the engravement are additional parameters which might influence the bonding strength of multi-functional parts. Further, the relationship between 3D printing process parameters (e.g. nozzle diameter, layer height) and the depth of the engravement should be investigated too for unrevealing possible relationships. In addition, the investigation of different material combination may also enlarge the application area of the hybrid design approach.

By systematically investigating the influencing parameters for designing hybrid structures, a set of recommendations may be defined for enabling the industrial application of the presented approach.

References

1. Wimmer, R., Steyrer, B., Woess, J., Koddenberg, J., & Mundigler, N. (2015). 3D Printing and Wood. *PROLIGNO 2015, 11(4),* (pp. 144–149). Retrieved from https://publik.tuwien.ac.at/files/PubDat_243647.pdf.
2. Mathias, D., Snider, C., Hicks, B., & Ranscombe, C. (2019). Accelerating product prototyping through hybrid methods: Coupling 3D printing and LEGO. *Design Studies, 62,* (pp. 68–99). https://doi.org/10.1016/j.destud.2019.04.003.
3. Jüntgen, T. (2020, January 1). *Kohäsion und Adhäsion Grundlagen des Klebens erklärt: Voraussetzung, Adhäsion, Kohäsion.* Retrieved from https://www.konstruktionspraxis.vogel.de/grundlagen-des-klebens-erklaert-voraussetzung-adhaesion-kohaesion-a-794496/
4. N.N. (2021, June 6). *Leitfaden Kleben – aber richtig*. Retreived from https://leitfaden.klebstoffe.com/0-5-benetzung/.
5. Butzke, J. (Ed). (2019). Verfahrenstechnische Weiterentwicklung des Fused Layer Manufacturing zur Reduzierung der Anisotropie im Bauteil. Berlin: Universitätsverlag der TU Berlin. http://dx.doi.org/https://doi.org/10.14279/depositonce-7651.
6. Kneidinger, G. (Ed.). (2019). *Interaktion und Adhäsion zwischen lignozellulosischen Regeneratfasern und synthetischen Polymeren.* Universität für Bodenkultur Wien.

7. Coogan, T. J., & Kazmer, D. (2017). Healing simulation for bond strength prediction of FDM. *Rapid Prototyping Journal*, *23(3)*, 551–561. https://doi.org/10.1108/RPJ-03-2016-0051.
8. Gleich, H. (2004). *Zusammenhang zwischen Oberflächenenergie und Adhäsionsvermögen von Polymerwerkstoffen am Beispiel von PP und PBT und deren Beeinflussung durch die Niederdruck-Plasmatechnologie*. Fakultät für Ingenieurwissenschaften, Abteilung Maschinenbau der Universität Duisburg-Essen.
9. Achereiner, F. (2009). *Verbesserung von Adhäsionseigenschaften verschiedener Polymerwerkstoffe durch Gasphasenfluorierung*. Universität Erlangen-Nürnberg.
10. Sapkal, S., Harne, M. S., Umakant Landage, U., & Pathan, A. (2020). Parametric investigations of 3D-printing of fused deposition manufactured (FDM) structures of polylactic acid (PLA). *International Journal for Research in Applied Science & Engineering Technology, 8(XII)*, 328–332. https://doi.org/10.22214/ijraset.2020.32486.
11. Meyer, P., Döpke, C., & Ehrmann, A. (2019). Improving adhesion of three-dimensional printed objects on textile fabrics by polymer coating. *Journal of Engineered Fibers and Fabrics, 14,* 1–7. https://doi.org/10.1177/1558925019895257.
12. Sanatgar, R. H., Campagne, C., & Nierstrasz, V. (2017). Investigation of the adhesion properties of direct 3D printing of polymers and nanocomposites on textiles: Effect of FDM printing process parameters. *Applied Surface Sciences, 403*, 551–563. https://doi.org/10.1016/j.apsusc.2017.01.112
13. Jüntgen, T., & Juschkat, K. (2019, February 4). *Grundlagen des Klebens: Wann Klebverbindungen versagen—und warum*. Retreived from: https://www.konstruktionspraxis.vogel.de/grundlagen-des-klebens-wann-klebverbindungen-versagen-und-warum-a-
14. El-Soudani, S. M. (1978). Profilometric analysis of fractures. *Metallography, 11(3),* 247–336. https://doi.org/10.1016/0026-0800(78)90045-9.

Customer Benefit Oriented Approach on the Application of Additive Manufacturing Potentials Based on Product Property Trade-Off's

Sebastian Kuschmitz, Daniel Fuchs, and Thomas Vietor

Abstract

Advances in process and material technology of Additive Manufacturing (AM) and the design freedom resulting from the layer-by-layer build-up principle provide new possibilities in product design. In order to utilize the resulting AM potentials in product development in a focused and effective manner and thus to increase the overall product performance, the research field "Design for Additive Manufacturing" (DfAM) supports the identification of difficulties and provides suitable solutions, such as databases for the transfer of AM-specific knowledge, or design methodologies for the product development context. In this paper, a customer benefit oriented approach based on product property trade-offs for the application of AM potentials considering existing DfAM methods is presented and evaluated by academic and industrial workshops. For this purpose, the workshop concept and the required tools for the identification of possible conflicts of objectives and other DfAM tools are explained and exemplary results of the conducted workshops are presented.

Keywords

Design for Additive Manufacturing (DfAM) • Additive Manufacturing • Design Potentials • Identification of conflicts of Interests

S. Kuschmitz (✉) · T. Vietor
Technische Universität Braunschweig, Langer Kamp 8, 38106 Braunschweig, Germany
e-mail: s.kuschmitz@tu-braunschweig.de

D. Fuchs
Volkswagen AG, Berliner Ring 2, 38440 Wolfsburg, Germany

R. Lachmayer et al. (eds.), *Innovative Product Development by Additive Manufacturing 2021*, https://doi.org/10.1007/978-3-031-05918-6_20

1 Introduction

Although additive manufacturing (AM) technologies have emerged from the rapid prototyping context over the last 30 years, the industry continues to experience dynamic growth within the last decade [1]. This development is also evident from the amount of patents granted during the last few years. In 2011, 3.111 3D printing related patents were granted worldwide, in 2018 this number increased to an annual growth of 24.245 granted patents with an rising trend [2]. The market volume of additive manufactured final parts has also risen in recent years, although the share of final product applications that can be economically implemented in the medium term is in a single-digit percentage range [3]. As a result of its unique design and manufacturing freedoms, AM enables novel design potentials that enable innovative product designs and business models. In order to increase the purposeful and economically feasible application of AM in the long term, the customer benefit oriented use of AM potentials must be enhanced in order to ensure that the additional design freedom is taken into account in the early stages of the product development process benefitting the products overall performance. As shown in more detail in the following section, this motivates the field of research “Design for Additive Manufacturing (DfAM)”. DfAM pursues the goal of clarifying both facets of AM, the freedom in design and production as well as the restrictions, developing corresponding tools for knowledge provision and application. By developing suitable methods for the DfAM processes, customer benefit oriented use of AM design potentials can be achieved, thus promoting the creativity of the engineering designers simultaneously enabling the efficient and effective use of those potentials [4–6]. Currently, engineering designers familiar to conventional manufacturing processes (e.g. milling, casting, and molding) sometimes lack the necessary knowledge to develop products exploiting AM potentials in a purposeful and efficient manner, rarely considering them in the early stages of the product development process. One possible consequence is that the selective use and consideration of individual design potentials of AM does not always benefit product performance [6, 7].

To counteract this problem, this paper presents a customer benefit oriented approach for the application of AM potentials based on product requirement trade-offs. Thereby existing DfAM methods are taken into account and the achieved results evaluated by means of an academic and industrial workshop are portrayed. With the help of the introduced approach, product developers and engineering designers shall be equipped with a guideline for the customer benefit oriented application of AM potentials, which furthermore also indicates helpful tools in the specific development phases of the product. In the scope of this contribution, basic information on the state of the art in the field of research DfAM is provided, followed by the introduction and description of the developed approach for customer benefit oriented application of AM potentials, including a detailed description of the individual procedural phases and the necessary tools. Additionally, the setting of the conducted industrial and academic workshops is explained and discussed. Finally, the concluding results are summarized and discussed as well as the outlook formulated.

2 Design for Additive Manufacturing: Current View

AM technologies present engineering designers with special challenges in the application of design potentials, since a multitude of potentials combinations exist, often increasing development complexity. In addition, due to the increasing application of AM, the need for tools and methods for the customer benefit oriented application of AM potentials is gaining relevance.

The DfAM research field addresses this problem with the provision of knowledge in form of different methods and tools [8]. However, it is also important that a change in mindset occurs in the early conception and design phases of product development, as otherwise the design freedoms of AM processes cannot be fully exploited [9, 10]. Thus, traditional design patterns based on manufacturing constraints and potentials with respect to conventional processes must also be adapted [10, 11].

Additional aspects are that not only conventional manufacturing restrictions are the cause for suboptimal part design and layout, but also lack of knowledge during the design phase, insufficient or missing design tools as well as time capacities. For this reason, the DfAM field of research develops and provides methodological tools for the targeted application of AM [8, 12].

In addition to considering design options and design freedoms, the process restrictions of AM processes [8, 13–18] are increasingly included and integrated into the development of methods and tools. Those might be the necessity of support structures, achievable material properties and surface qualities, post-processing efforts, amongst other process-specific restrictions.

In the research field DfAM meaningful application of newly gained design freedom and manufacturing flexibility and thus of a widened solution space for product design and resulting business models is targeted. As a result of this stage it is important to point out, that AM does not always lead to non- consideration of manufacturing restrictions and additionally no cost-neutral increase in geometric complexity can be expected, since the decreased complexity due to tool-less manufacturing on production often results in increased development complexity [19].

3 Customer Benefit Oriented Application of AM Potentials

Due to the layer-by-layer and tool-less build-up process, AM processes enable a multitude of novel design possibilities related to the functional and geometrical composition of a product. As a result, complex lattice structures, undercuts or bionic shaped geometries can be manufactured without significant additional effort during production [15, 20, 21]. However, these potentials should only be purposefully integrated into product design, otherwise the AM implementation does not result in any optimization of the parts performance. For example, solely additively manufacturing a brake caliper series geometry initially designed for casting processes without a redesign most likely won't lead to an increase in parts performance neither exploit AM design potentials in a holistic manner. Therefore the comparison of casted and the additively manufactured component with the same initial geometry is not expedient for a technology assessment.

In order to enable a customer benefit oriented implementation of AM potentials in the conception and design process, the research field DfAM provides the necessary information and tools for engineering designers during product development. The *systematic network of AM design potentials* according to Kumke [15] categorizes several levers consisting of design potentials and the value propositions achievable through their implementation into thematic groups such as form and material complexity, cost reduction, or overall product benefit. With each respective design lever an associated value proposition can be achieved. Both, lever and value preposition, represent one AM design potential, which summed up result in a holistic far-reaching design potential network. This way the engineering designer is enabled to directly identify which product properties might benefit by the implementation of a specific AM potential [15].

However, the use of AM potentials does not necessarily have to have exclusively beneficial effects on the properties of a product, but may also cause selective negative effects. Therefore, conflicting value propositions were identified by Fuchs et al. and compared in a matrix of conflicting AM potentials [19]. This matrix represents an additional DfAM tool and is intended to be utilized in combination with the systematic network of AM design potentials. The matrix of conflicting AM potentials is structured in a pair-by-pair comparison of all product related AM value propositions indicating physical correlations and general trade-offs amongst them. Thereby the matrix of conflicting AM potentials enables the engineering designer eager to exploit multiple AM potentials in one product to acquire additional information regarding the desired combination of AM potentials. This way, specific trade-offs are outlined, which on the one hand point out possible challenges and on the other hand serve to sensitize the user. In addition, suggestions for possible solutions are provided to the engineering designer for the identified trade-offs of interest. This way, a customer benefit oriented exploitation of AM potentials avoiding hidden collateral effects is facilitated, even if engineering designers are not AM experts.

Table 1 shows an excerpt from the matrix of conflicting AM potentials.

In order to receive purposeful consideration of AM technologies in the product development process, an approach for the customer benefit oriented application of AM potentials was developed in the context of this work. This approach is intended to be applied in the early stages of the product development process with the objective to optimize trade-offs in opposing product properties. In the early phases of the product

Table 1 Extract from the pair-by-pair matrix of conflicting AM potentials (freely translated from [19]) displaying conflicts of the value preposition "design space reduction" (lines) with other value prepositions (columns) derived from the systematic network of AM design potentials by Kumke et al. [4]

Product benefits	Description	2. Weight reduction	3. Higher efficiency in energy conversion and transport	4. Energy absorption improvement	…	12. Insulation improvement
1. design space reduction	⚡ = conflict	⚡	⚡	⚡	…	⚡
	Description	Lattice structures might leads to an increase in design space and a decrease in weight	Reduction of design space might decrease curvature radii and thus lead to flow losses	Design space reduction might reduce the transmission area and worsen energy absorption		Mesoscopic structures can improve the insulation but increase the design space
	Design levers related to value proposition in line	Lattice structures, honeycomb structures, irregular porous structures	Free-form geometries in cavities etc.	Lattice structures		Lattice structures, honeycomb structures, irregular porous structures
	Design levers related to value proposition in column			Integral design, small distances between features, large cross-section changes		
	Alternatives to defuse conflicts	Topology optimization, lattice structures + wall thickness combination, multiple materials in one component		Multi-material design		Multiple materials, wall thickness combination, surface textures

development process the holistic exploitation of AM potentials is most promising, as the functional structure and the partitions of the components are not yet determined.

Figure 1 gives an overview of the developed approach including the main phases to

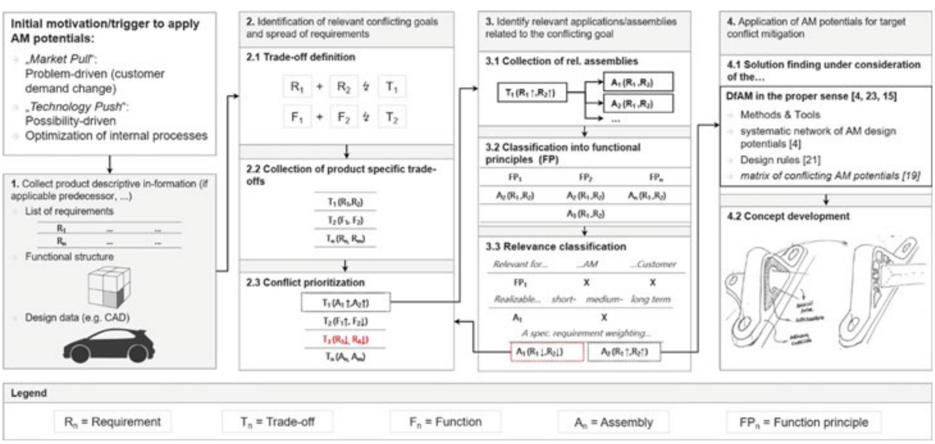

Fig. 1 Overview of suggested approach for a customer benefit oriented application of AM potentials targeted optimization of product property trade-offs including methods and tools from [15, 19, 21, 23]

be executed including helpful tools to do so. A market pull or a technology push is assumed as potential initial triggers for the application of AM potentials. A market pull describes a problem-driven approach, which can be caused, for example, by changes in customer requirements or by unforeseen technical problems. The Technology Push, on the other hand, describes a possibility-driven approach which, for example, enables component optimization through further developments in manufacturing technology, so that an increase in performance or a cost saving might occur [22].

In the first phase, the necessary information about the product, the assembly or the part to be developed is collected. This being either an original design, an adaptive design or a variant design [24]. The product specification including the list of requirements or specifications, the functional product structure and existing 3D data such as design space and package models and possible predecessor parts are taken into account as relevant information.

After all relevant information has been gathered, all product requirements and derived functions are subsequently examined and possible conflicts arising from contradicting requirements are identified in the second phase (see Fig. 1, phases 2.1 and 2.2). In this phase, the product requirements are assessed for trade-offs independently of the part and components partitions, ensuring that conflicting requirements are identified regardless of conventional part geometry and other part-specific characteristics of previous designs that narrow down the solution space. In phase 2.3 the identification of relevant trade-offs and diverging requirements is concluded with the prioritization of the individual target conflicts. Prioritization is based on the relevance of the identified trade-off for the overall product performance from a customer perspective.

In the subsequent third phase, the identified requirement trade-offs on product level are assigned to affected components and assemblies. (See Fig. 1 phase 3.1) Those respective assemblies are structurally categorized into basic functional principles (e.g. kinetic energy absorption, fluid-, heat- transfer, vibrational resistance, etc.…) necessary to realize product specific features. This way the suitability of AM for a specific assembly can be assessed based on the functional principles to be realized and not only on the predecessors embodiment. Subsequently in Fig. 1 phase 3.3 a classification of the suitability of AM for the optimization of identified component or assembly is assessed. In focus of this assessment are in general the compatibility of the component specific functional principles with general AM characteristics based on DfAM knowledge and simultaneously process AM restrictions specific to the considered technology (e.g. build volume, accuracy, material properties, etc.). Assemblies with low classified fit to AM characteristics and restrictions are not further considered. Otherwise, components have been identified for the following conception phase. The analysis is intentionally carried out on component/assembly and not on part level. This way opportunities for functional integration and part consolidation are not excluded in the early stage of the analysis.

However, in order to exploit the AM optimization potential for the identified components and assemblies as holistically as possible, in the fourth phase it is required to rethink and if necessary redesign the component of interest including its assemblies and parts with support of the indicated DfAM tools. As particularly suitable for the development of conceptual solutions are those DfAM methods indicated in Fig. 1. After completion of conceptual solutions, part design concepts are developed based on identified AM potentials and their relations among each other (see Fig. 1, phase 4.2). As a result, a design concept is derived, which addresses customer relevant product requirement trade-offs, which is suitable for a certain AM process and takes AM potentials systematically into consideration. The derived concept is suggested for further detailed development activities according to the product development process of choice.

Overall, the proposed approach for the customer benefit oriented application of AM potentials represents an opportunity to examine existing and new products for optimization potentials using AM processes, including the direct relation to customer relevant product properties and assistance for the concrete implementation of the targeted solution ideas. The applicability of the approach was further tested in the academic and in the corporate environment by means of two interactive workshops explained in further detail in the following chapter.

4 Validation Workshops

The feasibility of the presented approach for the customer benefit oriented application of AM potentials was tested in the context of this work in two separate workshops, one conducted in the academic and one in the corporate environment, both based on the use-case of a front section of a premium sports car. For this purpose, a total of 12 participants mainly with expertise in the field of automotive engineering, design and product development as well as manufacturing experts were invited. The workshops were conducted equally in both environments. Only the professional background of the participants varied slightly, as half of them are primarily active in the research environment and the other half in the corporate environment. The vast majority of the participants were 25–34 years old males with two exceptions, one being younger than 25 and one older than 50.

The workshops were designed and conducted as online workshops to comply with health and safety measures due to the occurring COVID-19 pandemic. At the beginning of the workshops, a short introduction to the topic of AM and DfAM was given, so that each participant was provided with basic AM knowledge. The main topic was focused on engineering design using exemplary digitally visual objects. Additional aspects regarding economic and ecological potentials of AM were also mentioned. Furthermore, do’s and don’ts examples of AM show-cases were shown to enhance the awareness of the workshop participants for purposeful and less purposeful AM applications. As mentioned in

Sect. 2, additive manufacturing of parts geometries developed for conventional manufacturing processes without rethinking the conceptual design is most likely not exploiting AM potentials properly. As positive examples, AM applications were demonstrated that were explicitly developed for AM, taking different potentials and limitations of AM into account.

Subsequently to the introduction and briefing, the interactive work phases were conducted. Overall, the workshop was structured in two main phases, each of them consisting of a work phase and a result presentation (1st phase compare Fig. 1, phase 2 and 3, 2nd phase compare Fig. 1, phase 4). The first work phase comprises the identification of product properties trade-offs and components/assembly of interest on the exemplary vehicle. The objective of the first work phase was to use the provided approach and tools to identify competing requirements and functions in the requirements list and functional structure of the front end section of the vehicle of interest. Figure 2 shows the provided worksheet as simplified specification sheet including a list of requirements, an abstract extract of the functional structure as well as an overview of the front end assembly of the vehicle. The 3D-Data of the front end was provided as an interactive 3D PDF enabling the participants to continuously rotate and hide/show individual parts of the assembly during the workshop.

The list of requirements in Fig. 2 indicates exemplary types of requirements in the areas of driving dynamics, comfort, consumption and safety. The function structure suggests exemplary functional groups from the vehicle areas of body, chassis, electronics, interior equipment and assemblies. In the first work phase, the workshop participants were supposed to identify competing requirements and functions. Exemplarily the requirements maximized vehicle velocity and maximized vehicle range can be mentioned as opposing objectives in the vehicles properties. The requirements of maximum velocity and low

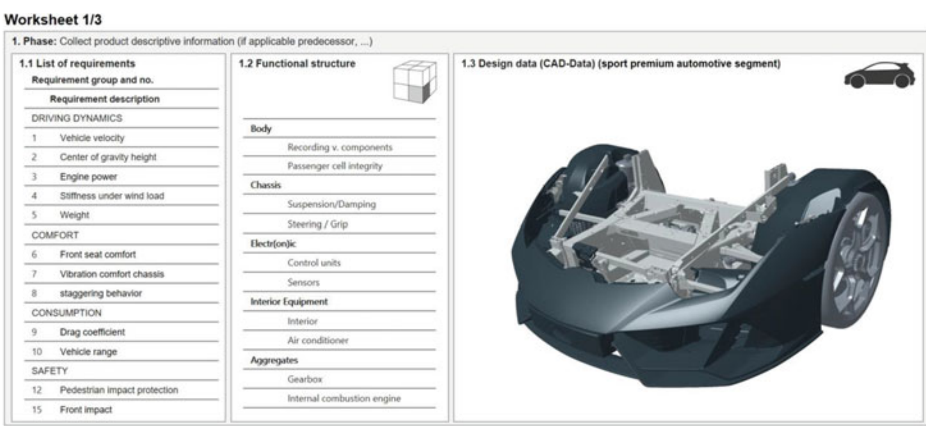

Fig. 2 Worksheet for identifying requirement conflicts in the requirements list and the functional structure

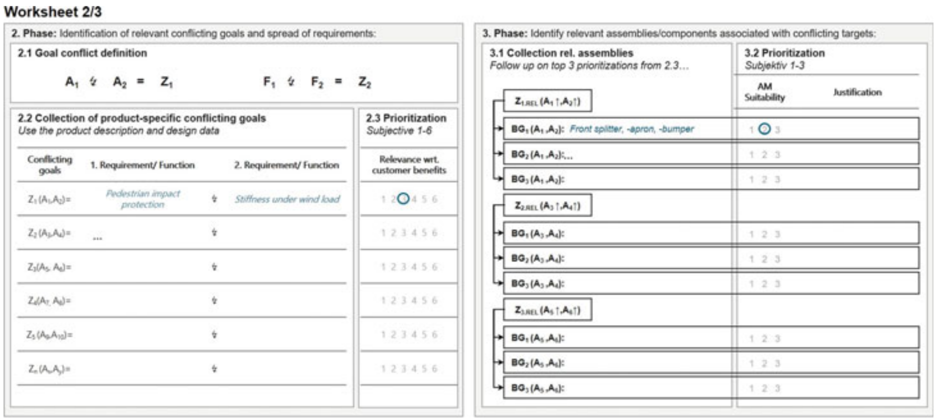

Fig. 3 Worksheet to identify relevant conflicting goals and spread of requirements

drag coefficient, on the other hand, can be considered compatible. All competing requirements and functions identified by the workshop participants were transferred to the second worksheet (see Fig. 3).

Figure 3 shows the second worksheet of the first workshop work phase, in which the identified trade- offs are entered, prioritized and assigned to concrete involved vehicle assemblies. Subsequently, all target conflicts are subjectively prioritized on the basis of their relevance for the customer (see phase 2.3 in Fig. 3). For example, requirements such as vehicle range and seat comfort are rather perceived by the customer than frontal impact energy dissipation and stiffness under aerodynamic wind pressure, although these requirements are highly important as well. In the two workshops, several specific assemblies were assigned as potentially beneficial for the customer, for example wheel carriers, brake calipers, bumpers and axle components in general were identified as potential assemblies with optimization potential linked to customer perceived vehicle properties. In addition to the identification of the parts and assemblies, their AM suitability was also rated according to the background knowledge of the participants. In particular, large volume shell parts such as bumpers were found to have little potential for additive manufacturing, mostly due to their size in comparison with available build volumes. After all trade-offs were identified and assemblies were assigned, the first work phase was concluded and the results were presented to the workshop participants. In this way, the participants were able to compare results and take away inspiration for the second work phase.

With a presentation of the helpful tools, the second work phase was initiated. The tools used were the systematic network of AM design potentials [15], the matrix of conflicting AM potentials [19], design rules for AM [21] and ideation sheets. The task of the participants in this phase was to select 2–3 identified assemblies and to generate concepts on how to optimize them with the help of the tools provided. The ideas developed for the selected components were documented in the ideation sheets (see Fig. 4).

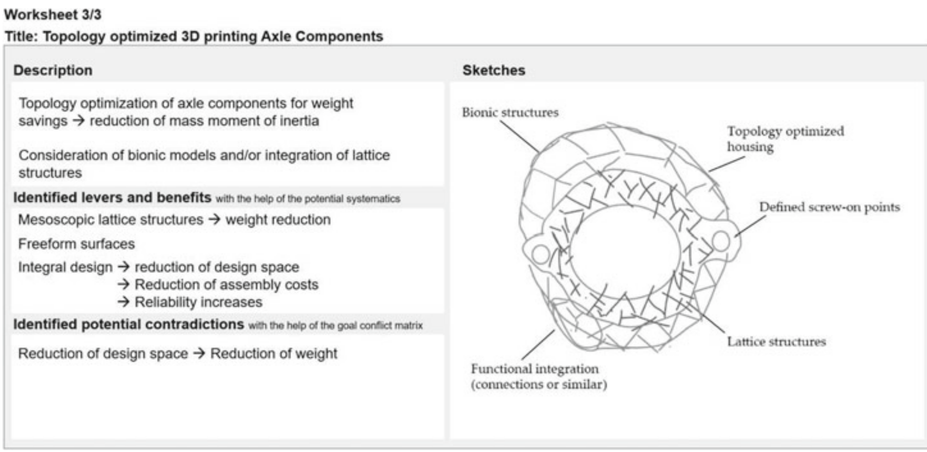

Fig. 4 Ideation sheet to specify and document the applied AM potentials according to identified trade-offs

Figure 4 shows an exemplary sketch of a topology-optimized axle component for AM. The idea of this adapted axle component is to achieve weight savings by means of topology optimization in order to reduce the rotational mass and therefore the moment of inertia. Identified levers and value propositions in the systematic network of AM design potential were the mesoscopic lattice structures, weight reduction, free-form surfaces, integral design, design space reduction, assembly cost reduction and reliability increase. Conflicting AM potentials identified by the participants were “design space reduction” versus “weight reduction”, as a weight reduction often goes hand in hand with increased cross-sections. On the right hand side of the idea sheet a virtual sketch illustrates the re-imagined axle component. With the completion of the ideation sheets, the second work phase of the workshop was attained and finalized with the presentation of the results to all participants.

A total of five comprehensible conceptional ideas were developed during the workshops and two further ideas were sketched out. Additional exemplary resulting ideas were heading towards additively manufactured joints in the crash structure of the vehicle and damping elements to accommodate the steering assembly as well as topology-optimized axle components. In the context of these concepts, 10 design levers and 12 value propositions from the systematic network of AM design potentials were applied and five potential contradictions were identified using the matrix of conflicting AM potentials. The ideation sketches varied greatly in their comprehensibility, due to digital challenges such as sketching with a mouse and time constraints. In addition, even though the conceptual ideas differed slightly in between participants, no general differentiation in the results of academic and the corporate participants were noticed. One reason for this could be the participants advanced experience in the field of AM. It is possible that noticeable differences between academic a corporate environment could occur when dealing with non-experts in this topic.

In conclusion, good and comprehensible concepts were developed in the course of both workshops, which, in addition to the AM potentials identified, were also able to highlight some conflicts among them, which could, however, be mitigated with the help of the matrix of conflicting AM potentials. However, it became clear that the user-friendliness of the matrix of conflicting AM potentials has room for improvement due to the documents size and therefore the time necessary to obtain the necessary information. Nevertheless, the general added value was confirmed in the evaluation and a transfer to a digital user friendly version was suggested. The online workshops conducted on the customer benefit oriented application of AM potentials were also positively rated by the participants and, according to the evaluation, both the approach procedure and the tools used were rated as useful and helpful for the purposeful application of AM potentials.

5 Conclusion and Outlook

In the context of this paper, an approach for the customer benefit oriented application of AM potentials was presented and carried out in two workshops, one industrial and one academic. Furthermore, the necessary tools for the presented approach were utilized and strengths and weaknesses were identified accordingly. Although the research work presented addresses some challenges in the field of AM processes, there is still a great need for action in the field of DfAM to ensure a customer benefit oriented application of AM potentials and thus to fully exploit the optimization potential offered by this technology. The workshops held were rated positively overall by the participants, and the tools used and the approach presented for the customer benefit oriented application of AM potentials were also considered helpful. The evaluation of the workshops showed that the implementation and the workshop concept were approved by the participants and that the structure of the work phases and the integration of own ideas was successful. Overall, most participants were satisfied with the workshop results and rated the approach suggested as purposeful. In the area of methods and tools, the systematic network of AM design potentials [15], the matrix of conflicting AM potentials [19] as well as their use were assessed as goal-oriented and useful. In addition, the general procedure for the optimization of parts was also rated useful and comprehensible. The general accessibility to the 3D-Data as 3D-PDF was rated as helpful by the participants. All in all, the workshops were a success in which good and useful results were achieved by the participants with the help of the approach presented and the tools used. The tools are helpful in finding conflicting product requirements or identifying relevant components or assemblies. It was also found that the systematic network of AM design potentials [15] and the matrix of conflicting AM potentials [19] exhibit symbioses and complement each other, facilitating product development for additively manufactured parts.

The approach presented and the tools used in the two workshops offered a good opportunity to compensate for the lack of AM knowledge and generates plausible solutions in a purposeful manner. Even though there is a far-reaching need for further research in the field of DfAM in order to fully implement the customer benefit oriented application of AM potentials in product development. In addition, tools such as the matrix of conflicting AM potentials offer optimization potential in terms of usability.

Another research focus with respect to DfAM is complexity management in the context of engineering design itself. The layer-by-layer build process allows complex structures to be manufactured often without significant manufacturing efforts. However, this complexity is distributed to the earlier phases of the product development process. This shift in complexity results in the fact that, for example, complex and highly optimized designs (e.g. bionic distinct lattice structures) are still challenging to be realized with conventional CAD and CAE tools, making the engineering design process significantly more complex. Some companies offer dedicated CAD tools for AM, however these tools are rather focused on AM process specific challenges and do not yet provide the required capabilities for highly optimized complex designs. Finally, enabling additional and otherwise not feasible customer value in future products is one mayor pillar to propel AM technologies. The approach presented here might contribute accordingly.

References

1. Wohlers, T., Wohlers Associates, Campbell I. et al. (2020) Wohlers Report 2020: 3D Printing and Additive Manufacturing State of the Industry. Wohlers Associates.
2. IPlytics GmbH (2019) Patent and litigation trends for 3D printing technologies. Retrieved June 16, 2021 from https://www.iplytics.com/de/report-de/patent-litigation-trends-3d-printing/.
3. Seidel, C. (2019). Direct Manufacturing: Status Quo innerhalb der Additiven Fertigung. 5. Fachkonferenz 3D-Druck: Additive Fertigung in der Automobilindustrie. 5. Fachkonferenz 3D-Druck: Additive Fertigung in der Automobilindustrie. SV Veranstaltungen, München.
4. Kumke, M., Watschke, H., Hartogh, P., et al. (2018). Methods and tools for identifying and leveraging additive manufacturing design potentials. *International Journal on Interactive Design and Manufacturing, 12*, 481–493. https://doi.org/10.1007/s12008-017-0399-7.
5. Yang, S., Page, T., Zhao, Y.F. (2018). Understanding the role of additive manufacturing knowledge in stimulating design innovation for novice designers. In: Volume 4: 23rd Design for Manufacturing and the Life Cycle Conference; 12th International Conference on Micro- and Nanosystems. American Society of Mechanical Engineers.
6. Richter, T., Watschke, H., Schumacher, F.,Vietor, T. (ed) (2018). Exploitation of Potentials of Additive Manufacturing in Ideation Workshops.
7. Pradel, P., Zhu, Z., Bibb, R., et al. (2018). A framework for mapping design for additive manufacturing knowledge for industrial and product design. *Journal of Engineering Design, 29*, 291–326. https://doi.org/10.1080/09544828.2018.1483011.
8. Thompson, M. K., Moroni, G., Vaneker, T., et al. (2016). Design for additive manufacturing: Trends, opportunities, considerations, and constraints. *CIRP Annals, 65*, 737–760. https://doi.org/10.1016/j.cirp.2016.05.004.

9. Bin Maidin, S., Campbell, I., & Pei, E. (2012). Development of a design feature database to support design for additive manufacturing. *Assembly Automation, 32*, 235–244. https://doi.org/10.1108/01445151211244375.
10. Gibson, I., Rosen, D., & Stucker, B. (2015) *Additive manufacturing technologies: 3D printing, rapid prototyping, and direct digital manufacturing*, 2nd (Eds.). Springer eBook Collection. Springer.
11. Rosen DW (2007) Design for Additive Manufacturing: A Method to Explore Unexplored Regions of the Design Space. The University of Texas at Austin.
12. Rosen, D. W. (2007). Computer-aided design for additive manufacturing of cellular structures. *Computer-Aided Design and Applications, 4*, 585–594. https://doi.org/10.1080/16864360.2007.10738493.
13. Hague, R., Mansour, S., & Saleh, N. (2004). Material and design considerations for rapid manufacturing. *International Journal of Production Research, 42*, 4691–4708. https://doi.org/10.1080/00207840410001733940.
14. Gao, W., Zhang, Y., Ramanujan, D., et al. (2015). The status, challenges, and future of additive manufacturing in engineering. *Computer-Aided Design, 69*, 65–89. https://doi.org/10.1016/j.cad.2015.04.001.
15. Kumke, M. (2018). Methodisches Konstruieren von additiv gefertigten Bauteilen. Dissertation.
16. Kuschmitz, S., Watschke, H., Schumacher, F. et al. (2019). Bereitstellung von Lösungsprinzipien für die additive Fertigung zur Unterstützung der Bauteilkonzeption in der industriellen Praxis. In: Kynast M, Eichmann M, Witt G (eds) Rapid.Tech + FabCon 3.D International Hub for Additive Manufacturing: Exhibition + Conference + Networking. Carl Hanser Verlag GmbH & Co. KG, München, pp. 75–88.
17. Watschke, H., Kuschmitz, S., Heubach, J., et al. (2019). A methodical approach to support conceptual design for multi-material additive manufacturing. *Proc Int Conf Eng Des, 1*, 659–668. https://doi.org/10.1017/dsi.2019.70.
18. Schumacher, F., Watschke, H., Kuschmitz, S., et al. (2019). Goal oriented provision of design principles for additive manufacturing to support conceptual design. *Proc Int Conf Eng Des, 1*, 749–758. https://doi.org/10.1017/dsi.2019.79.
19. Fuchs, D., Kuschmitz, S., Kühlke, K., et al. (2020). Identifikation von Zielkonflikten bei der Anwendung von Potenzialen additiver Fertigungsverfahren. In R. Lachmayer, K. Rettschlag, & S. Kaierle (Eds.), *Konstruktion für die Additive Fertigung 2019* (Vol. 65, pp. 223–244). Berlin Heidelberg: Springer.
20. Gebhardt, A., & Hötter, J.-S. (2016). *Additive manufacturing: 3D printing for prototyping and manufacturing*. Hanser Publications.
21. Adam, G.A.O. (2015). Systematische Erarbeitung von Konstruktionsregeln für die additiven Fertigungsverfahren Lasersintern, Laserschmelzen und Fused Deposition Modeling. Dissertation.
22. Martin, M.J.C. (1994). *Managing innovation and entrepreneurship in technology-based firms.* Wiley Series in Engineering & Technology Management. Wiley, New York, NY.
23. Kumke, M., Watschke, H., & Vietor, T. (2016). A new methodological framework for design for additive manufacturing. *Virtual and Physical Prototyping, 11*, 3–19. https://doi.org/10.1080/17452759.2016.1139377.
24. Pahl, G., Beitz, W., Blessing, L., et al. (eds.). (2007). *Engineering design: A systematic approach* (3rd ed.). Springer-Verlag, London Limited.

Correction to: Automated Identification of Geometric Structures with Potential for Functional Integration

Marcel Winkler, Georg Jacobs, Philipp Jonas Fastabend, and Christian Konrad

Correction to:
Chapter "Automated Identification of Geometric Structures with Potential for Functional Integration" in: R. Lachmayer et al. (eds.), *Innovative Product Development by Additive Manufacturing* 2021,
https://doi.org/10.1007/978-3-031-05918-6_16

The original version of the book was inadvertently published with incorrect figures 2 and 4 in chapter 16. Now, they have been replaced with the correct figure in the updated version.

The correction chapter and book have been updated with the change.

The updated original version of this chapter can be found at
https://doi.org/10.1007/978-3-031-05918-6_16

R. Lachmayer et al. (eds.), *Innovative Product Development by Additive Manufacturing 2021*, https://doi.org/10.1007/978-3-031-05918-6_21

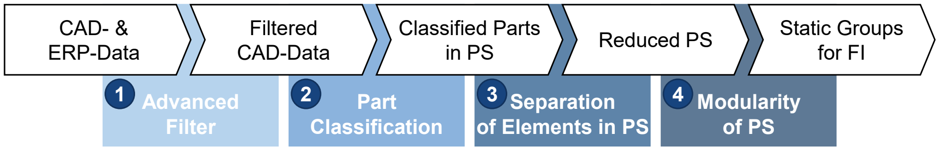

Fig. 2 Methodical approach for the identification of part groups with potential for functional integration

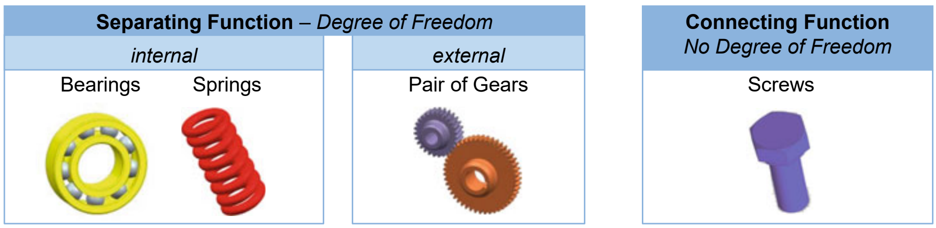

Fig. 4 Overview of different part classification groups with examples